Inclined Negatively Buoyant Jets and Boundary Interaction

by

Adam Timothy Crowe

Supervised by
Associate Professor Mark Davidson & Professor Roger Nokes

A thesis submitted in the partial fulfilment of the requirements for the Degree of Doctor of Philosophy in Civil Engineering

Department of Civil and Natural Resources Engineering
University of Canterbury
Private Bag 4800
Christchurch, New Zealand

Abstract

Inclined negatively buoyant jets are commonly used to dispose brine effluent produced by desalination plants. Desalination and associated research has expanded in recent years due to the continued depletion and degradation of natural potable water sources. Desalination plants are the preferred option for meeting water demand deficits in many countries around the world. Inclined negatively buoyant jets are produced when the brine is discharged at an upward inclined angle via an offshore pipeline and diffuser system. Previous experimental studies have focused on the rapid mixing and dilution achieved by these discharges, as well as geometric parameters. Dilution measurements between these experimental studies vary significantly, which is possibly due to variations in the location of a lower boundary on observed flow behaviour. In the present study, velocity field information is experimentally measured for inclined negatively buoyant jets and compared to integral model predictions. Experiments are conducted with and without a lower boundary influencing observed flow behaviour, thus allowing the effects of a lower boundary to be determined.

The particle tracking velocimetry experimental technique is employed to measure near field velocities of these discharges. Firstly, discharges with source angles between 15° and 75° are investigated without boundary influence in stationary ambient conditions. The source was a minimum of 655 mm above the bottom of the experimental tank to ensure there was no lower boundary influence on observed behaviour. Time-averaged and fluctuating data are extracted along the trajectory of discharges. All non-dimensionalised geometric and centreline velocity parameters are found to collapse. Empirical coefficients are compared to previous experimental studies and integral model predictions.

A new detrainment model is developed to predict the behaviour of inclined negatively buoyant jets without boundary influence. The model further develops recent attempts to allow for buoyancy flux reduction along the flow path. The reduction in buoyancy flux is dependent on the local parameters of the flow and simulates experimentally observed detrainment. Dilution, geometric, and velocity predictions are found to be improved over previous models when compared to experimental data.

Finally, a raised platform was placed inside the experimental tank to determine the influence of a lower boundary on inclined negatively buoyant jets. Source angles of 30°, 45°, and 60° are investigated at three different non-dimensional source heights. The

lower boundary is horizontal and ambient conditions are again stationary. Discharges impinge the lower boundary before forming a radially spreading layer along the boundary. Geometric and velocity data are compared to the first set of experiments in this study to determine the influence of the lower boundary on observed flow behaviour. Empirical coefficients at maximum height are similar with and without the influence of the boundary, whereas coefficients are substantially influenced at the return point when the boundary is present.

Acknowledgements

The writing of acknowledgements signifies the end of the PhD experience. I first started working on inclined negatively buoyant jets as a Masters' project, however this was extended to a PhD once the opportunity and funding became available. The development of the particle tracking velocimetry experimental system for submerged jet discharges was the first hurdle, which required a long stretch spent in the laboratory conducting experiments. The major earthquake events of September 2010 and February 2011 will be a memorable period in my life, while also providing complications to my research through damaged equipment. A PhD is a very singular experience as it requires working mostly alone on one project for a number of years (I was told three but got four). I have personally developed in many ways over the last few years, through the challenges and complications that accompany any research project.

The external support of many people provided the structure for a successful PhD. Firstly, I would like to thank my primary supervisor, Dr. Mark Davidson, for first proposing the topic and his continued support throughout. His belief in my ability to upgrade from a Masters' to a PhD was the push I needed. His advice from start to finish was always encouraging and his technical expertise was invaluable. The enthusiasm of my secondary supervisor, Dr. Roger Nokes, during my undergraduate courses sparked my initial interest in fluid mechanics. I was fortunate to use his Streams software extensively to analyse the laboratory experiments, which allowed the scope of my thesis to be expanded markedly. Although this project is outside of his research interests, his fundamental fluid mechanics knowledge improved this thesis tremendously.

I would also like to thank the laboratory technicians who helped me through the experimental phase of the project. Ian was always willing to help and obtain the needed consumables from suppliers in short order. Kevin was my go-to guy whenever I needed something made. His attention to detail and practical problem solving skills produced precisely constructed equipment that was easy to use. Alan provided much needed banter about motorcycles and many inane topics to get me through long days in the laboratory.

My fellow postgraduates provided help and advice through shared PhD experiences. Thanks to Cameron, Claire, Colin, and Sarah for the shared times in the fluid mechanics computer room. Also, thanks to my 3rd floor office mates, Debra, Julia, Greg, and

Craig for their demonstration of the hard work required to finish a PhD and for the company in the office.

I want to thank Davon Callander for all of her assistance and encouragement through the writing process. She gladly edited my engineer's spelling and grammar, with many comments about "how things are done in science". Finally, many thanks to my friends and family (Mum, Dad, Katrina, and Jemma) for their support throughout my many university years.

Contents

Chapter 1

Introduction

1.1 General Introduction

The depletion of natural potable water sources combined with increased water consumption has resulted in water demand deficits for an increasing number of communities. The quantity and quality of available natural potable water sources has degraded due to overuse, pollution, or salinisation (Lattemann *et al.*, 2010). The population of communities worldwide is increasing, resulting in increased water consumption for municipal, industrial, and agricultural purposes (Bleninger & Jirka, 2009). Arid regions such as the Middle East and North Africa have scarce natural water sources and require additional sources of fresh water to sustain their populations. Semiarid regions of Australia experienced a long drought period from 2003 - 2012 resulting in a need for more dependable fresh water sources.

Water demand deficits for large populations can be met through water conversation, wastewater recycling, and/or desalination. Water conservation through the modification of public behaviour and leak detection in the distribution network can reduce water deficits. However, water conservation is unable to compensate in regions with large water deficits. Wastewater recycling involves passing wastewater through treatment processes before being returned to the potable water network. There is strong public resistance to using recycled wastewater for food preparation and drinking. However, there is less resistance to using recycled water for garden watering and cleaning uses (Dolnicar & Schäfer, 2009). Desalination involves desalting saline water such as brackish water or seawater to produce potable water. However, the environmental effects and considerable energy demands of desalination need to be considered (Lattemann & Höpner, 2008). Large desalination plants have been the preferred option for meeting water demand deficits in many countries such as Saudi Arabia, United Arab Emirates, Oman, Qatar, Israel, USA, Spain, and Australia (Bleninger & Jirka, 2009).

Desalination technology was initially developed during World War II to supply

water to military bases in arid regions (Lattemann & Höpner, 2008). Development continued throughout the 20th century, with the first large scale plants built in the Middle East using distillation technology. Multistage flash (MSF) is the most common distillation process, however this process has a high energy consumption which requires large energy reserves. Reverse osmosis (RO) is a pressure driven membrane process that is more energy efficient than MSF (Einav *et al.*, 2003). Seawater reverse osmosis (SWRO) was the technology adapted in all six recently built large scale desalination plants in Australia (El Saliby *et al.*, 2009).

SWRO desalination plants are typically supplied with feedwater from the ocean through a pipeline connected to an open water intake, horizontal directional drilling system, or beach wells (Bleninger & Jirka, 2009). Pressure is applied to the feedwater on one side of a RO membrane filter. Water is able to pass through the membrane whereas salts are prevented from passing through. This results in potable water on one side of the membrane and hypersaline brine on the other side. Over 90 % of large desalination plants in operation dispose of their brine through an offshore ocean outfall (WHO, 2007). The potable water recovery rates are usually between 40 - 65 % of feedwater depending on the site specific seawater conditions and particular RO technology utilised (Voutchkov, 2011). The world's largest currently operating SWRO desalination plant in Ashkelon, Israel produces 330,000 m^3 of potable water per day (Lattemann *et al.*, 2010).

The potential impacts of each desalination plant project need to be evaluated individually. A comprehensive environmental impact assessment (EIA) is a mandatory requirement for any industrial project in many European countries, USA, and Australia (El Saliby *et al.*, 2009; Hodgkiess, 2009). Three of the main impacts that need to be considered for desalination are land use, energy consumption and brine disposal (Bleninger & Jirka, 2009). In terms of land use, SWRO desalination plants and pumping stations are built in coastal locations, which have competing interests with recreation and tourism uses (Einav *et al.*, 2003). In terms of energy consumption it was noted that MSF desalination plants are particularly energy intensive requiring approximately 15.5 KW h of energy for every cubic metre of water produced. RO desalination plants in contrast require significantly less energy with 4 - 7 kW h of energy used per cubic metre of water produced (Lattemann & Höpner, 2008). The cost of traditional sources of water continues to increase due to increased treatment and transportation costs. Whereas continuous technological improvements are reducing the energy consumption and other costs of desalinated water, so that desalination is becoming a viable option for many communities with water demand deficits. In addition to the impact of the brine discharge on marine life, impingement and entrainment of marine organisms are significant environmental issues for seawater desalination (Cooley *et al.*, 2006). Detrimental effects on marine organisms occur due to impingement when they become

trapped against mesh screens of open water intakes of the feedwater pipeline. Loss due to entrapment occurs when smaller marine organisms fit between the mesh screens and are drawn into the feedwater pipeline with no escape path.

The brine discharge not only contains high salt concentrations, but also chemicals used in the pretreatment of intake feedwater such as coagulants, antiscalants, or disinfectants (Cooley *et al.*, 2006; WHO, 2007; Dolnicar & Schäfer, 2009; Hodgkiess, 2009). However, the majority of chemicals are considered non-toxic to marine organisms or are discharged at non-critical concentrations (Bleninger & Jirka, 2009). Marine organisms have varying sensitivity to elevated salinity and a salinity tolerance test on the most sensitive site specific marine organisms is generally carried out as part of the EIA. The brine from SWRO desalination typically has a salinity 1.5 to 2 times greater than that of the ambient seawater at the disposal site (Voutchkov, 2011). The higher density of the brine makes it sink to the sea floor and this inhibits mixing. Thus the high volume flux brine discharge, which is continuous while the desalination plant is operating, can potentially damage marine fauna and flora near the disposal site (Einav & Lokiec, 2003). Benthic ecosystems such as seagrass meadows or macroalgae stands and related species such as urchins and shrimp are most susceptible to SWRO desalination discharges because they have limited movement. Fish, turtles and marine mammals are less affected as it is assumed they are able to avoid the discharge site (Lattemann *et al.*, 2010). Poikilosmotic organisms, such as molluscs, echinoderms, and annelids are particularly sensitive to changes in salinity as they are unable to regulate their osmotic pressure. Increases in salinity cause water to leave the cells of these organisms resulting in cell dehydration and possibly death (Voutchkov, 2011).

One option for brine disposal into the ocean is a surface discharge at the shoreline through an open channel. This option relies on the ambient motion of the ocean to mix and dilute the brine. This may be an alternative considered for high energy coastlines with less sensitive ecosystems. The second and most common discharge option in countries with discharge point effluent regulations, is disposal via an offshore pipeline and diffuser system. Figure 1.1 illustrates the behaviour of negatively buoyant brine discharging through a single port into the ocean. The brine is discharged at an upward inclined angle through a source (port outlet) with high velocity, which results in rapid mixing with the ambient seawater. Eventually the higher density of the brine causes the discharge to fall back to the sea floor, where it spreads laterally in all directions. The purpose of a diffuser system is to enhance the dilution of the brine, so that its salinity drops to a specified level, above the background salinity of ambient seawater. This reduction must occur within the mixing zone specified at the discharge location by the relevant regulatory authority. Diffuser systems for desalination plants typically have multiple ports, which are needed to achieve the required dilution given the large volume fluxes of brine generated.

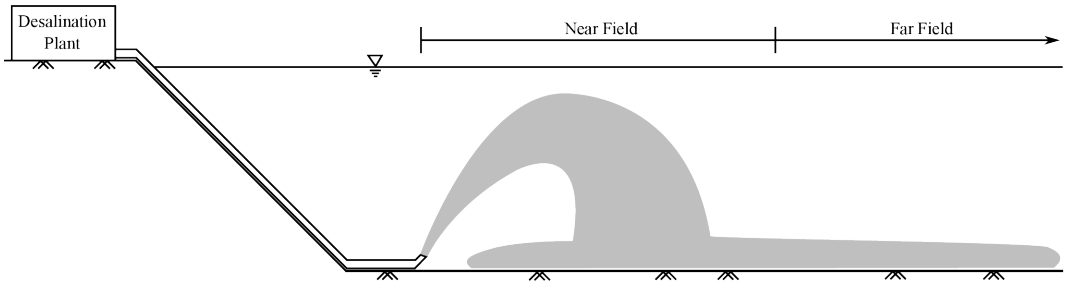

Figure 1.1 – Typical configuration for desalination plant outfall.

The behaviour of a brine discharge through a diffuser system can be separated into near and far field regions as shown in figure 1.1. The initial source characteristics determine the behaviour of the brine discharge in the near field region. The initial momentum flux, buoyancy flux, and discharge angle determine the trajectory and level of mixing achieved. The ocean or surrounding ambient motion can have a significant influence on the mixing in the near field region, but its presence enhances dilution and is not therefore critical in terms of diffuser design. The characteristics of the discharge at the source have limited influence on the behaviour after impingement, where the discharged fluid spreads laterally across the sea floor in the form of a gravity current. In this far field region, the ambient motion can again have a significant influence on the mixing and motion of the laterally spreading flow.

1.2 Scope of Research

This study focuses on the near field region of brine discharges, specifically inclined negatively buoyant jets (INBJs) and their boundary interaction with the sea floor. Recent experimental studies by Roberts *et al.* (1997), Cipollina *et al.* (2005), Kikkert *et al.* (2007), Shao & Law (2010), Papakonstantis *et al.* (2011a,b), Oliver (2012), and Lai & Lee (2012) have focused on the dilution and trajectory of INBJ discharges. The presence and location of a lower boundary in these experimental studies varied such that the dilution measured at the impingement point varied significantly at a particular discharge angle, and this variation was evident for all initial discharge angles. Commercial numerical models such as CORMIX, VISJET, and Visual Plumes are only valid along the discharge trajectory prior to the impingement, because boundary effects are not modelled (Palomar *et al.*, 2012b). Oliver (2012) states that *"a systematic experimental study should be undertaken to investigate and accurately characterise the effect of bottom-boundary interaction"*. Shao & Law (2010) and Lai & Lee (2012) provided limited velocity field information for these discharges alongside concentration data. The purpose of this research is to provide comprehensive experimental velocity field information for INBJs and to measure the effects of a lower boundary on these discharges. Experiments are conducted with and without a lower boundary influencing

the flow behaviour, thus allowing direct comparisons to be made.

Extensive research has been carried out over many years for positively buoyant jet discharges that result from municipal and industrial waste effluent disposal. These discharges consist mostly of fresh water with a waste contaminant and are typically less dense than seawater, resulting in the discharge rising to the surface of the ocean. Initial momentum driven jet regions and buoyancy driven plume regions are both present in positively and negatively buoyant diffuser discharges. Chapter 2 contains a summary of jet and plume research relevant to negatively buoyant jets. Previous INBJ experimental studies, including those mentioned above, are reviewed and compared.

Currently available numerical and analytical models use momentum and mass relationships with simplifying assumptions to predict discharge behaviour. These relationships and assumptions are examined in Chapter 3, where an alternative numerical model is also developed. Validation of the numerical model outputs and assumptions with experimental data is critically important, if predictions of desalination discharge behaviour are to be improved.

High quality experimental velocity field information was obtain using a flow visualisation technique known as particle tracking velocimetry (PTV). PTV involves seeding the discharge with tracer particles that are illuminated with a laser, thus allowing the velocity of the particles to be determined from images captured with a video camera. A two-dimensional velocity field of a thin centreline slice was determined for each experiment. The PTV experimental system is presented and verified in Chapter 4.

INBJ experiments were conducted with a wide range of initial angles and source conditions in a still ambient fluid. As noted above, a still ambient is the worst case scenario for discharges into the ocean, because the presence of ambient motion increases the mixing and associated dilution. A stationary ambient also simplifies the problem, allowing the discharge behaviour and mixing associated specifically with the source conditions to be isolated. Chapter 5 provides the results of inclined negatively buoyant experiments, where the lower boundary is sufficiently far from the source such that it had no influence on the observed behaviour. Existing models and the model developed in this study are compared to experimental data.

There is limited research regarding the complex lower boundary interaction of INBJs. An experimental investigation is conducted for the boundary interaction of INBJs for three initial discharge angles. The height of the source above the lower boundary is varied so that the boundary effects can be assessed. Chapter 6 contains the results of this investigation with comparisons made between the results of INBJ experiments with and without the influence of a lower boundary.

Overall conclusions from this study are drawn in Chapter 7, with areas for future work suggested.

[Intentionally left blank]

Chapter 2

Literature Review

2.1 Introduction

Inclined negatively buoyant jet discharges have distinct jet and plume regions. The jet region is located near the source on the rising side of the discharge where behaviour is dominated by the initial momentum flux. The plume region is located on the falling side of the discharge, where behaviour is dominated by the buoyancy flux resulting from the density difference between source and ambient fluids. A transition region also exists between the jet and plume regions where the behaviour is controlled by a combination of the initial momentum flux and buoyancy forces. The fundamental knowledge and governing equations relating to INBJs will be detailed in the following section. This will provide a base understanding of these discharges and turbulent statistics.

INBJs are typically turbulent at the exit of the source. The Reynolds number (Re) is a non-dimensional parameter that is a ratio between inertial and viscous forces as shown in equation 2.1.

$$Re = \frac{U_o d}{\nu} \tag{2.1}$$

where U_o is the initial uniform velocity, d is the inner diameter of the source, and ν is the kinematic viscosity of the fluid. The Reynolds number at which discharges become turbulent and independent of viscosity can not be predicted. However, discharges with $Re > 2000$ are considered turbulent, although turbulence is not fully developed until $Re \approx 4000$ (Fischer *et al.*, 1979).

The Navier-Stokes equations are the governing equations used to describe incompressible turbulent fluid flows. Equation 2.2 and 2.3 are the momentum and continuity relationships in index notation for incompressible turbulent flow, where u is the velocity of the fluid, t is time, x is spatial direction, and ρ is fluid density. The gravity term is absorbed into the pressure term to produce the modified pressure, p.

$$\frac{\partial u_i}{\partial t} + u_j \frac{\partial u_i}{\partial x_j} = -\frac{1}{\rho}\frac{\partial p}{\partial x_i} + \nu \frac{\partial^2 u_i}{\partial x_j \partial x_j} \tag{2.2}$$

$$\frac{\partial u_i}{\partial x_i} = 0 \tag{2.3}$$

Reynolds decomposition allows velocity to be separated into mean (time averaged) and fluctuating velocity components as shown in equation 2.4, where the overline bar indicates the mean term and prime indicates the fluctuating term.

$$u_i = \bar{u_i} + {u_i}' \tag{2.4}$$

Time averaging velocity in one spatial direction gives the mean velocity, i.e. $\overline{u_i} = \bar{u_i}$. However, time averaging two orthogonal components of velocity gives:

$$\overline{u_i u_j} = \overline{(\bar{u_i} + {u_i}')(\bar{u_j} + {u_j}')} = \bar{u_i}\bar{u_j} + \overline{{u_i}'{u_j}'} \tag{2.5}$$

Modified pressure in equation 2.2 can also be decomposed into mean and fluctuating terms in the same way as velocity in equation 2.4. Decomposing velocity and pressure terms in equation 2.2 and then averaging produces the Reynolds-averaged Navier-Stokes (RANS) equation for momentum shown below.

$$\frac{\partial \bar{u_i}}{\partial t} + \bar{u_j}\frac{\partial \bar{u_i}}{\partial x_j} = -\frac{1}{\rho}\frac{\partial \bar{p}}{\partial x_i} + \nu \frac{\partial^2 \bar{u_i}}{\partial x_j \partial x_j} - \frac{\partial \overline{{u_i}'{u_j}'}}{\partial x_j} \tag{2.6}$$

The last term in equation 2.6 is the gradient of the turbulent stress, which results from averaging the advection (second) term of equation 2.2. The turbulent stress is known as $-\overline{{u_i}'{u_j}'}$, which results in the following four important turbulent stress terms for jet and plume discharges; axial ($u'u'$), radial ($v'v'$), azimuthal ($w'w'$), and shear ($u'v'$). The circumferential symmetry of jet and plume discharges means shear stresses ($u'w', v'w'$) are zero (Pope, 2000). Normalising the important turbulent stress terms by the maximum mean cross-sectional velocity results in turbulent intensities. Turbulent intensities in the radial and azimuthal directions were found to be similar in experiments of jet discharges (Panchapakesan & Lumley, 1993; Hussein *et al.*, 1994). The turbulent statistics of pure jets are examined in section 4.5.2 and these are examined in section 5.3.2 for INBJs. The fundamental behaviour of INBJs is similar to pure jets and pure plumes. These provide a basis of comparison in this study for results of INBJ experiments (Chapters 5 and 6).

2.2 Pure Jets

The behaviour in the jet region of an INBJ is similar to pure jets. In the context of the present study, pure jets are created by discharging one fluid through a round source into a stationary ambient fluid of the same density. Both fluids are assumed to be incompressible and the flow through the source is assumed to be steady. The velocity profile exiting the source is uniform, resulting in the development of turbulent shear layers between the two fluids. The shear layers erode the edges of the uniform velocity profile as the flow moves away from the source. The mean velocity profile transitions to a Gaussian distribution over a distance of about six source diameters, known as the zone of flow establishment (ZFE) (Fischer *et al.*, 1979).

Pure jets have been studied extensively by numerous researchers including Corrsin & Uberoi (1951); Wyganski & Fielder (1969); Papanicolaou & List (1988); Panchapakesan & Lumley (1993); Hussein *et al.* (1994); Law & Wang (2000); Wang & Law (2002); Ying *et al.* (2004). Precedence is given to recent studies as experiments before the 1970s were criticised due to recirculation effects resulting from the limited size of experimental facilities (Law & Wang, 2000). The initial momentum flux from the source is conserved for a pure jet when discharged into an unlimited environment as no other forces are acting. The initial momentum flux (M_o) is defined as:

$$M_o = Q_o U_o \tag{2.7}$$

where the initial volume flux (Q_o) is defined as:

$$Q_o = \frac{\pi d^2}{4} U_o \tag{2.8}$$

After the ZFE, the centreline velocity (u_c, maximum velocity in mean cross-section profile) decreases at a rate inversely proportional to the distance from the source. The volume flux increases at a rate directly proportional to the distance from the source. A characteristic length scale (l_Q) defines the relative importance of initial volume and momentum fluxes in equation 2.9 (Fischer *et al.*, 1979).

$$l_Q = \frac{Q_o}{{M_o}^{1/2}} = \sqrt{\frac{\pi}{4}} d \tag{2.9}$$

Due to entrainment the relative size of l_Q is small such that the flow is considered independent of the initial volume flux after a short distance downstream of the source. Therefore, the flow is only dependent on the initial momentum flux and the distance downstream of the source or path length (s). The discharge spreads radially as shear layer generated eddies entrain ambient fluid. Mean Gaussian velocity profiles are self similar beyond the ZFE and axi-symmetric about the centreline. Jet width is defined as the radial distance from the centreline velocity to where the velocity is equal to $e^{-1}u_c$.

The radial spread rate is determined from the change in width with path length.

Panchapakesan & Lumley (1993) measured the turbulent and mean velocity properties of air jets using hot wire probes. Momentum was integrated over the cross-sectional profile and related to the initial momentum flux, M_o, with equation 2.10.

$$M = 2\pi \int_0^\infty \left[\bar{u}^2 + u'^2 - \frac{1}{2}\left(v'^2 + w'^2\right) \right] r\mathrm{d}r = M_o \tag{2.10}$$

Momentum flux along the path length of the jet was found to be within 5 % of the initial momentum flux indicating that the assumption of momentum conservation is correct. Hussein *et al.* (1994) took stationary hot wire, flying hot wire, and laser doppler anemometry (LDA) velocity measurements in air jets. Measurements of mean centreline velocity decay were found to be similar to those of Wyganski & Fielder (1969) and Panchapakesan & Lumley (1993). Momentum flux was found to be conserved and turbulent intensities were reported. Summary values from Panchapakesan & Lumley (1993) and Hussein *et al.* (1994) can be found in table 4.1 (Section 4.5.2).

2.3 Plumes and Transition Region

The plume region on the falling side of an inclined negatively buoyant discharge shares similar properties with a pure plume. The theoretical definition of a pure plume involves the discharge of one fluid into a stationary ambient fluid of a different density. The initial volume and momentum fluxes are assumed to be zero such that the discharge behaviour is only dependent on the initial buoyancy flux, B_o (Equation 2.11) and the path length.

$$B_o = \hat{g}_o Q_o \ , \tag{2.11}$$

where $\hat{g}_o$ is the initial reduced gravity defined by equation 2.12.

$$\hat{g}_o = \left(\frac{\rho_o - \rho_a}{\rho_a} \right) g. \tag{2.12}$$

Note that ρ_o is the initial density of the discharged fluid, ρ_a is the density of the ambient fluid, and g is the gravitational constant. Pure plumes have gravitational potential energy due to the density difference between the discharged and ambient fluids and this density difference creates buoyancy forces in the flow. Theses forces drive convective mixing processes, where the discharged fluid moves through and entrains ambient fluid thereby diluting the discharged fluid. The centreline velocity of a pure plume is proportional to vertical distance from the source (z) such that $u_c \propto z^{-1/3}$ and the dilution is $\propto z^{5/3}$.

The level of dilution achieved for the contaminant within the discharged fluid

is important for minimising the environmental impact and for meeting regulatory requirements. Dilution (S) is defined as

$$S = \frac{c_o - c_a}{c - c_a} = \frac{Q}{Q_o} \tag{2.13}$$

where c_o is the concentration of contaminant at the source, c is the local concentration of contaminant in the flow field, c_a is the ambient concentration of contaminant (typically $c_a = 0$ for laboratory experiments), and Q is the volume flux at a flow cross-section. The relationship between dilution and local volume flux assumes the discharged contaminant mass is conserved downstream of the source.

Real flows must have initial volume and momentum fluxes that are greater than zero. The simplest fully turbulent flow with a plume region is a vertical buoyant jet. A turbulent vertical buoyant jet involves discharging fluid with an initial buoyancy flux parallel to the direction of decreasing gravity potential, and initial volume and momentum fluxes such that the flow is turbulent. These discharges have a jet region initially, where the initial momentum flux dominates, followed by a plume region where buoyancy dominates flow behaviour. A characteristic length scale (l_M) defines the relative importance of initial momentum and buoyancy fluxes in equation 2.14 (Fischer *et al.*, 1979).

$$l_M = \frac{{M_o}^{3/4}}{{B_o}^{1/2}} \tag{2.14}$$

The flow is dependent on the size of l_M as this length scale determines how far downstream the transition from jet to plume behaviour occurs. The transition from jet to plume behaviour does not occur instantaneously, rather a transition region exists where a combination of initial momentum flux and buoyancy generated momentum flux control the behaviour of the discharge.

Papanicolaou & List (1988) investigated the velocity and concentration decay of round vertical turbulent buoyant jets. Values for mean and turbulent properties were reported for velocity and dilution. The analysis was separated into jet and plume regions with empirical constants determined for respective regions. Summary values for the jet region are included in table 4.1 (Section 4.5.2). The transition from jet to plume behaviour was also investigated. Jet behaviour was found to occur for $z/l_M < 1$ and plume behaviour was found to occur for $z/l_M > 5$ with the transition region occurring between these inequalities. Round turbulent buoyant jets were also investigated by Wang & Law (2002) where velocity and concentration measurements were made. Wang & Law (2002) found that the flow had jet behaviour for $z/l_M < 0.6$ and $z/l_M > 6$, which is consistent with the values from Papanicolaou & List (1988).

2.4 Previous Experimental Research

The purpose of this section is to review previous experimental studies that relate specifically to the behaviour of INBJs discharged into a stationary ambient fluid without the presence of a boundary. The previous research relevant to the impingement and subsequent spreading of INBJs with a lower boundary is reviewed in Section 6.2. The majority of research has been conducted in laboratories with limited data available from field studies. The ambient conditions of the ocean can not be controlled in field studies, relying on periods of slack water to take measurements when ambient motion is least. However, the ambient ocean conditions are never quiescent, which adds uncertainty to field measurements. There is greater control over conditions for laboratory experiments. Specific parameters that influence flow behaviour, such as source discharge angle, can be adjusted to determine their individual effects. It is important that results from the laboratory experiments can be scaled to field discharges, where in a desalination context the INBJs are much larger geometrically. The important scaling parameter for these discharges is the initial densimetric Froude number. The initial densimetric Froude number is a dimensionless number that determines the relative importance of inertial and gravitational forces at the source. The initial densimetric Froude number will be hereafter be referred to as the Froude number (F_o) and is defined in equation 2.15.

$$F_o = \frac{U_o}{\sqrt{\hat{g}_o d}} \tag{2.15}$$

The Froude number is proportional to the length scale, l_M, through the relationship shown in equation 2.16.

$$F_o = \frac{l_M}{\left(\frac{\pi}{4}\right)^{1/4} d} \tag{2.16}$$

All known laboratory experiments for INBJs are conducted by adding salt to the discharged fluid, which increases the relative density of the discharged fluid compared to the fresh tap water that is used as the ambient fluid. This approach is consistent with the Boussinesq approximation where small density differences are assumed negligible in the governing equations of motion with the exception of the buoyancy term. The nomenclature and definitions of important parameters used in previous studies varies. Therefore, it is important to define the parameters that will be used in this study. Figure 2.1 shows a schematic of a single INBJ impinging on a lower boundary.

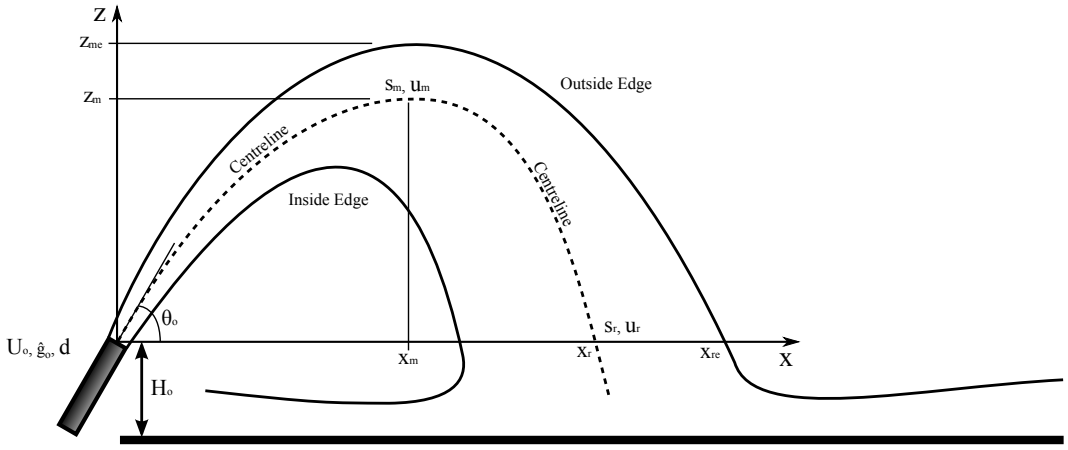

Figure 2.1 – Schematic of single port inclined negatively buoyant jet discharge.

The following nomenclature will be used in this study include:

– x_m : Horizontal distance to maximum centreline height

– z_m : Vertical distance to maximum centreline height

– z_{me} : Vertical distance to the outside edge at maximum height

– x_r : Horizontal distance to return point where discharge falls back to source height

– x_{re} : Horizontal distance to the outside edge at return point

– s_m : Centreline path length to maximum height

– s_r : Centreline path length to return point

– u_m : Mean centreline velocity at maximum height

– u_r : Mean centreline velocity at return point

– H_o : Elevation of source above lower boundary

– θ_o : Source angle above horizontal

The first significant laboratory experimental study into desalination plant brine discharges was conducted by Zeitoun (1970). Concentration experiments were carried out for source angles of 30°, 45°, and 60°. Rhodamine B dye was added to fluid discharged from the source at a known concentration, such that dilutions could be determined. Samples of fluid were drawn through hypodermic needles by vacuum at various locations and dye concentrations were measured with a fluorometer. Geometric outside edge parameters were determined by averaging five photographs of each experiment for steady state conditions. The source was placed 152 mm above the bottom of the experimental tank which established a lower boundary to the flow. The bottom of the tank was used

as a storage basin for discharged fluid with multiple experimental runs conducted within the same ambient fluid. Results for geometric parameters and dilution were found to linearly correlate with Froude number as predicted from dimensional arguments (Zeitoun, 1970). The source angle of 60° produced the maximum discharge trajectory and dilution compared to 30° and 45°. Subsequent experimental investigations by Roberts & Toms (1987) and Roberts *et al.* (1997) made use of this conclusion in defining the experimental configuration for their investigations. The experimental data obtained from relevant previous studies can be found in figures 5.15 - 5.21 (Section 5.2.3).

Roberts & Toms (1987) conducted experiments for inclined dense jets at source angles of 60° and 90° for different uniform crossflow angles and velocities. The crossflow parameter ($u_r F_o$) was varied between 0 and 1.87, where u_r is the uniform crossflow velocity divided by the initial discharge velocity. Results from experiments conducted with $u_r F_o = 0$ are relevant to the present study. Dilutions were determined using a similar method to Zeitoun (1970). A rack of sampling tubes was suspended in the experimental flume and samples of the discharge containing Rhodamine B dye were taken. The source protruded about 1 cm or 1 d above the bottom of the flume. The height of the outside edge was determined by averaging the outline of the discharge from several photographs taken with a still camera, which was positioned perpendicular to the flow. An additional dependence on the initial Froude number was found to occur for low Froude number experiments. The dilution at maximum height and the height of outside edge were found to be linearly dependent on Froude number for $F_o > 25$. The dilution at the return point was also found to be linearly dependent for all Froude numbers studied, $F_o > 12$. The initial volume flux was thought affect the behaviour of the discharge at maximum height for low Froude numbers.

Experiments were conducted by Lane-Serff *et al.* (1993) to verify a mathematical model that described the behaviour of vertical and inclined buoyant discharges or plumes. Values for the height of the outside edge at source angles between 15° and 75° were determined using shadowgraphs. Shadowgraphing is a non-intrusive flow visualisation technique that allows flow behaviour to be observed due to the difference in refractive index between fluids with different salt concentrations. Salt concentrations were also measured at fixed points in the flow using conductivity probes. The elevation of the source above the bottom of the experimental flume was not defined, however, an example shadowgraph indicates the source elevation was 50 mm above the bottom of the shadowgraph. The flow profiles were observed to be symmetrical close to the source, before asymmetries developed downstream as shown in figure 2.2 from Lane-Serff *et al.* (1993).

Using similar terminology as figure 2.1, they state that *"The upper side of the plume remains sharp and well defined while the lower* (inner) *side is diffuse and has no distinct edge... This asymmetry results from the opposite effects of the buoyancy force on the*

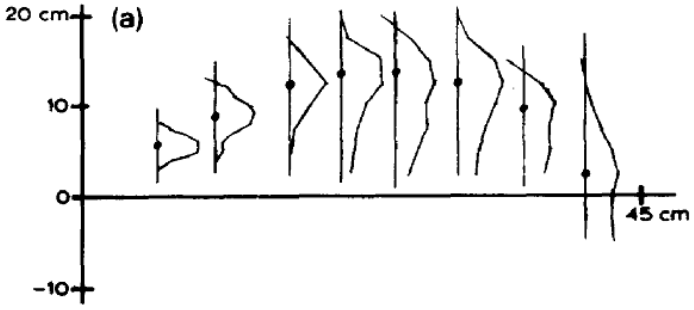

Figure 2.2 – *"Vertical time-averaged concentration profiles measured at various points along the plume centre-line. The injected fluid is denser than the surrounding fluid and was injected at 45° "*, (Lane-Serff *et al.*, 1993, Figure 18a).

two sides of the plume. On the upper (outer) *side, buoyancy forces create a stabilising stratification which tends to inhibit entrainment of the environmental fluid. On the lower side the buoyancy forces produce a convectively unstable configuration and there is enhanced mixing between the plume and the environment. Detrainment of plume fluid is observed on the lower side, a feature which is not observed in vertical plumes".* The prediction of the height of the outside edge by the mathematical model was within the uncertainty of experimental results for all source angles.

Lindberg (1994) investigated the behaviour of discharges with and without the presence of a crossflow. The source was pulled through a towing tank at a constant velocity simulating a uniform crossflow velocity. Shadowgraph photographs were taken perpendicular to the discharge to determine the geometric parameters for source angles of 30°, 45°, 60°, and 90°. A sheet of light was used to illuminate tracer paint in the discharged fluid and photographs were taken perpendicular to the discharge direction. The baseline results with no crossflow are of interest for the present study. The source was placed 100 mm above the bottom of the towing tank to allow for multiple experimental runs. The immediate descent of low momentum fluid near the source was observed for INBJs with $\theta_o < 90°$.

Roberts *et al.* (1997) conducted concentration experiments using laser-induced fluoresence (LIF). INBJs were discharged into stationary ambient fluid with a source angle of 60°. LIF is a common flow visualisation technique where fluorescent dye, typically Rhodamine, is mixed into the discharged fluid. A laser is used to create a thin sheet of light that illuminates a slice of the flow. Excitation of the fluorescent dye by the laser light results in the emission of fluoresced light with a longer wavelength. A video camera is used to record the fluoresced light from the discharged fluid. Experimental conditions are adjusted such that the intensity of fluoresced light is directly proportional to the concentration of dye. Roberts *et al.* (1997) used cylindrical lenses to produce a laser light sheet aligned through the centre plane of the discharges. The source

was placed 35 mm above a false wooden floor at the bottom of the experimental flume. Geometric parameters and dilutions were determined from mean LIF images. Dilution where the discharge centreline impinged the lower boundary was reported rather than the return point dilution. However, the influence of the lower boundary on the mixing of discharge was considered by examining concentration fluctuations. Concentration fluctuations were found to be highest on the outside edge of the falling plume at the impingement point. The concentration of the gravity current near the lower boundary could not be determined due to reflections of laser light off the false floor. A microconductivity probe was used to measure the concentration along the lower boundary. The turbulence of the gravity current along the boundary of the flow was sufficient to mix across the stable density gradient. The dilution was found to have increased by 60 %, compared to the dilution at the impingement point, at the location where the turbulence in the gravity current collapsed. The thickness of the gravity current above the boundary at this location was also reported. However, the gravity current was essentially a two-dimensional flow due to the restricted width of the experimental flume (Papakonstantis & Christodoulou, 2010). The gravity current was unable to spread radially and was reflected off the side walls of the flume.

Bloomfield & Kerr (2002) investigated the effect of the source angle on the height of the outside edge for different angles between 30° and 90°. Experiments were conducted in homogeneous and stratified ambient fluids. The shadowgraph experimental technique was used to identify the initial and final or steady state height of the outside edge. The experimental tank was tilted to achieve the different source angles, however this could have caused variable recirculation effects. The elevation of the source above the lower boundary was unlikely to influence measurements unless the brine build up at the bottom of the tank reached the height of the source. For 90° vertical discharges, the initial outside edge height was found to be higher than the final outside edge height due to down flow of fluid, after maximum height, being re-entrained by the rising plume. The re-entrainment increases the relative size of the buoyancy force for steady state conditions compared to the initial discharge that entrains only ambient fluid. The final outside edge height was found to increase rapidly as the source angle decreased from vertical as re-entrainment reduced. The maximum steady state height of the outside edge was found to occur for a source angle of 80°.

Otranto (2004) conducted experiments for INBJs with source angles of 30°, 45°, and 60°. The height of the outside edge at maximum height and horizontal distance to the outside edge at the return point were determined from flow visualisation experiments. A uniform light source was used to back light the experimental flume, such that a video camera was able to record the red coloured dye that had been mixed into the discharged fluid. A reference grid was used to determine the scale of the discharges from mean images. The source elevation was approximately 7 cm above the lower boundary of the

flume for 30° discharges, values for other angles were not specified.

Cipollina *et al.* (2005) studied discharges with source angles of 30°, 45°, and 60°. Experiments were conducted with a similar flow visualisation technique as Otranto (2004), which allowed geometric parameters to be determined. The effect of viscosity on the geometric parameters was also studied. Viscosity was found to have no significant effect, which indicates that the discharges are independent of Reynolds number. This is consistent with turbulent jets where $Re > 2000$. The height of the source above the bottom boundary of the experimental tank was not specified. However, a build up of dye on the bottom of the tank can be seen in the bottom right of figure 2.3 from Cipollina *et al.* (2005).

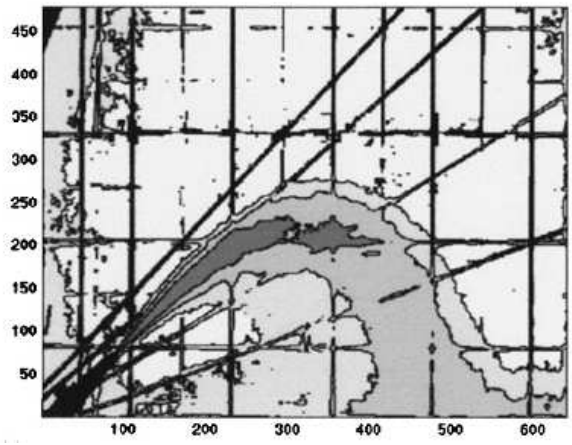

Figure 2.3 – *"Example of image processing... θ_o = 45°... MATLAB processed image"* (Cipollina *et al.*, 2005, Figure 1c).

Nemlioglu & Roberts (2006) conducted an experimental investigation for discharge source angles between 15° and 90° with a similar Froude number. They used a three-dimensional laser induced fluorescence (3DLIF) experimental technique to obtain geometric parameters and dilution at the same points as Roberts *et al.* (1997). The 3DLIF technique makes use of a standard planar LIF system, however multiple vertical slices of the discharge are taken sequentially at different distances away from the camera. The 15° discharge was found to achieve a lower dilution at the impingement point due to a shorter path length from the source. The 90° discharge was also found to have a lower dilution at the impingement point due to re-entrainment. Source angles of 30°, 45°, and 60° were found to have a similar dilution at the impingement point. The elevation of the source above the lower boundary was not specified.

An analytical model of INBJs was developed by Kikkert *et al.* (2007) and laboratory experiments were used for verification of the model. A range of source angles between 0° and 75° were investigated, with Froude numbers between 14 and 99, for a stationary ambient fluid. Concentration experiments were conducted using light attenuation (LA) and LIF techniques. LA is a flow visualisation technique that is based on the

attenuation of light by a coloured dye mixed with the discharged fluid. A uniform white light source is used to back light the discharges, such that a video camera captures an integrated view of the flow. Kikkert *et al.* (2007) assumed a Gaussian distribution for the discharge in the direction of integration for the mean concentration data. A calibration between pixel intensity and integrated concentration allowed the integrated dilution to be determined. The exact elevation of the source above the lower boundary of the experimental tank was not specified. However, it was noted that the source was placed at a height such that the dense layer of discharged fluid formed at the bottom of the experimental tank did not interfere with the flow. Integrated dilutions and geometric parameters were reported from LA experiments, while geometric parameters and profiles were reported from LIF experiments. The analytical model provided good predictions of geometric experimental data and improved predictions of dilutions. The predicted dilution at maximum height and return point by the analytical model was significantly closer to experimental results than commercial numerical models. Figure 2.4 shows the asymmetry of a mean cross-sectional concentration profile at the maximum height of a 45° discharge. The darker contours indicate higher concentrations near the centre of the profile. Detrainment is shown by the elongated contours on the inner (lower) side of the profile, which is consistent with observations in other studies. The elongation is shown to be most severe on the inner edge contours were velocities are lower. Buoyancy forces are likely to dominate fluid behaviour in this region, resulting in detrainment.

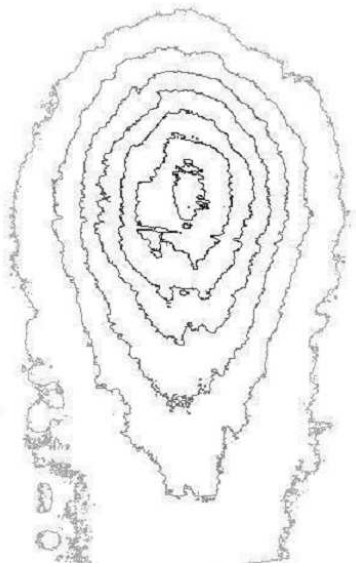

Figure 2.4 – Cross-sectional profile at maximum height for a source angle of 45° (Kikkert, 2006, Figure 6.19).

Ferrari & Querzoli (2010) conducted laboratory experiments using a light induced florescence technique that provided geometric and concentration information. The technique was similar to LIF, however slide projectors were used as the light source instead of a laser. Fluorescent dye was added to the discharged fluid and the dilution at

geometric locations was determined after normalisation with the measured concentration of dye at the source. A relatively long sampling period of 3 minutes 20 seconds was used, compared to the sampling period of 60 seconds used by the majority of researchers. Source angles between 45° and 90° were studied. Kelvin-Helmholtz instabilities were observed to form just beyond the source for experiments with $Re > 500$. Figure 2.5 shows that *"at the upper* (outer) *border, local stability permits the complete development of compact KH (Kelvin-Helmholtz) billows before their breaking, whereas the local unstable stratification tends to transform the growing waves in plumes propagating downwards at the lower* (inner) *boundary"* (Ferrari & Querzoli, 2010). They found that concentration fluctuations were more distributed and smaller on the inner side of the discharge due to the unstable stratification. The elevation of the source above the bottom boundary of the experimental flume was unspecified.

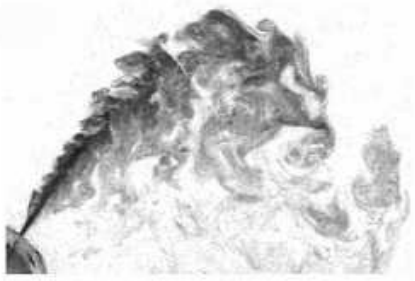

Figure 2.5 – Instantaneous visualisation of concentration field for inclined negatively buoyant jet with a source angle of 55°. *"High concentrations are indicated by dark grey, low concentrations pale grey"*, (Ferrari & Querzoli, 2010, Figure 1a).

Ferrari & Querzoli (2010) also found a significant interaction occurred between rising and falling sides of INBJs for angles above 75°. A Coanda effect was observed between the rising and falling sides of the discharge at high angles due to re-entrainment. The Coanda effect is the deflection of a discharge due to restricted entrainment on one side of the discharge creating a pressure difference across the flow. The falling side of the discharge was deflected towards the rising side of the discharge due to the strong entrainment of the rising side. This resulted in a reduction in maximum height for source angles above 80°, which is consistent with Bloomfield & Kerr (2002).

Shao & Law (2010) investigated the influence of the lower boundary on the initial jet region of INBJs at source angles of 30° and 45°. A combined particle image velocimetry (PIV) and LIF experimental system was used to simultaneously measure the velocity and concentration of discharges. PIV is a non-intrusive flow visualisation technique that involves seeding the discharged and ambient fluids with neutrally buoyant tracer particles. The tracer particles are illuminated by a thin laser light sheet, which is pulsed twice in quick succession. A video camera records the light scattered from the tracer particles in two separate images, one image captured with each light sheet pulse. Cross correlation is performed to determine the displacement of tracer particles between the

two images. The velocity of tracer particles is determined from the time step between laser pulses. Shao & Law (2010) used one video camera for PIV and a second video camera for LIF, allowing for simultaneous measurements of one experiment. Geometric parameters and dilution at maximum height and return point were reported. The centreline decay of velocity with path length was also reported for both angles. The Coanda effect of the lower boundary causing reduced entrainment on the inner side of discharges near the source was studied by varying the non-dimensional height of the source using two different length scales (H_o/l_M and H_o/d). H_o/l_M was found to be the variable that significantly changed the reported geometric parameters and dilution for 30°, whereas no significant change was found for 45°. The definition of the return point in Shao & Law (2010) is consistent with the present study. However, the influence of the lower boundary on the behaviour of the descending fluid has not been clearly defined.

Papakonstantis *et al.* (2011a,b) published results from an experimental investigation across two companion papers for six source angles between 45° and 90°. The first paper reported values for the geometric parameters obtained using a coloured dye flow visualisation technique similar to Otranto (2004). The source was about 10 cm above the bottom of the experimental tank to avoid re-entrainment of fluid from the gravity current spreading across the bottom of the tank. Papakonstantis *et al.* (2011a) reported that the flow was characterised by large scale structures at and beyond maximum height, where *"chunks of fluid separate from the main flow and descend almost vertically to the bottom"*. This is consistent with the observations of Lane-Serff *et al.* (1993); Kikkert *et al.* (2007) and Ferrari & Querzoli (2010) who noted detrainment on the inner side of the plume due to unstable stratification. The initial height of the outside edge of the discharge was measured and compared to the final or steady state outside edge height. The initial height of the outside edge was found to higher than the steady state value for all discharge angles. This was likely due to the initial discharge entraining more ambient fluid through the front of the flow, making it comparatively more diluted and reducing the buoyancy force compared to steady state conditions. The second paper focused on the dilution at the maximum height and return point. A conductivity probe was used to measure the concentration of the discharge at different fixed locations. The maximum turbulent concentration intensity at the maximum height was found to be consistent with plume region behaviour for all angles studied.

Lai & Lee (2012) investigated INBJs discharged into a stationary ambient at source angles between 15° and 60°. LIF was used to obtain concentration information and determine geometric parameters. Velocity field information was also obtained using PIV. The source was 5 cm above a Perspex false floor that represented a lower boundary for the discharges. Concentration profiles were Gaussian close to the source before profiles on the inner side of the discharge deviate from Gaussian for $s/d > 20$. Profiles

on the inner side continued to deviate from Gaussian up to maximum height and then remained self similar after maximum height. Profiles on the outer side always remained well defined and Gaussian in shape. Dilution at maximum height and return point were reported along with the geometric parameters for these locations. Limited velocity information was reported. The decay of velocity with path length for three experiments with a source angle of 60° was compared to the velocity decay of a pure jet discharge. The absolute centreline velocity was shown to be similar to that of a pure jet up to maximum height. Concentration results were compared to numerical model predictions made by VISJET. The experimental geometric parameters were higher than those predicted for all angles. The reason provided for these differences was that VISJET does not model the detrainment on the inner side of the discharge, which results in a loss of mass, momentum, and buoyancy from the main flow. The dilutions at maximum height and the return point were also under predicted by VISJET for all angles.

The PhD thesis of Oliver (2012) focussed on the behaviour of INBJs when the distance between the source and lower boundary was sufficiently large to avoid any influence on the flow at the return point. A review of literature by Oliver (2012) found that the proximity of the lower boundary was not stated in appropriate non-dimensional terms in many studies. Furthermore, data reported at the return point for some studies coincided with, or was just above, the impingement point of the discharge with the lower boundary. This was thought to be reason for the large variation in previously reported experimental data. LIF experiments were conducted to obtain data through the centre plane of discharges with source angles between 15° and 75°. Mean and temporal centreline and profile concentration data was reported for still ambient conditions. Dilution was found to increase at maximum height and return point for source angles up to 60°, with a slight decrease in dilution at these locations for 75°. Reported geometric parameters were found to be consistent with those of other studies. Analysis of temporal data found that a recording duration of at least 300 seconds should be used for INBJs. This was based on the cumulative average of concentration for small spatial areas near the return point of a 60° discharge taking 300 seconds to stabilise. Oliver (2012) suggests that further experimental research should be conducted to accurately determine the influence of the lower boundary and new integral numerical models should be developed to improve predictions of geometric parameters and dilutions.

2.5 Field Studies

There have been limited *in-situ* field studies conducted that relate to the near field behaviour of brine discharges from desalination plants. Conducting field investigations is particularly difficult due to the number of parameters that can not be controlled.

The local ambient ocean waters never remain stationary, but are continuously moving due to tidal currents, wind, and convection. Desalination plants operate continuously with brine flow rates related to plant operations. Determining brine dilution requires the measurement of elevated salt concentrations or alternatively adding a tracer to the brine discharge.

Marti *et al.* (2010) conducted a field study on the near field dilution of brine discharged into the Cockburn Sound from the Perth Seawater Desalination Plant in Australia. The diffuser system was located 500 m offshore, with 40 evenly spaced ports along the outfall pipeline and a source angle of 60°. Measurements were taken for three different flow rates that resulted in Froude numbers of 8.5, 15.4, and 23.8 corresponding to 1/3, 2/3, 3/3 of full flow. However, the majority of laboratory experiments have been conducted with $F_o > 20$ due to discharges being dependent on the source volume flux for low Froude numbers (Roberts & Toms, 1987).

A conductivity-temperature-depth (CTD) profiler was used to obtain data at different sampling points scattered over the area of the diffuser system. The dilution at the impingement point of the negatively buoyant discharge with the seabed was determined by averaging measurements near the calculated impingement point, using empirical relationships from Roberts *et al.* (1997), as precise geometric locations could not be determined by field measurements. The height of the gravity current was determined from elevated salinities near the seabed. The ambient currents during sampling periods were measured using an acoustic doppler current profiler and moored meteorological stations. Sampling was conducted for the three different flow rates when the ambient currents in the ocean were small, such that the ambient effects on the behaviour of the flow were minimised.

The height of the gravity current was found to be above the port height resulting in re-entrainment of the gravity current. The impingement dilution was similar to values reported in laboratory studies for $F_o = 23.8$. However, the dilutions were higher for the low Froude number experiments. Marti *et al.* (2010) recommended that further investigation was required into the behaviour of INBJs with low Froude numbers.

An *in-situ* field study was conducted by Loya-Fernández *et al.* (2012) to compare salinity measurements at the diffuser site with predictions of numerical models. The two Nuevo Canal de Cartagena desalination plants on the Mediterranean coast of Spain use a shared diffuser system for brine disposal. The 5100 m long submerged pipeline terminates with a single port at an angle of 60°. The port is elevated 4.5 m above the seabed and discharges 62,000,000 m^3 of brine per year. The ambient ocean conditions were measured with an acoustic doppler current profiler prior to the salinity measurements to determine the mean current direction. CorJet was employed to predict the geometric parameters of the discharge for the measured ambient conditions.

A SCUBA diver took salinity measurements using a CTD sensor within the area of

the discharge. The SCUBA diver took vertical profiles with the CTD sensor at different horizontal distances away from the diffuser port. Vertical profiles were taken up until the predicted impingement point of the brine discharge with the seabed, because numerical models do not consider boundary interactions (Loya-Fernández *et al.*, 2012). CorJet was found to overestimate the salinity near the diffuser and was therefore conservative.

2.6 Modelling

Brine discharge models are essential tools for desalination outfall diffuser design. Near field models provide an inexpensive method of considering the effects of different source parameters and allow project specific factors to be included. Commercial models used for INBJs have been adapted from models for positively buoyant jets (Palomar *et al.*, 2012b). These models have been extensively verified for positively buoyant jets such as municipal waste discharges (Lee & Cheung, 1990; Jirka, 2004). However, verification is lacking for negatively buoyant jets, where there are large differences between model predictions and experimental results (Oliver, 2012; Palomar *et al.*, 2012a). Flow behaviour differs substantially between positively and negatively buoyant jets. INBJs have additional flow features, including detrainment of discharged fluid due to the unstable stratification and re-entrainment for high source angles.

The analytical model proposed by Kikkert *et al.* (2007) for INBJs was based on analytical relationships developed for the trajectories of positively buoyant jets by Davidson & Pun (2000). The negatively buoyant analytical model predicts the location of geometric parameters and also the corresponding centreline dilutions at maximum height and return point. The model separates the discharge into distinct jet and plume regions and utilises momentum relationships for these idealised flow regimes to determine flow parameters. The discharge is modelled as a deflected pure jet for maximum height and is predicted to transition to plume behaviour before the return point for $\theta_o > 20°$. A virtual source is utilised for the prediction of plume behaviour at the return point, with relationships between locations of real and virtual sources relating these separate flow regimes.

The geometric and dilution predictions from the analytical model follow the trends of the experimental data in Kikkert *et al.* (2007). Predictions were significantly improved over the commercial integral models, especially for maximum height and return point dilutions at higher source angles. Geometric parameters predicted were within the scatter of experimental data. However, improved predictions of experimental data does not necessarily mean that the assumed physical processes was accurate. Experimentally observed physical processes of detrainment (Lane-Serff *et al.*, 1993; Kikkert, 2006; Papakonstantis *et al.*, 2011a,b; Oliver, 2012) and re-entrainment (Bloomfield & Kerr, 2002; Nemlioglu & Roberts, 2006) were not modelled in Kikkert *et al.* (2007). The

total initial momentum flux was assumed to be conserved up to maximum height in the jet region. However, the initial vertical momentum flux equals the buoyancy generated momentum flux at maximum height. This means that the total momentum flux at maximum height should be equal to the initial horizontal momentum flux. This alteration would significantly alter predictions at maximum height, especially for high source angles that have low initial horizontal momentum flux.

At the other extreme, the use of computational fluid dynamics (CFD) models has increased for a wide range of fluid flows due to the increased availability of relatively high powered computers. Turbulent jets and plumes have high Reynolds numbers and these have a high computational cost. Solving the Navier-Stokes equations directly using direct numerical simulation is not computationally affordable for these discharges with current computers (Palomar *et al.*, 2012b). There are limited CFD studies for INBJs. Oliver *et al.* (2008) used a k-ϵ transport model to close the RANS equations with the standard k-ϵ model constants. The model was also calibrated with positively buoyant jet experimental data by adjusting the turbulent Schmidt number, which controls the rate of tracer diffusion. The calibrated and standard models were then used to predict the behaviour of INBJs. The concentration profiles at maximum height of the standard model were more consistent with experimental profiles from Kikkert *et al.* (2007) than the calibrated model. The predicted dilutions of the calibrated model were better than the standard model at maximum height. However, the difference between predicted dilutions and experimentally measured dilutions was significant. The poor performance of both models for negatively buoyant discharges is consistent with previously noted difficulties in capturing the buoyancy effects accurately. In addition, the increased complexity of CFD models, when compared to other modelling techniques, makes them generally unsuitable for practical design applications. However, more sophisticated CFD techniques, such as large eddy simulations, have the potential to more accurately capture the physics of these discharges.

There are many integral models available in literature for INBJs. The models numerically integrate a system of simple ordinary differential equations that relate to the volume, momentum, and buoyancy fluxes of turbulent jets and plumes. The assumptions used to simplify and close the system of differential equations differs between models. These models do not consider boundary interactions and are therefore limited to the near field (Palomar *et al.*, 2012b). CORMIX, VISJET, and Visual Plumes are three software packages that are commonly used in practice for submerged outfall design. These software packages are able to model the discharge in the near and far field for different ambient conditions. A near field integral model that uses the entrainment assumption to close the system of differential equations is included in all of these software packages. CorJet (Jirka, 2004) and UM3 (Frick *et al.*, 2003) are two different Eulerian integral models included in CORMIX and Visual Plumes respectively.

JetLag (Lee & Cheung, 1990; Lee & Chu, 2003) is the Lagrangian integral model included in VISJET software. Papanicolaou *et al.* (2008) adjusted the entrainment coefficient of a standard integral model to improve predictions for INBJs. Yannopoulos & Bloutsos (2012) proposed a model that simulated detrainment by allowing mass flux to decrease with path length. The reduced buoyancy flux (RBF) model developed by Oliver *et al.* (2013) is an integral model that simulated pure jet behaviour up to maximum height. This resulted in a reduced buoyancy flux for the main flow, which is consistent with the detrainment process, and improved dilution predictions. Integral models developed for stagnant ambient conditions can be incorporated into more complex models that consider ambient motion and stratification. The analytical model by Kikkert *et al.* (2007) is not suitable for this kind of development as it would become increasingly complex and lose the advantage of simplicity. Integral models already have the framework in place to predict flow behaviour in moving and stratified ambient conditions. Therefore, the analytical model should be limited to stationary unstratified ambient conditions. The computation time for including variations in ambient conditions in CFD models is prohibitive due to their complexity. This makes the further development of integral models important for providing practical models for submerged outfall design for desalination plants. Integral models will be examined in more detail in chapter 3.

2.7 Summary

Research on INBJs that result from the submerged brine discharges of desalination plants is relatively new compared to positively buoyant discharges. There are well established models for positively buoyant jets that can accurately predict trajectory and dilution. Adopting positively buoyant jet models for negatively buoyant jets has had limited success due to additional detrainment and re-entrainment flow features of INBJs. However, INBJs exhibit similar features with distinct jet and plume regions where the initial momentum flux and buoyancy flux dominated flow behaviour respectively.

There are numerous experimental studies that empirically relate geometric parameters and dilution to source conditions. These empirical relationships are favoured over model predictions for practical design due to the significant underestimation of dilution by commercial models. Geometric maxima have been the focus of many experimental studies as these are important design parameters. These geometric parameters can be determined using relatively simple coloured tracer experimental techniques. More recent experimental studies have used sophisticated LIF and LA techniques that allow the concentration fields to be measured accurately. There have been limited velocity field experiments conducted. Models make assumptions about the concentration and velocity fields that need to be verified against experimental findings. Discrepancies need to be

examined and models adjusted. There are also differences in the location and definition of important geometric parameters. The height of the outside edge has been determined by visual inspection and by adding different multiples of the discharge width to the centreline height. The return point and the impingement point have both been used as important geometric parameters for the falling side of the discharge. There has been a wide variation in lower boundary conditions between studies, many not considering the potential effects of the lower boundary on conditions at the return point.

A review of the relevant literature has shown that additional experimental investigations are required to further understand the behaviour of INBJs without the presence of a lower boundary. Confirmation of dilution data reported by Oliver (2012) is required and as well as new velocity field data. This would allow for direct comparison to numerical models that assume an unlimited unbounded ambient environment. Integral models proposed specifically for INBJs have had varying levels of success. It is important that the assumptions used in numerical models have a physical significance such that they represent real flow features. The effect of the lower boundary on the flow needs further consideration through direct comparisons between discharges with and without the influence of a lower boundary. There is the potential for the lower boundary to influence discharge behaviour beyond a simple redirection of the flow and subsequent formation of gravity currents.

Chapter 3

Integral Modelling

3.1 Introduction

Integral models are an important tool for the practical design of desalination plant outfall diffusers. These models simulate the behaviour of INBJs to determine geometric parameters, momentum, and dilution of discharges in the ambient environment. Integral models are a mathematical representation of mean flow behaviour. This contrasts with the physically observed behaviour that is highly turbulent and fluctuating. However, the processing time of integral modelling is significantly less than CFD modelling, which solve some variation of the Navier-Stokes equations directly, e.g. Reynolds-averaged Navier-Stokes (RANS) equations. The governing equations for jet and plume discharges relate to mass, momentum, and buoyancy fluxes of the flow (Fischer *et al.*, 1979). The mass flux (Q) through a cross-sectional profile of the flow is given by equation 3.1,

$$\rho Q = \int_A \rho u \, \mathrm{d}A \tag{3.1}$$

where A is the cross-sectional area of the flow. The momentum flux (M) through the cross-sectional area is given by equation 3.2.

$$\rho M = \int_A \rho u^2 \, \mathrm{d}A \tag{3.2}$$

The buoyancy flux (B) is the weight of fluid passing through the cross-sectional area. Buoyancy flux is related to any tracer that changes the density of the fluid (e.g., salinity, temperature) and is given by equation 3.3.

$$\rho B = \int_A \rho u \hat{g} \, \mathrm{d}A \tag{3.3}$$

Volume (Q), momentum (M), and buoyancy (B) are all specific fluxes that differ from mass, momentum, and buoyancy fluxes by density. Volume, momentum, and buoyancy flux will herein refer to specific fluxes.

Simplifying assumptions are applied to the governing equations to reduce complexity without noticeably influencing the predictions of models. Water is assumed to be an incompressible fluid, hence the density of water does not depend on pressure or depth in the water column. The Boussinesq approximation utilised in the laboratory to conduct experiments at different densities (see section 2.4) is applied to the governing equations. Therefore, small density differences are only important for the buoyancy terms and density is assumed to be constant and eliminated from equations 3.1 - 3.3, except for the reduced gravity term ($\hat{g}$) (Morton *et al.*, 1956).

Integral models represent the mean three-dimensional physical form of vertical jets and plumes as a cone consisting of individual jet or plume elements, which are roughly cylindrical in shape along the path of discharges (Baumgartner *et al.*, 1994). The physical form of INBJs is essentially a bent cone. The governing equations are applied to the individual cylindrical elements or control volumes as they move through space and time (Lagrangian), or at specific locations in space as time passes (Eulerian). Some integral models assume the mean velocity and concentration profiles for each control volume have a Gaussian distribution (Jirka, 2004). This is consistent with velocity and concentration profiles of pure jet and plume discharges (Fischer *et al.*, 1979), which are defined in equation 3.4,

$$\frac{\bar{u}}{\bar{u_c}} = e^{-r^2/b^2} \qquad \frac{\bar{c}}{\bar{c_c}} = e^{-r^2/(\lambda b)^2} \tag{3.4}$$

where λ is the ratio of concentration to velocity spread that differs for jets and plumes regions of discharges (Wang & Law, 2002). Alternatively, top-hat integral modelling assumes that velocity and concentration profiles are uniform for each control volume (Cheung *et al.*, 2000). Conversion factors are applied to top-hat model parameters to ensure that volume, momentum, and buoyancy fluxes are identical to those of models that assume Gaussian distributions. Top-hat modelling is preferred in the present study due to the simplified formulation of the governing equations. The following section outlines the conversion factors between Gaussian and top-hat models.

3.1.1 Gaussian and Top-hat Conversion Factors

Converting between parameters of Gaussian and top-hat models is essential to ensure that predictions from each approach are equivalent. Figure 3.1 illustrates the Gaussian and top-hat mean velocity profiles used by integral models. A similar figure can be produced for mean Gaussian and top-hat tracer profiles (not shown here for brevity). Gaussian models use u_c, $\hat{g_c}$, and b to characterise local flow conditions for each control volume, whereas top-hat models use u_T, $\hat{g_T}$, and b_T. Reduced gravity ($\hat{g}$) is equivalent to the concentration of a tracer containment (c) as the dilution rates are identical.

The volume, momentum, and buoyancy fluxes for top-hat and Gaussian models are

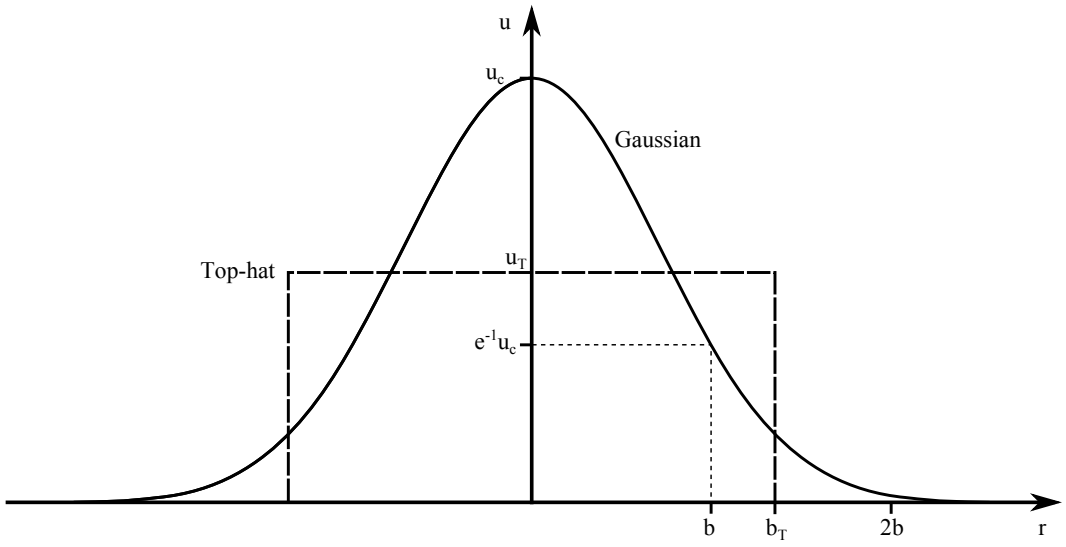

Figure 3.1 – Comparison of Gaussian and top-hat mean velocity profiles.

defined in equations 3.5 - 3.7,

$$Q = \pi u_T {b_T}^2 = \int_0^\infty u \; 2\pi r \; \mathrm{d}r = I_Q u_c b^2 \tag{3.5}$$

$$M = \pi {u_T}^2 {b_T}^2 = \int_0^\infty u^2 \; 2\pi r \; \mathrm{d}r = I_M {u_c}^2 b^2 \tag{3.6}$$

$$B = \pi u_T \hat{g_T} {b_T}^2 = \int_0^\infty u \; \hat{g} \; 2\pi r \; \mathrm{d}r = I_{QC} u_c \hat{g_c} b^2 \tag{3.7}$$

where I_Q, I_M, and I_{QC} are integration constants, defined in equations 3.9 - 3.11. Reynolds decomposition can be used to transform instantaneous velocity and concentration into mean and fluctuating terms as shown in equation 3.8.

$$u = \bar{u} + u', \qquad \hat{g} = \bar{\hat{g}} + \hat{g}' \tag{3.8}$$

The integration constants can be found by substituting equation 3.8 into equations 3.5 - 3.7. Time averaging these equations results in fluctuating terms (e.g. u') becoming zero. Therefore, the volume flux integration constant (I_Q) becomes:

$$I_Q = \int_0^\infty \left(\frac{\bar{u} + u'}{u_c}\right) \; \frac{2\pi r}{b} \; \frac{\mathrm{d}r}{b} = \int_0^\infty \left(\frac{\bar{u}}{u_c}\right) \; \frac{2\pi r}{b} \; \frac{\mathrm{d}r}{b} \tag{3.9}$$

Similarly, the time averaged integration constants for momentum (I_M) and buoyancy (I_{QC}) are defined in equations 3.10 and 3.11. However, the multiplication of fluctuating velocity and/or reduced gravity components is not zero.

$$I_M = \int_0^\infty \left(\frac{\bar{u} + u'}{u_c}\right)^2 \; \frac{2\pi r}{b} \; \frac{\mathrm{d}r}{b} = \int_0^\infty \left[\left(\frac{\bar{u}}{u_c}\right)^2 + \overline{\left(\frac{u'}{u_c}\right)^2}\right] \; \frac{2\pi r}{b} \; \frac{\mathrm{d}r}{b} \tag{3.10}$$

$$I_{QC} = \int_0^\infty \left(\frac{\bar{u} + u'}{u_c}\right)\left(\frac{\bar{\hat{g}} + \hat{g}'}{\hat{g}_c}\right)\ \frac{2\pi r}{b}\ \frac{\mathrm{d}r}{b} = \int_0^\infty \left[\frac{\bar{u}}{u_c}\frac{\bar{\hat{g}}}{\hat{g}_c} + \frac{\overline{u'\hat{g}'}}{u_c\hat{g}_c}\right]\ \frac{2\pi r}{b}\ \frac{\mathrm{d}r}{b} \tag{3.11}$$

The integration constants can be evaluated using experimental data and the definite integral for exponential functions defined in equation 3.12.

$$\int_0^\infty x\ e^{-ax^2}\ \mathrm{d}x = \frac{1}{2a} \tag{3.12}$$

Wang & Law (2002) found that turbulence added 10 % to mean momentum flux for both jets and plumes using PIV. Papanicolaou & List (1988) found that turbulence added roughly 16 % to the mean momentum flux for pure jets using laser-doppler anemometry. The total momentum was found to be 12 % higher than the initial momentum flux by Papanicolaou & List (1988). Therefore, the value determined by Wang & Law (2002) is thought to be more reliable and will be used in the present study. This gives:

$$\overline{\left(\frac{u'}{u_c}\right)^2} = 0.1\left(\frac{\bar{u}}{u_c}\right)^2 \tag{3.13}$$

Wang & Law (2002) also found that turbulence added 7.6 % to the mean mass flux for pure jets and added 15 % to the mean mass flux for pure jets. This gives:

$$\text{Jets:} \qquad \frac{\overline{u'\hat{g}'}}{u_c\hat{g}_c} = 0.076\frac{\bar{u}}{u_c}\frac{\bar{\hat{g}}}{\hat{g}_c} \tag{3.14}$$

$$\text{Plumes:} \qquad \frac{\overline{u'\hat{g}'}}{u_c\hat{g}_c} = 0.15\frac{\bar{u}}{u_c}\frac{\bar{\hat{g}}}{\hat{g}_c} \tag{3.15}$$

Equations 3.16 - 3.19 show the evaluation of integration constants using experimental data and the definite integral defined above for volume, momentum and buoyancy. Wang & Law (2002) found that λ was 1.217 for jets and 1.038 for plumes.

$$I_Q = \pi \tag{3.16}$$

$$I_M = 1.1\frac{\pi}{2} \approx 1.73 \tag{3.17}$$

$$\text{Jets:} \qquad I_{QC} = \frac{1.076\pi}{1 + 1/\lambda^2} \approx 2.02 \tag{3.18}$$

$$\text{Plumes:} \qquad I_{QC} = \frac{1.15\pi}{1 + 1/\lambda^2} \approx 1.87 \tag{3.19}$$

When conversion factors between the realistic Gaussian parameters and bulk top-

hat parameters are evaluated by manipulating equations 3.9 - 3.11, the following relationships are developed:

$$u_c = \frac{I_Q}{I_M} u_T \approx 1.82 u_T \tag{3.20}$$

$$b = \sqrt{\frac{\pi I_M}{{I_Q}^2}} b_T \approx 0.74 b_T \tag{3.21}$$

$$\text{Jets:} \qquad \hat{g_c} = \frac{\pi u_T}{I_{QC} u_c} \frac{b_T^2}{b^2} \hat{g_T} \approx 1.56 \hat{g_T} \tag{3.22}$$

$$\text{Plumes:} \qquad \hat{g_c} = \frac{\pi u_T}{I_{QC} u_c} \frac{b_T^2}{b^2} \hat{g_T} \approx 1.69 \hat{g_T} \tag{3.23}$$

where $\hat{g_c}$ and $\hat{g_T}$ can be substituted with c_c and c_T to determine the relationship between tracer concentration profiles.

3.1.2 Differential Equations

A system of differential equations derived from the governing equations for a top-hat integral model will be developed in the following section. An Eulerian specification will be used, therefore the differential equations will be dependent on the change in path length (ds). These differential equations are applied to the control volume of the flow and solved using numerical integration techniques such as the Runge-Kutta method (Jirka, 2004; Papanicolaou *et al.*, 2008; Palomar *et al.*, 2012b). The purpose of this section is to identify the main assumptions and equations used by the currently available integral models. Differences exist between these models, although the underlying assumptions are similar. The equations presented here are similar to those of Papanicolaou *et al.* (2008), Oliver (2012), and the RBF model (Oliver *et al.*, 2013). Differences between the entrainment and spread relationships used to close the system of equations will also be outlined. Flow parameters have been non-dimensionalised by their corresponding initial values for volume flux (Q_o), momentum flux (M_o), buoyancy flux (B_o), and reduced gravity ($\hat{g_o}$), which were defined in chapter 2. Distances are non-dimensionalised by the initial source diameter (d), and the initial Froude number (F_o) is used to remove the dependence on the scale of the flow. Non-dimensional parameters will be marked using a subscript star (e.g., $Q_\star$).

Volume, momentum and buoyancy flux for any control volume are defined by equations 3.24 - 3.26 for top-hat modelling (Papanicolaou *et al.*, 2008; Oliver, 2012). A schematic of the control volume in relation to the discharge and the relevant top-hat parameters are shown in figure 3.2.

$$Q_\star = 4u_{T\star}{b_{T\star}}^2 \tag{3.24}$$

$$M_\star = 4{u_{T\star}}^2{b_{T\star}}^2 \tag{3.25}$$

$$B_\star = 4u_{T\star}\hat{g_{T\star}}{b_{T\star}}^2 \tag{3.26}$$

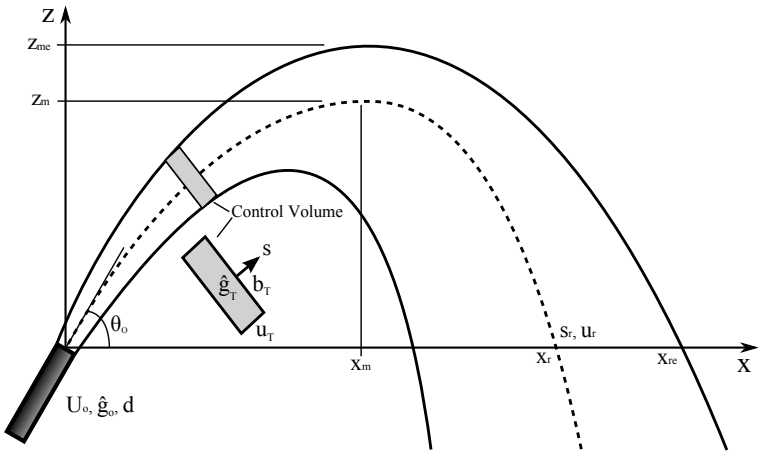

Figure 3.2 – Schematic of inclined negatively buoyant jet with top-hat modelling control volume.

The conservation of discharged fluid mass flux along the path of the flow is assumed by commercial integral models (CorJet, VISJET, Visual Plumes). The general form of the mass conservation for the control volume of a steady state flow is given by equation 3.27.

$$\int_{CS} \rho(\mathbf{u}\cdot\mathbf{n})\mathrm{d}A = 0 \tag{3.27}$$

Conservation of mass results in the conservation of buoyancy relationship shown in equation 3.28.

$$B_\star = \hat{g_{T\star}}Q_\star = 1 \tag{3.28}$$

The general form of the momentum conservation for the control volume of a steady state flow is given by equation 3.29.

$$\sum \mathbf{F} = \int_{CS} \mathbf{u}\rho(\mathbf{u}\cdot\mathbf{n})\mathrm{d}A = 0 \tag{3.29}$$

The net horizontal force on the control volume is zero, therefore there is no change in horizontal momentum as shown by equation 3.30.

$$\frac{\mathrm{d}M_{H\star}}{\mathrm{d}s_\star} = 0 \tag{3.30}$$

The change in vertical momentum due to the reduced gravity of the control volume was first proposed by Morton *et al.* (1956) and is shown in equation 3.31.

$$\frac{\mathrm{d}M_{V\star}}{\mathrm{d}s_\star} = \frac{4\hat{g_{T\star}}{b_{T\star}}^2}{{F_o}^2} \tag{3.31}$$

The change in total momentum is the vector addition of horizontal and vertical terms and is shown in equation 3.32. The last term of this equation is zero when equation 3.30 is applied.

$$\frac{\mathrm{d}M_\star}{\mathrm{d}s_\star} = \frac{M_{V\star}}{M_\star}\frac{\mathrm{d}M_{V\star}}{\mathrm{d}s} + \frac{M_{H\star}}{M_\star}\frac{\mathrm{d}M_{H\star}}{\mathrm{d}s} \tag{3.32}$$

The change in horizontal and vertical directions of the flow is dependent on the relative sizes of momentum fluxes, which is equivalent to the local angle of the control volume (θ), as shown in equations 3.33 - 3.34.

$$\frac{\mathrm{d}x_\star}{\mathrm{d}s_\star} = \frac{M_{H\star}}{M_\star} = \cos(\theta) \tag{3.33}$$

$$\frac{\mathrm{d}z_\star}{\mathrm{d}s_\star} = \frac{M_{V\star}}{M_\star} = \sin(\theta) \tag{3.34}$$

The entrainment, or spread relationship is used to close the system of differential equations as there is one more unknown than available equations. The entrainment relationship assumes that the velocity of entrained ambient fluid (u_e) through control surfaces is directly proportional to the centreline velocity ($u_e = \alpha u_c$) (Morton *et al.*, 1956). The entrainment coefficient (α) has been found to be constant for pure jets and plumes discharges ($\alpha_{jet} = 0.0535$, $\alpha_{plume} = 0.0833$) (Fischer *et al.*, 1979). The entrainment coefficient is multiplied by $\sqrt{2}$ for conversion to a top-hat entrainment coefficient (α_T) (Papanicolaou *et al.*, 2008). INBJs transition from jet behaviour on the rising side of the discharge to plume behaviour on the falling side. α is modified based on the local Froude number of the flow to model the transition from jet to plume behaviour (Cheung *et al.*, 2000; Jirka, 2004). The change in volume flux of the control volume evaluated using the entrainment assumption is shown in equation 3.35 (Papanicolaou *et al.*, 2008).

$$\frac{\mathrm{d}Q_\star}{\mathrm{d}s_\star} = 4\alpha_T\sqrt{M_\star} \tag{3.35}$$

The spread relationship assumes that the change in discharge width with path length is constant, as shown in equation 3.36. This is consistent with experimental data for pure jets and plumes (Fischer *et al.*, 1979). The experimental spreading rate (k_s) is

converted to a top-hat spreading rate (k_T) using the conversion factor for discharge width (Equation 3.21).

$$\frac{\mathrm{d}b_{T\star}}{\mathrm{d}s_\star} = k_T \tag{3.36}$$

The change in volume flux of the control volume evaluated using the spread assumption is shown in equation 3.37, which was used in the top-hat model of Oliver (2012) and the RBF model.

$$\frac{\mathrm{d}Q_\star}{\mathrm{d}s_\star} = \frac{b_{T\star}}{\sqrt{M_\star}}\frac{\mathrm{d}M_\star}{\mathrm{d}s_\star} + 2\sqrt{M_\star}\frac{\mathrm{d}b_{T\star}}{\mathrm{d}s_\star} \tag{3.37}$$

3.2 Commercial Models

Commercial integral models (CorJet (Doneker & Jirka, 2001), VISJET (Cheung *et al.*, 2000), and Visual Plumes (Frick, 2004)) are generalised models that are able to predict the behaviour of discharges for many different flow scenarios, including moving and stratified ambient conditions. The following subsections detail the important assumptions of each commercial model and their performance in predicting the behaviour of INBJs is evaluated in section 3.4.

3.2.1 CorJet

CORMIX is a commercial software package for the analysis, prediction and design of pollutant discharges into diverse bodies of water (Palomar & Losada, 2011). It is a collection of hydrodynamic models, invoked through a length-scale based classification scheme, that are interconnected to predict discharge flow behaviour (Bleninger & Jirka, 2009). CORMIX can simulate the behaviour of positively, neutrally, and negatively buoyant discharges into stagnant or moving ambient conditions, with stable or uniform stratification. (Palomar *et al.*, 2012b; Oliver, 2012). CORMIX1 and CORMIX2 are subsystems that can simulate the mixing behaviour of submerged single port and submerged multiport negatively buoyant discharges, respectively (Doneker & Jirka, 2001). CORMIX1 predictions of flow behaviour for single port INBJs are relevant to the present study. However, CORMIX1 applies the CorJet module directly when there is no interaction with the ambient water surface (Palomar *et al.*, 2012b), which is the scenario relevant to the present study.

CorJet is an Eulerian integral model that uses the entrainment relationship to close the system of differential equations. Jirka (2004) presents the governing equations of CorJet in three dimensions, where a Gaussian distribution is assumed. Mass, momentum, and buoyancy fluxes are all assumed to be conserved. The entrainment coefficient (α), which is dependent on the local flow parameters, is critical to the performance of

entrainment integral models. This allows for the different shear mechanisms of turbulent jet and plume entrainment (Jirka, 2004). Equation 3.38 states the entrainment coefficient for stationary ambient conditions from Jirka (2004). α tends to the value of 0.0825 in the plume region of discharges, which is similar to α_{plume} of 0.0833 defined by Fischer *et al.* (1979).

$$\alpha = \alpha_1 + \alpha_2 \frac{sin(\theta)}{{F_{Lg}}^2} \tag{3.38}$$

The terms α_1 and α_2 are the entrainment coefficients equal to 0.055 and 0.6, respectively. F_{Lg} is the local Gaussian Froude number given by the centreline velocity (u_c), centreline reduced gravity (g'_c), and Gaussian spread (b).

$$F_{Lg} = \frac{u_c}{\sqrt{\hat{g}_c b}} \tag{3.39}$$

The CorJet module was run within CORMIX 8.0[1] to produce predictions of dilution and geometric parameters for INBJs. Predictions were obtain for source angles between 0° and 90° at 5° increments for the following initial conditions: $d = 0.20$ m, $F_o = 40.0$. Outputs were subsequently non-dimensionalised for comparison to other models and experimentally measured values.

3.2.2 VISJET

VISJET is a flow visualisation tool (Cheung *et al.*, 2000), which incorporates the JETLAG integral model (Lee & Cheung, 1990) with a three-dimensional computer graphics display of the predicted discharge (Lee & Chu, 2003). VISJET allows the interaction of multiple port discharges to be viewed from different orientations. The predictions of the JETLAG model are pertinent to the present study. JETLAG is a Lagrangian integral model that uses the entrainment relationship to close the system of differential equations in top-hat form. Buoyant discharges into stagnant or flowing ambient conditions with a uniform or stratified density can be modelled. Lee & Cheung (1990) present the equations and verification of the model for positively and negatively buoyant discharges in a range of ambient conditions. Momentum and buoyancy fluxes are conserved between the plume elements. The entrainment coefficient for stagnant ambient conditions is similar to that of CorJet, as shown in equation 3.40. The $\sqrt{2}$ coefficient converts from the Gaussian to top-hat formulation.

$$\alpha = \sqrt{2}\left(\alpha_1 + \alpha_2 \frac{sin(\theta)}{{F_L}^2}\right) \tag{3.40}$$

JETLAG uses the α_1 and α_2 coefficients of 0.057 and 0.554, respectively, which are

[1]Evaluation version obtained from www.cormix.info

similar to the values of CorJet (0.055, 0.6). The local Froude number defined in equation 3.41 is in terms of local top-hat flow parameters. β is an unspecified proportionality constant (Lee & Cheung, 1990).

$$F_L = \beta \frac{u_T}{\sqrt{\hat{g}_T b_T}} \tag{3.41}$$

VISJET 2.5[2] was used to generate predictions for INBJs from the JETLAG integral model. Predictions from a single port discharge for source angles between 0° and 90° at 5° increments were obtained with identical initial conditions as for CorJet predictions (d = 0.20 m, F_o = 40.0). Outputs were again non-dimensionalised for comparative purposes.

3.2.3 Visual Plumes

Visual Plumes was developed by the US Environmental Protection Agency to assist the design of wastewater discharges into fresh or marine waters (Frick, 2004). Visual Plumes models the dilution and geometric parameters of discharges in the near and far field, and also has the capability to analyse time-series scenarios. This allows continuous performance of discharges to be modelled in variable ambient conditions. Visual Plumes was developed from DOS-based programs called PLUMES (Baumgartner *et al.*, 1994). UM3 is the near field Lagrangian integral model within these programs, which uses the entrainment relationship to close the system of differential equations. UM3 uses a top-hat formulation and discharges through the source are assumed to be steady. Mass, momentum and energy are assumed to be conserved. The conservation of energy allows temperature to be included in the determination of density difference between the discharge and ambient environments. Discharges in uniform stationary ambient conditions are relevant to the present study. The entrainment coefficient (α) is assumed to be constant, with a value of 0.1 recommended. However, the user of Visual Plumes is able to assign a different α constant value. This differs to CorJet and VISJET, where α is dependent on local flow parameters.

Predictions for INBJs were obtained from Visual Plumes[3] with the recommended α = 0.1. A single port discharge into uniform ambient conditions was specified for the same initial conditions as other commercial models (d = 0.20 m, F_o = 40.0). Predictions were obtained for different source angles between 0° and 90° at 5° increments. Top-hat output parameters were converted to their Gaussian equivalents using the conversion parameters specified in Baumgartner *et al.* (1994).

[2]Trial version obtained from www.aoe-water.hku.hk/visjet/visjet.htm
[3]Version 1.0 obtained from www.epa.gov/ceampubl/swater/vplume

3.3 Literature Models

Integral models in literature studies by Papanicolaou *et al.* (2008), Yannopoulos & Bloutsos (2012), and the RBF model (Oliver *et al.*, 2013) are limited to stationary ambient conditions. However, a stationary ambient is the worst case scenario for achieving a minimum dilution in the ambient environment. Commercial models are able to predict discharge behaviour in a range of different ambient conditions, however this generality restricts their applicability to specific flows. Literature models can be calibrated to inclined negatively buoyant discharges by manipulating assumptions and equations to simulate the unique behaviour of these discharges. The assumptions and reasoning of these models will be outlined before they are compared to commercial models and experimental data in section 3.4.

3.3.1 Papanicolaou

Papanicolaou *et al.* (2008) proposed two different integral models with top-hat and Gaussian profile distributions. The entrainment assumption was used to close the system of equations for both distributions. These models were found to produce different dilution and geometric predictions for identical initial conditions (Papanicolaou *et al.*, 2008). Volume, momentum, and buoyancy fluxes were all assumed to be conserved. The density of the ambient water column could be uniform or stratified. The entrainment coefficient was determined from equation 3.42,

$$\alpha = \alpha_j - (\alpha_j - \alpha_p)\left(\frac{R}{R_p}\right)^2 \tag{3.42}$$

where R is the local Richardson number defined by equation 3.43, and R_p is the limiting Richardson number for a pure plume ($R_p = 0.56$). α_j and α_p are entrainment coefficients for pure jets and plumes.

$$R = \frac{QB^{1/2}}{M^{5/4}} \tag{3.43}$$

Initially, values for the entrainment coefficients were taken from the study of Papanicolaou & List (1988) ($\alpha_j = 0.0545$, $\alpha_p = 0.0875$). However, a lower α_j of 0.030 was found to improve predictions of the vertical distance to the outside edge at maximum height in comparison to experimental values. The lower α_j value was justified as *"negative buoyancy decelerates the jet 'core', thus reducing the radial pressure gradient and consequently the strength of the local sink"*. However, Lai & Lee (2012) found that the initial velocity decay of INBJs followed closely that of pure jets for the source angles of 30° and 45°. Additionally, reducing α_j was found to decrease dilution predictions at maximum height and the return point (Papanicolaou *et al.*, 2008), further

under-predicting experimental results.

Section 3.1.1 demonstrated that conversions could be conducted between top-hat and Gaussian parameters if volume, momentum, and buoyancy fluxes were equated. Therefore, top-hat and Gaussian models should produce equivalent predictions if parameters are in the same form. Oliver (2012) found the conversion factor of $\sqrt{2}$ used to convert Gaussian entrainment coefficients to their top-hat equivalents was only applied to α_j and not α_p. Oliver (2012) found predictions from top-hat and Gaussian models were equivalent if the correct conversion factors were applied. Geometric predictions from the Gaussian integral model were obtained from Papanicolaou *et al.* (2008) for comparison to other models for the improved α_j value of 0.30.

3.3.2 Yannopoulos

An Eulerian integral model was proposed by Yannopoulos & Bloutsos (2012) for plane and round inclined buoyant jets. The form of the equations in this model are different to previously outlined models, as volume, momentum, and buoyancy fluxes are not conserved. This approach attempts to simulate the experimentally observed detrainment (Kikkert *et al.*, 2007; Ferrari & Querzoli, 2010) on the inner side of INBJs due to unstable stratification. Fluxes are lost from the control volume depending on the local parameters of the flow and an approximation of profile distributions. The zone of flow establishment is modelled, whereas other models do not attempt this, instead assuming self-similarity from an appropriate virtual source (Jirka, 2004; Papanicolaou *et al.*, 2008). The entrainment assumption is used to close the system of differential equations. The contribution of turbulence to momentum and buoyancy fluxes is determined dynamically at different distances from the source for the second order approach. The integral model of Yannopoulos & Bloutsos (2012) includes numerous factors that account for many different parameters of the flow. Most importantly, a proportionality constant between the tracer concentration of detrained fluid and the centreline tracer concentration is adjusted to minimise the difference between model predictions and experimental dilution and geometric values. Tabulated dilution predictions for a range of source angles were obtained from this study.

3.3.3 Reduced Buoyancy Flux (RBF)

The main assumptions of the RBF model were first proposed by Oliver (2012), with the model refined in Oliver *et al.* (2013). Volume and momentum fluxes are conserved by this model, whereas buoyancy flux is lost up to maximum height. Momentum flux is assumed to be conserved due to the reasonable accuracy of momentum conserving integral models at predicting geometric parameters (Oliver *et al.*, 2013). The loss of buoyancy flux simulates detrainment on the inner side of discharges. The decay

of reduced gravity is assumed to mimic the behaviour of a pure jet up to maximum height. The non-dimensionalised relationship for buoyancy loss with path length up to maximum height is shown in equation 3.44.

$$\frac{\mathrm{d}B_\star}{\mathrm{d}s_\star} = \frac{B_\star}{Q_\star}\left(\frac{\mathrm{d}Q_\star}{\mathrm{d}s_\star} - 2k_T B_\star\right) \tag{3.44}$$

Beyond maximum height, buoyancy flux is assumed to be constant as equation 3.44 becomes positive on the falling side of discharges (Oliver, 2012). This reduces dilution substantially and $B_\star$ would become greater than 1. The RBF model differs to all other models as the spread assumption is used to close the system of differential equations in Eulerian form. Dilution and geometric predictions were obtained in non-dimensionalised form.

3.4 Comparison of Current Models

Predictions of currently available integral models outlined in the previous sections will be evaluated by comparison to available experimental values. Geometric predictions of models will be compared to experimental data at source angles of 30°, 45°, and 60° (Table 3.1). Dilution at maximum height and the return point will be compared to available experimental data at all sources angles (Figures 3.3 - 3.4). An additional 'Detrainment Model' developed as part of the present study is included in the table and figures to reduce repetition. The assumptions and equations of this new model will be outlined in section 3.5, including a comparison to currently available models and experimental results.

Geometric maxima of INBJs are important parameters for the design of desalination plant outfalls. The vertical distance to the outside edge of the discharge at maximum height determines the minimum depth of the water column required to avoid impingement with the water surface. The horizontal distance to the return point is important to determine the approximate location of discharge impingement with the seabed. Geometric parameters of INBJs have been included in numerous studies. The experimental mean and standard deviation of geometric parameters were determined to allow for direct comparison of different integral models without considering the variation in data of individual experimental studies. The experimental mean and standard deviation of geometric parameters were determined from the following studies: Zeitoun (1970), Roberts & Toms (1987), Lindberg (1994), Roberts *et al.* (1997), Cipollina *et al.* (2005), Nemlioglu & Roberts (2006), Kikkert *et al.* (2007), Shao & Law (2010), Ferrari & Querzoli (2010), Papakonstantis *et al.* (2011a,b), Lai & Lee (2012), Oliver (2012). Geometric parameters in table 3.1 have been non-dimensionalised by the initial source diameter and initial Froude number. Individual geometric parameters from these

experimental studies are shown in figures 5.15 - 5.19 (Section 5.2.3).

Commercial integral models (CorJet, VISJET, Visual Plumes) underestimate all geometric parameters for the source angles assessed (Table 3.1). Their predictions of geometric parameters are also all beyond one standard deviation of the experimental means. VISJET predictions are closer to the experimental mean values than other commercial models, while Visual Plumes predictions are furthest from them. Limited geometric predictions were available from the integral model of Papanicolaou *et al.* (2008), however available predictions were generally better than those of commercial models. Predictions from Papanicolaou *et al.* were generally within or slightly below one standard deviation of the experimental means. However, the horizontal distance to the return point was overestimated beyond one standard deviation for the source angle of 45° by the integral model of Papanicolaou *et al.* (2008). Geometric predictions by the RBF model were far better than those of buoyancy conserving models (CorJet, VISJET, Visual Plumes, Papanicolaou *et al.*, 2008). RBF model predictions generally underestimated the experimental geometric means, with the exception of the horizontal distance to the return point at the source angle of 60°, which was overestimated. However, the geometric predictions by the RBF model were mostly within one standard deviation of the experimental means.

Table 3.1 – Comparison of non-dimensionalised geometric parameters at maximum height and the return point from experimental studies with model predictions for source angles of 30°, 45°, 60°. Geometric parameters: horizontal distance to maximum centreline height (x_m), vertical distance to maximum centreline height (z_m), horizontal distance to return point where discharge falls back to source height (x_r).

	30°			45°			60°		
	$\frac{x_m}{F_o d}$	$\frac{z_m}{F_o d}$	$\frac{x_r}{F_o d}$	$\frac{x_m}{F_o d}$	$\frac{z_m}{F_o d}$	$\frac{x_r}{F_o d}$	$\frac{x_m}{F_o d}$	$\frac{z_m}{F_o d}$	$\frac{x_r}{F_o d}$
Experimental Data									
Mean	1.89	0.68	3.15	1.89	1.16	3.17	1.69	1.68	2.80
Standard Deviation	0.26	0.07	0.11	0.14	0.05	0.17	0.16	0.08	0.25
Model Predictions									
CorJet	1.49	0.56	2.57	1.52	0.97	2.63	1.25	1.37	2.22
VISJET	1.54	0.57	2.69	1.59	1.01	2.79	1.35	1.43	2.41
Visual Plumes	1.34	0.49	2.32	1.35	0.85	2.37	1.10	1.19	2.01
Papanicolaou et al.	-	-	-	1.73	1.16	3.48	-	1.58	2.91
RBF	1.70	0.64	2.93	1.80	1.13	3.13	1.61	1.66	2.87
Detrainment Model	1.68	0.63	2.96	1.74	1.11	3.10	1.48	1.57	2.70

In general, geometric predictions by the flux conserving models (CorJet, VISJET, Visual Plumes, Papanicolaou *et al.*, 2008) were worse than predictions of the RBF model, the latter allowing buoyancy flux to be lost from the control volume. The improved

geometric predictions of maximum height and the return point of the RBF model reflect the impact of the loss of buoyancy flux from the main flow. Maximum height is reached by discharges when the buoyancy generated momentum flux equals the initial vertical momentum flux. The loss of buoyancy flux improves geometric predictions of maximum height as the path length required for these terms to become equal is increased. The loss of buoyancy reduces the reduced gravity of the control volume, reducing the buoyancy generated momentum flux on the falling side of discharges. Assuming the horizontal momentum flux is constant, the higher vertical distance of maximum height and the loss of buoyancy result in the control volume travelling further horizontally before reaching the return point.

Centreline or minimum dilutions at maximum height and the return point of INBJs are important parameters for determining the maximum mean concentration of contaminants in discharges at these locations. Figure 3.3 compares experimentally measured non-dimensionalised dilutions at maximum height from individual studies with predictions by integral models. Commercial integral models underestimate dilution at maximum height for all source angles. Predictions from these models are all outside the range of measured values for all source angles. Predictions all follow a similar trend for the range of source angles assessed. Dilution rises to a maximum at around 45° before decreasing for higher source angles. Predictions of Visual Plumes are slightly better than those of other commercial models for source angles above 30°. Predictions of CorJet underestimate the measured dilutions by the largest amount for source angles below 65°. Dilution predictions of the integral model by Yannopoulos & Bloutsos (2012) significantly overestimate measured dilutions for source angles between 15°-60°, and underestimated dilution for 75°. These overestimated dilution predictions were an average of 26 % greater at maximum height than those of any other current integral model (Figure 3.3). Dilution predictions at maximum height by the RBF model were greatly improved over those of commercial models. Dilution predictions of the RBF model underestimate the majority of experimentally measured values but were within the range of scatter. RBF model predictions were close to the predictions of the analytical model by Kikkert *et al.* (2007), which was included in figure 3.3 for comparison. The similarity of predictions by these models is likely due to the shared assumption that INBJs behave like pure jets up to maximum height.

Figure 3.4 compares experimentally measured non-dimensionalised dilutions at the return point from individual studies with predictions of numerical models. Commercial integral models (CorJet, VISJET, Visual Plumes) continue to underestimate dilution at the return point for all source angles. Dilution predictions fall outside the range of measured values for all source angles, with the difference between predictions and experimental values increasing for higher source angles. Predictions from these models all follow a similar trend, with the maximum dilution at the return point predicted

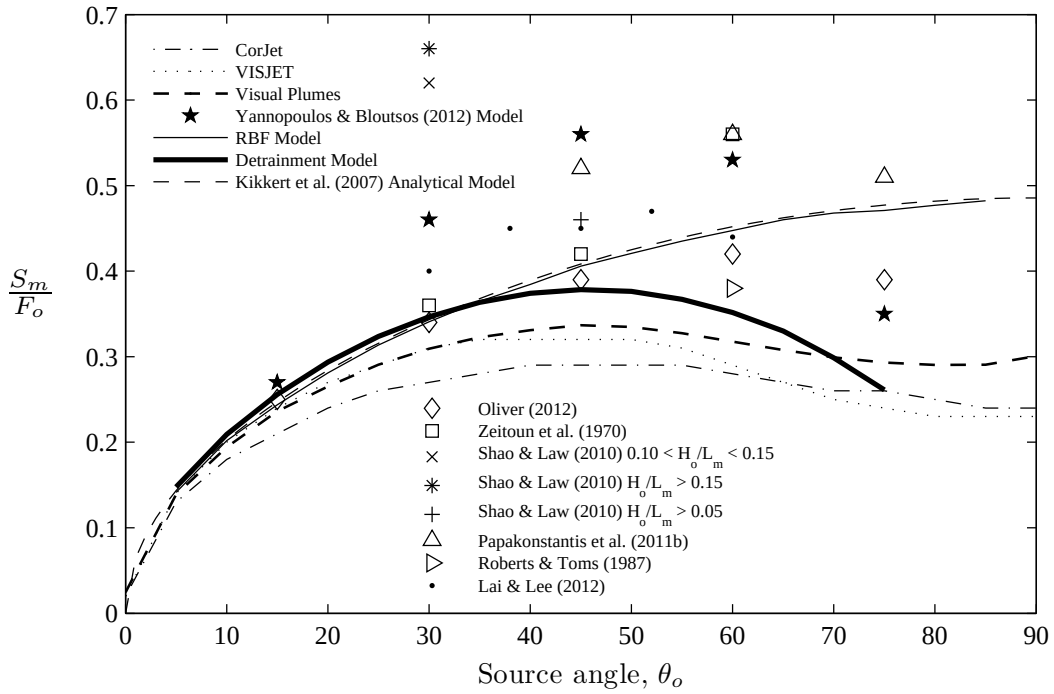

Figure 3.3 – Comparison of non-dimensionalised dilution at maximum height from experimental studies with model predictions for all source angles.

to occur for source angles between 50° and 65°. Predictions of VISJET were slightly better than those of other commercial models over the full range of source angles, as they are the nearest to measured values. Experimentally measured return point dilutions increase with source angle above 30°, whereas predictions of commercial models remain relatively constant for these source angles. The maximum dilution occurred at 60° for experimental studies that measured dilution at a range of high source angles (Papakonstantis *et al.*, 2011b; Oliver, 2012). Dilution predictions of the integral model by Yannopoulos & Bloutsos (2012) significantly overestimated measured dilutions at the return point. Dilution predictions are an average of 43 % greater than the experimental mean and an average of 102 % greater than those of any other current integral model (Figure 3.4). Dilution predictions of the RBF model are better than commercial models up to the source angle of 60°. Predictions underestimate the majority of measured values up to 60°, before the predicted dilution increases rapidly at higher source angles. Predictions of the analytical model of Kikkert *et al.* (2007) are lower than those of the RBF model and also underestimate the majority of measured values.

The dilution predictions of commercial integral models are very conservative as they substantially underestimate experimentally measured dilutions at maximum height and the return point (Figures 3.3 - 3.4). However, conservative predictions are desired for the design of desalination plant outfalls in order to meet or exceed regulatory requirements with a high level of certainty. There is significant scatter amongst the experimentally measured dilution values at the return point (Figure 3.4). This scatter is likely due

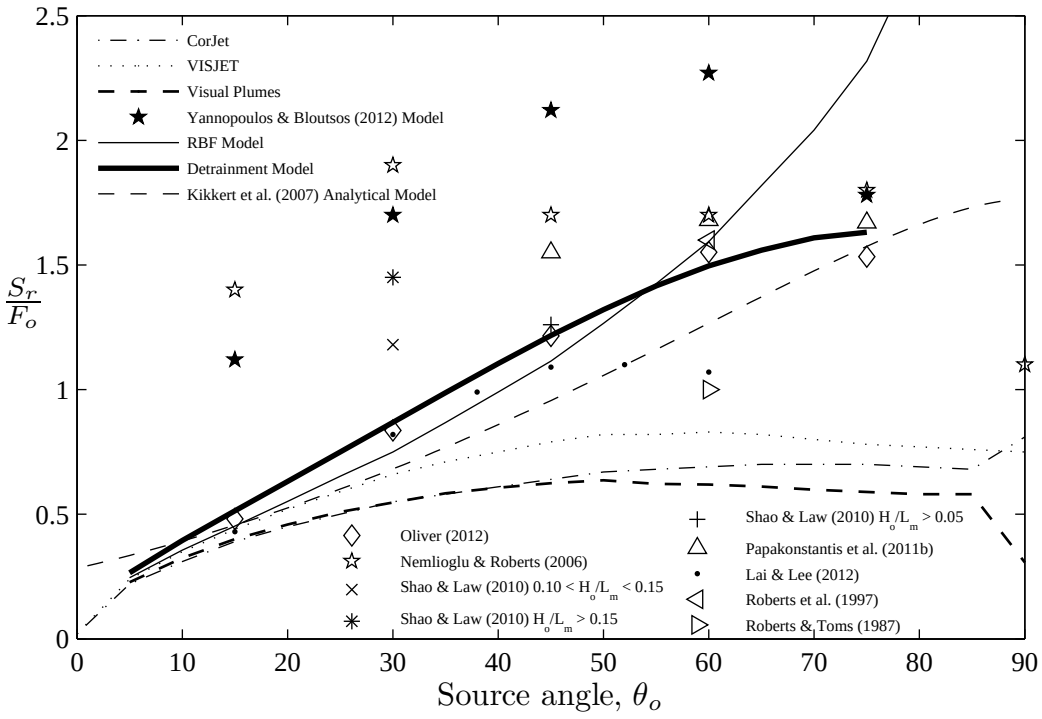

Figure 3.4 – Comparison of non-dimensionalised experimental dilution at the return point from experimental studies with model perditions for all source angles.

to the difference in experimental configurations between studies. The location of the lower boundary was different for all studies (Section 2.4). Only Oliver (2012) conducted experiments without the influence of a lower boundary on observed flow behaviour. This is critical, as all current integral models do not consider the influence of the lower boundary interaction on the flow and assume an unlimited ambient environment (Palomar *et al.*, 2012b). Therefore, the measured dilution values of Oliver (2012) are the only experimental values that should be directly compared to predictions by current integral models. However, comparisons are made with all measured dilution values due to the limited number of studies without lower boundary influence.

Commercial models and that of Papanicolaou *et al.* (2008) assume that mass, momentum, and buoyancy are conserved by INBJs. Predictions of commercial models significantly underestimated the measured dilution of discharges at maximum height and the return point (Figures 3.3 - 3.4). The RBF model and the integral model of Yannopoulos & Bloutsos (2012) show that the loss of fluxes from the control volume increase the predicted dilution of discharges at maximum height and the return point. The loss of buoyancy with path length simulates the detrainment of negatively buoyant fluid from the inner side of discharges due to unstable stratification, which has been observed experimentally in many studies (Lane-Serff *et al.*, 1993; Kikkert, 2006; Ferrari & Querzoli, 2010; Papakonstantis *et al.*, 2011a,b; Lai & Lee, 2012; Oliver, 2012). Predictions of Yannopoulos & Bloutsos (2012) overestimated dilution at these locations

indicating the mechanism of mass, momentum, and buoyancy flux loss is incorrectly modelled. Dilution predictions of the model by Yannopoulos & Bloutsos (2012) are very non-conservative and should not be used for the purpose of desalination outfall design. Dilution predictions of the RBF model were closer to experimental values at source angles below 65°. Geometric predictions of the RBF model are also significantly improved over those of commercial integral models (Table 3.1).

Re-entrainment of fluid from the falling side into the rising side of INBJs has been observed experimentally at high source angles above 75° (Bloomfield & Kerr, 2002; Ferrari & Querzoli, 2010; Oliver, 2012). The vertical distance to the outside edge at maximum height decreases for source angles $\geq 80°$ (Bloomfield & Kerr, 2002; Ferrari & Querzoli, 2010), despite the increased initial vertical momentum flux at these source angles. Re-entrainment adds buoyancy flux to the control volume on the rising side of discharges, increasing the reduced gravity of the flow. The flow mechanism of re-entrainment is not modelled by current integral models (Papanicolaou *et al.*, 2008; Palomar *et al.*, 2012b; Yannopoulos & Bloutsos, 2012). Therefore, comparison of integral model predictions to measured concentration and velocity values at source angles $\geq$ 75° should be limited.

3.5 Detrainment Model

The purpose of the 'Detrainment Model' developed here is to improve predictions of INBJs using a physically based mechanism to represent detrainment on the inner side of discharges. Current integral models from the previous sections were the basis of this new model, with the addition of a detrainment mechanism. Geometric and dilution predictions are compared to the currently available models and experimental values at the end of this section.

The performance of the RBF model indicated that the loss of buoyancy flux improves predictions if the amount of buoyancy flux loss is modelled appropriately. The RBF model assumes that INBJs have the same dilution rates as pure jets up to maximum height. This assumption results in the loss of buoyancy flux, which improves model predictions. However, this assumption does not model the mechanism of buoyancy flux loss, rather an assumption is applied that gives the required amount of buoyancy loss to improve predictions.

Detrainment on the inner side of discharges results from gravitational effects dominating the local flow behaviour. The formation of large scale turbulent eddies entrains ambient fluid on both sides of discharges near the source. Instantaneous velocities of fluid parcels near the outer edges of the flow can become very low in turbulent eddies during this entrainment process (Yannopoulos & Bloutsos, 2012). The unstable stratification on the inner side of INBJs suggests that the gravitational instability can

dominate the behaviour of fluid parcels with very low velocities. The gravitational instability then results in these fluid parcels falling downwards out of the flow, which has been experimentally observed by Kikkert *et al.* (2007) and Papakonstantis *et al.* (2011a). Detrainment from the flow occurs when these fluid parcels move sufficiently far enough away from the flow that the shear generated turbulent eddies are unable to re-entrain these fluid parcels. Therefore, detrainment is dependent on the local parameters that affect the inertial and gravitational forces of the flow. A detrainment velocity (u_D) is assumed to remove buoyancy flux from the flow, which is dependent on local top-hat parameters, as shown in equation 3.45.

$$u_D = f(\hat{g_T}, b_T, u_T) \tag{3.45}$$

Dimensional analysis results in the two dimensionless π groups shown in equation 3.46.

$$\pi_1 = \frac{u_D}{\sqrt{\hat{g_T} b_T}} \qquad \pi_2 = \frac{u_T}{\sqrt{\hat{g_T} b_T}} \tag{3.46}$$

Combining the two groups produces an equation for u_D with a dimensionless detrainment constant (k_D) as shown in equation 3.47,

$$u_D = k_D \frac{\hat{g_T} b_T}{u_T} = k_D \frac{\sqrt{\hat{g_T} b_T}}{F_L} \tag{3.47}$$

where the local densimetric Froude number (F_L) is defined below.

$$F_L = \frac{u_T}{\sqrt{\hat{g_T} b_T}} \tag{3.48}$$

Non-dimensionalising equation 3.47 produces the relationship shown in equation 3.49, where $F_{L\star} = F_L / F_o$.

$$u_{D\star} = \frac{k_D}{{F_o}^2} \frac{\hat{g_{T\star}} b_{T\star}}{u_{T\star}} = \frac{k_D}{{F_o}^2} \frac{\sqrt{\hat{g_{T\star}} b_{T\star}}}{F_{L\star}} \tag{3.49}$$

This relationship indicates that detrainment from the main flow is dependent on a ratio of gravitational to inertial terms as expected. The entrainment relationship from section 3.1.2 shows that entrainment by turbulent eddies is directly proportional to the axial velocity of the flow. Therefore, detrainment is suppressed by large entraining influences in high velocity regions as indicated by equation 3.49. Additionally, regions with highly concentrated gravitational potential (large $\hat{g_T}$, small b_T) are more likely to detrain fluid across the unstable stratification on the inner side of INBJs. The loss of buoyancy flux perpendicular to the control surface on the inner side of the control volume is given by equation 3.50. This relationship includes a dependence on local angles of the control volume (θ).

$$\frac{\mathrm{d}B}{\mathrm{d}s} = 2b_T\ \hat{g_T}\ u_D\cos(\theta) \tag{3.50}$$

The full system of differential equations for the detrainment model in non-dimensionalised top-hat form is shown below:

$$\frac{\mathrm{d}B_\star}{\mathrm{d}s_\star} = \frac{-8k_D}{\pi {F_o}^2}\frac{{B_\star}^2{b_{T\star}}^2}{Q_\star M_\star}\frac{M_{H\star}}{M_\star} \tag{3.51}$$

$$\frac{\mathrm{d}b_{T\star}}{\mathrm{d}s_\star} = k_T \tag{3.52}$$

$$\frac{\mathrm{d}M_{H\star}}{\mathrm{d}s_\star} = 0 \tag{3.53}$$

$$\frac{\mathrm{d}M_{V\star}}{\mathrm{d}s_\star} = \frac{4\hat{g_{T\star}}{b_{T\star}}^2}{{F_o}^2} \tag{3.54}$$

$$\frac{\mathrm{d}Q_\star}{\mathrm{d}s_\star} = \frac{b_{T\star}}{\sqrt{M_\star}}\frac{\mathrm{d}M_\star}{\mathrm{d}s_\star} + 2\sqrt{M_\star}\frac{\mathrm{d}b_{T\star}}{\mathrm{d}s_\star} \tag{3.55}$$

$$\frac{\mathrm{d}M_\star}{\mathrm{d}s_\star} = \frac{M_{V\star}}{M_\star}\frac{\mathrm{d}M_{V\star}}{\mathrm{d}s} \tag{3.56}$$

$$\frac{\mathrm{d}x_\star}{\mathrm{d}s_\star} = \frac{M_{H\star}}{M_\star} \tag{3.57}$$

$$\frac{\mathrm{d}z_\star}{\mathrm{d}s_\star} = \frac{M_{V\star}}{M_\star} \tag{3.58}$$

This system of differential equations was solved using the Runge-Kutta method with the following initial conditions: $M_{H\star o} = \cos(\theta_o)$, $M_{V\star o} = \sin(\theta_o)$, $M_{\star o} = 1$, $Q_{\star o} = 1$, $B_{\star o} = 1$, $b_{T\star o} = 0.5$, $s_{\star o} = b_{T\star o}/k_T$, $x_{\star o} = s_{\star o}\cos(\theta_o)$, $z_{\star o} = s_{\star o}\sin(\theta_o)$.

Initial simulations of the detrainment model found the k_D value of 0.25 produced dilution and geometric predictions that were similar to experimental values over a wide range of source angles. k_D is an important input parameter that is unique to the detrainment model. It determines the magnitude of u_D and subsequently the amount of buoyancy flux lost from the control volume. A sensitivity analysis was conducted to determine the response of model output parameters to k_D at source angles of 30°, 45°, and 60°. k_D was varied around the base value of 0.25, to minimum and maximum values of 0 and 0.50. The return point dilution (S_r) had the greatest response to changes in k_D for the source angle of 30° (Figure 3.5). The response of maximum height dilution (S_m) was approximately half the magnitude of S_r. However, the response of dilution was far greater than geometric or velocity output parameters. Geometric output parameters (x_m, z_m, x_r) had a maximum response of 4 % for the maximum 100

% change in k_D. Therefore, geometric output parameters can be considered relatively insensitive to k_D. Response of velocity output parameters at maximum height (u_m) and the return point (u_r) are inversely related to changes in k_D. The magnitude of the response for u_r is approximately twice that of u_m. The path length to the return point is roughly twice the path length to maximum height. Therefore, the magnitude of response for velocity and dilution output parameters must also be dependent on path length, as the magnitude of response for u_r and S_r are twice that of u_m and S_m. The relative response magnitudes for different output parameters at 45° and 60° are similar to the responses at the source angle of 30° (Figures B.1 - B.2, Appendix B). The response magnitude increases for increasing source angle and the response of geometric and dilution parameters are slightly greater for $k_D = 0.50$ than for $k_D = 0$.

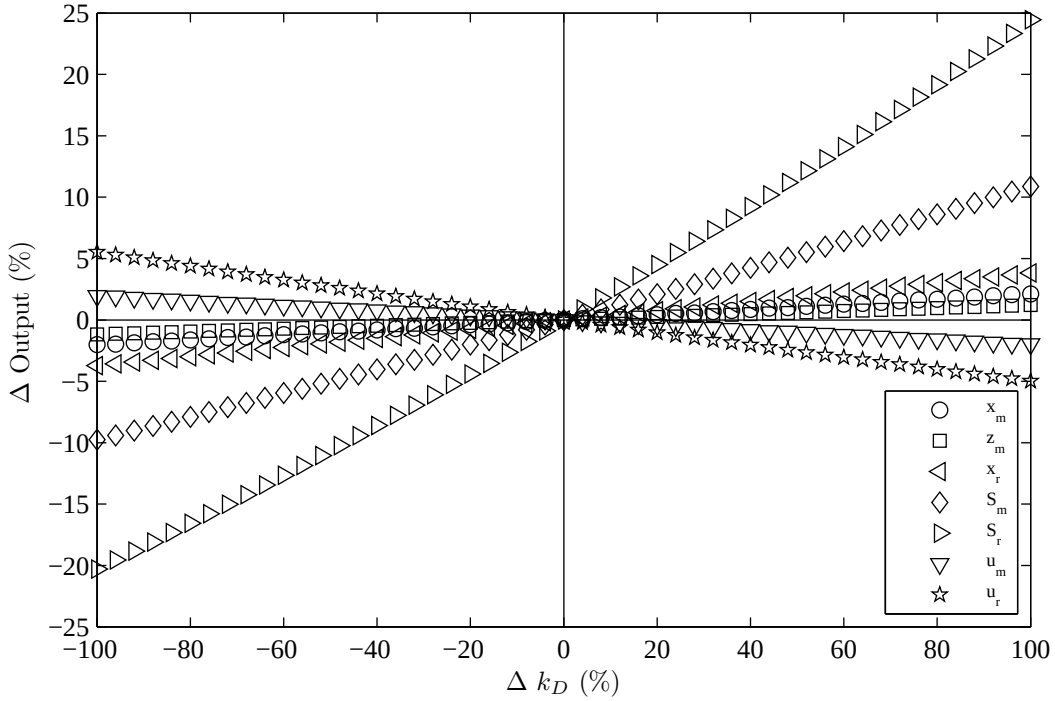

Figure 3.5 – Sensitivity analysis of detrainment model output parameters to k_D at the source angle of 30°, base k_D value of 0.25.

Dilution predictions were found to have the largest response to changes in k_D, and the capability to accurately predict dilutions at the return point is important for meeting regulatory requirements of desalination plant outfalls. Therefore, a final k_D value of 0.23 was found to provide the optimum predictions at this location over a wide range of source angles. INBJs are complex asymmetric flows that are unable to be fully represented by integral models. Direct comparison of u_D from equation 3.49 with experimentally measured values from the present study cannot be conducted as the radial distance at which u_D is defined is unknown. However, the form of u_D is similar to experimental values at a fixed radial distance on the inner side of discharges for all source angles studied (Figures 5.36 - 5.37, Section 5.3.1.3).

Geometric predictions by the detrainment model underestimate the experimental mean for the source angles assessed. Predictions are within or close to one standard deviation from the experimental mean (Table 3.1). Geometric predictions are better than those of commercial models (CorJet, VISJET, Visual Plumes) and similar to those of the RBF model. Full geometric predictions of the detrainment model will be compared to individual studies across all source angles in section 5.2.3. Dilution predictions by the detrainment model underestimate experimental values at maximum height (Figure 3.3). Predictions are within the scatter of experimental values for source angles of 15° and 30°. However, predictions are outside the scatter of experimental values for higher source angles. Predictions of the detrainment model are better than those of commercial models at maximum height, however predictions are worse than those of the RBF model and the analytical model of Kikkert *et al.* (2007) for source angles $\geq 45°$. Experimentally measured dilution values increase up to a maximum of 60°, before decreasing slightly at 75°. This differs from the maximum dilution predicted by the detrainment model, which occurs at 45°. Dilution predictions subsequently decrease for higher source angles, with the gradient of predictions increasing with increasing source angle (Figure 3.3). For higher source angles, momentum decreases rapidly before maximum height and a constant spread rate is assumed. This results in negative values of $\mathrm{d}Q_\star/\mathrm{d}s_\star$ (Equation 3.55) and a reduction in dilution with path length. Negative values were found to occur for source angles $\geq 70°$, however a reduction in the rate of dilution occurred for lower source angles. This issue is not limited to the detrainment model, rather it is common to integral models that use the spread assumption. Integral models that use the entrainment relationship also predict unrealistic behaviour for high source angles, which is not observed in physical experiments. Spread predictions by CorJet and the integral model of Papanicolaou *et al.* (2008) increased rapidly near maximum height for source angles above 60° (Oliver, 2012). Predictions of discharge width tend towards infinity at maximum height as $\theta_o \to 90°$ (Oliver, 2012). Therefore, the behaviour of INBJs at maximum height for high source angles is an unresolved issue for all integral models. Both spread and entrainment relationships used by integral models result in outputs that do not represent observed or expected behaviour of discharges at this location. These are underlying issues for integral models at higher source angles. These issues are not specifically related to the complex detrainment and re-entrainment behaviour observed physically at higher source angles as this behaviour is typically not considered by models.

Dilution predictions at the return point by the detrainment model are within the scatter of experimentally measured values (Figure 3.3). As previously mentioned, model predictions should only be directly compared to the experimental values of Oliver (2012) as this is the only experimental study without the influence of a lower boundary. Dilution predictions of the detrainment model are close to the experimental values of

Oliver (2012) for all source angles. Predictions by the detrainment model are better than those of all other models at the return point. Predictions are close to the RBF model predictions for source angles up to 60°. Predicted dilution by the RBF model increases rapidly for higher source angles, whereas predictions by the detrainment model level off for higher source angles, following the trend of experimental values. The improved dilution predictions by the detrainment model at the return point, compared to predictions at maximum height, indicate that the overall loss of buoyancy flux is being represented well by the detrainment mechanism. The loss of buoyancy flux occurs rapidly for the source angle of 75° at maximum height ($s/F_o d = 2.24$, Figure 3.6). The majority of detrainment occurs near maximum height due to the relatively small size of momentum flux and inertia for high source angles. This increases the relative size of the gravitational potential, which increases detrainment. For real flows, there is likely to be differences in velocity between inner and outer sides of discharges due to detrainment on the inner side. Detrained fluid moves in the opposite direction to the main flow, which could slow down fluid in the main flow on the inner side of discharges. Therefore, the rapid detrainment of buoyancy flux by the detrainment model could occur earlier than predicted, resulting in higher dilution predictions at maximum height, closer to experimentally measured dilutions (Figure 3.3).

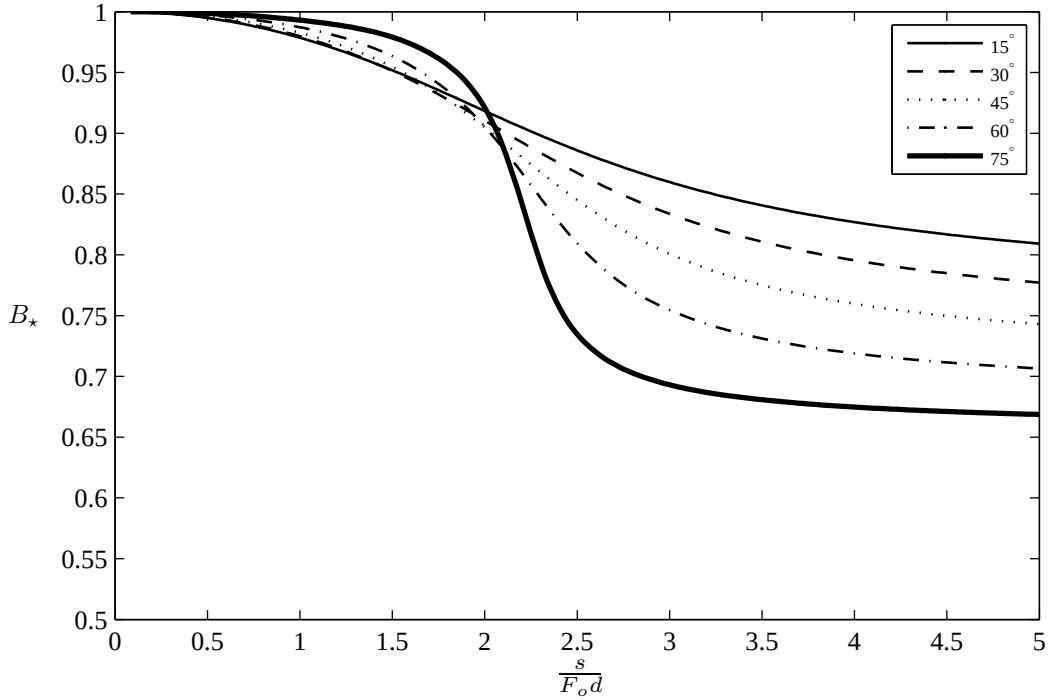

Figure 3.6 – Buoyancy flux against non-dimensionalised path length for the detrainment model at a range of source angles.

[Intentionally left blank]

Chapter 4

Experimental Systems

4.1 Introduction

The purpose of the experimental system was to obtain detailed velocity field information from inclined negatively buoyant jets discharged into a stationary ambient fluid. High quality two-dimensional velocity fields for these discharges were obtained using the flow visualisation technique called particle tracking velocimetry (PTV). A system for PTV analysis was developed by Blackett (1994) for experimental fluid flows. The system was verified against artificial flows with a known structure and velocity, along with laboratory stirring experiments. This system provided the basis of PTV analysis for the Streams software Nokes (2012), which was used extensively in this study. PTV is a non-intrusive technique that involves seeding the discharged fluid and ambient fluid with small tracer particles that have a similar density to water. The particles are illuminated with a light source, which allows the motion of particles to be recorded by a video camera located perpendicular to the light sheet. The light source used in these experiments was a laser that produced a thin sheet of light, when reflected through a system of mirrors (Figure 4.1). The sheet of laser light passed directly through the centreline of the discharge to produce a two-dimensional view of the flow. The location of particles is recorded by a video camera at a constant frame rate, allowing the velocity to be determined by the change in location of the particles between images. The velocity of the fluid can be directly inferred from the velocity of the small particles as they are fully mixed and essentially alike.

Particle image velocimetry (PIV) is a similar flow visualisation technique to PTV, but differs in the timing that images are recorded by the video camera. For PIV, the video camera records two images separated by a very small time interval that correspond to two pulses of laser light. PIV tracks particle patterns through the computation of cross-correlations between these two images. PIV has been used by previous researchers (Law & Wang, 2000; Wang & Law, 2002) in a combined system with LIF for velocity and

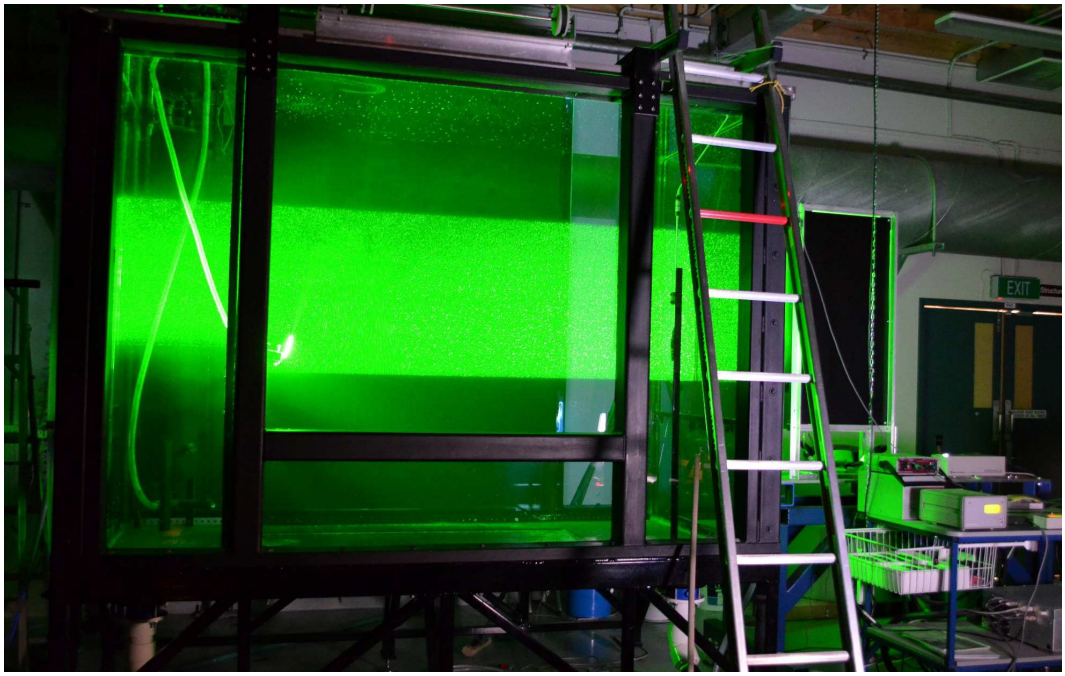

Figure 4.1 – Photo of the experimental tank with laser sheet illuminating tracer particles.

concentration measurements of discharges. Lai & Lee (2012) conducted PIV experiments to take velocity measurements of INBJs.

A comprehensive review and comparison of PIV/PTV can be found in *"Particle Image Velocimetry: A Practical Guide"* (Raffel *et al.*, 2007). PTV was used in this study due to the simplified experimental configuration required and the versatile particle matching algorithms available.

This chapter details the PTV technique developed for the physical experiments in this study. The configuration and calibration of equipment is shown, as well as the method utilised to conduct the experiments. A detailed explanation of the image analysis processes used in the Streams software is provided. This is followed by verification of the PTV system using pure jet experiments, which have been extensively investigated in the literature (Wyganski & Fielder, 1969; Fischer *et al.*, 1979; Panchapakesan & Lumley, 1993; Hussein *et al.*, 1994; Wang & Law, 2002).

4.2 Equipment Configuration

Physical experiments were conducted in the Fluid Mechanics Laboratory of the Civil and Natural Resources Engineering Department at the University of Canterbury, located in Christchurch, New Zealand. All experiments were conducted with the equipment configuration similar to that shown in figure 4.2, depending on the requirement of boundary influence for each experiment. The raised platform was removed from the tank if no boundary influence was specified, which allowed the negatively buoyant

discharge to fall unobstructed out of the view of the video camera.

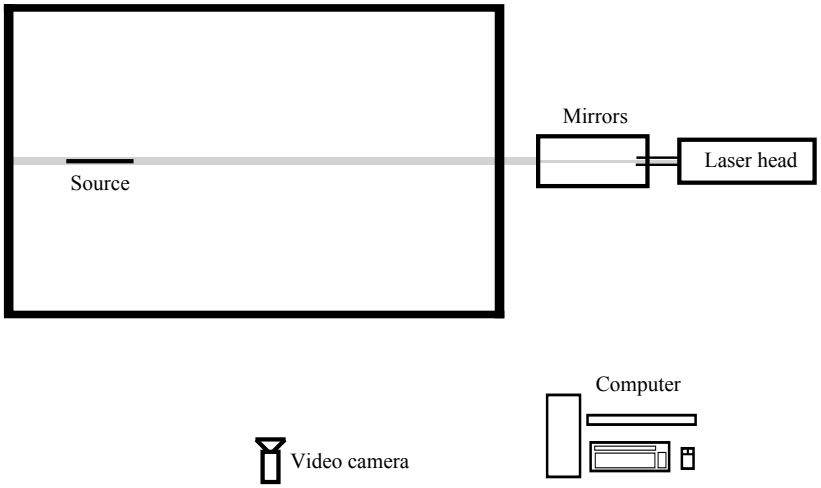

(a) Plan view

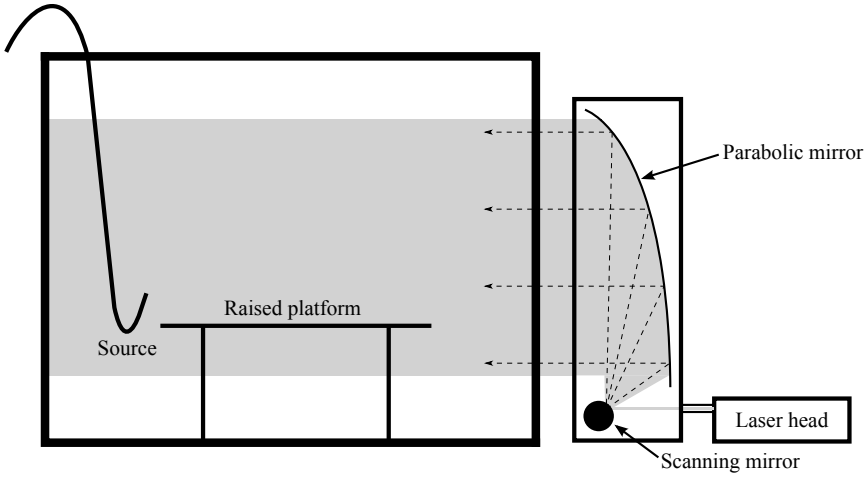

(b) Elevation view

Figure 4.2 – Schematic of the typical experimental configuration.

The experimental tank had dimensions of 2.30 m wide, by 1.23 m deep by 1.78 m high. All sides of the tank were made of glass. This allowed the laser sheet to pass through the centre of the tank from the right hand side (Figure 4.2). The motion of illuminated particles was recorded through the front glass of the tank. Two different lasers were used during the experiments. The original 2 W Spectra-Physics Millennia II laser was damaged during the 4$^{\text{th}}$ September 2010 Christchurch earthquake and subsequent aftershocks. This was replaced by a 2 W CNI laser. Otherwise, the laser system remained unchanged. Lasers produce a focused point source of coherent light with very low divergence. This property makes lasers an ideal light source for illuminating only specific portions of fluid flows. Section 4.2.3 looks at the specific details of the laser system and the effect of the Christchurch earthquakes.

The camera viewed the motion of illuminated particles through the front glass window which had maximum viewable dimensions of 1.25 m by 1.25 m. The camera was

placed at a perpendicular distance of 3.04 m or 4.26 m from the laser sheet, depending on the scale of the flow. The inner side of the rear glass was painted with matt black paint to prevent reflections of laser light from the source being visible to the camera. The video camera used was a JAI Pulnix TM-2030CL single CCD, with a GoYo 1" 50 mm f/0.95 lens, that produced greyscale images at 32 Hz. Raw images from the camera were transferred to the computer via a CameraLink interface and written to a high speed hard drive. Raw images were converted to lossless bitmap images before being analysed using the process described in section 4.3.

If no boundary influence was required, the raised platform shown was removed allowing the discharge to fall out of the camera view prior to reaching the bottom of the tank. There was a minimum distance of 655 mm from the bottom of the images to the bottom of the tank. This allowed the discharge to be undisturbed by the bottom boundary in the camera view.

The angle of the source was set between 0° and 75° with an inclinometer to an accuracy of ± 1°. An image of the source was captured with the camera and the angle tool in GIMP software (www.gimp.org) was used to verify the angle. The raised platform used as the lower boundary for the discharges had a diameter of 1040 mm and was levelled in all directions using a 1200 mm digital level with an accuracy of ± 0.1°. There was a minimum distance of 100 mm between the edge of the raised platform and the side of the experimental tank to allow discharged fluid to fall off the edge of the raised platform.

4.2.1 Header System

A header system supplied discharged fluid to the source for the physical experiments (Figure 4.3). The system provided a constant head or constant water surface elevation of at least 2.7 m above the exit of the source to ensure the flow of fluid was constant throughout the duration of each experiment. Fluid was pumped into the pressurised tank, which was then pressurised with the reticulated compressed air supply. The pressurised tank was used to keep the temperature of discharged fluid at a similar temperature, typically ± 0.5 °C, to the ambient fluid. A SMC AR20 pressure regulator kept the air pressure constant throughout the experiment. Fluid in the pressurised tank was forced up to the constant head tank above. Two identical Krohne IFC 010D electromagnetic flow meters were used to measure the flow rate in the system. The flow rate up to the constant head tank was always 50 % greater than the flow rate out of the source. This ensured that fluid would overflow the constant head tank constantly throughout the experiment. A globe valve was used to control the flow rate of fluid out of the source as tracer particles would clog and restrict the flow through needle valves.

The Krohne IFC 010D flow meter measuring the flow rate out of the source had a

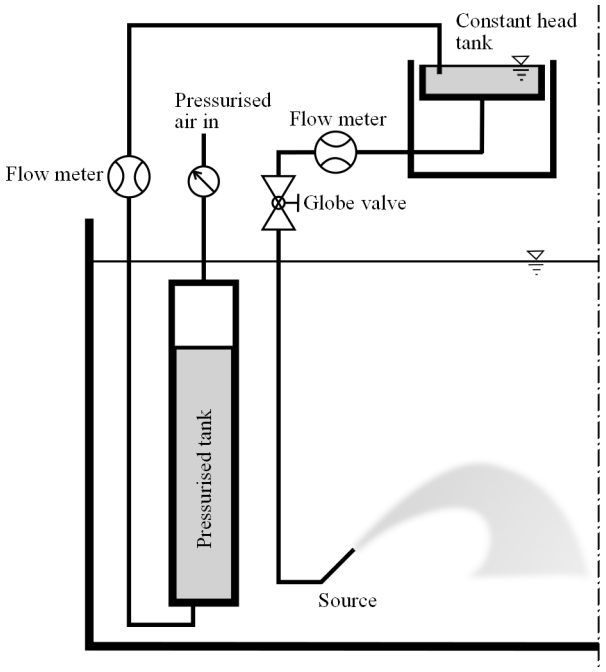

Figure 4.3 – Schematic of the header system that supplied discharged fluid to the source.

voltage output (0-5 VDC) that was proportional to flow rate. The voltage output was connected to a computer via a LabVIEW software controlled data logger. A calibration between the real flow rate and the flow measured by the flow meter and data logger was performed. The real flow rate was measured by a bucket and stopwatch test. The valve to the source was opened and the flow was allowed to stabilise. The time taken to fill two 2000 mL volumetric flasks was recorded. Any overfill of the volumetric flasks was pipetted and measured using a 50 mL measuring cylinder to accurately determine the total volume. The flow rate measured by the data logger was time averaged for the same period. This test was repeated for a range of flow rates. The relationship between real and recorded flow rates was linear for a range of different flow rates (Figure 4.4). The coefficient of determination (R^2) was 0.9994, which shows that the flow rate recorded by the flow meter and data logger is an accurate predictor of the real flow rate.

The flow rate for each experiment was logged. The measured flow rate corresponding to the analysed images was extracted and converted to the actual flow rate using the proportional relationship shown in figure 4.4. The variation of the flow rate with time for a typical experiment is shown in figure 4.5. There are small fluctuations in flow rate over time that can be partially attributed to electrical noise in the voltage output of the flow meter.

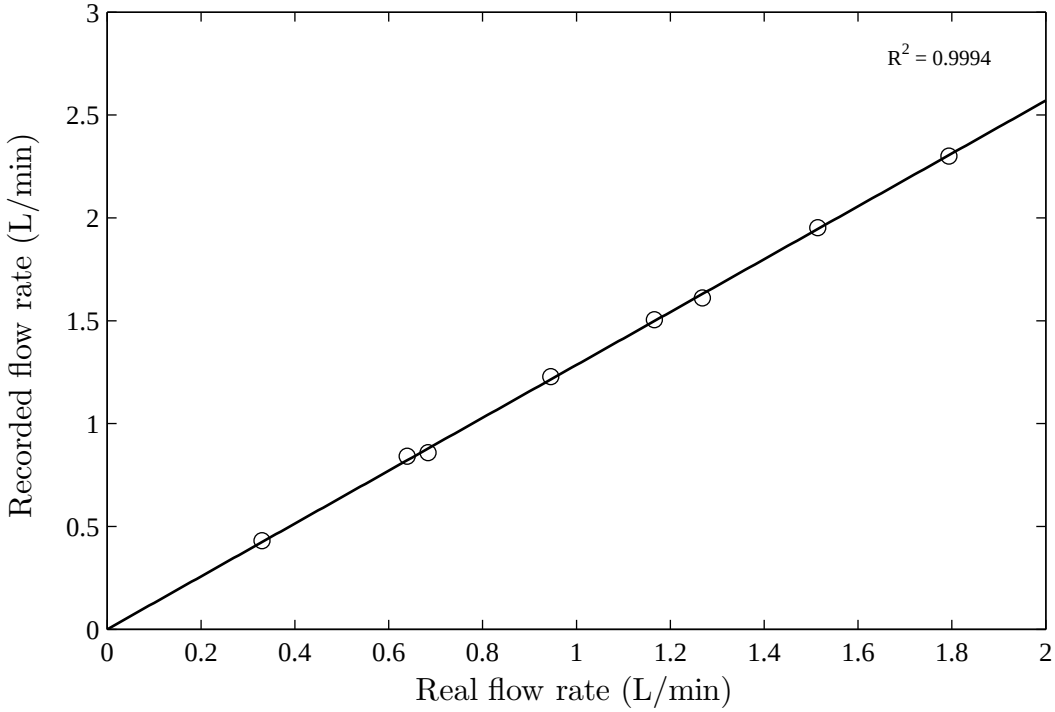

Figure 4.4 – Flow rate recorded by the flow meter using a data logger against the real flow rate measured using the bucket and stopwatch test.

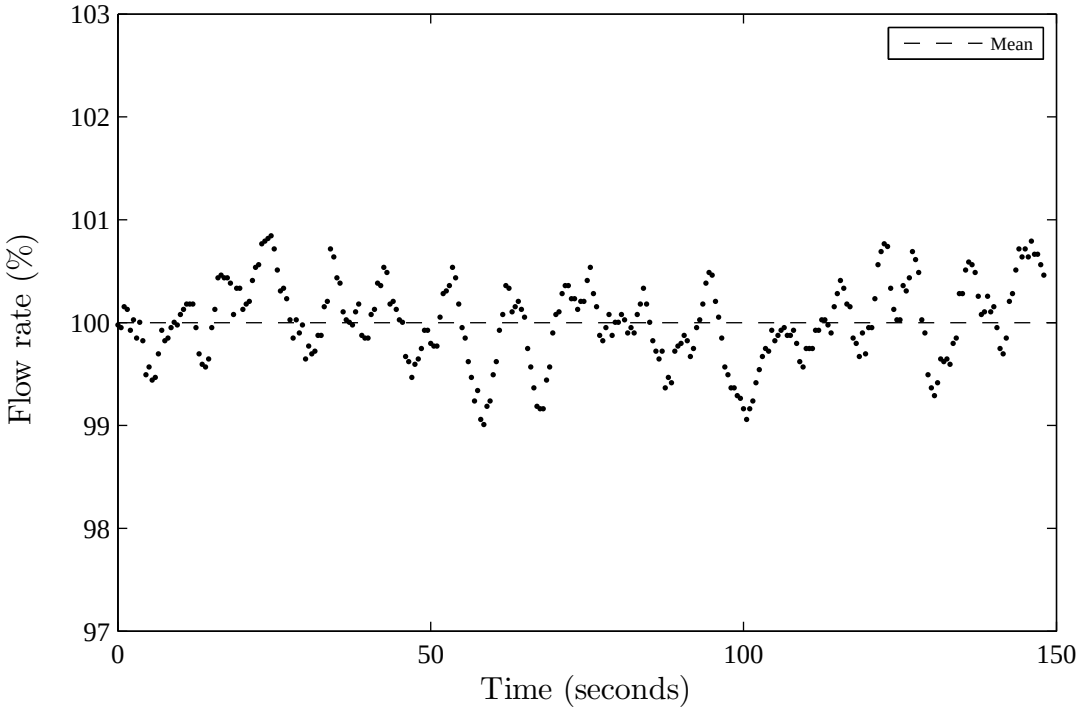

Figure 4.5 – Variation in the flow rate as a percentage of the time-averaged flow rate over time for a horizontal pure jet experiment ($d = 4.40$ mm, $Re = 4300$).

4.2.2 Camera

The JAI Pulnix TM-2030CL is a progressive scan scientific camera that allows manual control of shutter speed, gain, offset, and raw image depth to produce low noise digital images. The camera was coupled to a GoYo 1" lens with a fixed focal length of 50 mm and a maximum aperture of f/0.95. PTV experiments are conducted in low light conditions that require video and lens settings that achieve minimum pixel intensity levels in order to identify tracer particles. The camera had the capability to capture images at three different pixel depths or pixel intensity levels of 8 bit (256 levels), 10 bit (1024 levels), and 12 bit (4096 levels). Using the highest pixel depth is desirable for the highest quality images, however this requires more data to be written to a storage device. The 300 GB high speed hard drive had a minimum write speed of 75 MB/s up to 50 % capacity (Oliver, 2012, *Figure 4.7*). The hard drive write speed limited the available pixel depths. All pixel depths could be used if images were captured at 16 Hz. Only a pixel depth of 8 bit could be used at 32 Hz. The following subsections describe the configuration of camera and lens for the physical experiments.

4.2.2.1 Gain and Offset Calibration

The JAI Pulnix camera had a single charge-coupled device (CCD) that captured images in greyscale with a resolution of 1980 horizontal pixels by 1080 vertical pixels. A CCD converts the intensity of light at each pixel to an electrical charge. The intensity of light at each pixel is determined by the number of photons of light over the area of each pixel. Therefore, a higher intensity of light in an image would result in a higher electrical charge. An analogue to digital converter (ADC) converts the analogue voltage signal of the electrical charge to a digital signal. The analogue voltage signal could be amplified (gain) and/or offset to change the range of the digital signal. The JAI Pulnix camera has single-tap and dual-tap mode capability. In single-tap mode, one ADC converted the full resolution of the images. The frame rate of captured images would double to 32 Hz in dual-tap mode as two ADCs each converted half the image. The doubled frame rate was utilised as this halved the distance each tracer particle would travel between subsequent images, increasing tracer particle matching performance. Dual-Tap AccuPiXEL series camera-control manufacturer software allowed the gain and offset to be controlled through the CameraLink connection. The master offset and gain for the full resolution could be given values between 0 and 4095. The offset and gain for the right side of the image could be finely adjusted and matched to the left side of the image with values between 0 and 4095 as the conversion by each ADC was slightly different.

The two sides of the image captured by the camera in dual-tap mode needed to be similar such that tracer particles could be followed from one side of the image to

the other. Figure 4.6 shows the set up used to balance each side of the image. A linearly gradated greyscale image created using Inkscape software[1] was printed onto A4 sized paper and attached to the front of a translucent white perspex sheet. The A4 paper was levelled such that the gradation occurred vertically in the view of the camera. The camera lens was out of focus to smear light across an area that resulted in a smooth gradation of light intensity. The light source was an array of fluorescent tubes that produced a uniform sheet of light after passing through two separated sheets of translucent white perspex. Preliminary experiments had shown that master offset and gain values of 2000 were required to clearly identify tracer particles. The right fine offset and gain were iteratively adjusted until the right side of the captured images closely matched the left side of the captured image. Thirty seconds of images were captured for each iteration and then time averaged to removed fluctuations due to noise. 50 pixels in the horizontal direction either side of a vertical slice through the centre of the image were spatially averaged. This allowed the intensity of pixels on left and right sides of the image to be compared at a location where the intensity of pixels should be almost identical. Figure 4.7 compares the left and right sides of the captured images with a right fine offset value of 2940 and right fine gain value of 1550. These were the final settings used for the experiments in this study. The difference between left and right sides of the captured images is minimal across a range of greyscale intensities. The mean absolute difference between the left and right sides was 0.44 or 0.29 %. The range of intensities in the figure was limited to those available from the gradated image on the A4 paper, which was adjusted to be similar to the typical range of tracer particle intensities.

[1]Version 0.48 obtained from www.inkscape.org

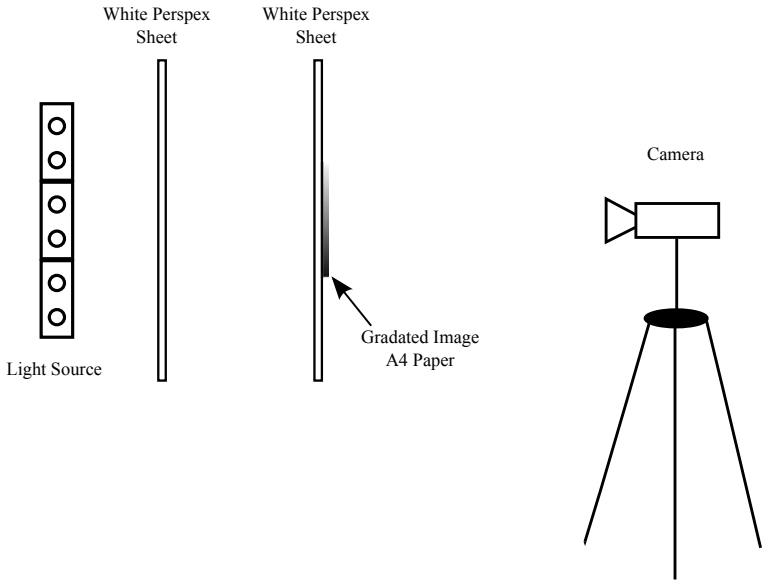

Figure 4.6 – Schematic of the set up used to balance gain and offset of the dual tap JAI Pulnix camera.

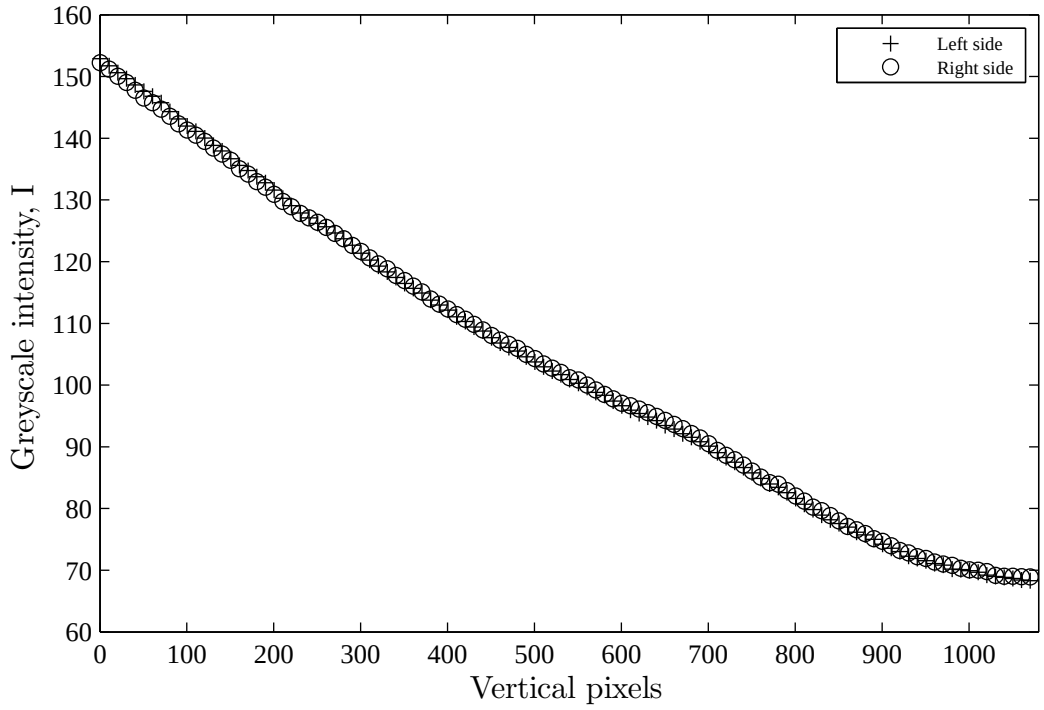

Figure 4.7 – Spatial average of 50 pixels in the horizontal direction either side of a vertical slice through the centre of a time-averaged image.

4.2.2.2 Optical Effects

Aberrations and imperfections that exist in all optical systems need to be quantified to ensure that images captured are of the highest quality possible and are a true representation of the physical experiments. A camera lens is an optical device that converges the light beams of an object on to a smaller area to be captured. Every lens converges light slightly differently resulting in unique behaviour.

Barrel and pincushion effects are the distortion of objects in images by enhancing or diminishing the magnification of the image surface. These distortions are common for all optical devices and there are well documented equations to remove these distortions (Nokes, 2012). Images captured by the standard experimental configuration were tested for barrel and pincushion effects. A sheet of white plastic with a regular square grid marked in black was placed in the experimental tank perpendicular to the camera and aligned with the laser sheet. The tank was filled with water and images were captured with the same settings used in the experiments. A perfectly square grid was superimposed on top of the images using Streams software. The images required a slight rotation to level the physical grid with the superimposed grid. Barrel or pincushion effects could be identified where the vertical and horizontal lines of the physical grid were not parallel with the superimposed grid. There were no detectable barrel or pincushion effects in the images captured.

The PTV experiments were conducted in low light conditions, which required a low f/stop number to get sufficient light onto the CCD. A high shutter speed was also required because velocities near the source were very high and hence tracer particles would smear with low shutter speeds. Using a low f/stop resulted in a very small depth of field or depth of focus away from the camera. Petzval curvature of the image through the lens caused imperfect focussing (Figure 4.8). This effect is the result of difference in shape of the lens image and the CCD. The object in figure 4.8 represents the illuminated tracer particles in experimental images. A CCD is a flat surface and therefore is different to the curved converged image produced by the lens. The lens was focused in the centre of the image as this was the location of the main flow in the image. This caused the outside edges of the images to be slightly out of focus. The vertical edges were more out of focus due to the longer horizontal dimension of the CCD.

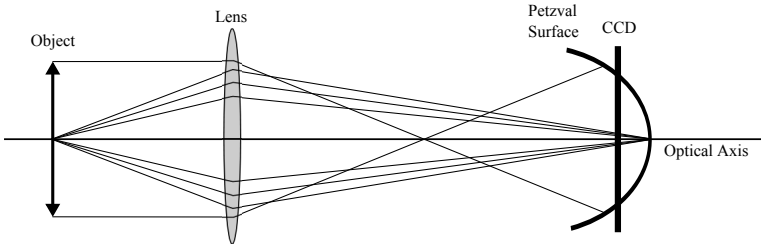

Figure 4.8 – Schematic of petzval curvature of a lens.

Optical vignetting is caused by the edges of optical elements inside the lens being shaded by other elements resulting in a reduction of pixel intensity in the corners of the image. The same set up as shown in figure 4.6 was used to test for this effect. A constant intensity greyscale image was used instead of a gradated intensity image. This produced an image with a constant intensity across the full image resolution, assuming the light source produced a uniform intensity of light. The captured images showed some reduction of pixel intensity in the corners of the images. The reduced pixel intensities coincided with areas that were out of focus due to petzval curvature. The optical vignetting effects were not corrected for as the identification of out of focus tracer particles on the outside edges of images was not necessary.

The effect of parallax can be seen when there is a change in position of an object for two different lines of sight. Parallax was assumed to be insignificant for the experimental configuration in this study due to the camera being stationary and being placed as far as possible from the laser light sheet. The depth of field was also very small due to the low f/stop number used, as noted above. The highest parallax errors would also occur in the corners of images, which were slightly out of focus due to petzval curvature.

4.2.2.3 Physical Scale and Alignment

A relationship between the physical size of the experiments and the pixel size of the experiments was required to relate the movement of illuminated tracer particles recorded by the camera to their physical velocity. A length to pixel ratio was determined for the horizontal and vertical directions for the different camera positions used. Horizontal and vertical stainless steel rulers were aligned with the laser sheet passing through the centre of the tank. The rulers were levelled in each direction and held in place with clamps. The experimental tank was then filled with water and any bubbles formed were wiped away. Images recorded by the camera were then cropped to physical marks on each of the rulers from which length to pixel ratios were determined for each direction. The ratios were identical for each direction for all camera positions, within the uncertainty of measurements.

The camera was aligned perpendicular to the laser sheet to ensure the physical scale did not vary in the horizontal direction. A laser pointer was placed on one side of the camera and the laser beam was reflected off the front side glass of the experimental tank. The camera was adjusted about the vertical axis until the laser beam reflected back in the same direction as the laser pointer. The laser pointer was iteratively placed on each side of the camera to average out any skew between sides of the camera body and any skew of the laser pointer beam. The camera was levelled about the horizontal axes using a bubble level placed inside the tank. Legs of the tripod were adjusted until the bottom of captured images was parallel to the bottom edge of the level. If required, the height of the camera was adjusted and then levels were rechecked.

4.2.2.4 Settings

The standard camera and lens settings used in this study will be detailed for completeness. The aperture of the lens was f/1.4 instead of the maximum f/0.95 to reduce petzval curvature effects. This maximised the area of the image in focus while being able to clearly identify tracer particles. The lens was focussed with the method described in the Optical Effects subsection. Dual-Tap AccuPiXEL software was used to specify the camera settings. A frame rate of 32 Hz was used with an 8-bit image depth. The electronic shutter speed was 1/100 seconds, which reduced smearing of high velocity tracer particles. The master gain and offset were values of 2000. The right fine offset value was 2940 and right fine gain value was 1550 using the method described in the Gain and Offset Calibration subsection. The pixel intensities were not modified with a positive linear look up table.

4.2.3 Lasers and Mirrors

The configuration of the laser head unit and mirror system is shown in figure 4.2(b). The point source of laser light was reflected onto a scanning mirror that rotated at 16,000 RPM. The laser light then reflected off the parabolic mirror to produce a vertical laser sheet approximately 5 mm thick. The point source of laser light was continuously moving up and down the tank at a very high rate such that it appeared to the camera and the human eye as a continuous sheet of light. Two different laser units were used in this study. The original 2 W Spectra-Physics Millennia II laser had a low optical noise at 2 W of ≤ 0.4 % RMS. This laser had previously been utilised for LIF flow visualisation experiments that required low optical noise. A 7.1 magnitude (MMS) earthquake on 4$^{\text{th}}$ September 2010 in Christchurch, New Zealand caused damage to the laser head unit of the Millennia II laser. The laser warm-up time increased markedly and performance varied on a daily basis. Subsequent aftershocks of lower magnitude may have also continued to damage the Millennia II laser. Experiments were still able to be conducted as laser output stabilised after an hour of operation. The laser output was measured for each experiment with a Newport 1918-R power meter. Laser power varied between 1.0 and 2.0 W for all experiments. This did not adversely affect experiments as the threshold particle identification intensity could be varied for each experiment (see section 4.4.1 for more details). A 6.3 magnitude (MMS) earthquake on 22$^{\text{nd}}$ February 2011 resulted in terminal damage to the Millennia II laser and no further experiments could be conducted with this laser. A replacement 2 W CNI laser was purchased to complete this study. The CNI laser had a higher optical noise at 2 W of ≤ 1 % after four hours of operation. A difference in tracer particle identification was not observed with the replacement CNI laser. The earthquakes and subsequent aftershocks also affected the parabolic mirror. The mirror would move slightly due to

the shaking. This resulted in a misalignment of the laser sheet with the experimental tank. Vertical lines were placed down the centre of the glass where the laser should enter and exit the tank. The laser sheet was aligned to these vertical lines with the parabolic mirror before each experiment.

4.3 Method

The procedures used to conduct each experiment were rigorously followed. This ensured no significant variations existed such that experiments were repeatable. The procedures followed are explained in section 4.3.1 below. The post-processing procedures used to extract velocity field data from the physical experiments are explained in section 4.3.2.

4.3.1 Physical Experiments

The routine followed to conduct the physical experiments was similar for all experiments, with deviations needed for different experimental configurations. A typical experiment took between six and eight hours to complete.

The inside glass of the empty experimental tank was cleaned with glass cleaner, containing butoxyethanol, acetone, and propanol, before each experiment. Methylated spirits was applied to inhibit the formation of bubbles on the surface of the glass. The 5000 L tank was filled with Christchurch city municipal tap water that had passed through a 5 μm filter to remove any particulate matter. Filling the tank typically took 45 minutes and was turned off using a float system, such that the tank filled to the same height for each experiment. The tank was left for one hour to allow for the formation of bubbles on the glass sides of the tank.

A 2000 L tank was used to store brine with a density approximately 3 % greater than tap water made from Grade 27 salt (NaCl) dissolved in 5 μm filtered tap water. Sixty to seventy litres of brine were drained into a high-density polyethylene barrel for each experiment while the experimental tank was filling. A sample of brine was placed in a 400 mL plastic container to which 1 mL of Triton® X-100 surfactant was added to lower the surface tension of the fluid. Approximately 1 cm^3 of Pliolite S6H resin (sifted to 125-180 μm diameter) were added as the tracer particles. The tracer particle solution was then fully mixed with the brine in the plastic barrel. The brine solution was pumped into a 80 L pressurised tank that was located inside the experimental tank. This kept the brine solution at a similar temperature to the water in the experimental tank.

After the experimental tank had been left for one hour, bubbles were wiped off the sides and floor of the tank using a sponge mop. The tank was left for an additional hour for further bubble formation and bubbles were removed if necessary. Water from the

experimental tank was placed in a 400 mL plastic container to which 5 mL of surfactant and approximately 15 cc of Pliolite resin was added. This solution was then fully mixed into the experimental tank using a paddle and Little Giant 5-MSPR-WG submersible pump. The tank was not disturbed for a further hour as the experimental conditions required a stationary ambient fluid. The motion of water in the experimental tank was visually checked for movement through manual inspection of illuminated particles suspended in the ambient fluid. If motion was detected, the tank was left undisturbed for a longer period of time until no motion was detected.

The laser was turned on prior to each experiment. The Millennia II laser was highly stable and was turned on fives minutes prior to the start of the experiment. The CNI laser was turned on four hours before each experiment as it took longer to become stable. See section 4.2.3 for detailed characteristics of each laser.

Immediately prior to conducting the experiment, the flow rate logging was started. The valve between the pressurised tank and constant head system was opened fully and then partially closed once the constant head tank was over flowing. The pipes between the constant head system and source were bled to remove any air pockets. The globe valve to the source was then opened until the required flow rate was achieved. Once a steady state flow regime was reached, usually after about 30 seconds, the recording of images was initiated. Images were recorded onto the high speed hard drive for approximately eight minutes before the valves, loggers, camera, and laser were all turned off. A sample of discharged fluid was taken from the constant head tank and the density was measured with an Anton Paar DMA 5000 density meter. The sample was filtered through 11 μm filter paper to remove the Pliolite resin as particulate matter caused incorrect measurements. The raw images on the high speed hard drive were transferred to a storage hard drive. The high speed hard drive was then reformatted for the next experiment as this maintained the high writing speed. The experimental tank was then drained and cleaned with tap water.

4.3.2 Post-processing

The physical experiments provided a source of electronic data from which velocity field information was extracted. Raw images captured of each experiment were put through an ordered routine that produced velocity field information suitable for comparison between different experimental conditions.

The raw images were converted to lossless colour 8 bit bitmap images with all three RGB channels at the same intensity level to produce greyscale images. A computer program was used to convert the JAI Pulnix TM-2030CL raw image format to the standard bitmap image format (Oliver, 2012). One background image was created for each experiment, using the minimum intensity at each pixel from the first minute of

images. The background image was then subtracted from every image analysed for that experiment. The purpose of subtracting the background image was to remove reflections or blemishes that were constantly present throughout the experiment to ensure they were not identified as tracer particles.

Streams software was used for the main processing stages of the image analysis. The bitmap images were put through the same pipeline of steps to obtain velocity field information for each experiment. Tracer particles were identified in every image before the matching of tracer particles occurred between images. Instantaneous velocity information is obtained from the path of a matched tracer particle representing a parcel of fluid. The instantaneous velocities are interpolated onto a regular grid before further statistical analysis is performed to obtain mean and turbulent velocity information. A detailed review of the Streams processing is provided in section 4.4 below.

4.3.2.1 Profile Fitting

Experimental turbulent flow data is commonly time averaged to obtain important parameters of the flow because instantaneous data is highly variable. Mean velocity fields were saved from Streams to a comma-separated values (CSV) file providing velocity information at each node of a regular grid. The centreline velocity was unlikely to coincide directly with a node, therefore further analysis was required to determine the important parameters of each experiment. The analysis used for pure jet experiments is detailed below.

Mean velocity profiles of pure jet and pure plume discharges have a Gaussian distribution. The centreline velocity and discharge width can be determined by fitting a Gaussian distribution to profiles along the centreline path of the discharge. The method is based on equation 4.1 below for the mean velocity $\bar{u}$ as a function of radial distance r.

$$\frac{\bar{u}}{\bar{u_c}} = e^{-\left(\frac{(r-r_o)^2}{b_u^2}\right)} \tag{4.1}$$

where r_o is the offset of each profile from the centreline. Taking the natural logarithm of both sides and then fitting a polynomial curve to the data results in values of $\bar{u_c}$, b_u, and r_o for each profile. However, profiles of INBJs are not axisymmetric. The outer side of the discharge has a Gaussian distribution whereas the inner side does not due to the unstable stratification. Oliver (2012) used equation 4.1 for INBJs but limited Gaussian fitting to -0.25 $\leq \frac{r}{b} \leq$ 1.0 of the profile. This avoided fitting profiles to non-Gaussian data on the inner side of the discharge. The distance between data points of the regular grid meant this technique did not work for velocity field data. The alternative method used in this study is described below.

A MATLAB algorithm was written to determine the important local parameters for each experiment. The primary purpose of the algorithm was to track the centreline

velocity of the discharge, which originated at the source. The algorithm was iterative such that the highest maximum centreline velocity for each profile would be found. The geometric locations of centreline velocity for each profile produced a roughly semi-circular path for INBJs. The algorithm is detailed below:

1. Three centreline points were created within the first six diameters ($0d$, $3d$, $6d$) away from the source at the source angle. This provided initial points near the source for the centreline path curve fitting in step 8.

2. The end points of an initial profile were specified perpendicular to the velocities near the source and this provided a starting point for the algorithm.

3. Velocities were interpolated for the profile, from the velocity field, at regular intervals equal to the grid spacing of the field.

4. The maximum velocity in the profile was determined. Another profile was taken perpendicular to the new maximum velocity. This process was repeated two additional times to ensure convergence.

5. The inner and outer profile widths were identified on either side of the centreline using interpolation. The profile width was defined as the location where the velocity parallel with the maximum velocity was e^{-1} of the maximum velocity.

6. A new profile was then taken parallel to the previous profile, at a distance equal to the grid spacing of the velocity field in the direction of maximum velocity.

7. Steps 3 - 6 were repeated until the centreline path reached the edge of the velocity field.

8. The splinetool of the MATLAB Curve Fitting Toolbox was used to apply a least squares curve fit (order 4 - 7) to the locations of centreline velocity.

9. The least squares curve was used to take repeat steps 3 - 7 before repeating step 8. This process was repeated two additional times to ensure convergence.

10. Important local parameters were determined from the final least squares curve and saved to a Microsoft Excel spreadsheet. Profile information from steps 3 - 7 was saved to a separate spreadsheet.

The mean properties provided the basis for further analysis of each discharge. Mean properties of the discharge quantify the important geometric parameters. Subsequently, turbulent velocity field data was extracted from the velocity field for important geometric parameter using additional MATLAB code.

4.4 Streams

Streams software was the primary analysis tool for the PTV experiments. Streams was developed by Roger Nokes at the University of Canterbury to analyse fluid dynamics experiments that utilise flow visualisation techniques. The main experimental techniques that can be analysed using Streams include LIF, LA, and PTV. Streams was used to obtain velocity field information from images captured during the physical experiments. This required a pipeline of individual processes within Streams. Typically 9600 images (5 minutes) of each experiment were analysed with Streams. Each experiment was analysed in two sections of 4800 images and concatenated together due to random access memory (RAM) limitations of the computers used. The location of tracer particles was determined in every image by a process called particle identification (Section 4.4.1). The locations of tracer particles were matched between consecutive images based on an optimisation algorithm using multiple conditions (Section 4.4.2). The velocities of matched tracer particles were then determined and these velocities were interpolated onto a regular grid (Section 4.4.3).

4.4.1 Particle Identification

The purpose of particle identification is to determine the precise location of illuminated tracer particles visible within an image. Tracer particles are differentiated from the background of an image as localised regions of high pixel intensity. The horizontal and vertical location of the centre of the high pixel intensity regions is equivalent to the centre of mass of the tracer particles. The location and size of every identified particle is stored for use in the particle matching process (Section 4.4.2). The performance of particle matching is strongly linked to the particle identification process. The same tracer particles need to be identified in consecutive images in order for a high percentage of tracer particles to be matched between images. The total number of particles identified in each image is a key indicator of the performance of the particle identification process and should be relatively constant throughout the duration of images. Tracer particles were introduced to the discharged and ambient fluids because particles would move out of the view of the camera. Therefore, tracer particles were added to the discharged fluid to maintain the total number of particles in the view of the camera. Tracer particles would also move into and out of the laser light sheet as a component of fluid velocity was orthogonal to the laser light sheet.

A dual threshold identifier was utilised for the particle identification process (Nokes, 2012). A threshold pixel intensity was specified as the minimum pixel intensity. A pixel intensity higher than the threshold identifies a pixel as having a sufficiently high intensity to be considered part of an illuminated particle. The intensity of pixels in each image were compared to the threshold intensity and if the threshold was exceeded, the

connecting pixels were searched for the highest pixel intensity in the localised region. An edge factor was also specified as a decimal between 0 and 1. The edge factor was multiplied by the maximum pixel intensity to determine the threshold that defines the edge of a particular particle. The connecting pixel intensities were compared to edge threshold in order to define the edge of the particle. The location of the tracer particle was the centre of the pixel area comprising pixels above the edge threshold intensity. This process was repeated for all pixels in every image analysed. A maximum tracer particle diameter was specified to exclude large localised regions of high intensity that were unlikely to be tracer particles.

There were approximately 6000 to 8000 particles identified in each image of a typical experiment. A peak threshold intensity was defined in Streams for each experiment from trial and error with the first 100 images. A value was required that identified tracer particles exiting the source. The velocity of tracer particles was high in this region and this would smear the reflected light, lowering the intensity. Identifying tracer particles in this region was critical to obtaining particle matches and subsequently velocity field information close to the source. A region around the source was excluded from particle identification as high intensity light would reflect off the source. Regions near the edges of the image were excluded from particle identification to avoid Streams software errors in particle matching algorithms. The area of the raised platform in the image was also excluded from particle identification for boundary experiments.

Figure 4.9(a) shows an bitmap image captured from a typical experiment, which has been inverted here for clarity. Localised regions of high pixel intensity are shown as dark spots. The source can be seen in the bottom left of the figure. Figure 4.9(b) shows the locations of tracer particles identified in the same image, with the source region excluded.

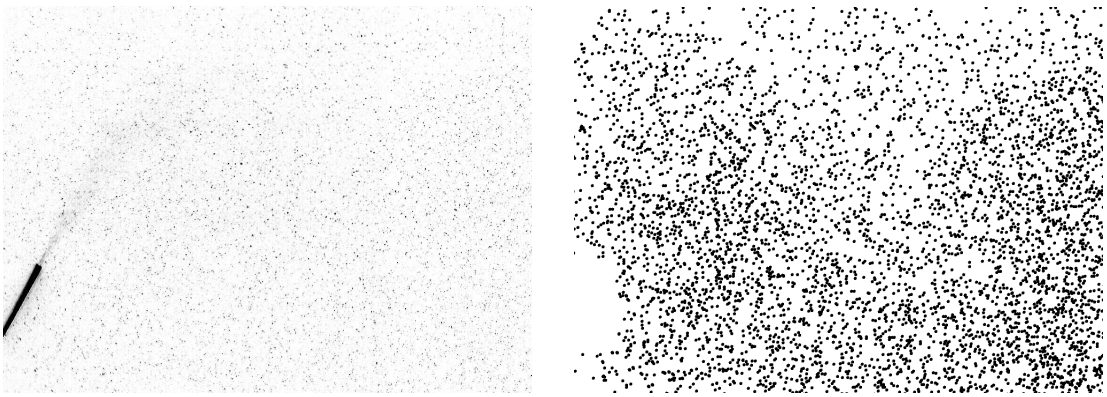

(a) Captured image, inverted for clarity. (b) Identified particles, enlarged for clarity.

Figure 4.9 – Particle identification for 60° experiment ($d = 4.40$ mm, $F_o = 27.5$).

4.4.2 Particle Matching

The performance of the particle matching process is of critical importance to the quality of velocity field information produced by the analysis. The purpose of this process is to match the same particle across consecutive images (from the 6000 - 8000 identified particles). Algorithms are used to find the best possible match of all tracer particles identified. Good algorithms will maximise the total number of correct matches while minimising the unavoidable incorrect matches in the flow field. The user has the ability to adjust many parameters relating to the algorithms to achieve the desired quality of matching. Thus the user has control over which particle matches are considered correct or incorrect.

Particle matching between consecutive images is an optimisation problem known as the assignment problem. Tracer particles in image one need to be assigned to tracer particles in image two. The problem is complex as all tracer particles in image one are not present in image two as tracer particles move into and out of the light sheet, as mentioned in section 4.4.1. Streams software utilises an auction algorithm to match tracer particles between consecutive pairs of images. Costing algorithms assign a cost to each possible match of particles from image one to image two. The goal of the auction algorithm is to minimise the overall cost of matches.

A search window was specified that reduced the computation time of the matching process. This window limited the number of possible matches considered for a particle in image one to particles in a small area of image two. A maximum matching cost (MMC) was specified for each costing algorithm. This was the maximum allowable cost of a particle match between images and was the deciding parameter for a good or bad match. There are two different types of costing algorithms. The state based costing algorithms use the locations of tracer particles in images for particle matching. Matching based costing algorithms use good matches from the state based costing algorithms and previous matching based costing algorithms. Each matching based costing was iterated through all images five times in forward and reverse directions to maximise the number of particle matches (Blackett, 1994). The costing algorithms use sub-windows similar to the search windows mentioned above. Tracer particles in a small area of image one are compared to a small area of image two for matches. The costing algorithms used in this study are summarised below. A detailed description of the auction algorithm and all available costing algorithms is available in Nokes (2012).

Correlation Costing

The correlation costing is a stated based costing that is based on the cross-correlation of the intensity fields created by identified tracer particles. The intensity fields of sub-windows are cross-correlated for consecutive images. The performance of this

costing was improved by increasing the size of identified particles in the intensity fields. Two correlation costings were used consecutively with different sub-window sizes to match particles that were influence by different scales of fluid flow. This costing is very similar to the cross-correlation undertaken in PIV experimental systems.

Local Velocity Costing

The local velocity costing is a matching based costing that is based on the velocity of previously matched particles in a sub window around each particle. An unmatched particle is likely to be moving in a similar direction to nearby matched particles and the likely location of the unmatched particle can be predicted in the next image. Two local velocity costings were used consecutively with different sub-window sizes to match tracer particles that were influence by different scales of fluid flow.

Sundry Costings

The *recent velocity* costing is a matching based costing that uses the velocity of each particle in the previous image to predict the likely location of the particle in the next image. The *time average velocity* costing is a matching based costing that uses the velocity of each particle, in the all previous images, to predict the likely locations of particles in the next image. The *space average acceleration* costing is a matching based costing that is based on the acceleration of previously matched particles, in a sub window around each particle, to predict the location in the next image.

Figure 4.10 shows the motion of successfully matched tracer particles in the fluid flow. The streaks show the movement of each matched particle over 0.5 seconds. Longer streaks near the source on the left of the figure indicate high velocities. A large eddy can be seen entraining fluid on the outside of the discharge, on the bottom left of figure 4.10. This shows the particle matching process is able to capture the movement of the flow the majority of the field, except near the very high velocities close to the source.

4.4.3 Velocity Field Creation

The velocity fields were created using a Eulerian specification of the flow field, where the motion of the fluid is evaluated at a fixed locations within the field over time. The instantaneous velocity of individual matched particles, in each image, was determined using a central difference approximation from the positions of each particle in the previous and following images. If the position of the particle was known only in the previous or following image, a backward or forward difference approximation was used.

The locations in the flow field where the instantaneous velocity was known varied over a series of images, because particles would not pass the same location in every image. A regular grid was placed over the two-dimensional flow field and the instantaneous

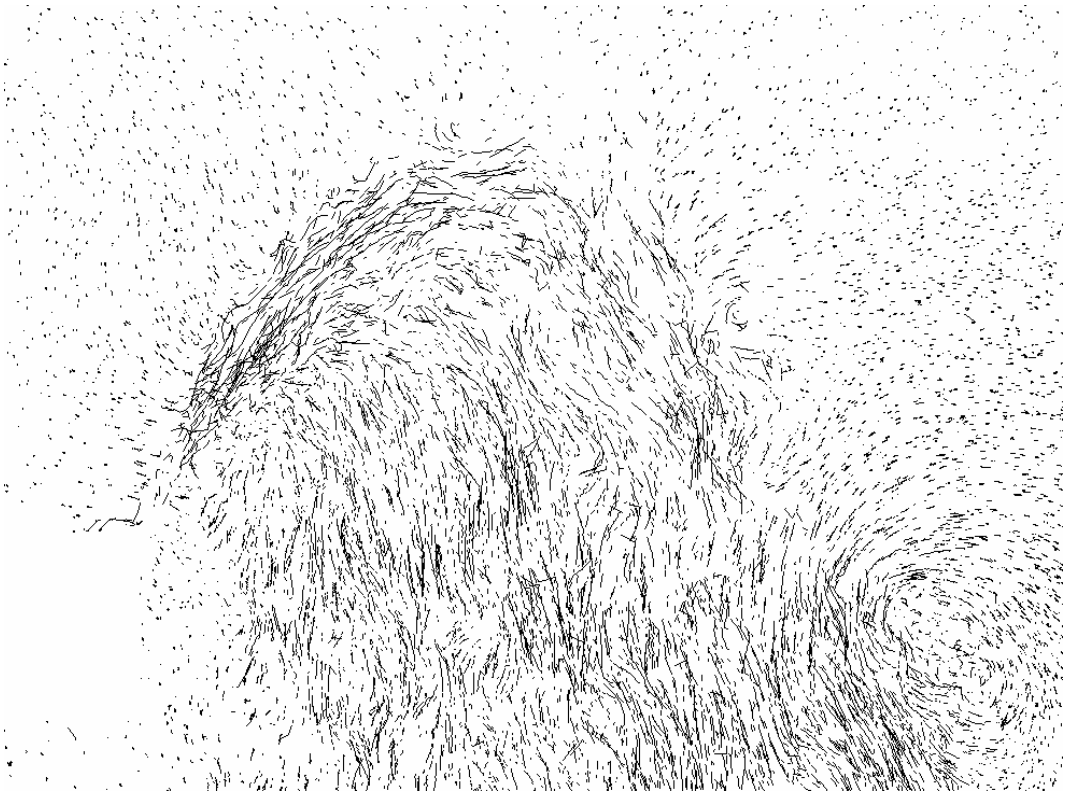

Figure 4.10 – Particle matches across 16 images (0.5 seconds) for 60° experiment ($d = 4.40$ mm, $F_o = 27.5$).

velocities of particles were interpolated onto the grid. Binning and triangulation were the two methods utilised for interpolation onto the regular grid. Binning requires specification of the dimensions of a rectangular bin (box) which is placed over each grid point. The velocity at each grid point is determined from the average of particle velocities that fell within the bin. Specifying a large bin size includes particles that are far from the grid point, thus not giving an accurate representation of the velocity at a specific grid point. This is of particular concern, where a large bin size is used in regions with high velocity gradients. Specifying a small bin size provides the basis for a more accurate representation of the velocity at each grid point, however it can result in no particles being located within the bin for each image. This would leave the velocity undefined at some grid points. It also requires longer sampling times for accurate time-averaged velocities and can result in poor temporal velocity data at grid points. Streams provides a coverage calculator that expresses how often the velocity is defined at each grid point as a decimal between 0 and 1.

Interpolation of the velocity field based on triangulation involves creating a mesh of triangles between particles in each image. The velocity at grid points is determined from finite element interpolation of particles that form the corners of the triangle encompassing each point. Triangulation provides a continuous record of velocity at each grid point as long as the grid points are encompassed by a triangle in each image.

The continuous record of triangulation interpolation makes it favourable compared to binning, however triangulation shares similar issues of having a large bin size in high velocity gradients. If triangle sizes are large, then the velocity is interpolated from particles far from the grid points giving a poor representation of the velocity. Streams allows a maximum triangle size to be specified, such that the velocity is undefined if the triangle encompassing the grid point is too large. Secondary interpolation using binning can also be used if the velocity is left undefined at grid points using triangulation. Binning requires only one particle near the grid point, compared to the multiple particles required for triangulation. Secondary binning provides a more complete record of the flow field.

The selection of bin size and triangle limits influences the velocity field created for the flow field. The accuracy of measured velocity at grid points needs to be balanced with the coverage of the flow field in the time domain. A set of artificial images was created to replicate the flow field of a horizontal pure jet, as described in section 4.5.1. The artificial images were passed through the processes described in sections 4.4.1 and 4.4.2 producing a matched particle record. The velocity field creation settings were specified with differing bin sizes and triangle limits. The mean velocity field was compared to the known velocity field used to create the artificial images. The coverage calculator was used to compare the completeness of different settings in the area of particle motion.

Figure 4.11 compares the accuracy of the measured velocity with the coverage factor for different velocity field creation settings. The percentage difference in the mean velocity field is determined by a spatial average of the absolute difference between calculated and known velocity field, normalised by the known velocity field. The percentage difference is a bulk measure of performance used to compare different settings as accuracy varies over the entire field. As described in section 4.4.2, the particle matching processes are unable to match high velocity particles near the source. This means there are large differences between calculated and known velocities near the source. The general trend for all settings shows an increase in coverage results with a decrease in accuracy of the measured velocity. Triangulation with no limit on triangle size has a coverage factor of one but also the highest percentage difference (Figure 4.11). Smaller bin sizes and triangle limits have higher accuracy but very low coverage factors. There is a comprise between accurate mean measured velocities and meaningful temporal flow statistics that require a high coverage factor. Triangulation with a triangle size limit of 18 mm, with secondary interpolation using a bin size of 7 mm, produced the best compromise between accuracy and coverage. This setting results in the mean velocity field percentage difference, over the majority of the velocity field, being less than one percent while having a high coverage factor.

A velocity field was calculated using triangulation with no limit on triangle size,

which was used for spectral calculations where a continuous record was required. This resulted in the smoothing of velocity field data, however this was unavoidable in order to carry out the calculations.

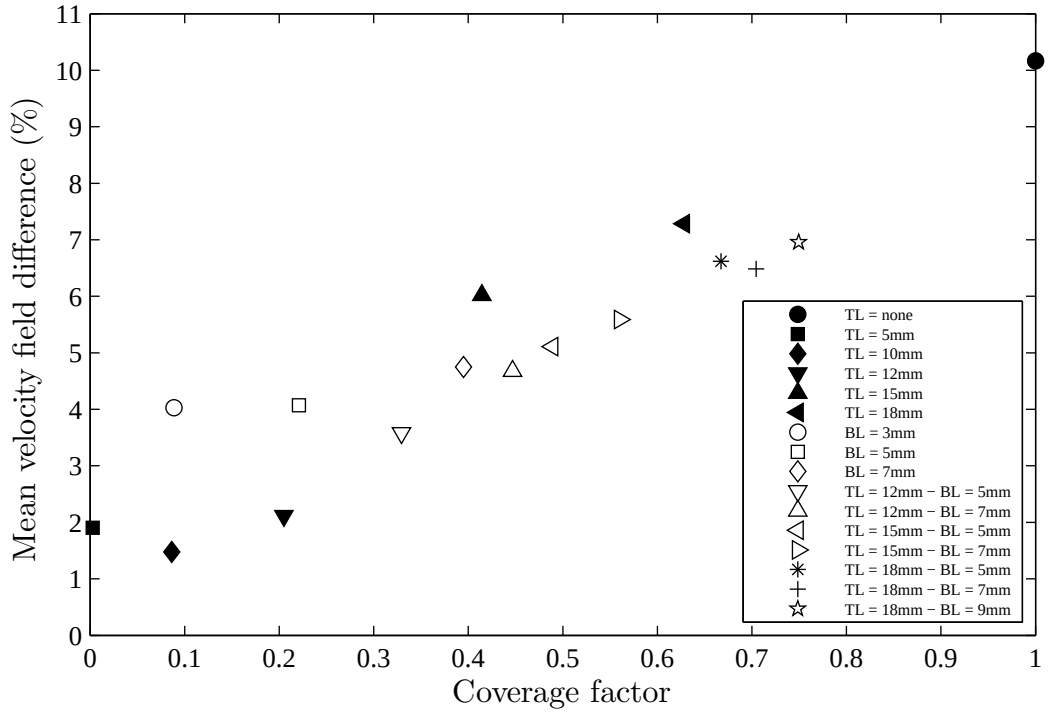

Figure 4.11 – Comparison of velocity field creation techniques. TL: Triangle size limit, BL: Binned size limit.

4.5 Verification

The PTV system utilised for the physical experiments was developed as part of this study and therefore validation of the outputs from the system is required. Pure jet experiments were used to verify the PTV system as the velocity of pure jets have been studied extensively. A verification of Streams software was conducted independently of the overall PTV system to ensure that the velocity fields were determined accurately. This allowed the error associated with processing of images to determined separately from the physical experiments.

There are well known equations that describe the velocity and spread of a pure jet (Wang & Law, 2002; Papanicolaou & List, 1988; Fischer *et al.*, 1979). Equations 4.2 and 4.3 describe the centreline velocity decay and spread with distance from the source, s. Equation 4.4 describes the Gaussian distribution profile of velocity. k_u and k_s are empirical constants for velocity and spread.

$$\frac{U_o}{\bar{u_c}} = k_u \frac{s}{d} \tag{4.2}$$

$$\frac{b}{d} = k_s \frac{s}{d} \tag{4.3}$$

$$\bar{u} = \bar{u_c} e^{-\left(\frac{r}{k_s s}\right)^2} \tag{4.4}$$

4.5.1 Image Processing

The accuracy of the velocity field depends on the particle identification, particle matching, and velocity field creation described in sections 4.4.1-4.4.3, as well as the extraction of the velocity field information described in section 4.3.2. A set of images was created to replicate a horizontal pure jet experiment with a pre-defined velocity field. The Python programming language was used to create the set of images that had identical image size, time step, and scale as those produced during an experiment. The set of images had approximately 8000 randomly seeded particles per image that were moved using equations 4.2 - 4.4 between images. The resulting velocity from these equations is uni-directional and has no turbulent time dependent term to represent turbulence. The velocity constant (k_u) was specified as 0.16 and the spread constant (k_s) was specified as 0.11.

The physical location of a particle was distinguished in an 8-bit image by changing the intensity at the nearest pixel from 0 to 256. The physical location of each particle was stored independently from the set of images, so that the error in assigning the physical location of particles to the nearest pixel was minimised. The particles moved from left to right in the images, which caused particles to move past the right hand edge of the images. New particles were added to each image randomly over the area of a small rectangle on the left hand side of the image. This replicated fluid entering the flow from a source and kept the number of particles per image relatively constant. The set of images had a duration of five minutes and was analysed using the same processes as a physical experiment outlined previously.

Figure 4.12 shows the decay of centreline velocity for the set of images with a specified pure jet velocity extracted after the standard Streams processing. The non-dimensionalised (inverse) centreline velocity decay is linear with a gradient of 0.158, compared to the specified 0.16. The 1.2 % difference is not considered significant compared to the overall error associated with the PTV experimental system. Figure 4.13 shows the spread extracted after the standard Streams processing is linear with distance from the source. The gradient is 0.109, compared to the specified 0.11. The 1.0 % difference is not considered significant. Figure 4.14 shows profile velocities for different path lengths. The profiles are distinctly Gaussian as specified by equation 4.4.

Turbulent intensities (not shown) were high near the source, where particle matching was error-prone with significant time gaps between matches. This caused artificial

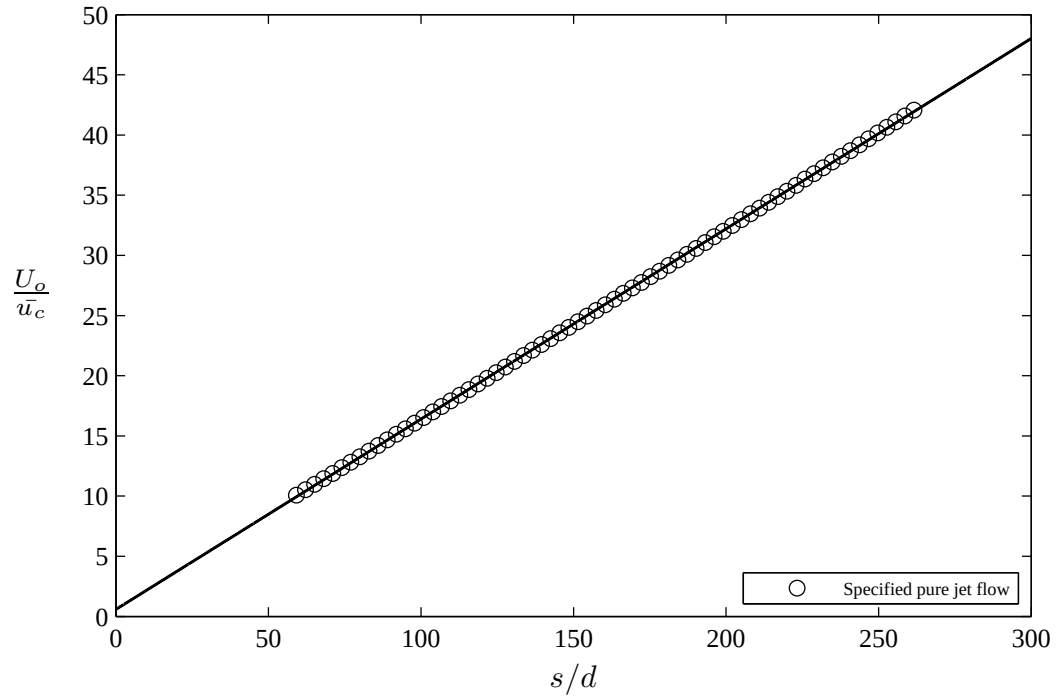

Figure 4.12 – Non-dimensionalised centreline velocity against path length for the specified flow with linear regression.

fluctuations in the velocity field in this region. There were no fluctuations in the specified velocity. Turbulent intensities were minimal further from the source where particle matching was accurate. This indicated that pseudo-turbulence generated by the image processing was not significant. Overall, these results indicate the Streams processing and subsequent post-processing was able to extract highly accurate velocity field information from images. The differences between specified and extracted values are small. The artificial turbulent intensities are minimal when consistent particle matches were made away from the source. Therefore turbulent intensity velocity fields generated for physical experiments, in this region, should not be influenced by the image processing.

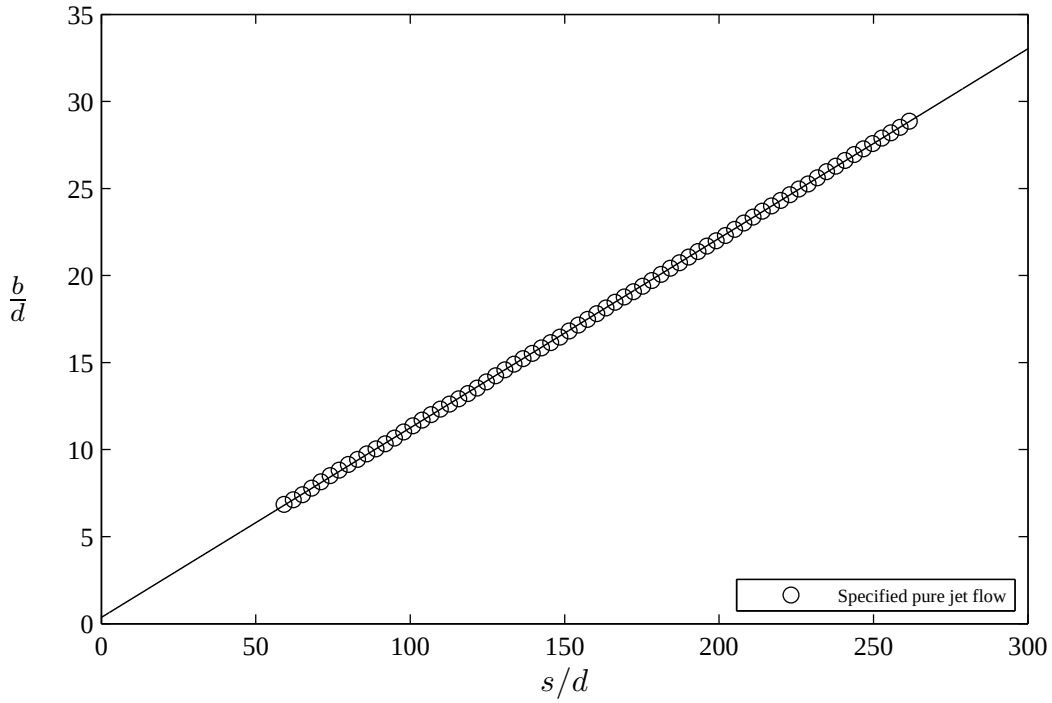

Figure 4.13 – Non-dimensionalised spread against path length for the specified flow with linear regression.

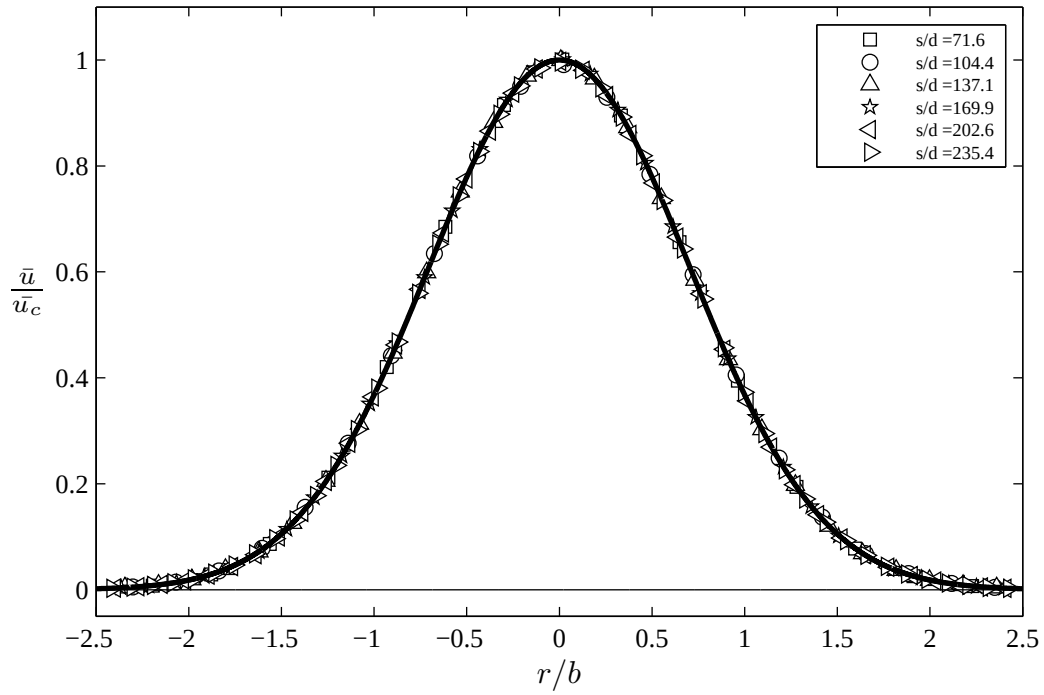

Figure 4.14 – Non-dimensionalised velocity at different path lengths for the specified flow. Gaussian distribution shown for comparison.

4.5.2 Pure Jet Experiments

Eight horizontal turbulent pure jet experiments were conducted for verification of the system used in this study. The method used to conduct the experiments was similar to the method described in section 4.3 except that filtered tap water was used instead of brine for the discharged fluid. Six experiments were conducted with the original 2 W Spectra-Physics Millennia II and two experiments were conducted with the 2 W CNI laser due to earthquake damage described in section 4.2.3. The two experiments conducted with the 2 W CNI laser had identical initial conditions (d = 4.40 mm, Re = 4300). A recording time of five minutes at 32 Hz (9600 images) was used to analyse all pure jet experiments.

The empirical constants obtained in this study with those of previous researchers for pure jets are compared in table 4.1. Experimental coefficients for velocity and spread were determined from mean velocity fields. Turbulent characteristics were determined using a finite difference approximation to the velocity derivatives at each grid point. k_u from this study (0.148) compares well with 1.49 obtained by Papanicolaou & List (1988) and is slightly below values obtained by others (Panchapakesan & Lumley, 1993; Hussein *et al.*, 1994; Wang & Law, 2002). k_s is within the range of values obtained by previous studies in table 4.1. The centreline axial turbulent intensity $\left(\frac{\sqrt{\bar{u'^2}}}{\bar{u_c}}\right)$ value of 0.224 is slightly below previously reported values. The centreline normal turbulent intensity $\left(\frac{\sqrt{\bar{v'^2}}}{\bar{u_c}}\right)$ value of 0.184 is close to 0.185 obtained by Panchapakesan & Lumley (1993) and is again slightly lower than some values from previous studies. The lower turbulence characteristic values is likely due the spatial resolution of the system preventing the movement of small scale eddies from being fully captured. The PTV system captured the large scale eddies, which contain the majority of the momentum and energy. However, missing the small scale fluctuations results in a small underestimation of turbulent characteristics. Nonetheless, it can be concluded that the PTV system is able to obtain good quality mean and turbulent velocity field information for pure jet fluid flows.

Table 4.1 – Comparison of characteristic values for pure jet velocity.

	k_u	k_s	$\frac{\sqrt{\bar{u'^2}}}{\bar{u_c}}$	$\frac{\sqrt{\bar{v'^2}}}{\bar{u_c}}$
Present Study	0.148	0.111	0.224	0.184
Fischer *et al.* (1979)	0.161	0.107	-	-
Papanicolaou & List (1988)	0.149	0.104	0.25	0.17
Panchapakesan & Lumley (1993)	0.165	0.115	0.24	0.185
Hussein *et al.* (1994)	0.172	0.113	0.276	0.217
Wang & Law (2002)	0.154	0.106	0.27	0.19

The centreline velocity for all eight pure jet experiments is shown in figure 4.15. The

data conforms to the linear gradient predicted by equation 4.2 and a linear regression line was applied to the data. The gradient is similar to previously reported values (Table 4.1). The positive intercept on the vertical axis of the regression line is likely related to the zone of flow establishment (ZFE), Papanicolaou & List (1988) also found a positive intercept for jets. However, Wyganski & Fielder (1969) and Hussein *et al.* (1994) found this intercept to be negative. In this study, inconsistent particle matching in the high velocity region near the source results in the underestimation of the mean velocity and could also contribute to the positive intercept.

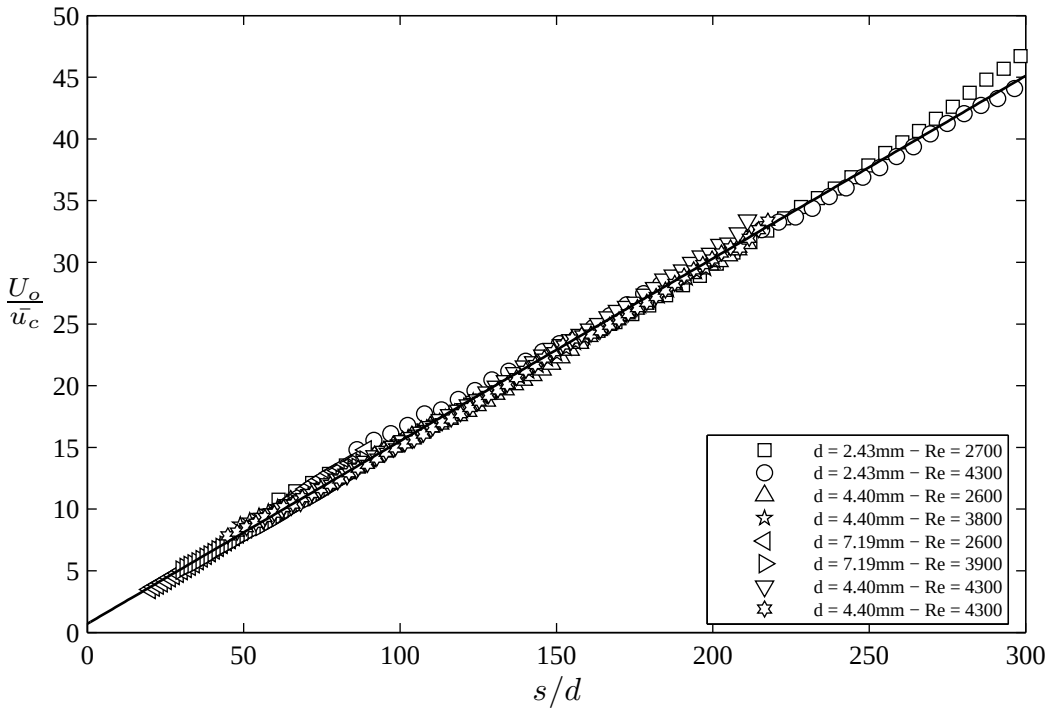

Figure 4.15 – Non-dimensionalised centreline velocity against path length for horizontal pure jets.

Figure 4.16 shows the spread of the pure jets conforms to the linear spread assumption of equation 4.3. The linear regression line also has a positive intercept on the vertical axis, which is the same as for centreline velocity (Figure 4.15). Again, this is likely related to the ZFE.

Velocity profiles at different path lengths are shown in figure 4.17. The experimental data matches the Gaussian distribution very well and profiles are self similar. This is consistent with previous observations of pure jet experiments.

Experimental turbulent velocity statistics are important for understanding the behaviour of the fluid flow that is missed during examination of mean velocity information. Temporal velocity data quantifies the turbulent fluctuations resulting from eddies that drive the mixing of contaminants for jet discharges. Figure 4.18 shows the axial turbulent intensity along the centreline of the discharge for all pure jet experiments is reasonably constant with path length, which is consistent with the study of Papanicolaou & List

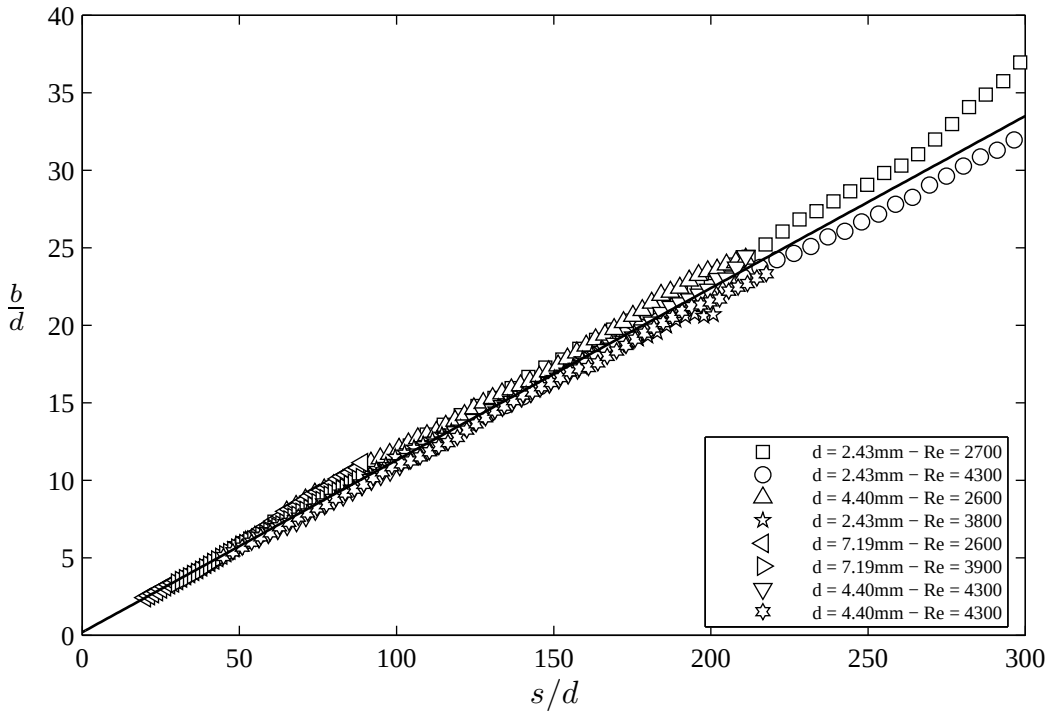

Figure 4.16 – Spread against path length for horizontal pure jets.

(1988). Normal turbulent intensity along the centreline is also reasonably constant with path length (Figure 4.19).

Figure 4.20 shows the axial turbulent intensity of profiles at different path lengths. There is a distinct dip in turbulent intensities on the centreline, with the maximum intensities occurring at approximately $r/b \pm 0.5$. The location of the peak value is consistent with profiles from previous studies (Panchapakesan & Lumley, 1993; Hussein *et al.*, 1994). The turbulent intensity decreases symmetrically with radial distance on both sides of the centreline and profiles are self-similar at different path lengths. Figure 4.21 shows the normal turbulent intensity decreasing with radial distance and profiles are again self-similar at different path lengths. Profile shapes of axial and normal turbulent intensities are consistent with those found by Papanicolaou & List (1988), Panchapakesan & Lumley (1993), and Wang & Law (2002). Figure 4.22 shows that the shear turbulent intensity (Reynolds stress) is of equal but opposite magnitude on either side of the centreline, consistent with previous studies (Wyganski & Fielder, 1969; Panchapakesan & Lumley, 1993; Wang & Law, 2002). The peak shear turbulent intensity is approximately 0.19 and is located at approximately $r/b \pm 0.6$ on both sides of the centreline, which is consistent with that maximum of 0.2, located at $r/b \pm 0.62$, found by Wang & Law (2002) for jets. Panchapakesan & Lumley (1993) found the peak turbulent shear intensity to be approximately 0.19, located at $r/b = 0.7$. Hussein *et al.* (1994) found the peak intensity to be 0.20, located at approximately 0.7. Therefore, the turbulent shear intensities determined from the experimental system used in this

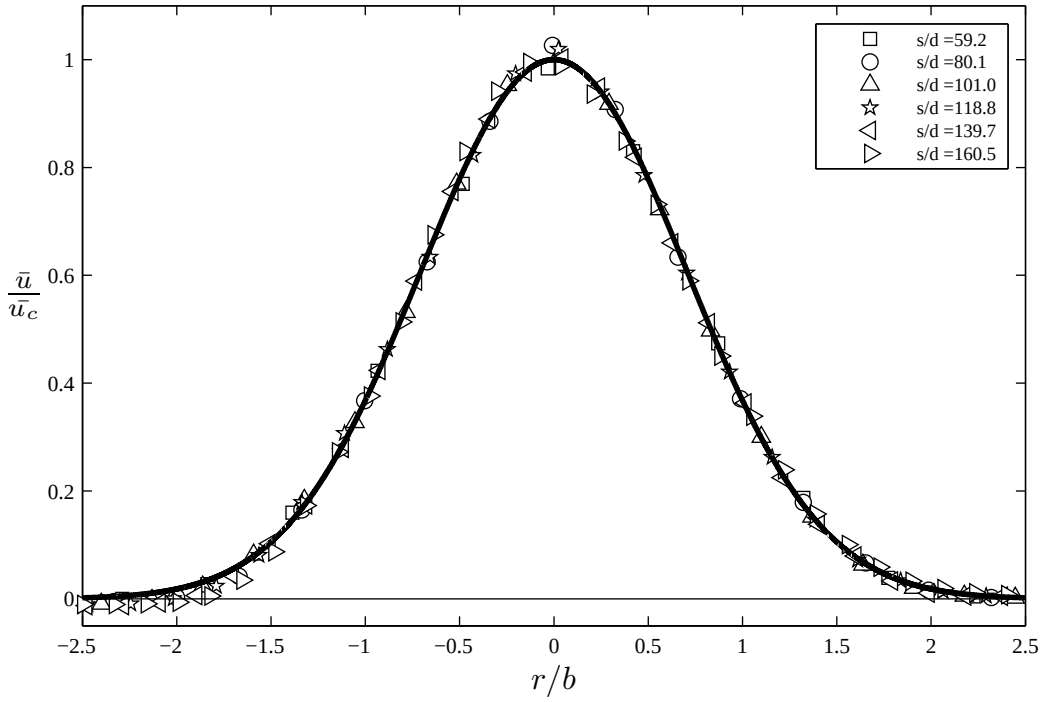

Figure 4.17 – Profile velocities against radial distance for a horizontal pure jet at different path lengths ($d = 4.40$ mm, $Re = 4300$).

study are very similar to values from previous studies for pure jets.

Overall, the performance of the current PTV experimental system in determining the mean and turbulent statistics of jet discharges is satisfactory. The results of the two pure jet experiments conducted with the CNI laser were not different to the results with the Spectra-Physics Millennia II laser. Mean centreline velocity and spread are within the values of previous studies (Table 4.1). Turbulent intensity profiles are very similar in shape to previous studies and profiles are all self-similar for different path lengths. The centreline magnitudes of axial and normal turbulent intensities are lower than previous studies. This could be due to the limited scale of eddy sizes captured by the PTV experimental system. The spatial resolution of the system prevented the movement of small scale eddies from being fully captured. The PTV system did capture the movements of large scale eddies, which contain the majority of momentum and energy in the flow. The inability of the system to capture small scale movements results missing small fluctuations that contribute to turbulent intensities, which leads to lower measured values. Additionally, interpolation of the velocity field could result in the smearing of velocity, also resulting in a decrease in measured turbulent intensities. This is investigated further in section 5.3.2.1.

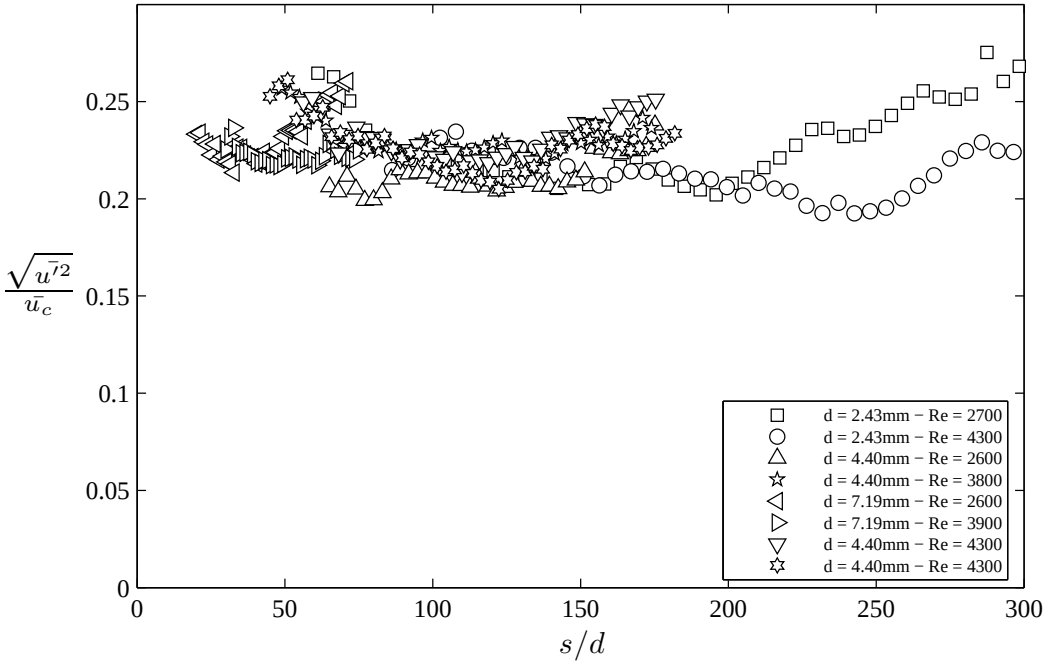

Figure 4.18 – Centreline axial turbulent intensity against path length for horizontal pure jets.

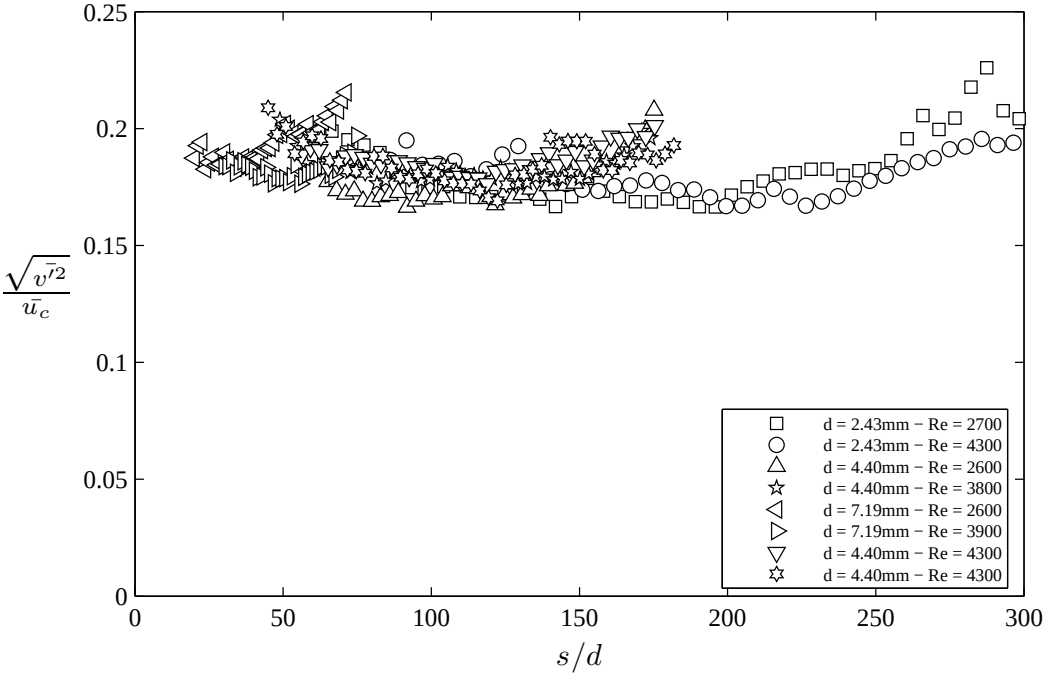

Figure 4.19 – Centreline normal turbulent intensity against path length for horizontal pure jets.

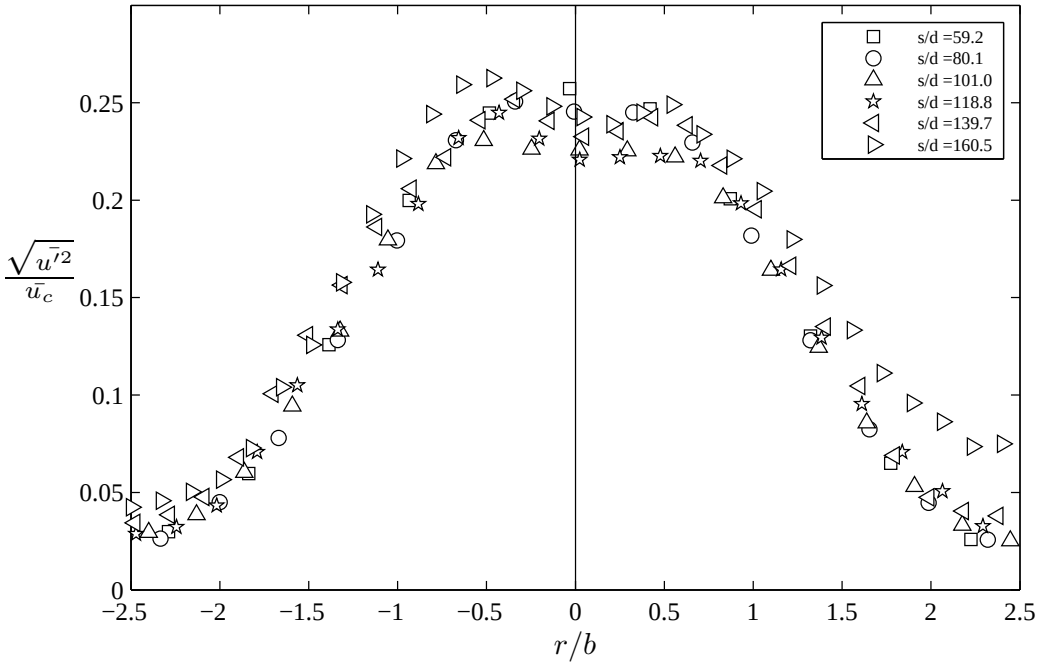

Figure 4.20 – Axial turbulent intensity profiles against radial distance for a horizontal pure jet at different path lengths ($d = 4.40$ mm, $Re = 4300$).

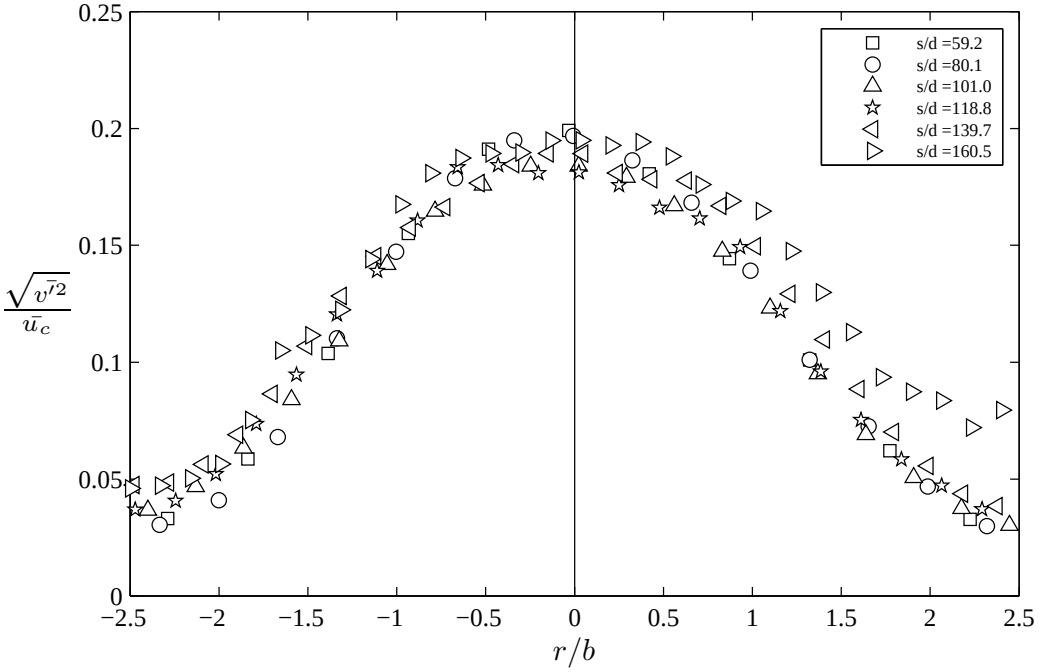

Figure 4.21 – Normal turbulent intensity profiles against radial distance for a horizontal pure jet at different path lengths ($d = 4.40$ mm, $Re = 4300$).

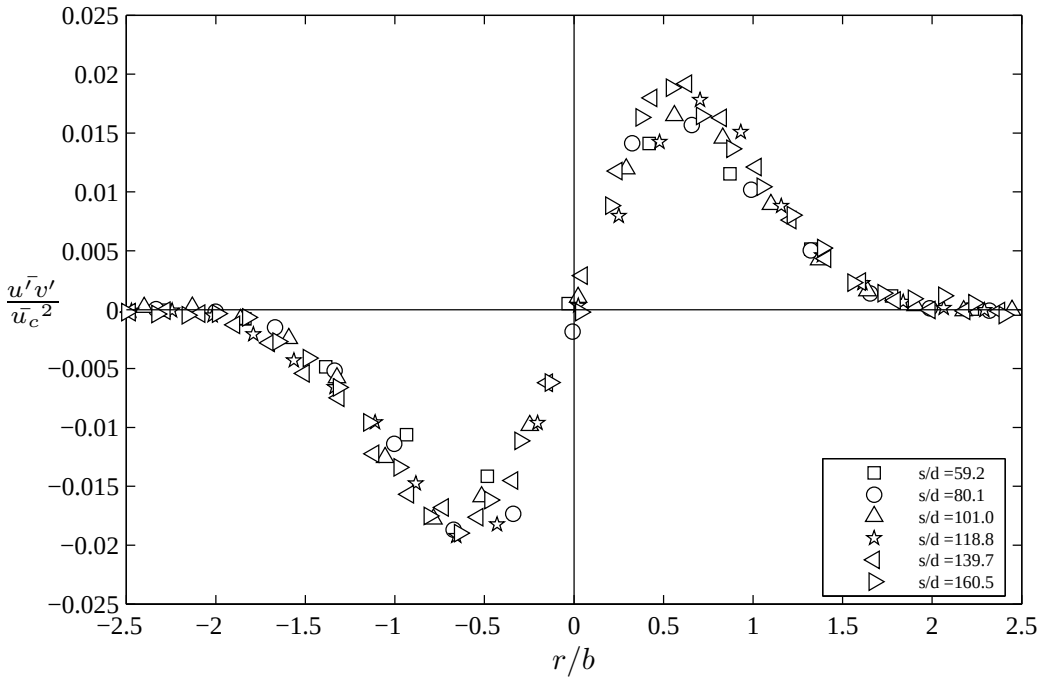

Figure 4.22 – Shear turbulent intensity profiles against radial distance for a horizontal pure jet at different path lengths ($d = 4.40$ mm, $Re = 4300$).

[Intentionally left blank]

Chapter 5

Inclined Negatively Buoyant Jets

5.1 Introduction

This chapter investigates the results of particle tracking velocimetry (PTV) experiments for inclined negatively buoyant jets (INBJ) without a lower boundary influence. There was no raised platform present in the experimental configuration and the lower boundary of the experimental tank is expected to have no influence on the observed behaviour. The lower boundary of the experimental tank was a minimum of 655 mm below the bottom of the captured images. Oliver (2012) found that lower boundary of the experimental tank had no influence on concentration measurements, using the same experimental equipment as the present study. As noted in section 2.7, the majority of experimental studies by previous researchers have been conducted with a lower boundary present. Integral models do not consider boundary influences (Palomar *et al.*, 2012b) and model assumptions about the concentration and velocity fields need to be verified with experimental data under the same flow conditions. The purpose of this set of experiments is to provide high quality velocity field information from INBJs without a lower boundary influence, which allowed for direct comparison with integral models. In total, 49 physical experiments were conducted for source angles of 15°, 30°, 45°, 60°, 65°, 70°, and 75° with Froude numbers between 10.1 and 81.0. Appendix A (Table A.1) contains the important initial conditions for each experiment in this chapter.

The source angles of 30°, 45°, and 60° will be the main focus of the following sections as these angles are practically relevant to desalination plant brine discharges and illustrate the unique behaviour of negatively buoyant jets at different angles. Other source angles will be examined where flow behaviour differs significantly to these angles, with important parameters tabulated for all angles.

The trajectory and spread determined from velocity fields of INBJs are examined in section 5.2. Geometric parameters at maximum height and the return point are compared to previously defined dimensional relationships. The spread on the inner

and outer side of discharges at the practically relevant source angles are compared. Geometric coefficients from the present study are compared to coefficients from previous experimental studies and the predictions of the Detrainment model outlined in section 3.5.

Mean and fluctuating velocity data extracted from INBJ experiments are investigated in section 5.3. A dimensional analysis is preformed for mean centreline velocity and compared to experimental results. Velocity experimental coefficients are compared to predictions of integral models (CorJet, VISJET, Detrainment model). Fluctuating velocity data allows for the comparison of turbulence and mixing between the inner and outer side of INBJs.

Figure 5.1 provides a generalised characterisation of an INBJ without the presence of a lower boundary. Important parameters are located at maximum height (subscript m) and the return point (subscript r).

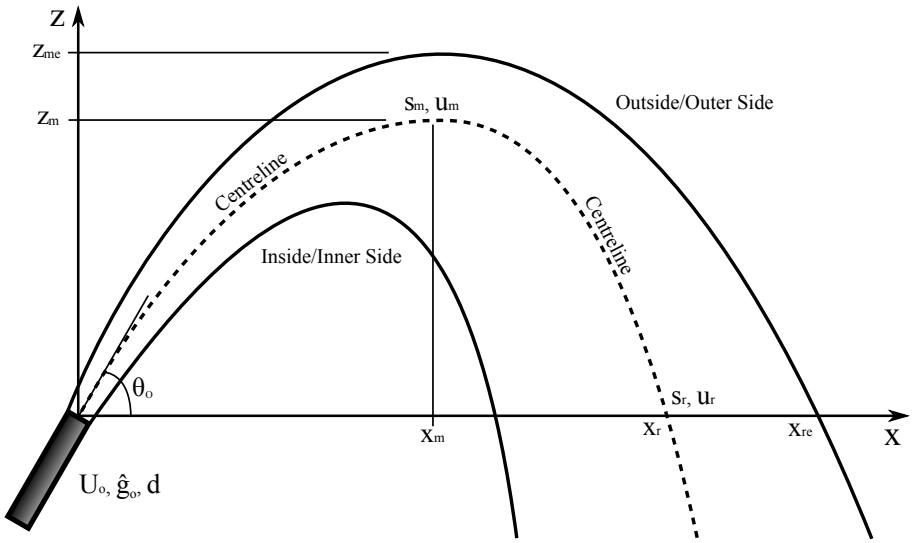

Figure 5.1 – Important parameters of INBJ trajectories depicted in this diagram: Horizontal and vertical distance to maximum centreline height (x_m, z_m), vertical distance to the outside edge (z_{me}), horizontal distance to return point and to outside edge (x_r, x_{re}), centreline path length to maximum height and return point (s_m, s_r), mean centreline velocity at maximum height and return point (u_m, u_r).

5.1.1 Experimental Observations

The following subsections outline the characteristics of flow behaviour that were visually observed during the physical experiments for different source angles. Visual observation of the physical experiments with the human eye was important as some subtle flow behaviour was difficult to capture with the PTV experimental technique. Flow behaviour was only visible to the human eye on the centreline plane of discharges, where the laser illuminated tracer particles.

15°

Discharges with a source angle of 15° had significantly more initial horizontal momentum than higher source angles. The negative gravity potential had minimal effect on the behaviour of discharges at maximum height and return point. Entraining eddies were visible at regular intervals on the inner and outer sides of discharges past the return point. Minimal detrainment was visible on the inner side of discharges compared to higher angles. Small parcels of fluid with low horizontal velocity were observed to fall out of discharges beyond maximum height at very intermittent time intervals. The trajectory of discharges eventually became primarily downwards past the return point, out of view of the camera.

30°

Regular eddy formation was visible on the outer side of discharges up to maximum height. Eddies were visible on the inner side of discharges near the source. Detrainment started to occur intermittently halfway between the source and maximum height. The amount of detrainment gradually increased with distance from the source, before it occurred regularly just before maximum height. There was a continuous progression of detraining fluid beyond this point on the inner side of discharges, which extended past the return point. Large scale eddies formed on the outer side of discharges after maximum height, which increased in size down the falling side of discharges. The trajectory of discharges had a large downwards component at the return point as the gravity potential dominated flow behaviour.

45°

Regular detrainment was visible halfway between the source and maximum height. Detraining fluid dominated the flow behaviour on the inner side of discharges past the return point. Large scale eddies formed on the outer side of discharges at roughly maximum height. There was substantial variation in size of these eddies, with larger eddies forming at increasingly irregular intervals. The trajectory of the main flow was largely downwards past the return point, with detrained fluid continuously falling past the return point elevation on the inner side of discharges.

60°

The inner side of discharges had significant detrainment for discharges with a source angle of 60°. Detrainment was seen on a regular basis halfway between the source and maximum height. The rising and falling sides of discharges were relatively close together at this higher source angle. Strong entrainment near the source outlet would

infrequently re-entrain small parcels of fluid that had been detrained above. This re-entrainment was unlikely to significantly affect discharge behaviour due to the small volume of re-entrained fluid, which was likely to be highly diluted. Eddies were visible at regular intervals on the outer side of discharges up to maximum height, which was the same flow behaviour observed for lower source angles. Again, large scale eddies of varying size and frequency formed on the outer side of discharges near maximum height.

75°

Continuous detrainment and re-entrainment of fluid was observed on the inner side of discharges. The horizontal distance between rising and falling sides of discharges was small. Strong entrainment on the rising side of discharges near the source would continuously entrain fluid from the falling side of discharges. Substantial fluctuating interactions between the rising and falling sides of discharges were also observed.

5.2 Trajectory and Spread

The following section examines the geometric characteristics of INBJs. Geometric experimental data from the present study are compared with previously developed dimensional relationships (Chapter 2). Inner and outer velocity spread or width of discharges are reported. Geometric experimental coefficients from the present study are compared with values reported in previous studies for all source angles. Geometric predictions by the Detrainment model developed in chapter 3 are compared to experimental coefficients from all studies.

5.2.1 Trajectory

Dimensional analysis of important geometric parameters allows for the development of previously documented relationships (Zeitoun, 1970; Roberts & Toms, 1987; Roberts *et al.*, 1997; Shao & Law, 2010). These relationships relate to parameters shown in figure 5.1, and are dependent upon the source angle of the discharge (θ_o). Geometric parameters non-dimensionalised by the source diameter were found to be directly proportional to the initial Froude number by the above studies. The k-notation used previously by Cipollina *et al.* (2005), Kikkert *et al.* (2007), and Oliver (2012) will also be used in this study. Examples of the k-notation for geometric parameters at maximum height are shown in equations 5.1 - 5.3.

$$\frac{x_m}{F_o d} = k_{xm}\left(\theta_o\right) \tag{5.1}$$

$$\frac{z_m}{F_o d} = k_{zm}\left(\theta_o\right) \tag{5.2}$$

$$\frac{s_m}{F_o d} = k_{sm}\left(\theta_o\right) \tag{5.3}$$

The non-dimensionalised trajectory generally collapses for source angles of 30°, 45°, and 60° (Figures 5.2 - 5.4), indicating the geometry of discharges is proportional to the initial Froude number. The source was located at the origin in all these figures. The inability of the experimental system to successfully match high velocity tracer particles near the source ($0.44\ ms^{-1} < U_o < 2.14\ ms^{-1}$ for laboratory experiments) results in the gap before the first data point for these trajectories. Two experiments indicate that geometric parameters may have low Froude number dependence at 45° ($F_o = 10.2$, Figure 5.3) and 60° ($F_o = 10.4$, Figure 5.4) as data points are below the scatter of higher Froude number experiments. Low Froude number dependence is addressed in section 5.2.1.1.

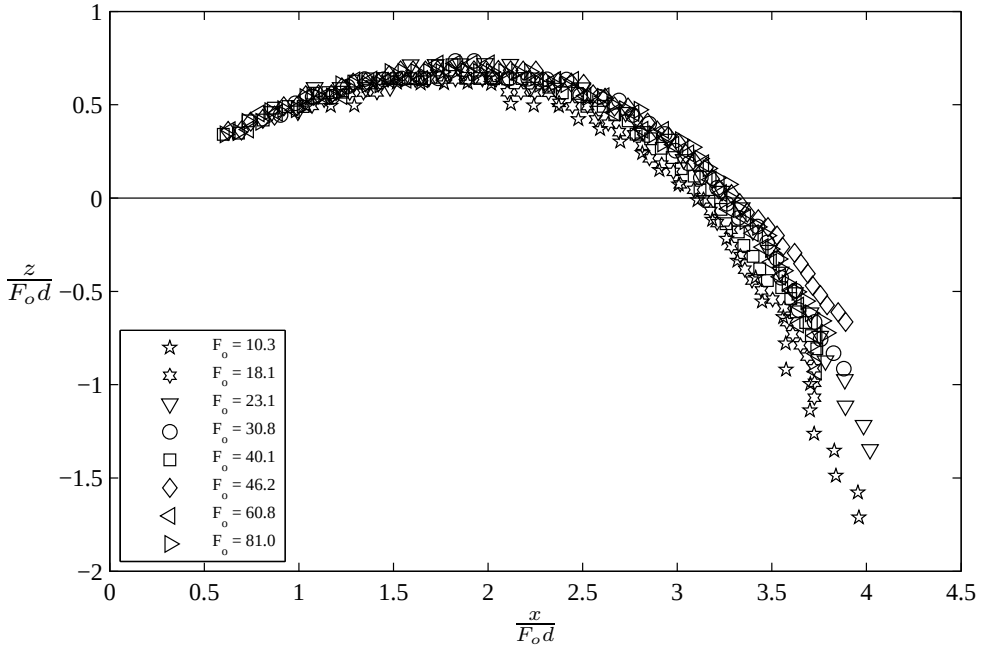

Figure 5.2 – Non-dimensionalised centreline trajectory of 30° INBJ experiments for varying Froude numbers. The source is located at the origin.

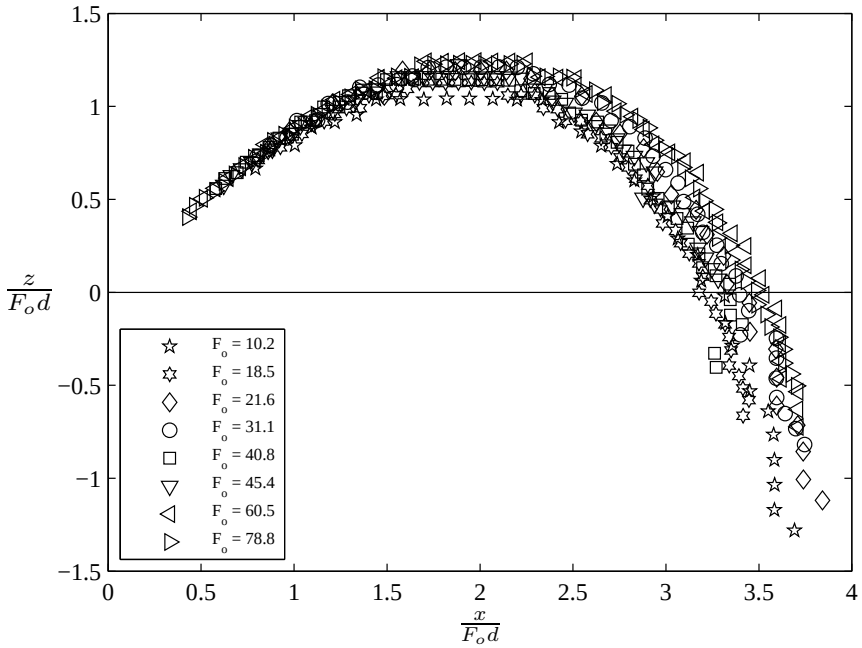

Figure 5.3 – Non-dimensionalised centreline trajectory of 45° INBJ experiments for varying Froude numbers. The source is located at the origin.

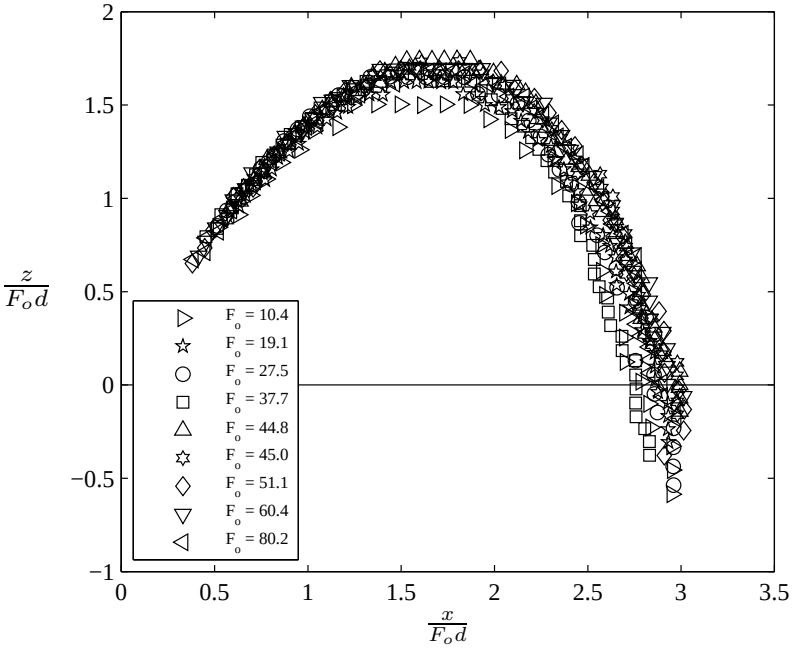

Figure 5.4 – Non-dimensionalised centreline trajectory of 60° INBJ experiments for varying Froude numbers. The source is located at the origin.

Important geometric parameters were extracted from the centreline trajectory of the discharges. These parameters have been non-dimensionalised by the source diameter and are found to be linearly dependent on the initial Froude number (Figures 5.5 - 5.11). The data is consistent with the dimensional analysis relationships shown in equations 5.1 - 5.3 and previous experimental findings (Zeitoun, 1970; Roberts & Toms, 1987; Roberts *et al.*, 1997; Cipollina *et al.*, 2005; Kikkert *et al.*, 2007; Shao & Law, 2010; Oliver, 2012). A linear regression of the geometric data was carried out for each respective source angle. The gradient of each linear regression is shown in table 5.2 (section 5.2.3) for the geometric locations of all angles using the k-notation for each parameter. The standard deviation is also stated. Figures 5.5 and 5.8 show that the horizontal distance to maximum height and return point are similar for source angles of 30°, 45°, and 60°. The horizontal distance to the outside edge at the return point was determined using the same approach as Kikkert *et al.* (2007) who employed, $x_{re} = x_r + \frac{2b}{-sin(\theta_r)}$, where θ_r is the angle of centreline trajectory at the return point. Figure 5.9 shows that the horizontal distance to the outside edge is similar for these source angles, and follows the behaviour of the horizontal distance to the return point in figure 5.8. Figure 5.6 shows the vertical distance to maximum height increased for increasing source angle. The vertical distance to the height of the outside edge was determined by $z_{me} = z_m + 2b$, and is shown in figure 5.7 to increase with increasing source angle. This follows the behaviour of the vertical distance to maximum height in figure 5.6. Centreline path length to maximum height and the return point are similar for source angles of 45° and 60°, whereas this distance is lower for 30° (Figures 5.10 - 5.11).

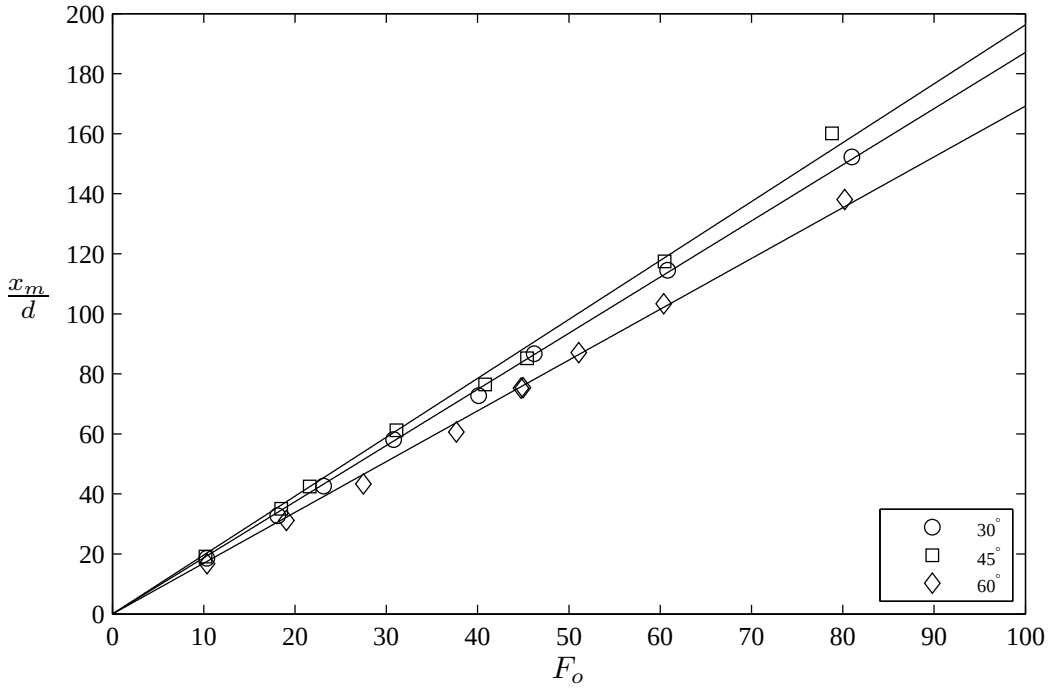

Figure 5.5 – Horizontal distance to centreline maximum height (x_m)for 30°, 45°, and 60° experiments.

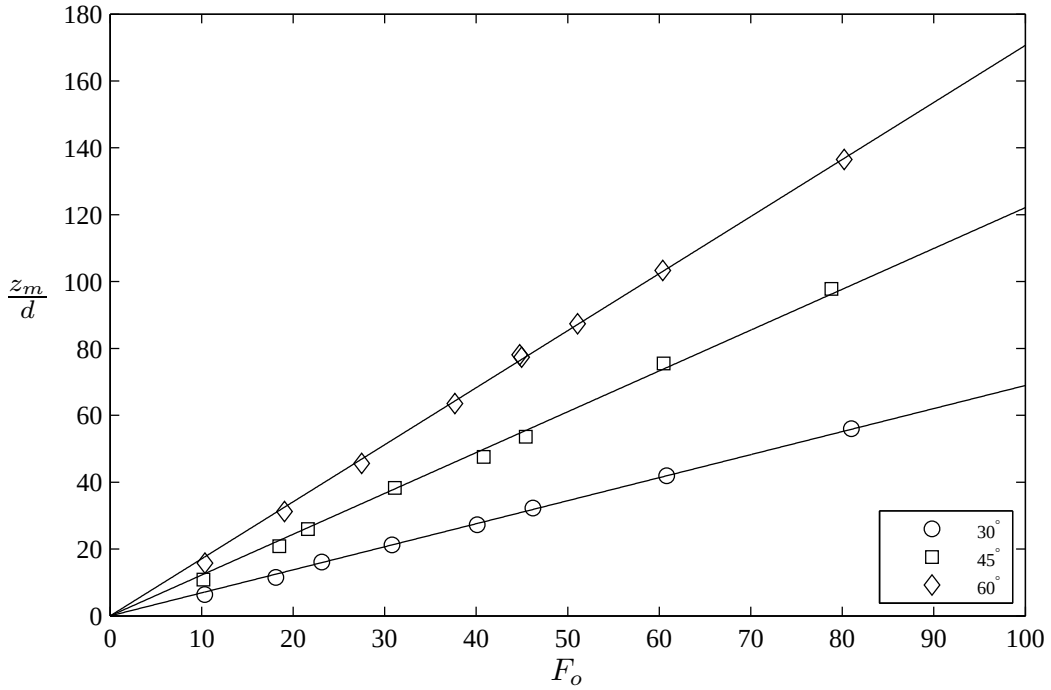

Figure 5.6 – Vertical distance to centreline maximum height (z_m) for 30°, 45°, and 60° experiments.

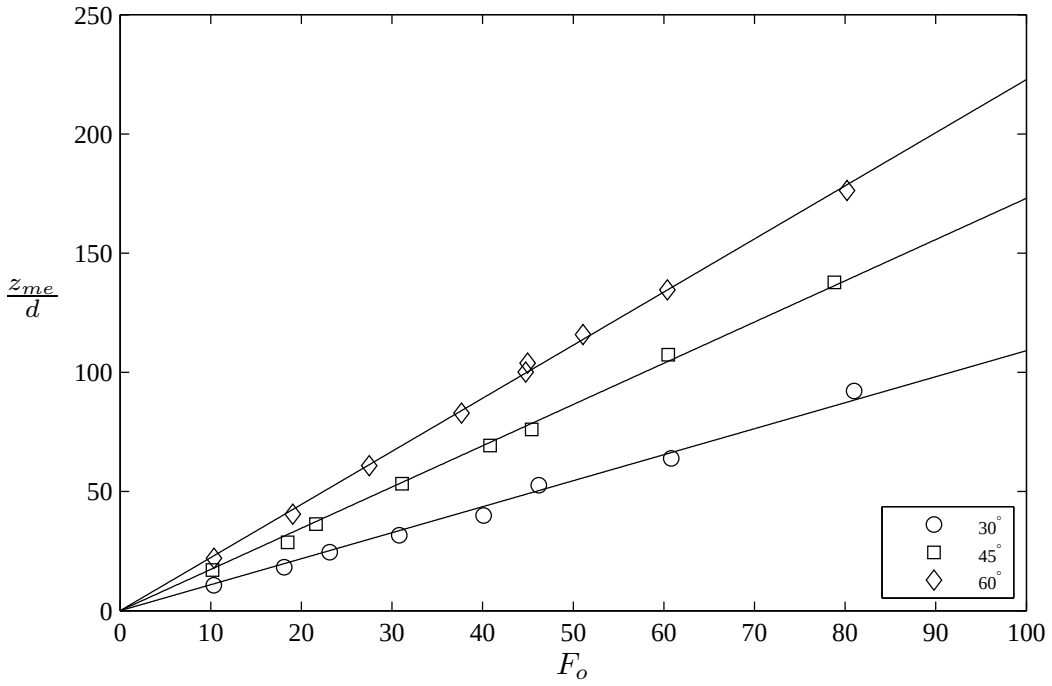

Figure 5.7 – Vertical distance to the outside edge at maximum height (z_{me}) for 30°, 45°, and 60° experiments.

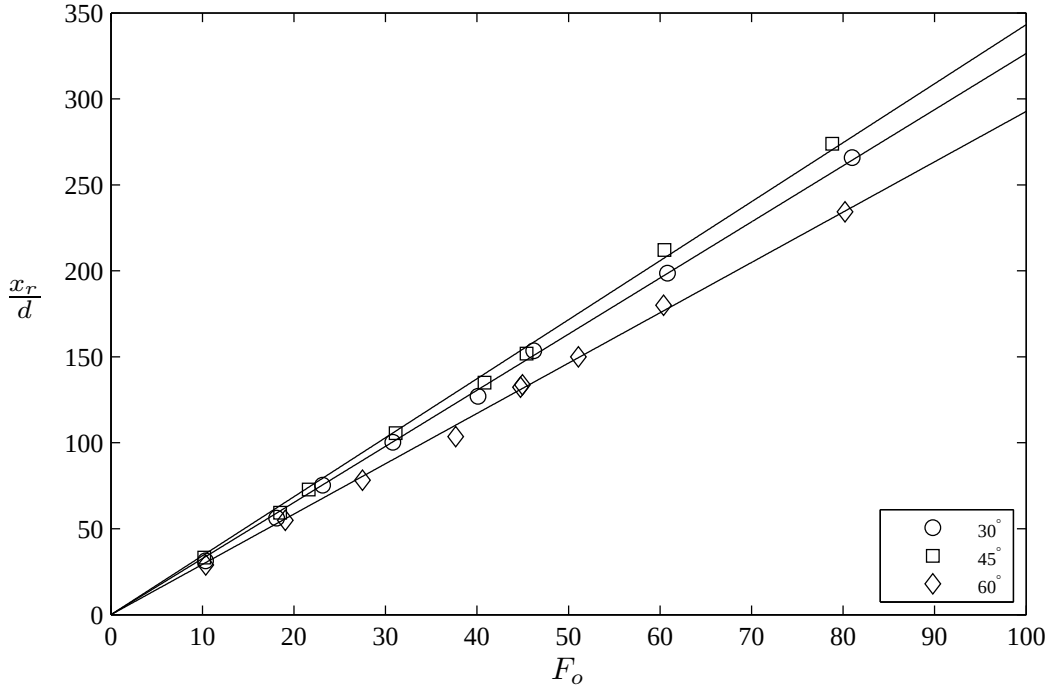

Figure 5.8 – Horizontal distance to the return point (x_r) for 30°, 45°, and 60° experiments.

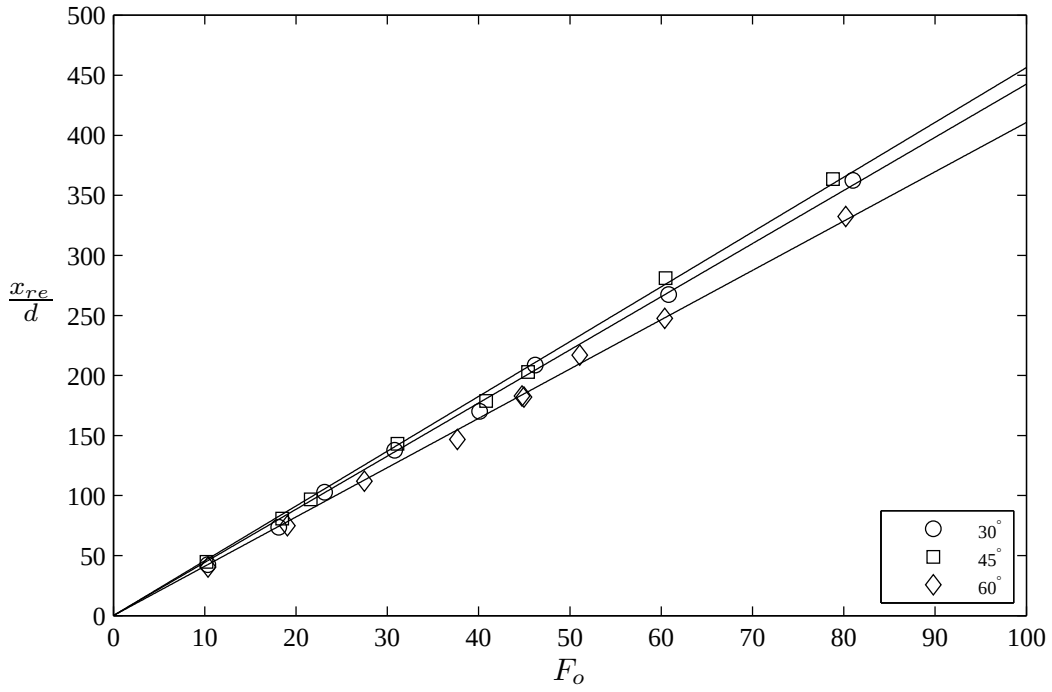

Figure 5.9 – Horizontal distance to the outside edge at return point (x_{re}) for 30°, 45°, and 60° experiments.

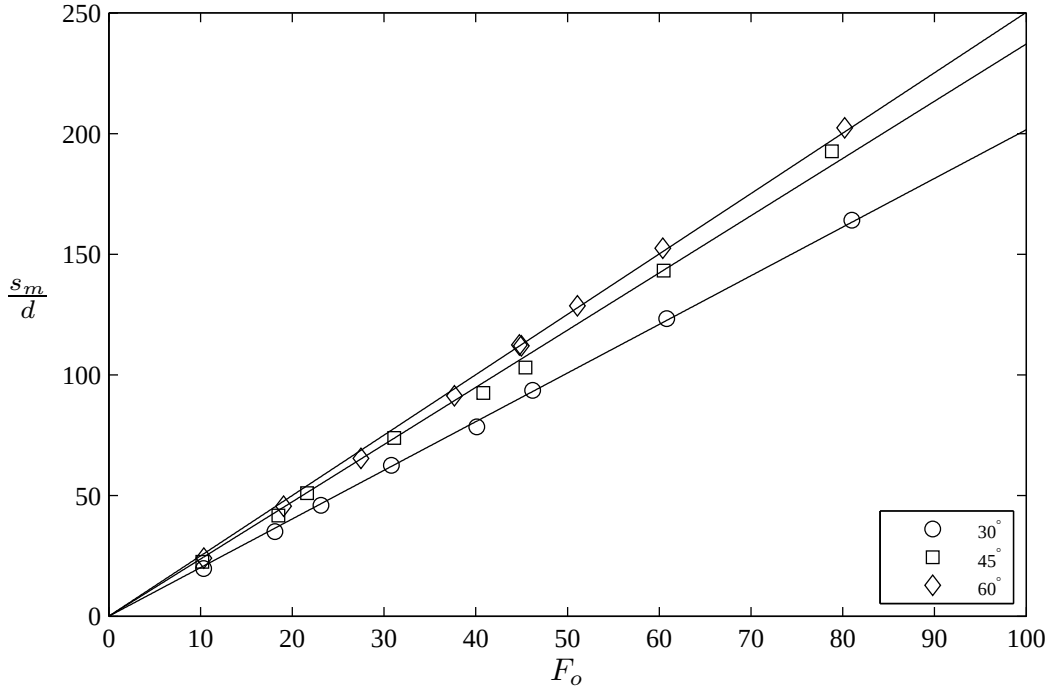

Figure 5.10 – Path length to maximum height (s_m) for 30°, 45°, and 60° experiments.

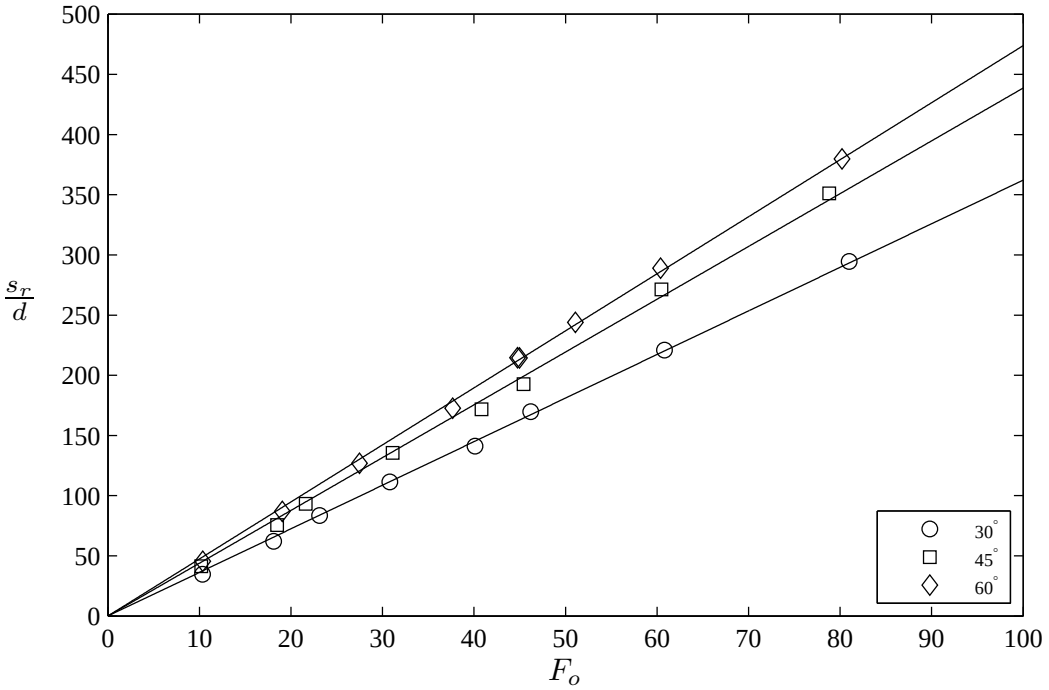

Figure 5.11 – Path length to return point (s_r) for 30°, 45°, and 60° experiments.

5.2.1.1 Low Froude Number Dependence

The non-dimensionalised trajectory indicated that the geometric parameters of two experiments at 45° and 60° may introduce a non-linear dependence on the Froude number (Figures 5.3 - 5.4). These experiments had low Froude numbers of 10.2 and 10.4, respectively. Roberts & Toms (1987) found that the vertical distance to the outside edge at maximum height was linearly dependent on Froude number for $F_o > 20$. The vertical distance to the outside edge and dilution were found to increase at maximum height for INBJs with lower Froude numbers (Roberts & Toms, 1987). In the present study, Grubbs' test (NIST-SEMATECH, 2012) was applied to each of the main non-dimensionalised geometric parameters (x_m, z_m, x_r) to determine whether experiments with any particular Froude number were significantly different from others. Grubbs' test was used to determine if one outlier exists in a normally distributed population, where the standard deviation is determined from the sample (NIST-SEMATECH, 2012). The only confirmed outlier of the entire set of experiments is the low Froude number experiment at 60° for the vertical distance to maximum height (P = 0.019, Table 5.1). This experiment was removed from the linear regression of the experimental coefficient for that geometric parameter. P-values for source angles of 30°, 45°, and 75° are relatively low for the vertical distance to maximum height (Table 5.1), however these are not significant ($P < 0.05$). Experiments with unique behaviour were removed from the sample set for 75° before applying the Grubbs' test (see Section 5.2.4).

Table 5.1 – Grubbs' test outcomes for low Froude number experiments. Geometric parameters: horizontal distance to maximum centreline height (x_m), vertical distance to maximum centreline height (z_m), horizontal distance to return point where discharge falls back to source height (x_r). Factors in bold were significantly different ($P < 0.05$).

		P-value		
θ_o	F_o	$\frac{x_m}{F_o d}$	$\frac{z_m}{F_o d}$	$\frac{x_r}{F_o d}$
15°	10.1	0.219	2.935	0.566
30°	10.3	1.266	0.271	0.395
45°	10.2	3.033	0.251	2.618
60°	10.4	3.847	**0.019**	1.775
75°	10.1	1.366	0.192	2.028

5.2.2 Spread

The spread of INBJs was determined from the relationship between discharge width and path length. The width of discharges was defined as the radial distance from the centreline velocity to where the velocity is equal to $e^{-1}u_c$ (see section 2.2). Discharge width will be determined independently for inner and outer sides, even though the flow is asymmetrical because this definition provides a consistent reference location. Dimensional analysis of pure jet and plume discharges imply that discharge width is linearly dependent on path length (Fischer *et al.*, 1979). Previous experimental studies have confirmed this relationship and reported empirical constants for pure jet spread are shown in table 4.1 (Section 4.5.2).

Lane-Serff *et al.* (1993) and Kikkert (2006) reported asymmetry in the profiles of INBJs, indicating that discharge width is different for inner and outer sides of INBJs. Discharge width has been determined separately for inner and outer sides of profiles from the mean velocity field of each experiment, along the centreline path. Discharge width was calculated using interpolation of axial velocities for each profile.

Figure 5.12 shows outer discharge width of INBJs at 30° had an approximately linear relationship with path length, consistent with pure jet and plume behaviour. The spread rate (k_s) is the gradient of data shown in figure 5.12. The overall outer spread rate is 0.114 ± 0.013 (mean ± SD) for the full path length of all experiments at 30°. This spread rate encompasses the rising and falling sides of discharges that represent jet and plume regions, respectively. Wang & Law (2002) found that the spread rate of velocity in the jet region of a vertical buoyant jet was 0.106 and was 0.105 in the plume region. Papanicolaou & List (1988) also found that the velocity spread rate was very similar in the jet and plume regions of vertical buoyant jets with spread rates of 0.104 and 0.105 in these regions. The outer spread rate of 0.114, reported for INBJs at 30°, is similar to the spread rate of 0.111 reported for pure jet experiments in this study

(Table 4.1, Section 4.5.2).

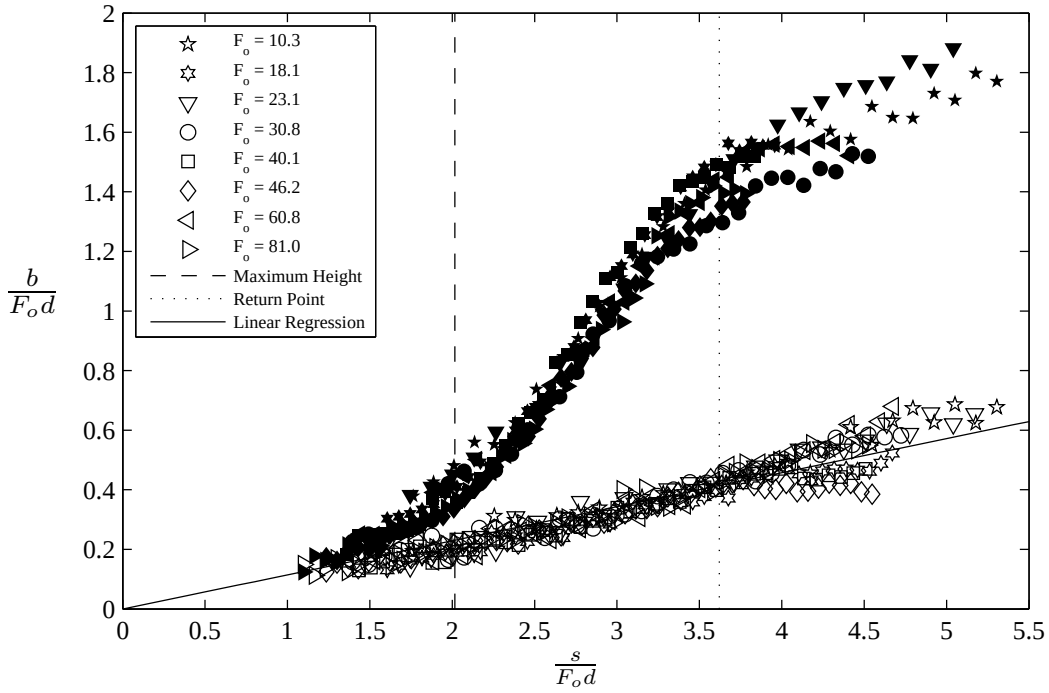

Figure 5.12 – Discharge width against path length for 30° experiments. Unfilled symbols: outer side, filled symbols: inner side.

The inner spread rate of discharges had a non-linear relationship with path length (Figure 5.12). The inner spread rate is similar in magnitude to the outer spread rate well before maximum height, but then increases rapidly compared to the outer spread rate before the return point. The inner spread rate decreases after the return point, however, it has a spreading rate of 0.249 ± 0.170 for $s/F_o d \geq 3.5$ that is greater than the outer spread rate. The rapid increase in inner spread rate indicates a widening of the discharge. This is likely due to detrainment near maximum height for 30° discharges, as noted in section 5.1.1. The nature of outer and inner spread rates are consistent across all experiments as the non-dimensionalised data collapses upon Froude number. Lai & Lee (2012) reported that the ratio between inner and outer spread rates was approximately one near the source before increasing to about two at maximum height for 30° discharges. The spread rates in figure 5.12 are consistent with these findings. However, Lai & Lee noted that the ratio remained constant after maximum height, which differs from the behaviour shown in figure 5.12. Lai & Lee had a lower boundary present in their experimental configuration, which influenced observed flow behaviour. The close proximity of the lower boundary would likely change the inner spread rates on the falling side of discharges.

The spread rates for 45° discharges showed similar trends to 30° discharges (Figure 5.13). The non-dimensionalised data collapses upon Froude number and the outer spread rate is approximately constant with path length. The inner spread rate increases

rapidly around maximum height, before the spread rate decreases between maximum height and the return point. The discharge width data in figure 5.13 shows that the inner spread rate of 0.255 ± 0.203 for $s/F_o d \geq 3.5$ remains greater than the outer spread rate. The outer spread rate is 0.117 ± 0.013 for 45° discharges, which is similar to the value of 0.114 ± 0.013 reported above for 30° discharges. The previous study by Shao & Law (2010) included figures that compared inner and outer velocity spread rates for discharges at 30° and 45°. The spread rates of Shao & Law shared similar qualities with the spread rates from this study. The inner and outer spread rates were similar near the source and the outer spread rate remained relatively constant for the full path length. The inner spread rates of Shao & Law increased rapidly before maximum height, which is consistent with this study. However, their inner spread rates decreased after maximum height, which differs from this study. The reason for this discrepancy is most likely due to the different lower boundary conditions used. The discharge was in close proximity to the lower boundary for the study by Shao & Law, which could have substantially changed the behaviour of discharges between maximum height and the return point. The influence of a lower boundary on spread rates is investigated in the following chapter (Section 6.4.3).

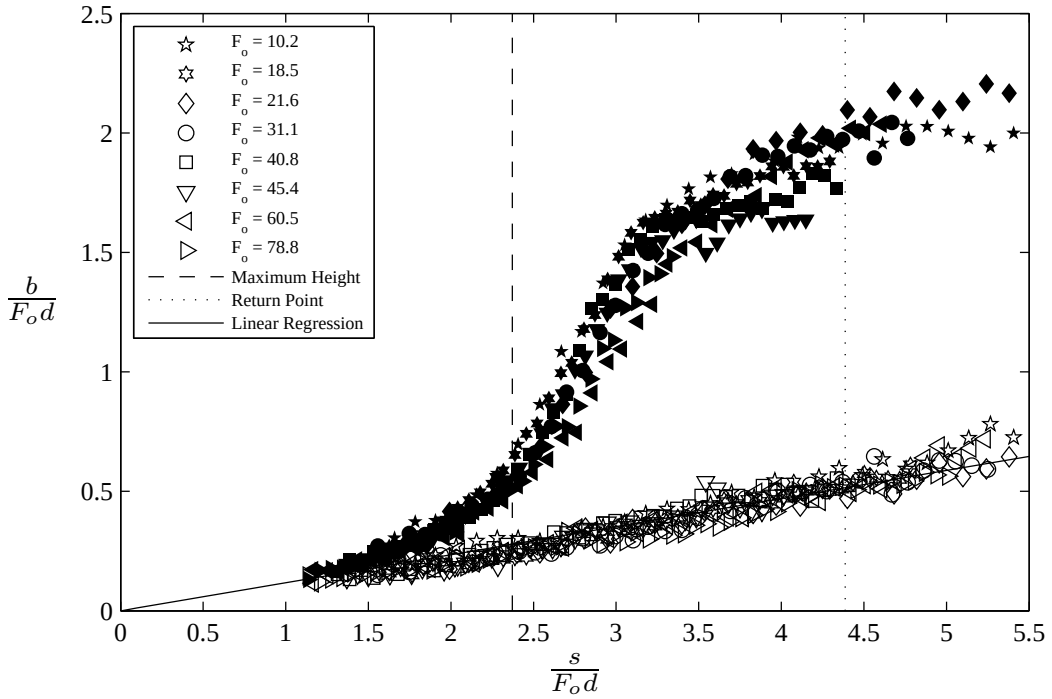

Figure 5.13 – Discharge width against path length for 45° experiments. Unfilled symbols: outer side, filled symbols: inner side.

The outer spread rate is again constant for 60° discharges at 0.114 ± 0.012 (Figure 5.14), which is virtually identical to the value reported for 30° discharges. The inner spread rate for 60° discharges shows the largest increase in spread rate around maximum height over the shortest path length. The inner spread rate then decreases markedly

just after maximum height to a magnitude of 0.108 ± 0.158 for $s/F_o d \geq 3.2$, which is very similar to the outer spread rate. Outer spread is relatively independent of source angle for discharges at 30°, 45°, and 60° (Figures 5.12 - 5.14). The inner spread rate is an indicator of detrainment on the inner side of discharges, with greater inner spread rates at higher angles indicating a higher degree of detrainment. This is consistent with the visual observations of the experiments in section 5.1.1. The inner spread rate for 60° on the falling side of the discharge was similar to that of the outer spread rate indicating the flow was falling similar to a plume. The inner spread rates for 30° and 45° discharges were higher as they were still moving horizontally on the falling side of discharges in the view of the camera. However, it is expected these discharges would have similar characteristics to a falling plume if measured for sufficient vertical distance below the source.

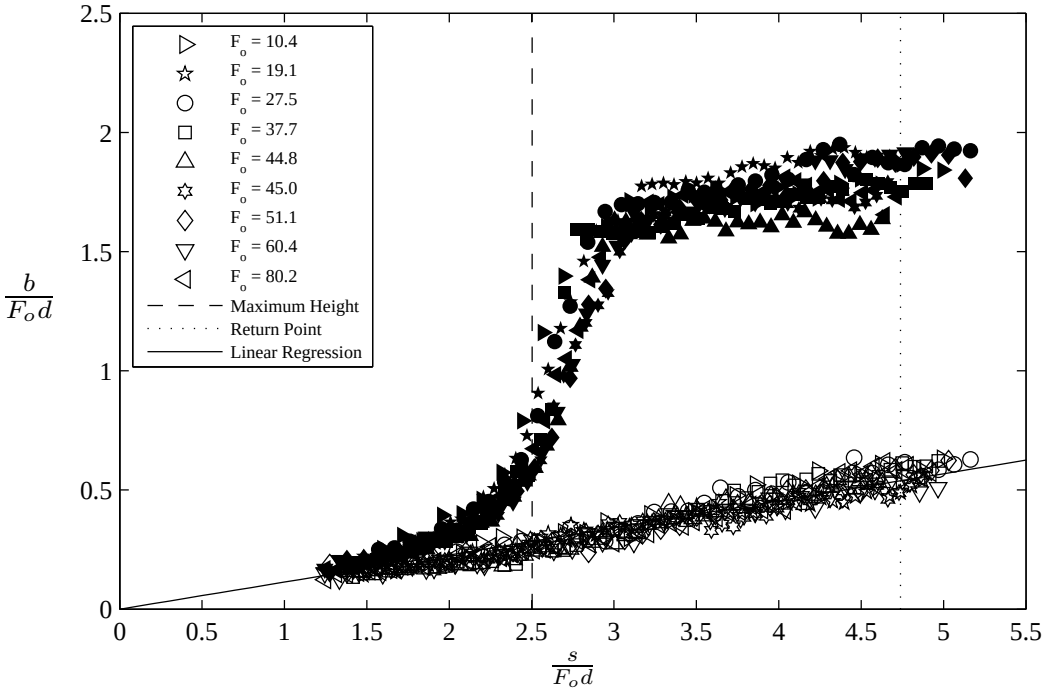

Figure 5.14 – Discharge width against path length for 60° experiments. Unfilled symbols: outer side, filled symbols: inner side.

5.2.3 All Source Angles

The preceding sections have focussed on the trajectory, geometric parameters, and spread of discharges with source angles of 30°, 45°, and 60°. Experimental data from all source angles will now be examined. The k-notation introduced in section 5.2.1 will be utilised to report the experimental coefficients for important geometric parameters of INBJs (Figure 5.1). Experimental coefficients were found using a linear regression between the geometric parameters non-dimensionalised by the source diameter and the

initial Froude number. The experimental coefficients are shown in table 5.2 with the standard deviation of the data associated with the linear regression. The geometric data from individual experiments is shown in table A.1, appendix A. Section 5.2.4 describes the unique behaviour of a limited number of experiments at the higher source angles of 70° and 75°, which were found to be outliers and were not included in the linear regression for the respective source angles.

Table 5.2 – Experimental geometric coefficients with standard deviations. * see section 5.2.4.

θ_o	k_{xm}	k_{zm}	k_{zme}	k_{sm}	k_{xr}	k_{xre}	k_{sr}
15°	1.45 ± 0.04	0.25 ± 0.01	0.57 ± 0.03	1.48 ± 0.04	2.51 ± 0.06	3.72 ± 0.09	2.58 ± 0.06
30°	1.87 ± 0.03	0.69 ± 0.01	1.09 ± 0.06	2.02 ± 0.03	3.56 ± 0.05	4.43 ± 0.10	3.62 ± 0.06
45°	1.96 ± 0.07	1.22 ± 0.04	1.73 ± 0.05	2.37 ± 0.08	3.43 ± 0.09	4.56 ± 0.10	4.39 ± 0.12
60°	1.69 ± 0.04	1.71 ± 0.02	2.23 ± 0.04	2.50 ± 0.04	2.93 ± 0.06	4.11 ± 0.09	4.74 ± 0.07
65°	1.50 ± 0.03	1.82 ± 0.01	2.28 ± 0.07	2.47 ± 0.03	2.53 ± 0.06	3.85 ± 0.16	4.69 ± 0.05
70° *	1.34 ± 0.02	1.96 ± 0.01	2.49 ± 0.03	2.49 ± 0.03	2.28 ± 0.03	3.49 ± 0.09	4.78 ± 0.01
75° *	1.10 ± 0.04	2.02 ± 0.04	2.59 ± 0.03	2.43 ± 0.04	1.87 ± 0.06	3.23 ± 0.07	4.72 ± 0.09

The experimental coefficients from the present study for important geometric parameters (Table 5.2) are compared to experimental coefficients of previous studies in figures 5.15 - 5.21. It is important to note that the experimental coefficients from all previous studies in these figures were obtained from concentration field measurements, whereas coefficients from the present study were obtained from velocity field data. Experimental coefficients relating to geometric parameters, which have been non-dimensionalised by the source diameter and initial Froude number, will be referred to by their respective geometric locations in the following sections.

5.2.3.1 Maximum Height

Figure 5.15 shows that the values for the horizontal distance to maximum centreline height (k_{xm}) from the present study compare well with previous studies and are within the scatter of previous studies for the majority of source angles. k_{xm} experimental coefficients increase with source angle up to a maximum of 45°, before decreasing for higher source angles. The scatter of values across all experimental studies is greatest for 30° discharges. The k_{xm} value of Lindberg (1994) is considerably higher than those of other studies at 30°, whereas k_{xm} values for 45° and 60° discharges are similar to other studies. The reason for this difference is unclear as the method used to determine the location of maximum height was not provided by Lindberg (1994). The k_{xm} value of Shao & Law (2010) at 30° for experiments with higher non-dimensionalised source heights ($H_o/L_m \geq 0.15$) is lower than the those of the majority of other studies at 30°. Shao & Law found that a lower boundary influenced the behaviour of discharges when

the non-dimensionalised source height was $0.10 \leq H_o/L_m \leq 0.15$, as k_{xm} comparatively increased while vertical distance to maximum height remained unchanged. However, the k_{xm} value when the lower boundary was found to influence discharge behaviour is more comparable to experimental data from other studies. The scatter between the majority of other studies, not mentioned specifically here, is likely due to the different experimental techniques and methods used to determine the location of maximum height.

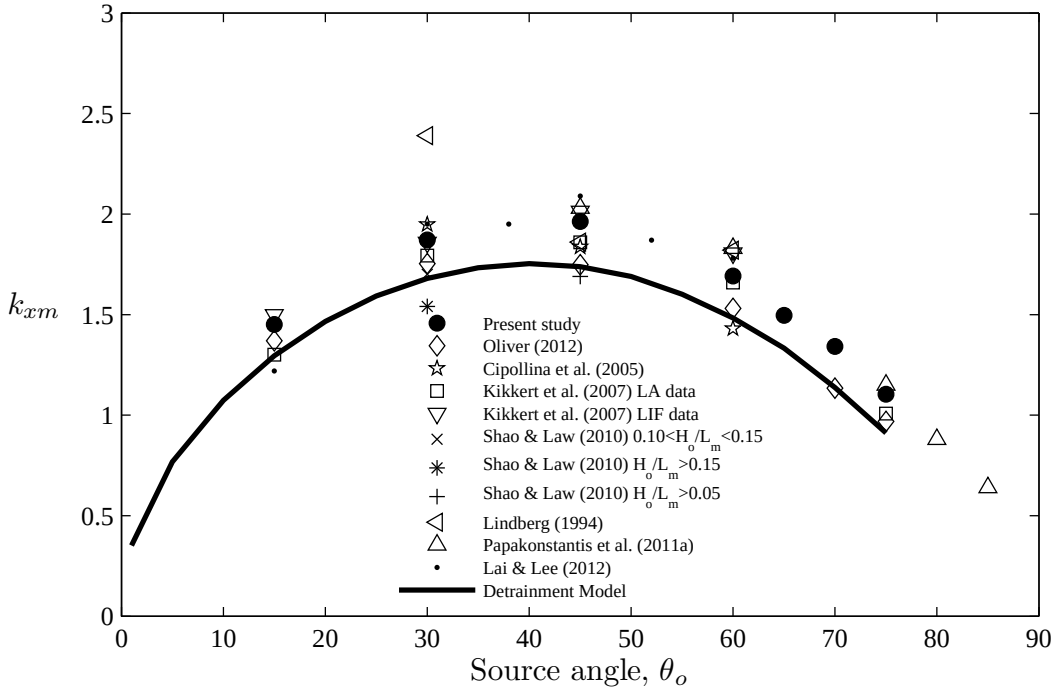

Figure 5.15 – Coefficients for the horizontal location of maximum height (k_{xm}) for all angles.

Figure 5.16 shows that values for the vertical distance to maximum centreline height (k_{zm}) from the present study again compare well with previous studies. The scatter in k_{zm} experimental data is considerably less than for k_{xm}. k_{zm} values increase with source angle up to 75° for the experimental data (Figure 5.16). The increase in k_{zm} values is roughly linear for source angles between 15° and 60°, before the increase in k_{zm} flattens off for higher angles. Values from the present study are at the higher end of scatter in experimental coefficients for source angles of 15°, 45°, 70°, and 75°. In particular, the value of k_{zm} at 75° from the present study is outside the bounds of coefficients from previous studies, using standard deviations stated in Table 5.2. This discrepancy could arise from the difference in location of the local maximum concentration and velocity at maximum height, where significant distortion of profiles occurs due to detrainment on the inner side of discharges (Lane-Serff *et al.*, 1993). The values of k_{zm} at 30° and 60° by Cipollina *et al.* (2005) are higher than those of other studies. Cipollina *et al.* used a reference grid at the rear of the experimental tank to determine geometric parameters from mean dye tracer images. The difference between the location of discharges and

the reference grid introduces a scaling error. This error would falsely increase the size of geometric parameters, explaining the higher values of k_{zm} relative to other studies.

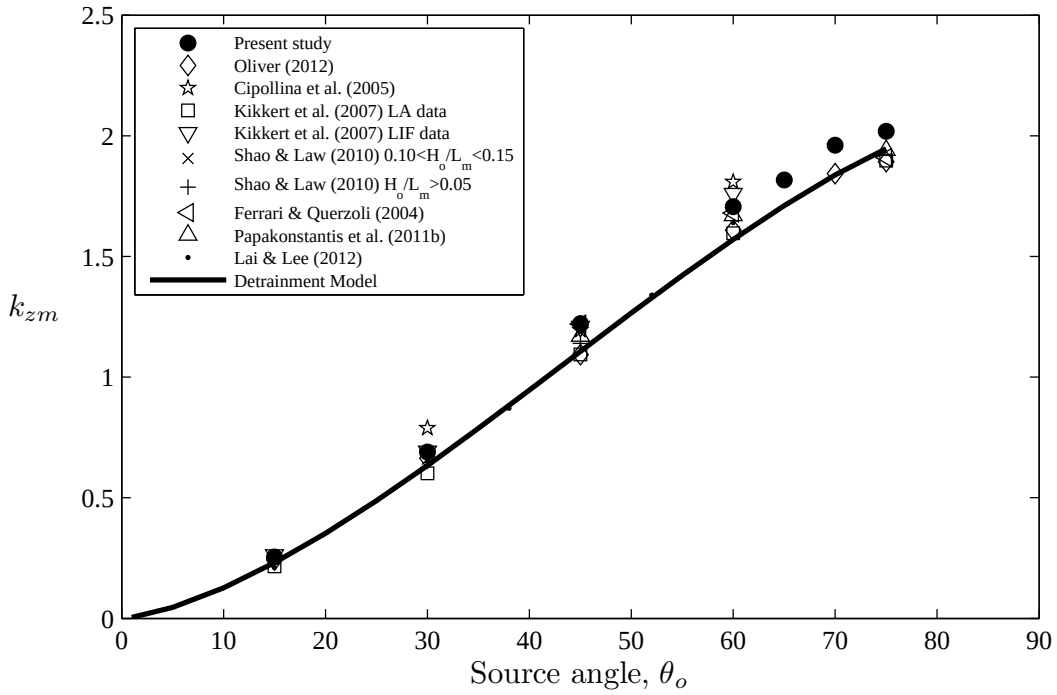

Figure 5.16 – Coefficients for the vertical location of maximum height (k_{zm}) for all angles.

Figure 5.17 shows that values for the vertical distance to the outside edge at maximum height (k_{zme}) share similar overall trends with k_{zm} (Figure 5.16). k_{zme} values increase with a roughly linear relationship with source angle up to 60°, before again flattening off at higher source angles. The experimental data of Nemlioglu & Roberts (2006) and Papakonstantis *et al.* (2011a) shows that k_{zme} decreased when the discharges were turbulent fountains ($\theta_o = 90°$). Turbulent fountains fall back on themselves, resulting in the re-entrainment of mixed (discharged and fully mixed ambient) fluid in the rising part of discharges. This increases the relative negative buoyancy flux of discharges and results in reduced k_{zme} values. The experimental values from the present study compare well with data from previous studies and are in the centre of scatter for the majority of source angles. The scatter between experimental studies is more substantial, with the exception of 15°, when compared to other geometric parameters. The relatively large scatter is likely due to a range of definitions for k_{zme} and different experimental techniques used between studies.

All experimental data from previous studies in figure 5.17 has been determined from concentration experiments. The vertical distance to the outside edge at maximum height has been found by visual observation (Lindberg, 1994; Otranto, 2004), applying a 3 % cutoff to concentration data at maximum height (Shao & Law, 2010), using the 25 % contour of maximum concentration (Lai & Lee, 2012), or using the formula $z_{me} = z_m + 2b_c$, where b_c is concentration width of the discharge (Kikkert *et al.*, 2007;

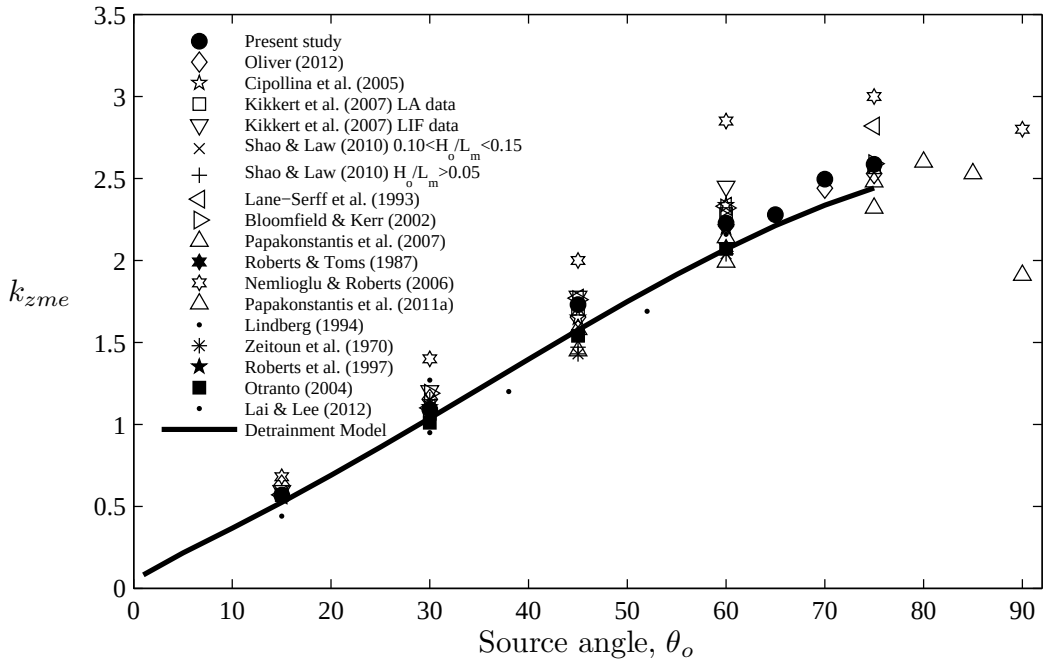

Figure 5.17 – Coefficients for the vertical location of maximum rise height (k_{zme}) for all angles.

Oliver, 2012). The spread rates of concentration and velocity have been found to be different for pure jets and plumes (Fischer *et al.*, 1979; Papanicolaou, 1984; Wang & Law, 2002). Wang & Law (2002) found that the ratio of concentration to velocity spread ($\lambda = b_c/b$) was 1.217 for a jet and 1.038 for a plume. Therefore, an error is introduced when comparing k_{zme} from concentration and velocity experiments that use the formula for z_{me} above. However, this error is likely to be smaller than discrepancies due to the different methods used to define the vertical distance to the outside edge at maximum height by previous studies, noted above. The experimental data of Nemlioglu & Roberts (2006) is consistently high for all angles. Nemlioglu & Roberts conducted only one experiment at each source angle, except at 60°, where two experiments were conducted. The two k_{zme} values reported for the 60° experiments were 2.6 and 3.1, indicating that repeatability could be an issue with their experimental system. The 3D-LIF experimental system used by Nemlioglu & Roberts captured 39 slices through the flow, at different horizontal offsets, sequentially at 100 frames per second. Therefore, frames were recorded with relatively low frequency of roughly 2.5 Hz at the location of z_{me}. Additionally, the total recording times of experiments was not specified for this study.

Model Performance

The geometric predictions of maximum height by the Detrainment model are shown in figures 5.15 - 5.17. Predictions were purposefully limited to source angles $\leq 75°$, due to re-entrainment occurring for source angles $> 75°$ (Section 5.1.1; Bloomfield &

Kerr, 2002; Ferrari & Querzoli, 2010; Oliver, 2012), which was not accounted for by the Detrainment model. k_{xm} predictions follow the trends of experimental coefficients and are within the scatter for all source angles except 75° (Figure 5.15), however predictions are lower than the majority of k_{xm} experimental coefficients. k_{zm} and k_{zme} predictions by the Detrainment model follow the trend of experimental coefficients closely and predictions are in the centre of scatter for most source angles (Figures 5.16 - 5.17).

5.2.3.2 Return Point

Figure 5.18 and 5.19 show that values for the horizontal distance to the discharge centreline at the return point (k_{xr}) and to the outside edge (k_{xre}) from the present study compare well with coefficients from previous studies. Experimental coefficients from all previous studies will be compared despite the possible influence of a lower boundary on measurements. This is due to limited data without lower boundary influence available for comparison and the influence of the boundary on previous measurements is unknown. k_{xr} values from the present study increase with source angle up to 45°, before k_{xr} values decrease substantially for source angles above 60°. There is considerable scatter in the experimental data for all angles, especially at 30°, 45°, and 60°, where the majority of studies have been conducted. In previous studies, a wide range of lower boundary conditions and many different definitions of k_{xr} have been used. Two common definitions are; the horizontal distance to the return point or source height, and the horizontal distance to the impingement point of discharges with the lower boundary. Crowe *et al.* (2010) found that for 60° discharges, the velocity centreline was deflected significantly in the direction of the discharge by the presence of the lower boundary. This indicates that geometric parameters at the return point would be influenced by lower boundary conditions. k_{xr} values from the present study are slightly higher than the majority of coefficients from previous studies at all source angles. Shao & Law (2010) obtained concentration and velocity data from a combined LIF and PIV experimental system. Shao & Law found that the concentration centreline mostly coincided with the velocity centreline, however, the concentration centreline descended sooner than the velocity centreline on the falling side of discharges. This is consistent with the trends of values based on velocity fields from the present study and values based on concentration measurements from previous studies (Figure 5.18). The majority of concentration based k_{xr} values are lower than the velocity based values for all source angles, indicating the more rapid descent of the concentration centreline. Oliver (2012) conducted concentration experiments without the influence of a lower boundary and the k_{xr} values from that study are lower for all source angles, when compared to coefficients from the present study.

k_{xre} values from the present study increase up to a maximum at 45° before decreasing for higher source angles (Figure 5.19). k_{xre} values are again higher than experimental

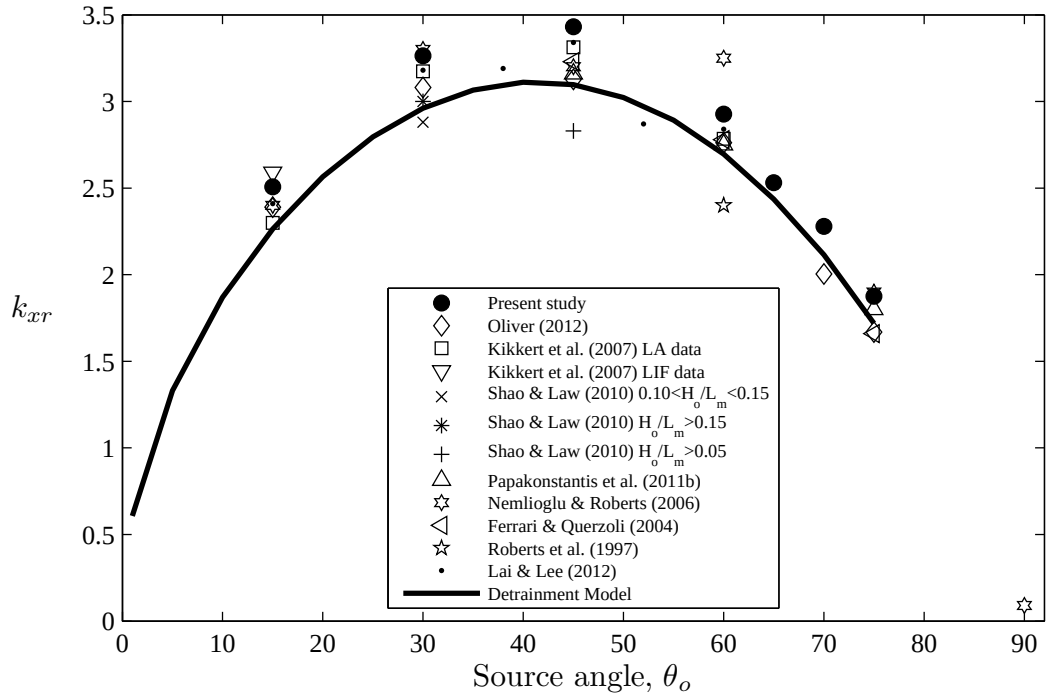

Figure 5.18 – Coefficients for the horizontal location at return point (k_{xr}) for all angles.

coefficients from previous studies for all source angles. The reasoning provided above for the differences between k_{xr} values from the present study and previous studies holds for k_{xre} values as they are a function of k_{xr} values. There is substantial scatter amongst k_{xre} data for all source angles. A lower boundary was present in the experimental configurations of Zeitoun (1970), Papakonstantis *et al.* (2011a), and Otranto (2004), which could influence observed flow behaviour. k_{xre} values from these studies are much lower than values from the present study and that of Oliver (2012), where no lower boundary influenced flow behaviour. These findings are counter intuitive, because the lower boundary deflects discharges further from the source (Crowe *et al.*, 2010). The studies of Zeitoun (1970), Papakonstantis *et al.* (2011a), and Otranto (2004) used visual observation of time-averaged images to determine the outside edge, whereas the present study and that of Oliver (2012) employed the equation, $x_{re} = x_r + \frac{2b}{-sin(\theta_r)}$. The different methods of determining k_{xre} is likely the reason for the differences in value.

Model Performance

The geometric predictions of the return point by the Detrainment model are shown in figures 5.18 and 5.19. k_{xr} and k_{xre} predictions follow the trends of experimental coefficients closely across the full range of source angles. Predictions are within the scatter of experimental coefficients for both locations at all source angles, except for 15° discharges where k_{xr} and k_{xre} are underestimated by the model. However, 15° discharges were not investigated by earlier experimental studies (Zeitoun, 1970; Otranto, 2004; Papakonstantis *et al.*, 2011a). k_{xr} predictions are below the majority of experimental data, especially at 15°, 30°, and 45° (Figure 5.18). k_{xre} predictions by the Detrainment

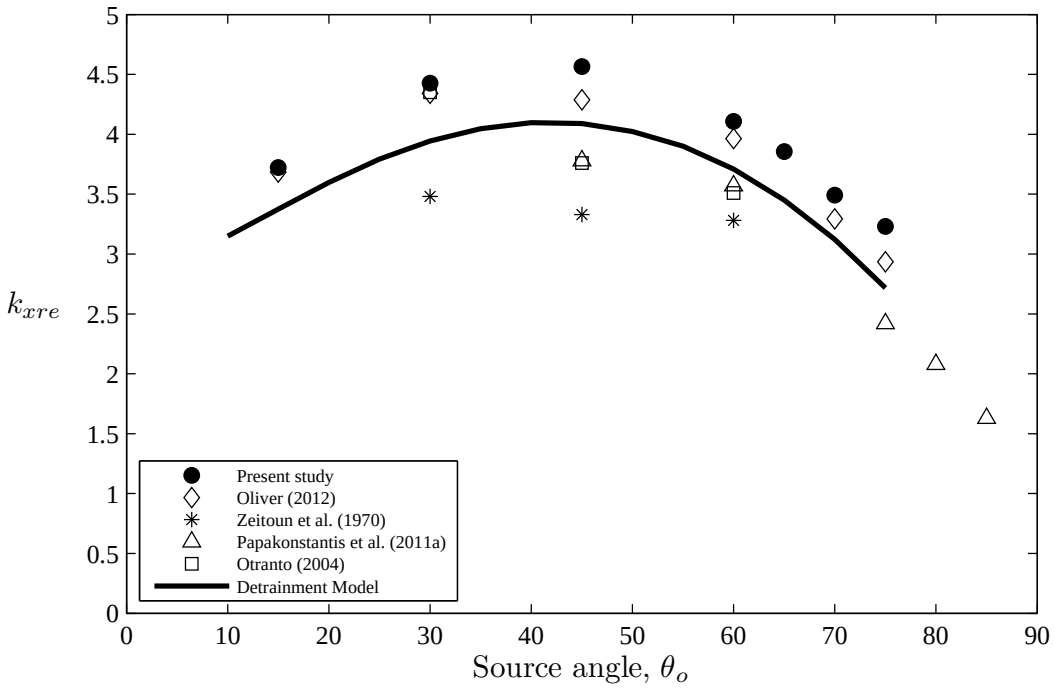

Figure 5.19 – Coefficients for the horizontal location outside edge at return point (k_{xre}) for all angles.

model are lower than the coefficients of studies without a lower boundary present and higher than those with a boundary present (Figure 5.19).

5.2.3.3 Path Length

Figures 5.20 and 5.21 compare values for the path length to maximum height (k_{sm}) and to the return point (k_{sm}), from the present study, with the experimental coefficients of Oliver (2012). Values from the present study, at both these locations, follow the trends of Oliver (2012). Path length increases with source angle up to 60°, before decreasing slightly for higher angles. k_{sm} and k_{sm} values from the present study are higher than those of Oliver for all source angles. Different post-processing algorithms used to determine path length for each experiment is likely to contribute to the discrepancy between coefficients at each source angle. Oliver (2012) took profiles through discharges at 2° increments about a point between maximum height and the return point. Path length was calculated using the Pythagorean theorem between locations of the maximum concentration for each profile. In the present study, a least squares curve fit was used to determine trajectory path through locations of maximum velocity in each profile for the present study. Path length was determined using the Pythagorean theorem between points determined from the curve fit, which was evaluated at increments of 0.1 mm. Another contributing factor to the difference between the k_{sm} values is the early descent of the concentration centreline compared to the velocity centreline (Shao & Law, 2010). This influence on the discrepancy would be smaller at maximum height

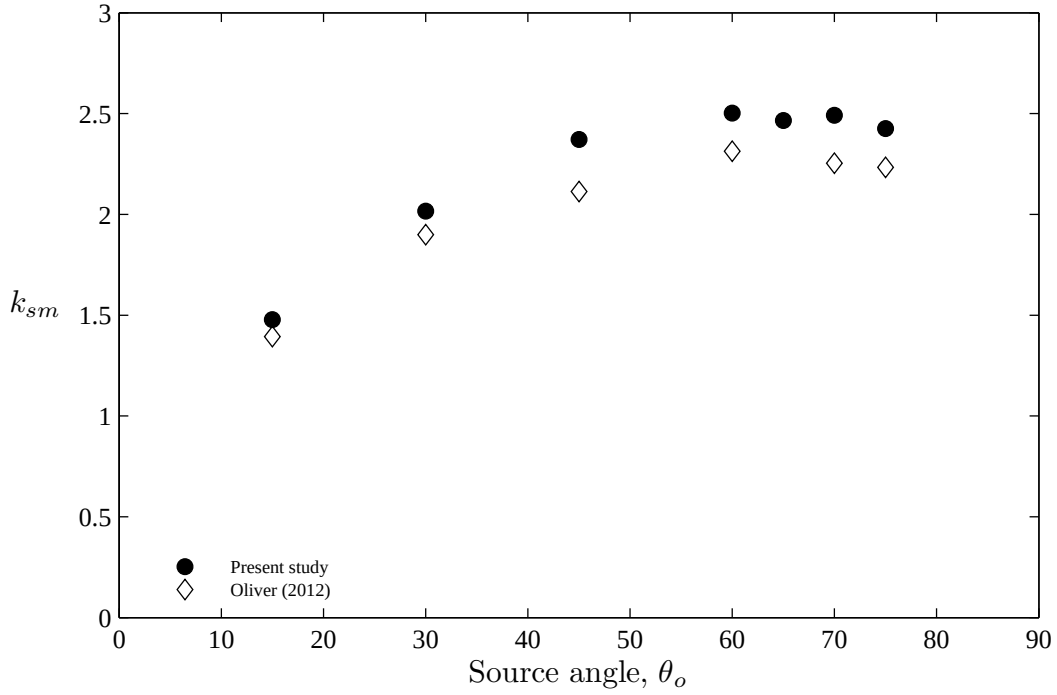

Figure 5.20 – Coefficients for the path length to maximum height (k_{sm}) for all angles.

compared to the return point. However, the mean percentage difference in k_{sr} values across all source angles from Oliver (2012) and the present study is 6.5 %. Whereas, the mean percentage difference in k_{sm} values is 7.9 %.

Figure 5.21 compares the path length to the return point (k_{sr}) and shows that the coefficients from the present study follow the trends of coefficients from Oliver (2012). k_{sr} values from the present study increase with source angle up to 60°, before remaining relatively unchanged for higher angles. k_{sr} values from the present study are again higher than those of Oliver for all source angles. The reasoning for the differences in figure 5.20 hold for k_{sr} values.

5.2.3.4 Summary

The geometric parameters of INBJs for different source angles shown in figures 5.15 - 5.21 indicate that the behaviour of these discharges changes at 45°. The horizontal geometric parameters all have a maximum coefficient at the source angle of 45°. The total initial momentum flux of discharges can be separated into vertical and horizontal components whose relative magnitudes depend on source angle. The initial vertical momentum flux is opposed by the buoyancy generated momentum flux as discharges rise through the water column. Buoyancy generated momentum flux increases with path length and is equal to the initial vertical momentum flux at maximum height. After maximum height, buoyancy generated momentum flux dominates, resulting in discharges falling back down through the water column. Discharges with higher source

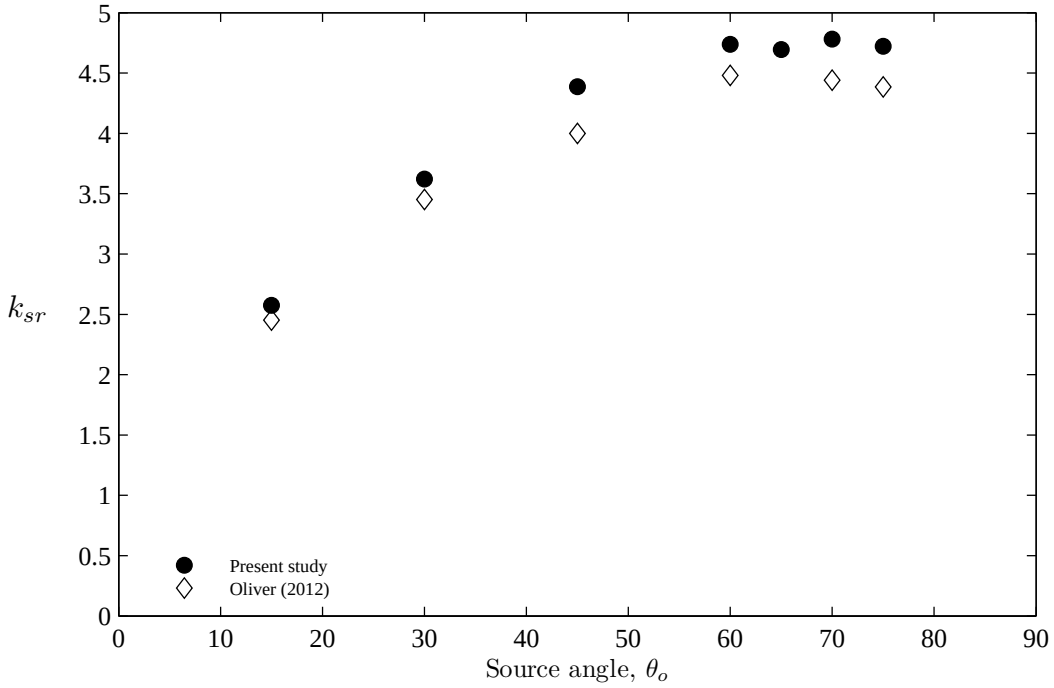

Figure 5.21 – Coefficients for the path length to return point (k_{sr}) for all angles.

angles have greater initial vertical momentum flux, meaning that discharges have a longer path length to maximum height (Figure 5.20) and reach a higher vertical distance in the water column (Figures 5.16 - 5.17). Discharges with lower source angles have greater initial horizontal momentum flux, so the horizontal location of maximum height should increase with decreasing source angle. However, the longer path lengths of higher source angles mean that the longest horizontal distance to maximum height is at 45° for the angles studied (Figure 5.15). This trend continues for the horizontal distance to the return point (Figures 5.18 - 5.19). Lower source angles have greater initial horizontal momentum flux but have shorter path lengths (Figure 5.21) due to the lower initial vertical momentum flux. Higher source angles have greater initial vertical momentum flux and longer path lengths, but have lower initial horizontal momentum flux. Therefore, the longest horizontal distance to the return point is for 45° discharges for the angles studied.

The experimental geometric coefficients from the present study were generally within the scatter of data of other experimental coefficients from previous studies (Figures 5.15 - 5.21). Experimental coefficients from the present study were generally higher than previous values across the range of source angles. The higher geometric coefficients from the present study could be due to a number of reasons. There is some evidence in the literature that there is a difference in the location of local maximum concentration and local maximum velocity. Shao & Law (2010) found that the concentration centreline descended sooner than the velocity centreline on the falling side of discharges. Additionally, the different definitions of important geometric parameters

and different experimental techniques influence coefficient values. The presence of a lower boundary in the experimental configuration deflects discharges (Crowe *et al.*, 2010), which influences the values of geometric coefficients at the return point.

The geometric predictions by the Detrainment model were found to follow the trends of experimental data across all source angles at all locations (Figures 5.15 - 5.21). Geometric predictions were generally lower than the majority of experimental coefficients, but were within the scatter of data. The ability of the Detrainment model to follow the trends of experimental coefficients for different source angles indicates that the relative magnitudes of horizontal and vertical momentum flux were modelled appropriately. The geometric predictions by the Detrainment model were substantially better than predictions of buoyancy conserving models (CorJet, VISJET, Visual Plumes, and Papanicolaou *et al.* (2008)) and similar to those of the RBF model (Table 3.1, Section 3.4). Therefore, the loss of buoyancy flux is critical to the performance of integral models in predicting the behaviour of INBJs.

5.2.4 Experimental Outliers

The behaviour of a limited number of experiments at high source angles showed substantially different behaviour to other experiments at the same source angles. One experiment at 70° (F_o = 61.0) and three experiments at 75° (F_o = 30.8, 60.1, 78.7) shown in table A.1 (Appendix A) were suspected outliers. These four experiments exhibit similar behaviour, which is illustrated by comparison of the geometric coefficients of suspected outliers with principal data for 70° and 75° discharges (Table 5.3). k_{xm}, k_{zm}, k_{zme}, and k_{sm} values show the location of maximum height is slightly lower for the suspected outliers at 70° and 75°. However, k_{xr} values are 52 % and 39 % lower for suspected outliers at 70° and 75° respectively. The ratio of k_{xr} to k_{xm} for the principal data is 1.7 for both angles, whereas this ratio is 1.0 for 70° and 1.1 for 75° for the suspected outliers. This indicates that the horizontal location of the return point is approximately vertically below the horizontal location of maximum height for the suspected outliers.

Table 5.3 – Comparison of experimental geometric coefficients, * indicates outliers. 70° outlier data has no ± SD as it represents only a single experiment.

θ_o	k_{xm}	k_{zm}	k_{zme}	k_{sm}	k_{xr}
70°	1.34 ± 0.02	1.96 ± 0.01	2.49 ± 0.03	2.49 ± 0.03	2.28 ± 0.03
75°	1.10 ± 0.04	2.02 ± 0.04	2.59 ± 0.03	2.43 ± 0.04	1.87 ± 0.06
70° *	1.10	1.83	2.22	2.23	1.10
75° *	1.01 ± 0.07	1.93 ± 0.04	2.44 ± 0.08	2.27 ± 0.08	1.14 ± 0.07

The Grubbs' test (NIST-SEMATECH, 2012) was applied to all suspected experimental outliers at these source angles. Suspected experimental outliers were individually tested with the principal experiments for 75°, as the Grubbs' test should only be applied to a sample where one outlier exists due to multiple outliers considerably increasing the standard deviation of the sample. The suspected outliers are all found to be significantly different at the horizontal distance to the return point (k_{xr}) ($P < 0.05$, Table 5.4). These outliers were not included in the determination of geometric coefficients from the principal data in table 5.2.

Table 5.4 – Grubbs' test outcomes for suspected experimental outliers. Factors in bold were significantly different ($P < 0.05$).

		P-value				
θ_o	F_o	k_{xm}	k_{zm}	k_{zme}	k_{sm}	k_{xr}
70°	61.0	**0.066**	**0.045**	0.061	**0.016**	**0.006**
75°	30.8	**0.020**	0.854	5.088	0.164	**0.001**
75°	60.1	3.453	5.472	1.083	4.399	**0.002**
75°	78.7	0.506	2.311	0.473	1.166	**0.003**

Examination of the velocity fields of the outlier experiments revealed that the centreline or maximum local velocity behaved similarly to the principal experiments up to a point just past maximum height. However, the location of maximum local velocity then went horizontally backwards, towards the source. The maximum local velocity subsequently went straight downwards with minimal changes in the horizontal location of local maximum velocity. Matched tracer particle records of outlier experiments showed that tracer particles near maximum height fell directly downwards, similar to the behaviour of mixed fluid at maximum height of turbulent fountains. Ferrari & Querzoli (2010) found that there was an interaction between rising and falling sides of INBJs at source angles above 80°. The falling side of discharges was found to be deflected towards the rising side of discharges due to the strong entrainment of the rising side. Bloomfield & Kerr (2002) showed that there was a significant difference between the initially transient and steady state behaviour of discharges by measuring k_{zme} throughout the development of steady state behaviour. The horizontal momentum flux at maximum height is relatively small for high source angles, making discharges vulnerable to ambient motion in the experimental tank. Ambient motion in the tank could be the result of not waiting long enough after disturbing the ambient fluid before conducting an experiment. Alternatively, undesirable motion could be induced in the ambient fluid during the initially transient discharge conditions as the valve was opened to obtain the required flow rate of discharged fluid through the source. Ambient motion deflecting the discharge could result in the attachment of the falling side to the rising

side due to the strong entrainment of the rising side. The attachment could remain throughout the duration of the experiment, even once the steady state flow rate was reached, due to the low horizontal momentum flux and low velocity at maximum height for high source angles, such as 70° and 75°.

5.3 Velocity

The following section examines the velocity characteristics of INBJs. The mean absolute velocity field determined by the PTV experimental system had a high velocity core region that existed near the source, with velocity decreasing radially on either side (Figure 5.22). The extended contours on the inner side of the discharge indicate that detrainment is occurring. Velocity parameters were extracted from the mean velocity field for each experiment. Dimensional analysis determines the important parameters at the source which influence centreline velocity. Dimensionless relationships are compared to experimental results. Integral model predictions by the two main commercial models (CorJet, VISJET) and the new Detrainment model are compared to experimental coefficients. The development of mean velocity along the trajectory is investigated by extracting profiles from discharges at different path lengths. Finally, fluctuating velocity characteristics of INBJs are examined.

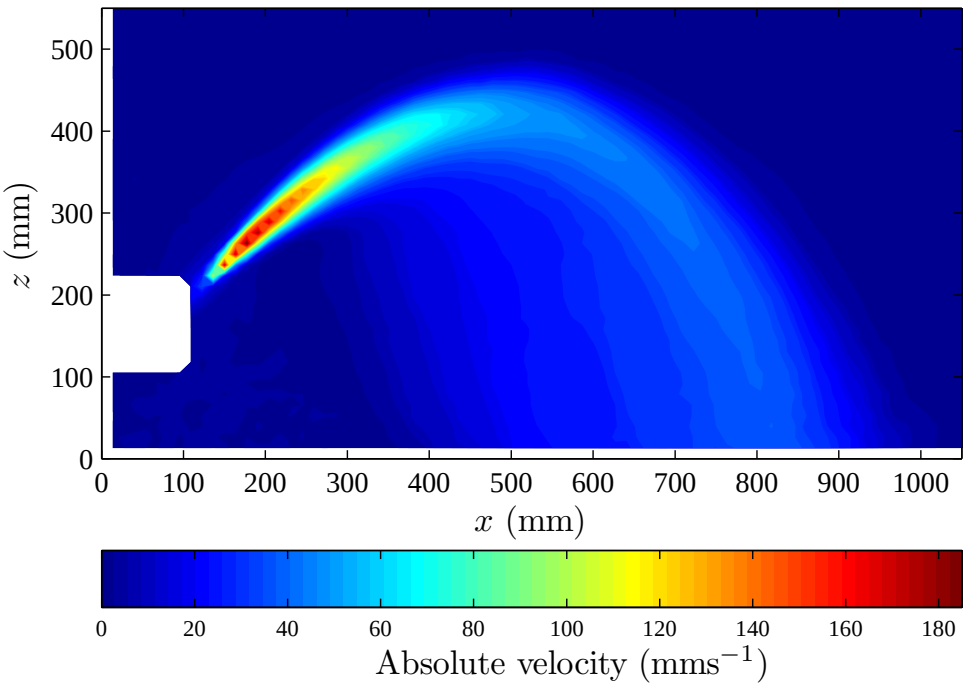

Figure 5.22 – Contours of mean absolute velocity for 45° experiment, $F_o = 78.8$. The source outlet is located in the white rectangle. This area is excluded from the PTV analysis due to reflections off the source.

5.3.1 Mean Velocity

Mean or time averaged velocity field data is important for determining the bulk behaviour of INBJs. Discharges are highly turbulent and the instantaneous velocity at a single physical location in the flow is constantly fluctuating with time. Time averaging provides the predominant magnitude and direction of the flow at that location. All of the experimental data presented in this subsection refer to the mean velocity and the overline (overbar) on velocity symbols representing mean quantities is neglected.

Dimensional analysis relationships for non-dimensionalised geometric parameters and dilutions have been shown to be directly proportional to the initial Froude number for different source angles (Zeitoun, 1970; Roberts & Toms, 1987; Roberts *et al.*, 1997; Cipollina *et al.*, 2005; Kikkert *et al.*, 2007; Shao & Law, 2010; Oliver, 2012). Dimensional relationships for centreline velocity, at important geometric locations, can be derived in a similar way to equations 5.1 - 5.3 for geometric parameters. Parameters important to the centreline velocity of the flow at a particular location are shown in equation 5.4, which were defined in chapter 2.

$$u_c = f(Q_o, M_o, B_o, \theta_o) \tag{5.4}$$

Dimensional analysis of the important parameters using the Buckingham π theorem with Q_o and M_o as repeaters results in two dimensionless π groups (Equations 5.5 - 5.6).

$$\pi_1 = \frac{u_c Q_o}{M_o} \equiv \frac{u_c}{U_o} \tag{5.5}$$

$$\pi_2 = \frac{B_o {Q_o}^2}{{M_o}^{5/2}} \equiv F_o \tag{5.6}$$

Therefore, centreline velocity, which has been non-dimensionalised by the initial source velocity, is dependent on the initial Froude number and source angle as shown in equation 5.7.

$$\frac{U_o}{u_c} = f(F_o, \theta_o) \tag{5.7}$$

The centreline velocities at maximum height (u_m) and the return point (u_r) were extracted from the mean velocity field using the same MATLAB algorithm that determined the trajectory of the discharges outlined in section 4.3.2. Figures 5.23 - 5.25 show that centreline velocities at maximum height and the return point, which have been non-dimensionalised by the initial source velocity, are linearly dependent on the initial Froude number for 30°, 45°, and 60° discharges. u_m is greater than u_r at source angles of 30° and 45° (Figures 5.23 - 5.24), whereas u_m is similar to u_r at the higher source

angle of 60° (Figure 5.25). u_m for one experiment at 60° ($F_o = 37.7$) was treated as an outlier and excluded from the linear regression (Figure 5.25). Examination of images from this 60° experiment revealed that the camera was out of focus in the centre of the images due to Petzval curvature, which was detailed in section 4.2.2.2. Light reflected off tracer particles was smudged in images, resulting in the identification of minimal tracer particles and subsequently a significant underestimation of u_m. Two experiments were conducted with similar initial Froude numbers of 44.8 and 45.0 at 60° to determine the repeatability of results. The experimental system had good repeatability as u_m and u_r are very similar for both these experiments (Figure 5.25).

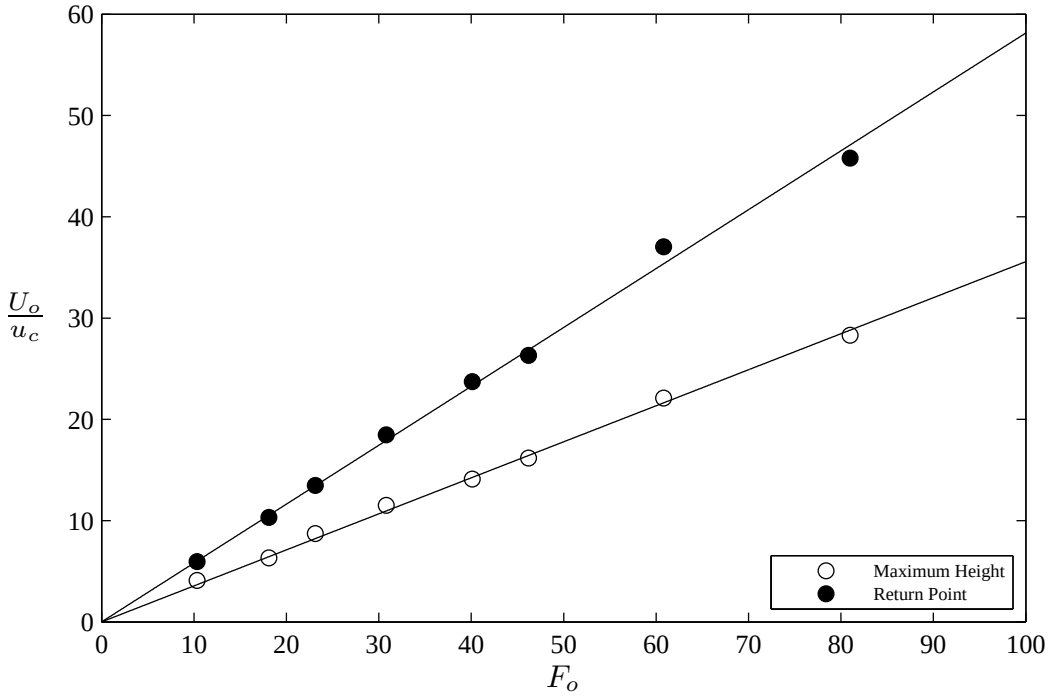

Figure 5.23 – Centreline velocity at maximum height (u_m) and return point (u_r) for 30° INBJ experiments.

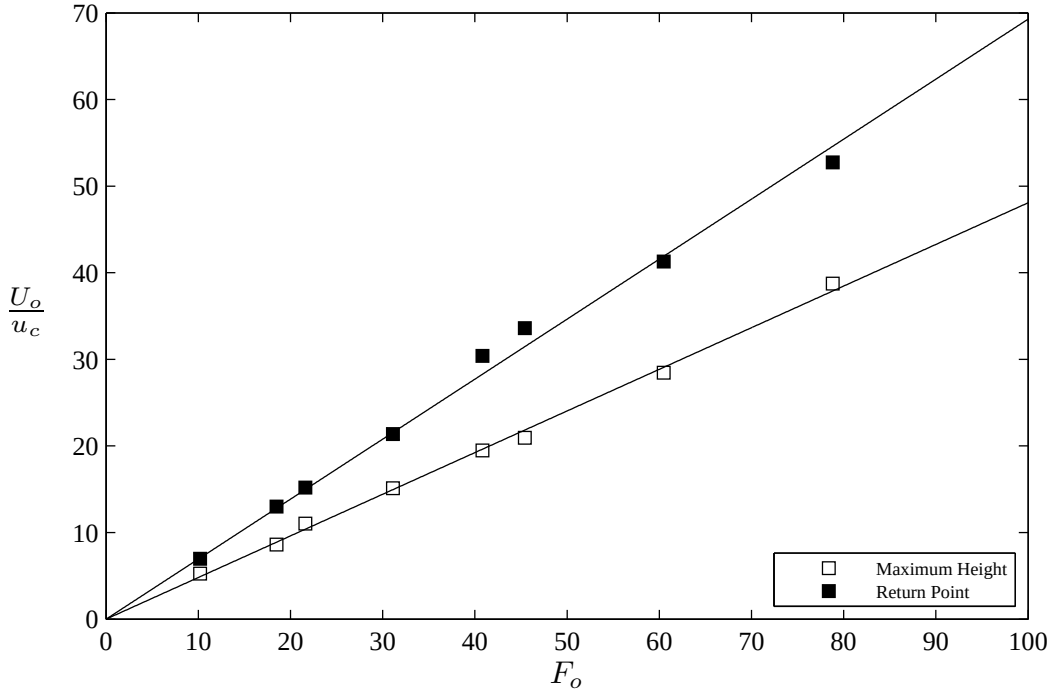

Figure 5.24 – Centreline velocity at maximum height (u_m) and return point (u_r) for 45° INBJ experiments.

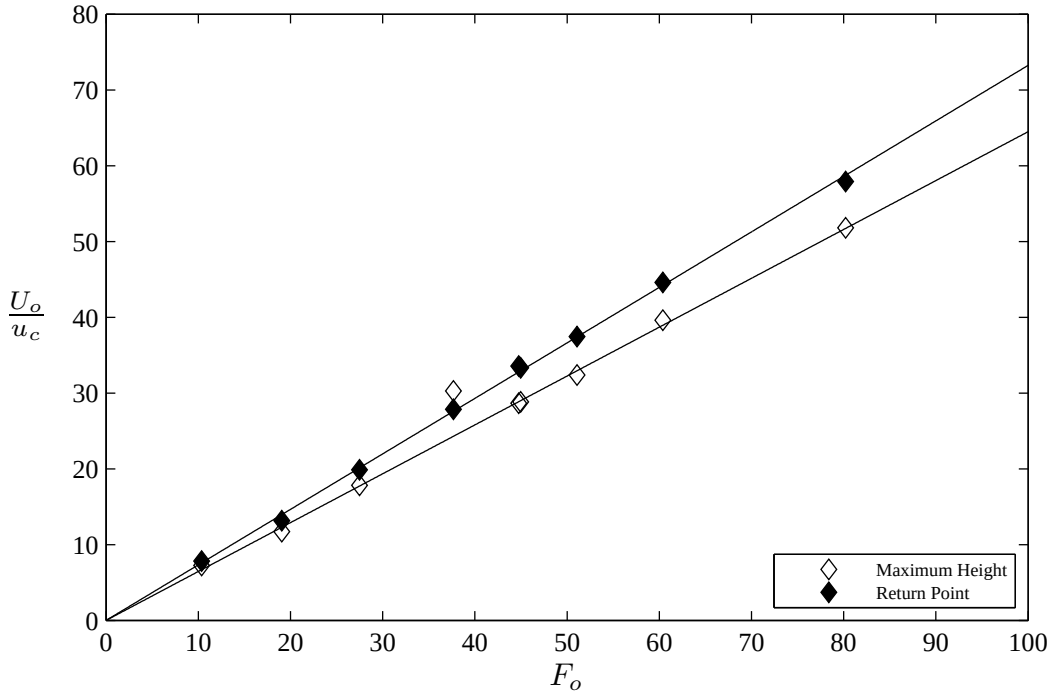

Figure 5.25 – Centreline velocity at maximum height (u_m) and return point (u_r) for 60° INBJ experiments. Outlier at $F_o = 37.7$ was excluded from linear regression.

The centreline velocity data at maximum height and the return point are consistent with the dimensional analysis relationships for geometric parameters and dilution, as predicted by equation 5.7. A linear regression was fitted through the non-dimensionalised centreline velocity data for each source angle. The k-notation used in equations 5.1 - 5.3 for geometric parameters will also be used for the centreline velocity at maximum height and the return point. Equations 5.8 - 5.9 show the empirical relationships between important parameters for centreline velocity, which are dependent on the initial source angle of discharges.

$$\frac{U_o}{F_o u_m} = k_{um}\left(\theta_o\right) \tag{5.8}$$

$$\frac{U_o}{F_o u_r} = k_{ur}\left(\theta_o\right) \tag{5.9}$$

Table 5.5 shows the gradient of the linear regression applied to centreline velocity data at maximum height and return point for all source angles in this study using the k-notation. The local angle of centreline velocity at maximum height (θ_m) and the return point (θ_r) are not dependent on the initial Froude number and were averaged across all experiments at each source angle. However, θ_m and θ_r depend on the source angle (Table 5.5). θ_m values are slightly positive, which indicates that centreline velocity is upwards, while the bulk movement of the flow would be horizontal at maximum height. This is due to maximum height being defined as the location where trajectory reaches its highest vertical distance in the water column, rather than the location where centreline velocity is horizontal. θ_m values generally increase with increasing source angle. Therefore, the difference between the direction of centreline velocity and bulk flow behaviour increases for higher source angles. θ_r values decrease with increasing source angle, which is due to the ratio of vertical to horizontal momentum flux at the return point increasing for increasing source angle.

Table 5.5 – Experimental coefficients (± SD) for velocity parameters determined by linear regression. k-notation used.

θ_o	k_{um}	θ_m (rad)	k_{ur}	θ_r (rad)	$\frac{u_m}{u_r}$
15°	0.251 ± 0.015	0.014 ± 0.011	0.404 ± 0.015	-0.399 ± 0.023	1.613
30°	0.356 ± 0.010	0.042 ± 0.013	0.581 ± 0.020	-0.745 ± 0.027	1.635
45°	0.481 ± 0.014	0.076 ± 0.028	0.693 ± 0.031	-1.1018 ± 0.028	1.441
60°	0.645 ± 0.010	0.081 ± 0.064	0.732 ± 0.012	-1.238 ± 0.022	1.136
65°	0.704 ± 0.016	0.109 ± 0.029	0.742 ± 0.037	-1.311 ± 0.048	1.054
70°	0.768 ± 0.013	0.106 ± 0.017	0.703 ± 0.008	-1.315 ± 0.007	0.915
75°	0.872 ± 0.033	0.155 ± 0.044	0.702 ± 0.015	-1.381 ± 0.015	0.805

There is limited experimental velocity data available for comparison to the present study. Shao & Law (2010) plotted non-dimensional centreline velocity experimental data against non-dimensional path length on a logarithmic scale for 30° and 45° discharges. Non-dimensional centreline velocity was found to collapse for a range of Froude numbers for both angles. However, the non-dimensional path length to maximum height and the return point was not provided in their study. Therefore, direct comparisons can not be made to the present study at maximum height and the return point. Lai & Lee (2012) plotted experimental data of centreline velocity against path length for three experiments with different initial Froude numbers at 60°. The location of maximum height was illustrated on the figures for each experiment. The centreline velocity at maximum height for these three experiments was extracted from the figures and a linear regression applied to obtained an experimental coefficient for 60°.

Figure 5.26 shows that values for the experimental coefficient of centreline velocity at maximum height (k_{um}) increases with increasing source angle. Alternatively, u_m decreases with increasing source angle. u_m decreases more rapidly as source angle increases due to the lower initial horizontal momentum flux at maximum height. s_m also increases with increasing source angle (Figure 5.20), resulting in additional centreline velocity decay. The k_{um} value of Lai & Lee (2012) at 60° was 0.548 ± 0.073, which is lower than the coefficient from the present study. The standard deviation in the experimental data of Lai & Lee (2012) is much greater than the standard deviation of experimental data from the present study at 60° (Table 5.5).

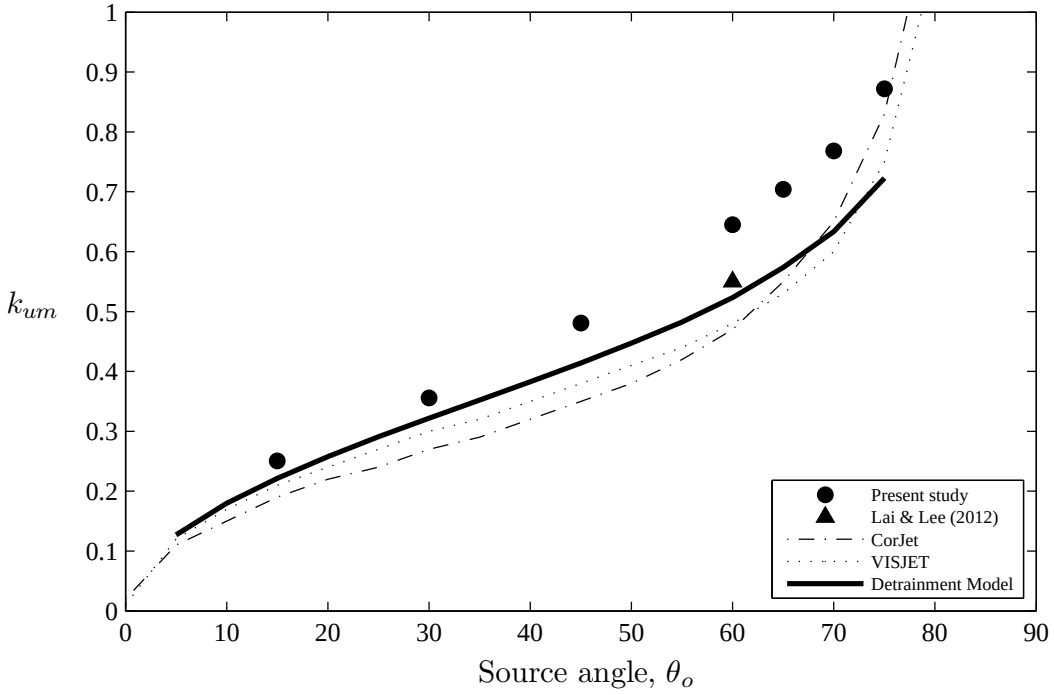

Figure 5.26 – Coefficients for centreline velocity at maximum height (k_{um}) for all angles.

Figure 5.27 shows that values for the experimental coefficient of centreline velocity

at the return point (k_{ur}) increases with source angle up to 65° for the present study. k_{ur} then decreases for the higher source angles of 70° and 75°, alternatively u_r increases for these higher source angles (Figure 5.27). Kikkert *et al.* (2007) conceptualised that the behaviour of INBJs could be separated into jet and plume regions on the rising and falling sides of the discharge, respectively. Therefore, $u_c \propto s^{-1}$ up to maximum height and $u_c = \propto z^{-1/3}$ on the falling side, where the origin of z is the location of a virtual plume source above maximum height (Kikkert *et al.*, 2007). Figure 5.28 compares the relative sizes of centreline velocity at maximum height and the return point ($u_m/u_r = k_{ur}/k_{um}$) for different source angles. u_m/u_r is much greater than 1 for the source angles of 15°, 30°, 45°. k_{sm} values are smaller for these angles (Figure 5.20), resulting in a higher u_m (Figure 5.26). k_{zm} values are also lower for these angles (Figure 5.16) so that buoyancy generated momentum flux before the return point is smaller for these angles. u_m/u_r is near 1 for source angles above 60° with $u_m/u_r = 1$ occurring between 65° and 70° (Figure 5.28). u_r is approximately constant for $\theta_o \geq 30°$ (Figure 5.27), therefore changes in u_m/u_r are directly linked to changes in u_m. k_{sm} values are larger for $\theta_o \geq 60°$ (Figure 5.20), resulting in a relatively low u_m (Figure 5.26). k_{zm} values are also higher for these source angles (Figure 5.16), so that buoyancy generated momentum flux before the return point would be larger. The spreading of the discharge on the falling side, where plume-like behaviour exists, should result in a decrease in u_r. However, u_r increases for the source angles of 70° and 75° (Figure 5.27). Re-entrainment is likely to restrict spreading on the inner side of discharges for these source angles, resulting in higher u_r measurements.

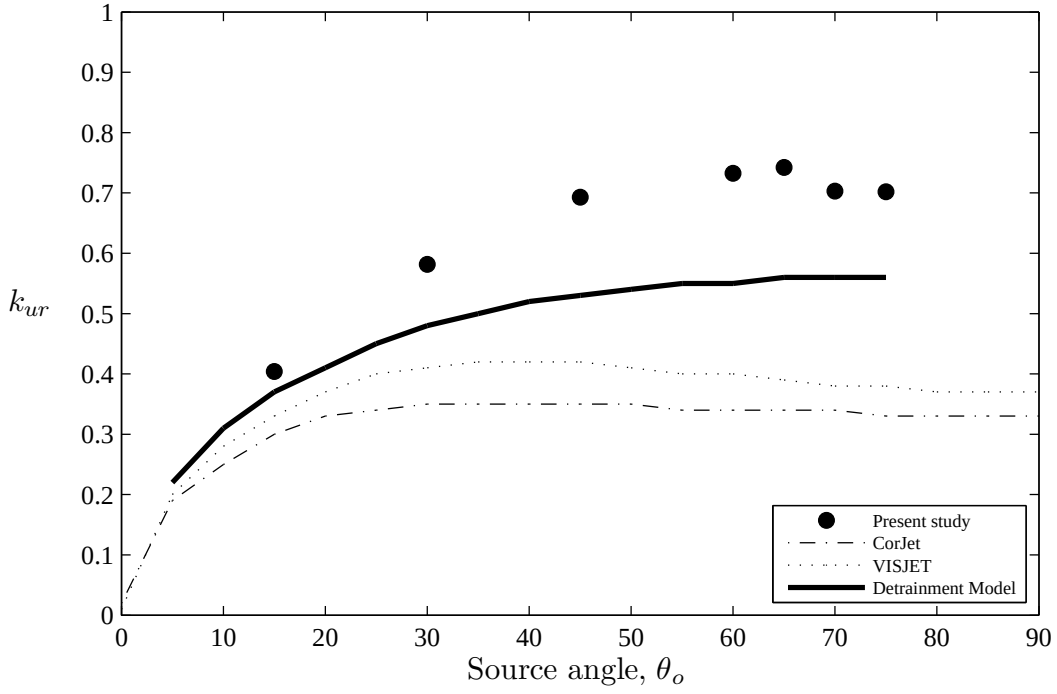

Figure 5.27 – Coefficients for centreline velocity at the return point (k_{ur}) for all angles.

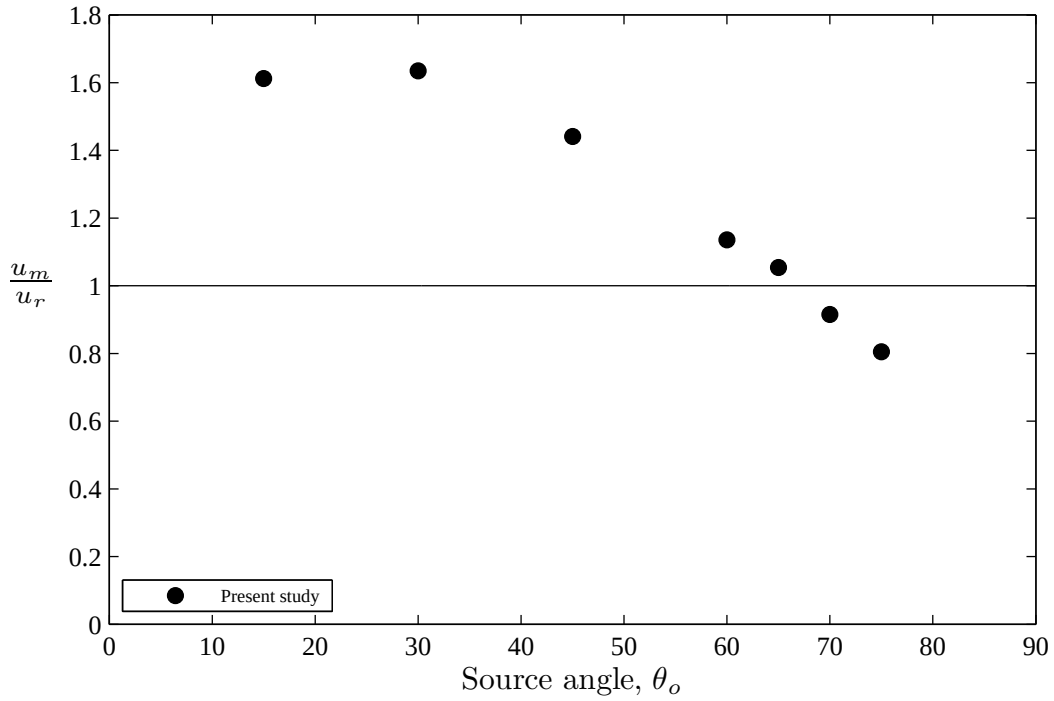

Figure 5.28 – Ratio of centreline velocity at maximum height to centreline velocity at the return point for all angles.

Model Performance

Integral model predictions by CorJet, VISJET, and the Detrainment model are compared to velocity experimental coefficients in figures 5.26 and 5.27. Predictions from all models underestimate k_{um} and k_{ur} experimental coefficients at both these locations. Predictions follow the general trends of experimental coefficients across the range of source angles. k_{um} and k_{ur} predictions by the Detrainment model are better than predictions of the buoyancy conserving models (CorJet, VISJET) (Figures 5.26 - 5.27). CorJet and VISJET predictions of k_{ur} values decrease slightly for source angles above 45° and are considerably lower than predictions of the Detrainment model. Detrainment model k_{ur} predictions increase for increasing source angle, following the trend of experimental coefficients (Figure 5.27). However, predictions from all models substantially underestimate experimental coefficients, especially at the return point. Centreline velocity predictions of integral models were determined from the magnitude of total momentum flux. A conversion factor was applied to the velocity predictions of top-hat integral models (VISJET, Detrainment model) to determine the corresponding centreline value (Equation 3.20, Section 3.1.1). The conversion factor accounts for turbulent fluxes and assumes the discharge is radially symmetric. However, INBJs are not radially symmetric due to detrainment on the inner side of discharges. The distribution of velocity over the full cross-sectional area is unknown for INBJs, therefore, a more realistic conversion factor for centreline velocity can not be determined.

5.3.1.1 Components of Centreline Velocity

Components of centreline velocity in the horizontal (u) and vertical (v) directions represent the predominant magnitude and direction of INBJs. Components of centreline velocity collapse upon source diameter and Froude number for all experiments at source angles of 30°, 45°, and 60° (Figures 5.29 - 5.30). The inverse of non-dimensional relationships developed in equations 5.8 - 5.9 are utilised in these figures to avoid non-dimensional vertical velocity becoming asymptotic as $v \to 0$ at maximum height. The magnitude of u is much greater than v before maximum height for 30° discharges (Figure 5.29). u continuously decreases with horizontal distance from the source. v decreases to a slightly positive value at maximum height, before becoming negative on the falling side. u and v have similar magnitude but opposite sign at the return point. The gradient of v reduces after the return point, whereas the gradient of u is approximately constant.

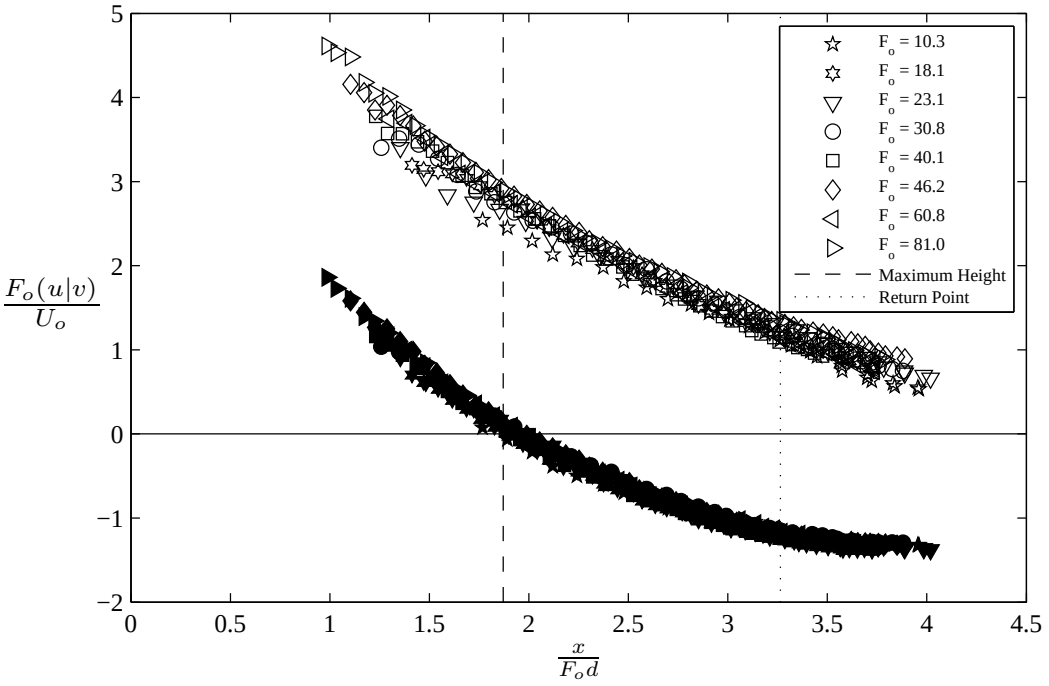

Figure 5.29 – Components of centreline velocity for all 30° experiments, unfilled symbols: horizontal velocity (u), filled: vertical velocity (v).

u and v are of similar magnitude near the source for 45° discharges (Figure 5.30), which is expected as initial vertical and horizontal initial momentum fluxes are equal. v is greater than u near the source for 60° discharges (Figure 5.31), before v decreases rapidly to maximum height. u again continuously decreases for the measured horizontal distance from the source for 45° and 60° discharges. This is due to the spread of discharges increasing, while the horizontal momentum flux remains constant. The gradient of v reduces around the return point for 30° and 45° discharges and the magnitude of v is much greater than u after the return point. Centreline velocity

components for one experiment at 60° ($F_o = 37.7$) are below the majority of other experiments (Figure 5.31). u_m for this experiment was treated as an outlier in the linear regression (Figure 5.25), due to the centre of recorded images being out of focus. However, u_r for this experiment was not treated as an outlier due to the images being in focus near the return point. Therefore, the focus of recorded images is critical to the performance of the PTV experimental system.

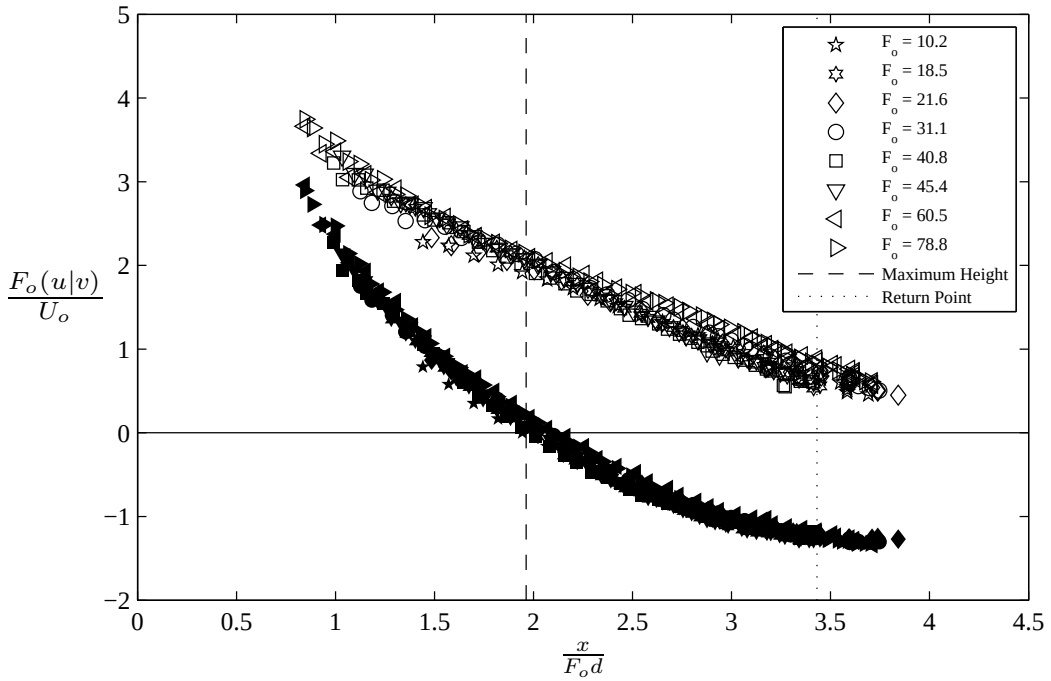

Figure 5.30 – Components of centreline velocity for all 45° experiments, unfilled symbols: horizontal velocity (u), filled: vertical velocity (v).

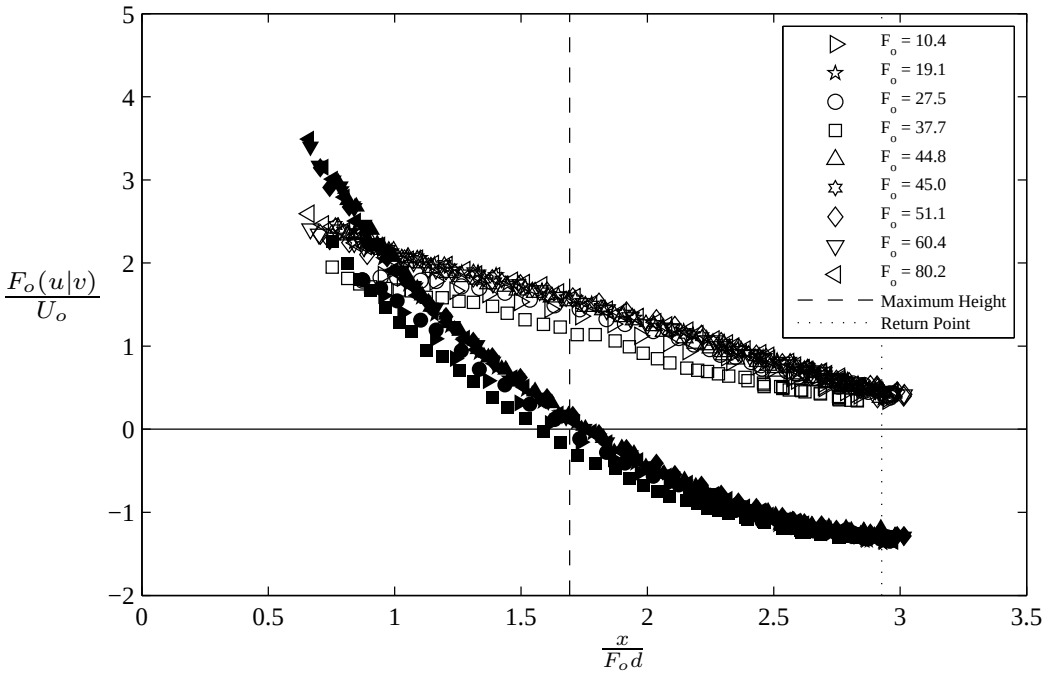

Figure 5.31 – Components of centreline velocity for all 60° experiments, unfilled symbols: horizontal velocity (u), filled: vertical velocity (v).

5.3.1.2 Velocity Profiles

Cross-sectional mean velocity profiles of discharges were taken perpendicular to the centreline velocity at maximum height and the return point, as well as along the centreline trajectory. The coordinate system used for these profiles is shown in figure 5.32, where the axial axis is the direction of centreline velocity and the radial axis is perpendicular to centreline velocity. The PTV system used in the present study measured a two-dimensional velocity field along the central plane of the discharges. Therefore, profiles extracted from the mean velocity field do not represent the behaviour of flow offset from the central plane. Velocity profiles of 60° discharges will be the focus of this subsection, as profiles of other angles shared similar trends and are not included in the main document for brevity.

Axial (u_s) and radial (u_n) velocity components at maximum height were non-dimensionalised by the centreline velocity for all experiments at 60° (Figure 5.33). The radial distance from the centreline has been non-dimensionalised by the outer discharge width. Non-dimensional u_s and u_n profiles collapses for all initial Froude numbers at maximum height (Figure 5.33). u_s on the outer side of the profiles (negative r/b) compares well with the Gaussian distribution. Numerous experimental studies reported that concentration profiles are Gaussian on the outer side of these discharges (Kikkert *et al.*, 2007; Shao & Law, 2010; Lai & Lee, 2012; Oliver, 2012). u_s on the inner side of discharges is non-Gaussian and decreases slowly away from the centreline with radial distance. This increases the inner discharge width of 60° discharges considerably (Figure

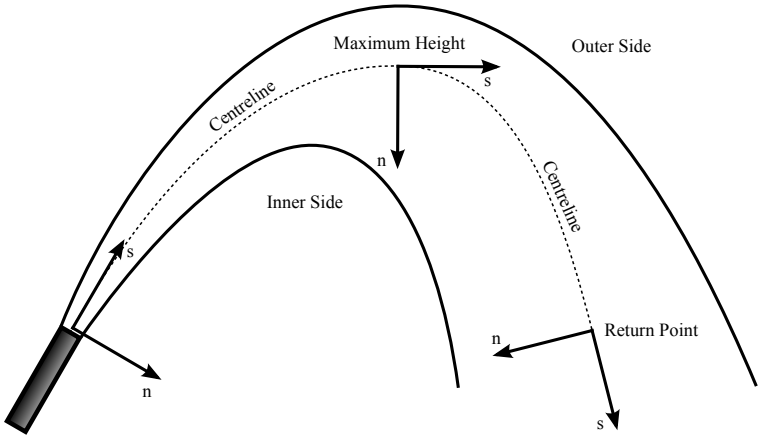

Figure 5.32 – Trajectory of INBJs with axial (s) and radial/normal (n) co-ordinate system used to determine velocity profiles of discharges.

5.14). u_n is generally positive on the outer side of discharges, indicating that ambient fluid is being entrained into discharges at maximum height. u_n is also positive on the inner side as well, which differs to the behaviour of jet and plume discharges that entrain ambient fluid symmetrically, where u_n would generally be negative (Ying *et al.*, 2004). Positive u_n values for INBJs demonstrate the previously observed detrainment on the inner side of discharges (Lane-Serff *et al.*, 1993; Kikkert *et al.*, 2007; Ferrari & Querzoli, 2010). u_n values on the inner side of discharges are much greater than those on the outer side of discharges, indicating significant detrainment of mixed fluid is occurring at maximum height on the central plane (Figure 5.33). It is also interesting to note that u_n is slightly negative between $-1 < r/b < 0$ on the outer side. The form and magnitude of radial velocities on the outer side are consistent with the values of jet and plume discharges found by Ying *et al.* (2004). The magnitude of radial velocity on the inner side of discharges decreases for the lower source angles of 30° and 45° at maximum height (Figures B.3 - B.4, Appendix B), otherwise profiles are similar to those of 60° discharges.

Non-dimensionalised axial and radial components of velocity at the return point are shown in figure 5.34 for 60° discharges. u_s on the outer side again compares well with the Gaussian distribution. u_s decays at a roughly constant rate with radial distance from the centreline on the inner side. u_n is positive on the outer side at the return point, which indicates entrainment is occurring. However, u_n is still positive on the inner side of discharges as well. Therefore, mixed fluid is still being detrained radially at the return point. The magnitude of u_n on the inner side is of similar magnitude to the outer side at the return point, which differs significantly to the behaviour at maximum height (Figure 5.33). The magnitude of u_n on the inner side increases for the lower source angles of 30° and 45° at the return point (Figures B.5 - B.6, Appendix B), otherwise profiles are similar to those of 60° discharges.

Figure 5.35 shows the non-dimensional axial and radial centreline velocity profiles

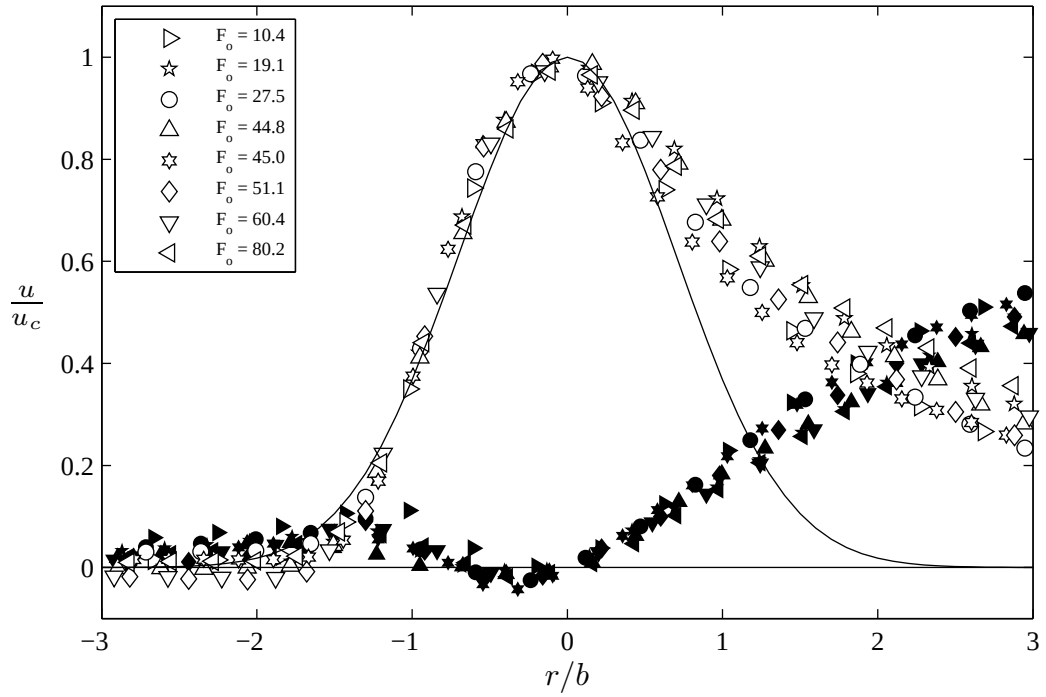

Figure 5.33 – Velocity profile components at maximum height for 60° experiments, unfilled symbols: axial velocity (u_s), filled symbols: radial velocity (u_n).

for a range of path lengths, which have been non-dimensionalised by the initial source diameter (d). Figure 5.35(a) shows that u_s is approximately symmetrical and Gaussian on both sides of the discharge near the source (s/d = 27.3, 40.6). However, there is some distortion on the inner side, which could indicate some detrainment is occurring. u_s on the outer side remains Gaussian for the full path length to the return point (s/d = 126.8). u_s on the inner side transitions from Gaussian near the source to a linear decay with radial distance for the first profile after maximum height (s/d = 78.1). Non-dimensional u_s profiles remained roughly self-similar after this asymmetric profile is reached. Figure 5.35(b) shows that non-dimensional u_n profiles collapse on the outer side and vary significantly on the inner side. As previously mentioned, the PTV experimental system was unable to capture the high velocities near the source outlet. This results in a gap before the first profiles can be taken. The first u_n profile (s/d = 27.3) shows that detrainment is already occurring close to the source on the inner side. Detrainment is shown to increase with path length from the source by increasing non-dimensional u_n values, which reach a maximum on the inner side at maximum height (s/d = 65.4). Non-dimensional u_n values on the inner side of the discharge then decrease after maximum height.

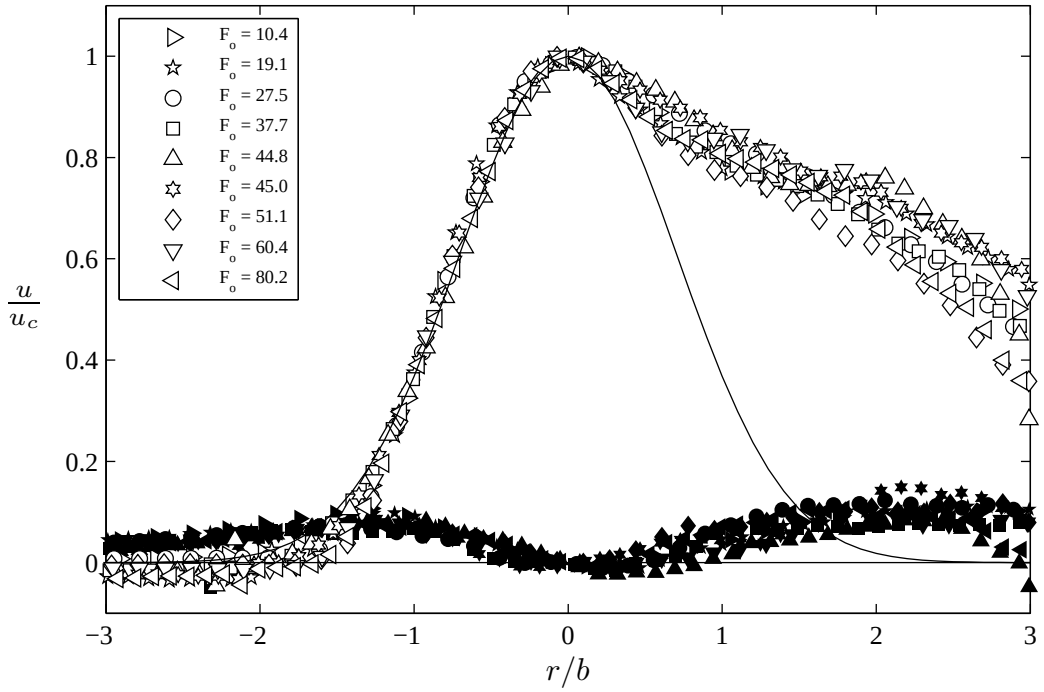

Figure 5.34 – Velocity profile components at return point for 60° experiments, unfilled symbols: axial velocity (u_s), filled symbols: radial velocity (u_n).

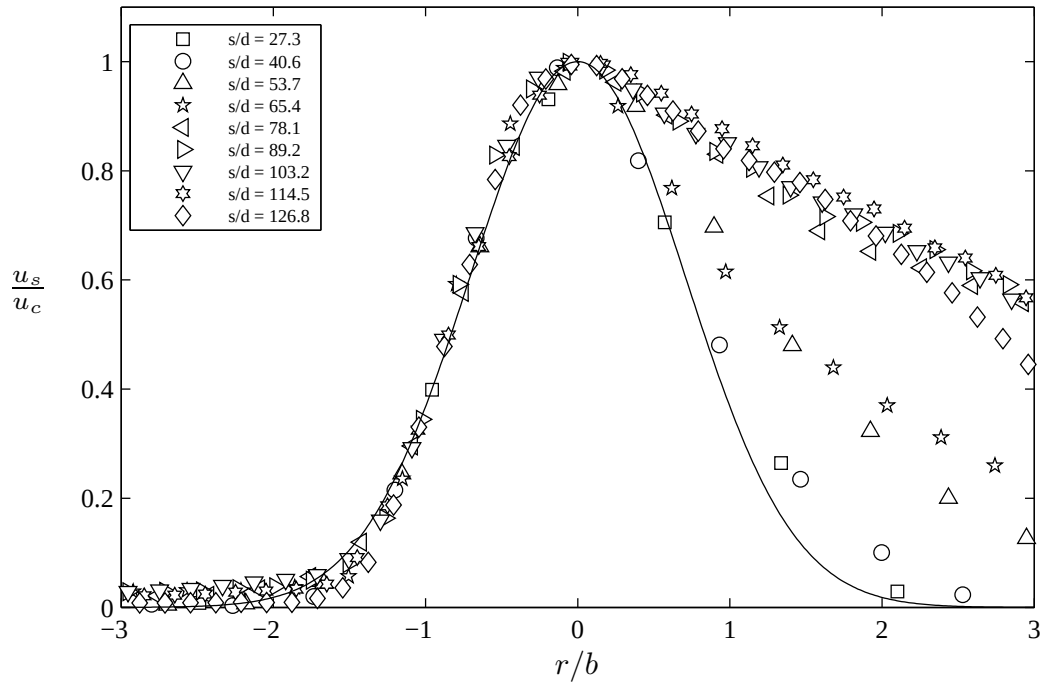

(a) Axial velocity

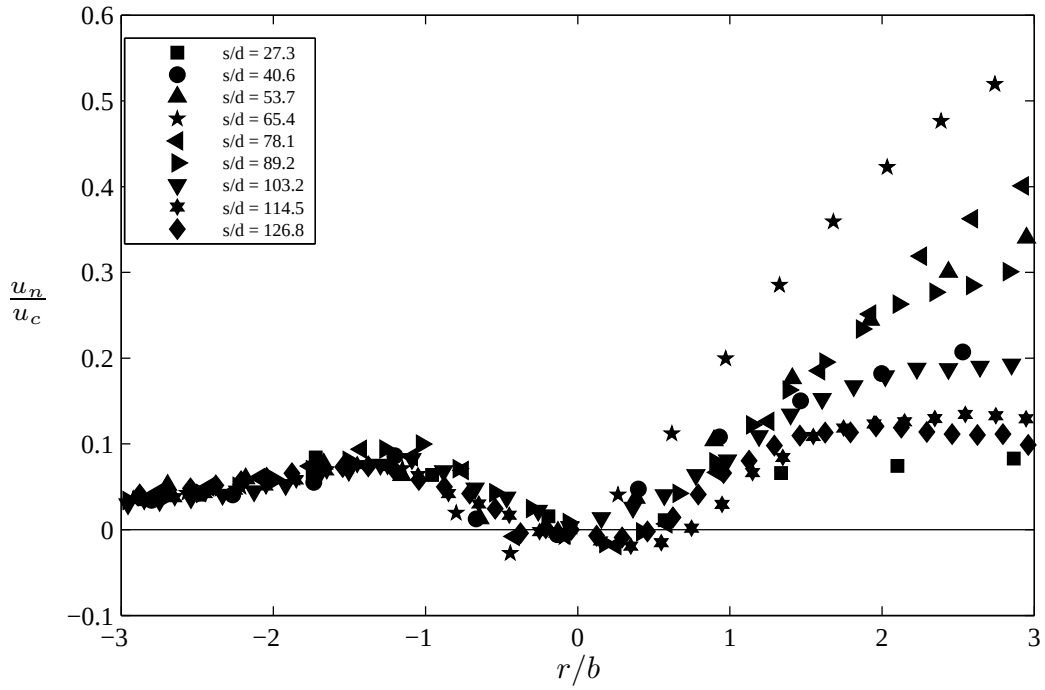

(b) Radial velocity

Figure 5.35 – Velocity profiles against path length for 60° experiment, $F_o = 27.5$.

5.3.1.3 Detrainment Velocity

Radial velocities on the inner side of INBJs indicate the loss of discharged fluid from the main flow changes with path length (Figure 5.35(b)). The Detrainment model proposed a mechanism for the loss of buoyancy flux from the control volume to account for the loss of discharged fluid through detrainment (Section 3.5). It was proposed that the loss of buoyancy flux was dependent on a detrainment velocity (u_D), which was proportional to local flow parameters. Comparison of predicted detrainment velocities to the experimentally measured values is important to determine if the detrainment mechanism has been modelled appropriately. A direct comparison of predicted and measured radial velocities is not possible as the Detrainment model does not assume radial velocity profiles. Therefore, the form and trends of predicted and measured radial velocities at different source angles is important. Experimentally measured non-dimensionalised radial velocities, at a fixed radial distance from the source ($r/b = 1$) on the inner side of discharges are shown in figure 5.36 for all source angles studied. Radial velocities were averaged across experiments for the same non-dimensional path lengths at each source angle. Negative radial velocities near the source show that entrainment occurred on the inner side of discharges, before values became positive ($s/(F_o d) \approx 1$). Beyond this point, radial velocities increase with path length for all source angles to a maximum near maximum height ($s/(F_o d) \approx 2.0$ - 2.5). Radial velocities at maximum height are higher for higher source angles. Values then decrease after maximum height for increasing path length at source angles above 30°. Measured radial velocities for higher source angles decrease rapidly, whereas values for 15° and 30° discharges plateau before decreasing slightly on the falling side of discharges. Predicted radial velocities by the Detrainment model show similar trends to experimentally measured values (Figure 5.37). 75° discharges are predicted to have the highest radial velocities near maximum height ($s/(F_o d) \approx 2.0$ - 2.5) and 15° discharges are predicted to have the lowest radial velocities, consistent with experimental radial velocities. Predicted radial velocities at higher source angles also increase and decrease rapidly, compared to radial velocities for 15° and 30° discharges that levelled off after maximum height. The magnitude of predicted radial velocities are lower than measured values but are within a factor of two of the measured values. The similar form and trends of predicted detrainment radial velocities to measured values indicates that u_D was appropriately related to local parameters.

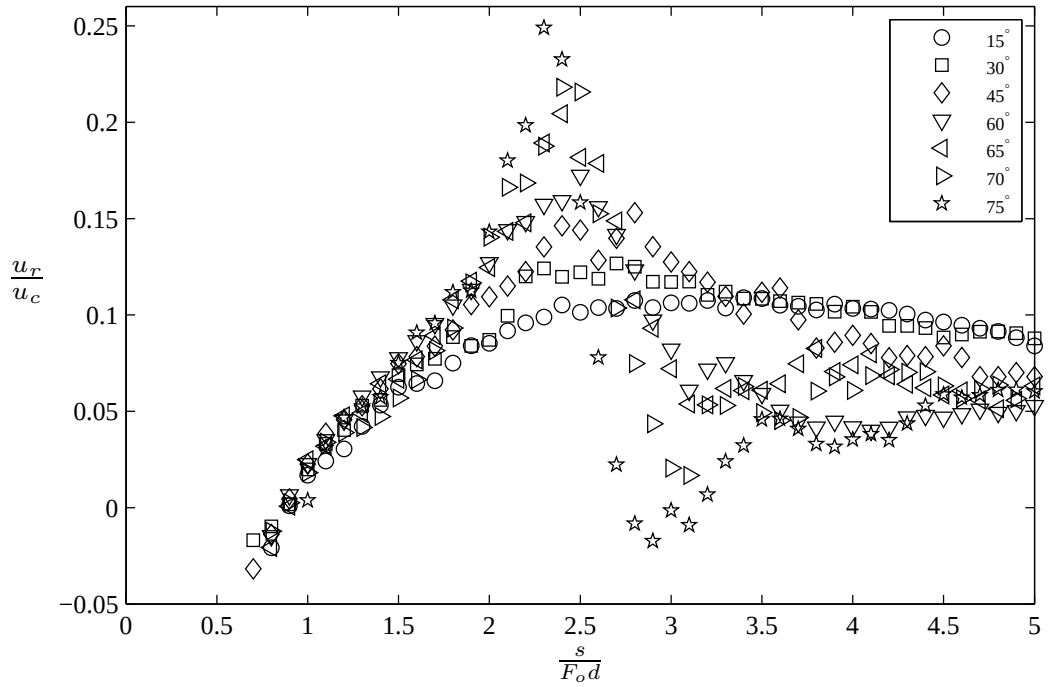

Figure 5.36 – Experimentally measured radial velocities at $r/b = 1$ on the inner side of discharges for all source angles against path length.

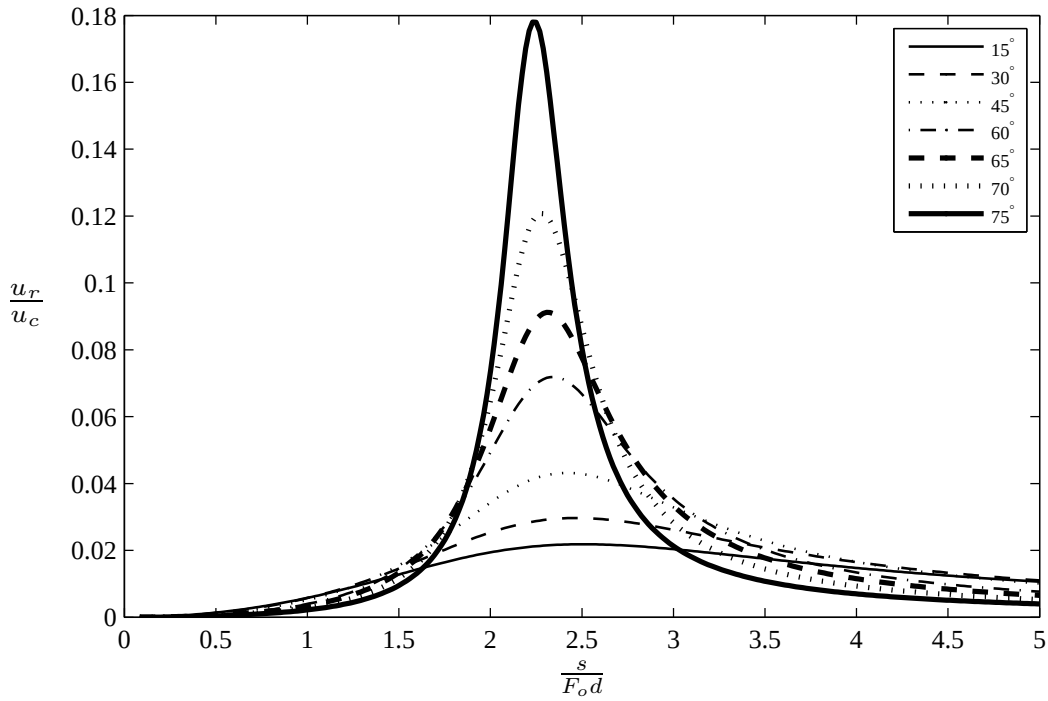

Figure 5.37 – Radial velocity ($u_D \cos(\theta)$) predicted by the Detrainment model for all source angles against path length.

5.3.1.4 Summary

The mean velocity experimental data illustrates the complex flow behaviour of INBJs. Non-dimensionalised centreline velocity at maximum height and the return point were found to be directly proportional to initial Froude number (Figures 5.23 - 5.25), conforming to the dimensional analysis relationships developed (Equations 5.8 - 5.9). Experimental coefficients at these locations were reported for all source angles studied (Table 5.5). Centreline velocity at maximum height was found to decrease for increasing source angle (Figure 5.26). Lower centreline velocities at higher source angles were consistent with lower horizontal momentum fluxes at higher angles, due to vertical momentum fluxes being zero at maximum height. Centreline velocity at the return point was found to decrease for increasing source angle up to 65°, before centreline velocity increased for higher source angles (Figure 5.27). The increase in centreline velocity was due to the increased buoyancy generated momentum flux from the higher vertical distance to maximum height at higher source angles (Figure 5.16). Limited velocity experimental data was available for comparison. An experimental coefficient at maximum height for 60° discharges was extracted from Lai & Lee (2012) and was found to be lower than the value from the present study (Figure 5.26). The horizontal component of centreline velocity decreased for the full path length of 30°, 45°, and 60° discharges (Figures 5.29 - 5.31). The vertical component of centreline velocity decreased faster for higher source angles and levelled off near the return point for these source angles.

Velocity profiles illustrate the unique asymmetric behaviour of INBJs that is not seen in pure jets and plumes or positively buoyant jets. Non-dimensionalised axial and radial velocity profiles collapsed at maximum height and the return point (Figures 5.33 - 5.34). Axial velocity profiles collapsed and remained Gaussian on the outer side of discharges for the full path length (Figure 5.35(a)). Radial velocity profiles on the outer side also collapsed and showed entrainment occurring (Figure 5.35(b)). Axial velocity profiles were non-Gaussian on the inner side of discharges (Figure 5.35(a)) and detrainment was shown by the radial velocity profiles on the inner side (Figure 5.35(b)). Velocity profiles on the inner side were dependent on path length, with the maximum radial detrainment velocities occurring near maximum height. Radial velocities in the inner side of discharges increased for higher source angles at maximum height (Figures B.3 - B.4, Appendix B). This was due to the lower total momentum flux or inertia at maximum height for higher source angles. This increases the relative size of gravity potential, increasing the amount of detrainment and increasing radial velocities.

Predictions by integral models underestimated the measured experimental coefficients for all source angles at maximum height and the return point (Figure 5.26 - 5.26). Predictions by the Detrainment model were found to be more accurate than those of

buoyancy conserving models (CorJet, VISJET). However, predictions underestimated experimental coefficients at the return point more than at maximum height, although to a lesser extent than buoyancy conserving models. This was likely due to less overall detrainment having occurred at maximum height, compared to the return point. Predictions of the radial velocities by the detrainment model were found to have similar form to measured radial velocities on the inner side of discharges (Figures 5.36 - 5.37). Velocities measured by the PTV experimental system were of the mixed fluid and ambient fluid. Therefore, measured radial velocities were not directly proportional to the loss of mass or buoyancy flux. Parcels of negatively buoyant detrained fluid drag the surrounding ambient fluid downwards, increasing the measured velocities. Therefore, measured radial velocities provide an upper limit to radial velocities of mixed fluid.

5.3.2 Fluctuating Characteristics

Mean velocity field results of INBJs provided the predominant magnitude and direction of the flow. Mean velocity profiles were asymmetric about the centreline due to the unstable density stratification on the inner side of the discharge. However, mean velocity characteristics do not show *how* INBJs are mixing into the ambient fluid. INBJs are highly turbulent and the fluctuating characteristics are important for understanding the mixing mechanics of these complex flows. Limited studies have investigated the fluctuating characteristics of INBJs, therefore comparisons will be made to the behaviour of pure jet and pure plume discharges where appropriate. Fluctuating characteristics of 60° discharges will be examined initially, before all source angles are compared.

5.3.2.1 60° Discharges

Fluctuating characteristics of 60° discharges will be used as an analogue for INBJs to determine the dependence on initial Froude number and path length. Similar figures to those produced for 60° discharges for 30° and 45° discharges can be found in Appendix B. Turbulent kinetic energy (k) is the energy associated with eddies in flow, which is transferred through the turbulent energy cascade and dissipated by viscous forces. The measurements are of two-dimensional turbulent kinetic energy as the velocity perpendicular to the laser light sheet is not measured. Two-dimensional k values will always be lower than three-dimensional k values due to the difference being the addition of the positive turbulent intensity value in the third dimension. INBJs are not radially symmetric like pure jets and plumes, therefore no assumptions were made about the turbulent intensities in the third direction. Turbulent kinetic energy will always refer to the two-dimensional values in the following sections. Turbulent kinetic energy profiles, which have been non-dimensionalised using the centreline velocity, are similar for all Froude numbers at maximum height and the return point (Figures 5.38

- 5.39). The mean peak non-dimensionalised k value across all Froude numbers at maximum height is 0.365 and occurs at r/b = -0.55 on the outer side (Figure 5.38). Values decrease rapidly on the outer side, whereas they decrease slowly on the inner side. Non-dimensionalised k profiles for pure jets would have two peaks either side of the centreline due to the axial turbulent intensities decreasing near the centreline (Figure 4.20, Section 4.5.2, Hussein *et al.* (1994)). Papakonstantis *et al.* (2011b) found the peak root mean square (RMS) concentration was approximately 0.45 and occurred at r/b = -0.32 for maximum height profiles of 60° discharges, while Oliver (2012) found that the peak RMS concentration was 0.348 and occurred at r/b = -0.86. The radial location of peak non-dimensionalised k value from the present study is within the radial location of peak RMS concentration from these studies (Papakonstantis *et al.*, 2011b; Oliver, 2012). The form of the RMS concentration profiles from both these studies are similar to the form of the non-dimensionalised k profiles in the present study, with a defined peak on the outer side and a slow decay on the inner side.

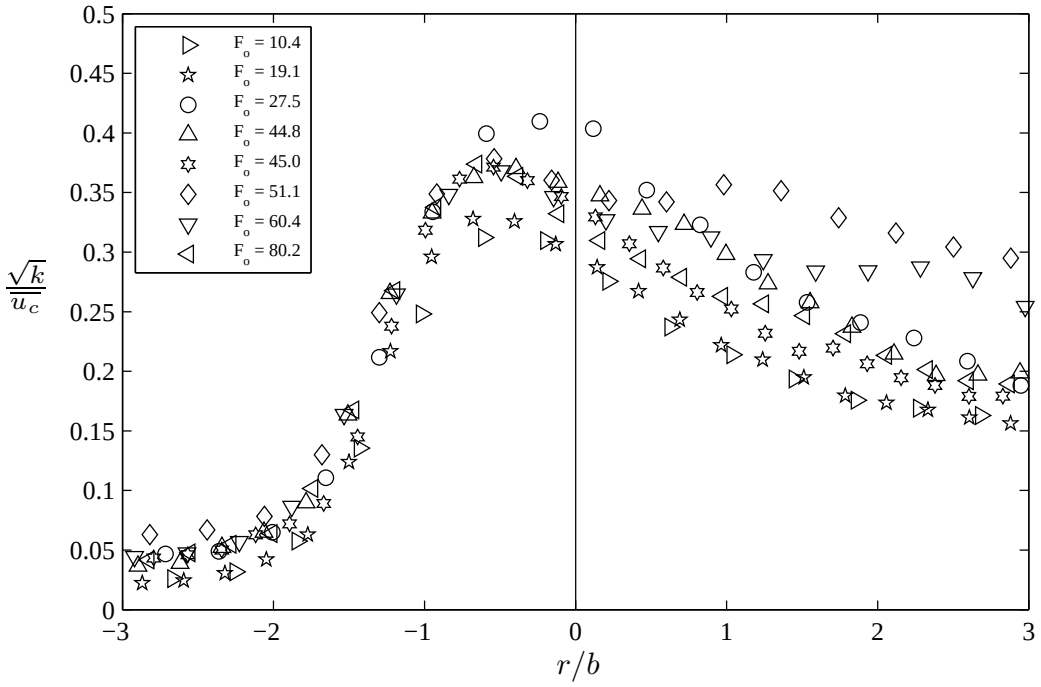

Figure 5.38 – Turbulent kinetic energy (k) profiles at maximum height for all 60° experiments.

The mean peak non-dimensionalised k value is 0.312 at the return point and occurred at r/b = -0.54 (Figure 5.39). Oliver (2012) found that the location of peak RMS concentration occurred closer to the centreline at the return point, however the peak remains at a similar radial distance for both locations in the present study. k values again decrease rapidly on the outer side, whereas they decrease slightly with radial distance on the inner side. Maximum k values are lower at the return point and have a less well defined peak compared to maximum height.

Turbulent shear intensity profiles at maximum height and the return point are

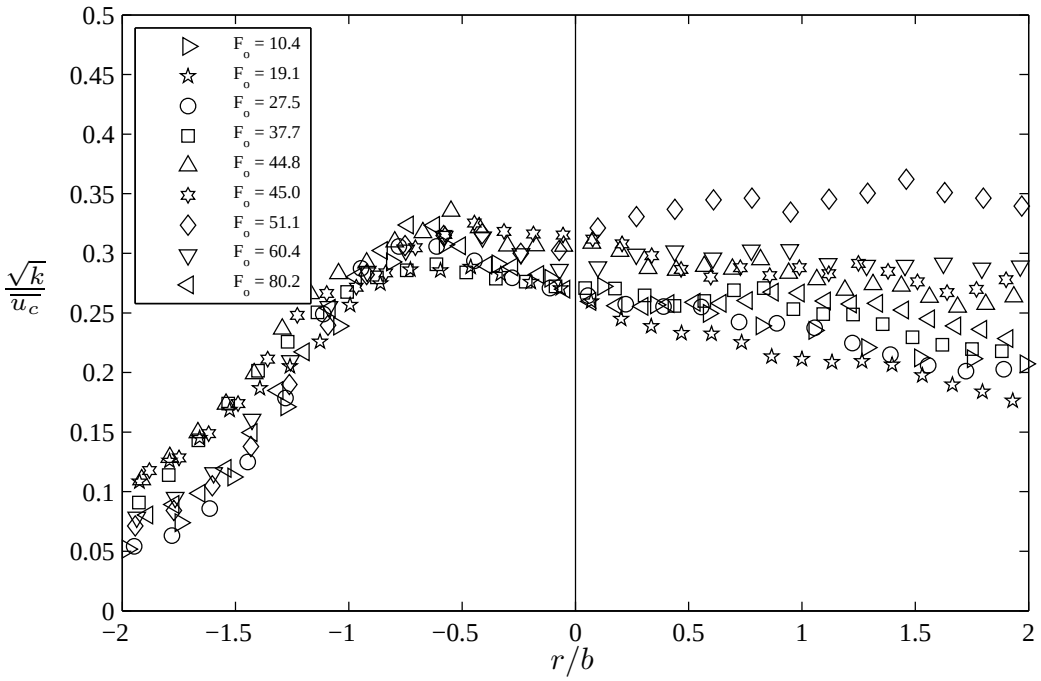

Figure 5.39 – Turbulent kinetic energy (k) profiles at return point for all 60° experiments.

asymmetric about the centreline and values are of similar magnitude for all Froude numbers at 60° (Figures 5.40 - 5.41). Turbulent shear intensity profiles of pure jets are an odd function about the centreline (Figure 4.22, Section 4.5.2). Turbulent shear profiles on the outer side of INBJs have a similar form to pure jet profiles, however the peak value is approximately 2.5 times greater than the peak value for pure jets for 60° discharges at maximum height and the return point. Wang & Law (2002) found the peak value for jets and plumes to be similar, 0.20 and 0.21 respectively. Therefore, peak values for turbulent shear intensities are also much greater than values for plumes. This is likely due to the reduction in centreline velocity for INBJs compared to jets and plumes. At maximum height, the location where values cross the horizontal axis is beyond the centreline at $r/b \approx 0.6$ (Figure 5.40). Turbulent shear intensities remain slightly negative further away from the centreline. The sign of turbulent shear intensity values is opposite to that of maximum height at the return point (Figure 5.41). The change in sign is an artefact of the co-ordinate system used to determine turbulent shear intensity values. A downwardly discharged pure jet will have turbulent shear intensity profiles equal but opposite sign of profiles for an upwardly discharged pure jet using the same co-ordinate system. Therefore, the change of sign is to be expected due to the change in direction of the flow between rising and falling sides with respect to the co-ordinate system. The mean strain rate also changes sign between maximum height and the return point. The sign change is opposite sign to that of turbulent shear intensity. This results in the turbulent kinetic energy term of the mean kinetic energy equation remaining negative, meaning that turbulence is always extracting energy from

the mean flow.

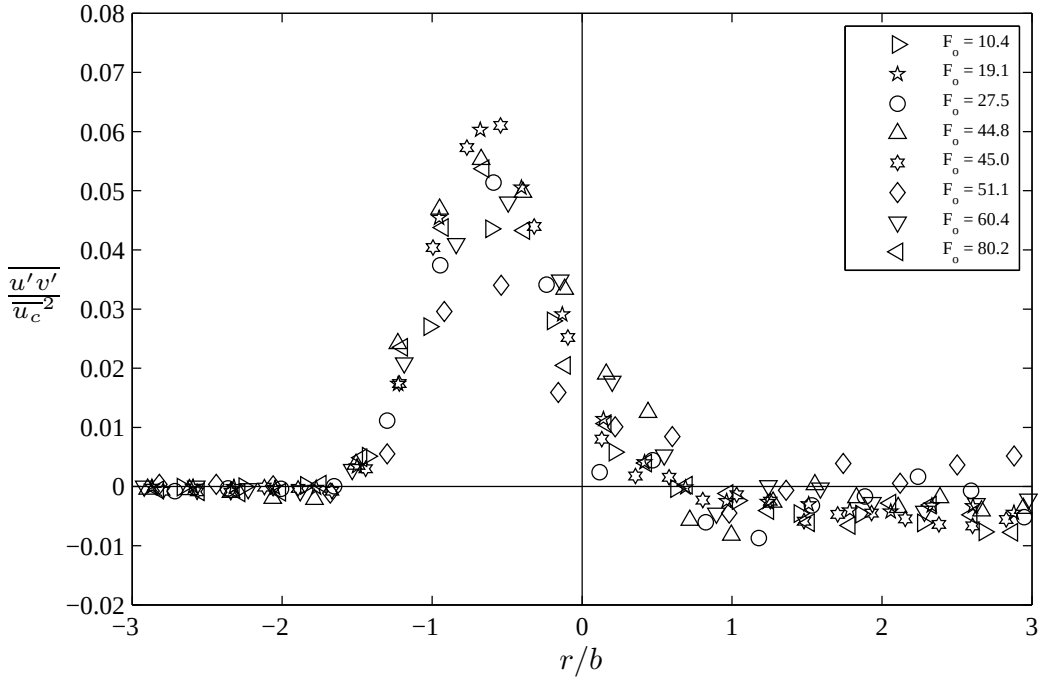

Figure 5.40 – Turbulent shear intensity profiles at maximum height for all 60° experiments.

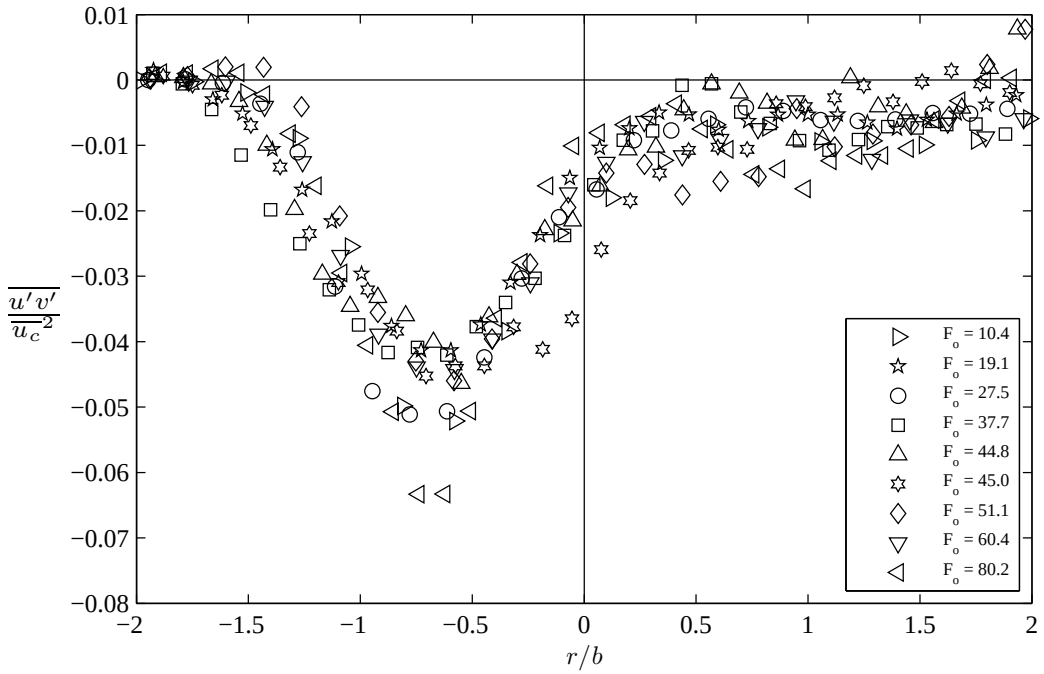

Figure 5.41 – Turbulent shear intensity profiles at the return point for all 60° experiments.

Turbulent kinetic energy and turbulent shear intensity profiles show that mixing on the outer side share similar characteristics to pure jet behaviour. However, these profiles also show the collapse of jet-like turbulent mixing structures on the inner side due to the unstable stratification. Similar energy is held by the eddies on inner and outer sides at maximum height and the return point (Figures 5.38 - 5.39). The form and magnitude of k profiles is similar for different path lengths from the source (Figure 5.42). Magnitudes of k are lowest near the source and highest at maximum height (s/d = 112.2), before decreasing towards the return point (s/d = 214.5).

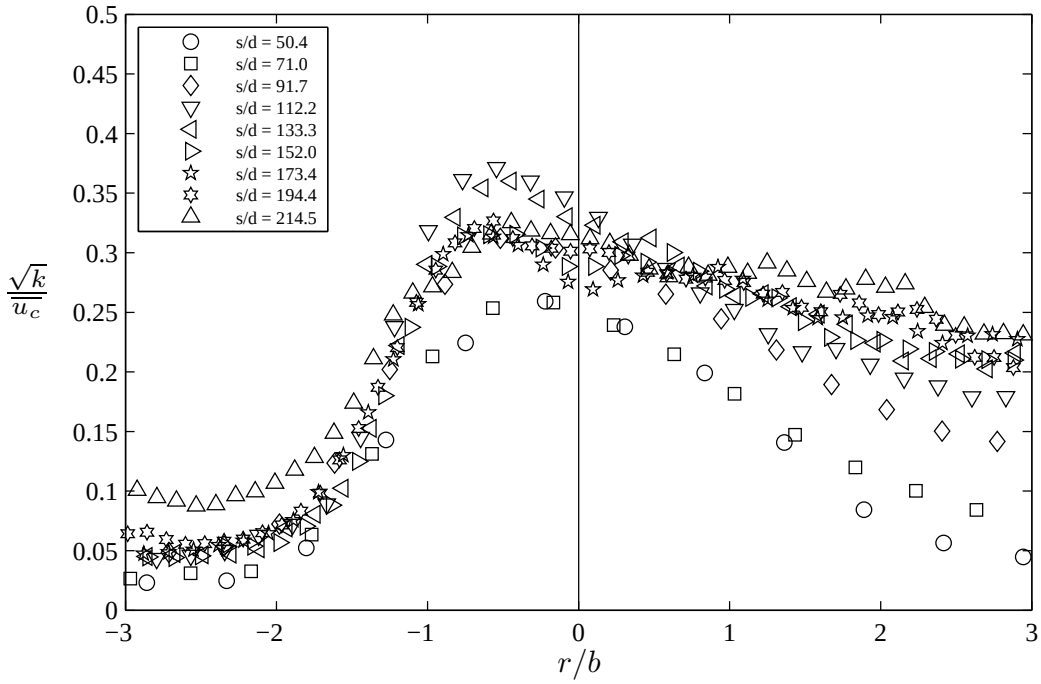

Figure 5.42 – Turbulent kinetic energy (k) profiles against path length for one 60° experiment, $F_o = 45.0$.

Mean vorticity profiles have been included in this section as they further describe the mixing processes of INBJs. Mean vorticity ($\overline{\omega}$) profiles at maximum height and the return point, which have been non-dimensionalised by path length and centreline velocity, have the same form for all Froude numbers at 60° (Figures 5.43 - 5.44). Mean vorticity profiles show positive and negative peaks of rotation on the inner and outer side of discharges at maximum height (Figure 5.43), which is expected as vorticity is a measure of the velocity gradient. The average peak non-dimensionalised $\overline{\omega}$ value is 7.11 at r/b = -0.83 on the outer side of discharges and values decrease to zero at $r/b \approx$ -2. The average peak value is -6.07 at $r/b = 0.54$ on the inner side and $\overline{\omega}$ values decrease slowly with radial distance. $\overline{\omega}$ profiles at maximum height show that the rate of eddy rotation is higher on the outer side. This could be related to the formation of large eddies on outer side of discharges near maximum height, which were observed during the physical experiments (Section 5.1.1). $\overline{\omega}$ values drop to zero on the outer side of the centreline and the negative peak occurs relatively close to the centreline. The rate of rotation remains below zero beyond $r/b = 3$ due to the detrainment of rotational fluid parcels on the inner side of discharges.

Mean vorticity profiles show only one peak of rotation on the outer side of discharges at the return point (Figure 5.44). The average peak non-dimensionalised $\overline{\omega}$ value is 6.68 at r/b = -0.79 on the outer side of discharge, while $\overline{\omega}$ values are scattered and negative on the inner side. $\overline{\omega}$ profiles on the outer side at the return point are similar to profiles at maximum height (Figure 5.43). Whereas, there is no peak in rotation on

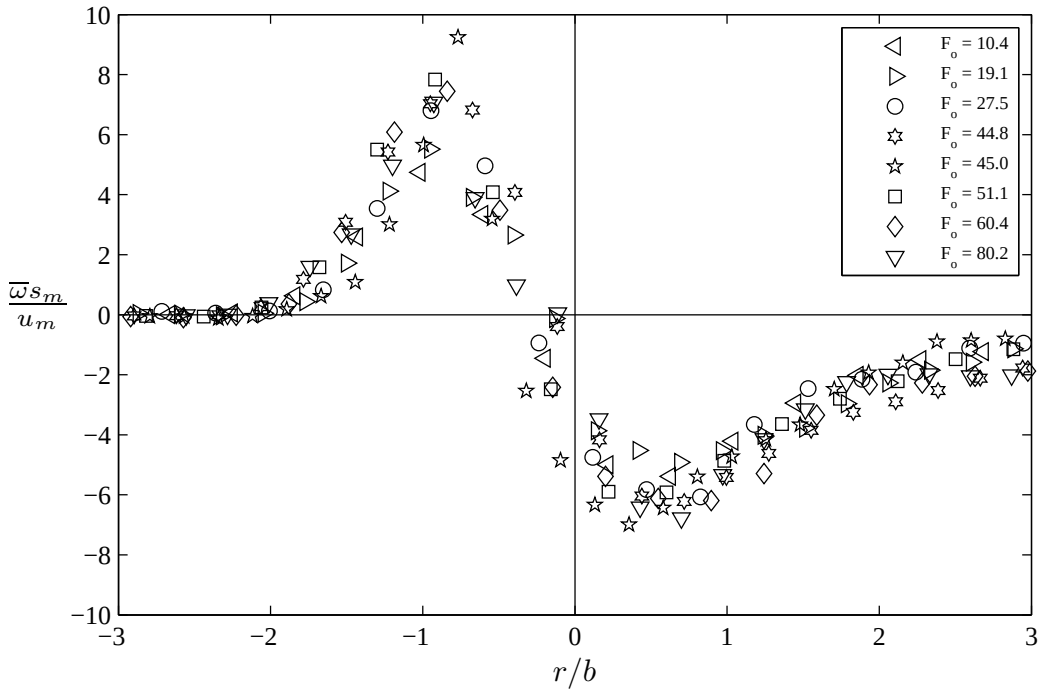

Figure 5.43 – Mean vorticity profiles at maximum height for all 60° experiments.

the inner side at the return point, with the magnitude of negative $\overline{\omega}$ values remaining roughly the same with increasing distance from the centreline. $\overline{\omega}$ values on the outer side show little dependence on the path length as values had a similar form and peak magnitude (Figure 5.45). The average peak non-dimensional $\overline{\omega}$ value is 6.47 at r/b = -0.84. $\overline{\omega}$ values on the inner side demonstrate a stronger dependence on path length. Peak negative $\overline{\omega}$ values are present near the source (s/d = 40.6, 53.7, 65.4), before $\overline{\omega}$ values transition to relatively constant values with radial distance from the centreline (s/d = 89.2, 103.2, 114.5, 126.8).

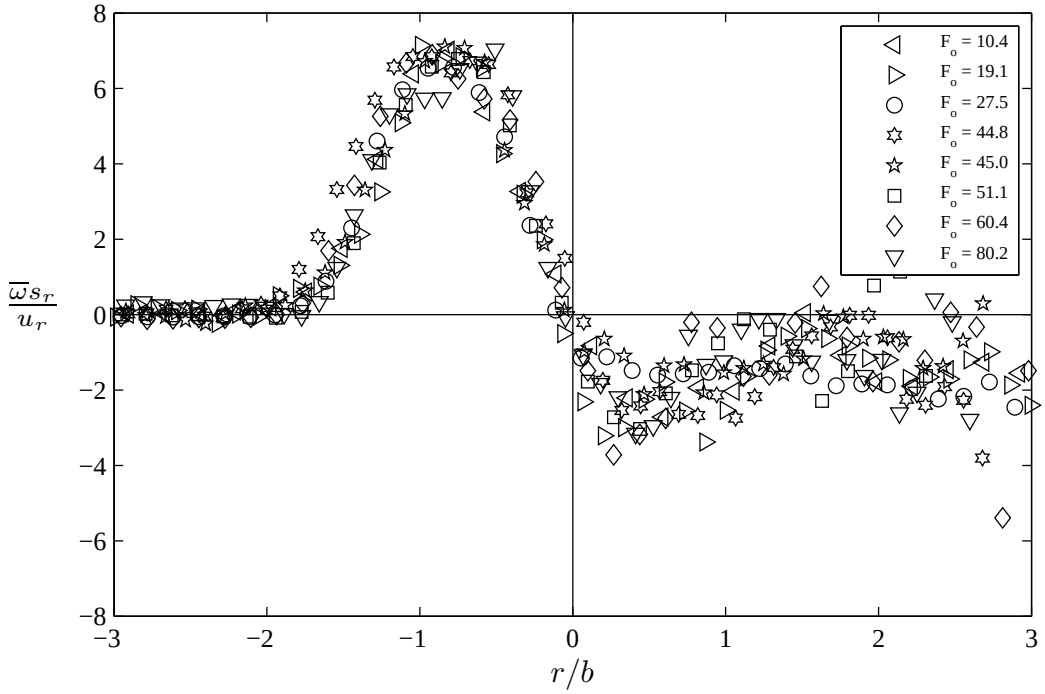

Figure 5.44 – Mean vorticity profiles at the return point for all 60° experiments.

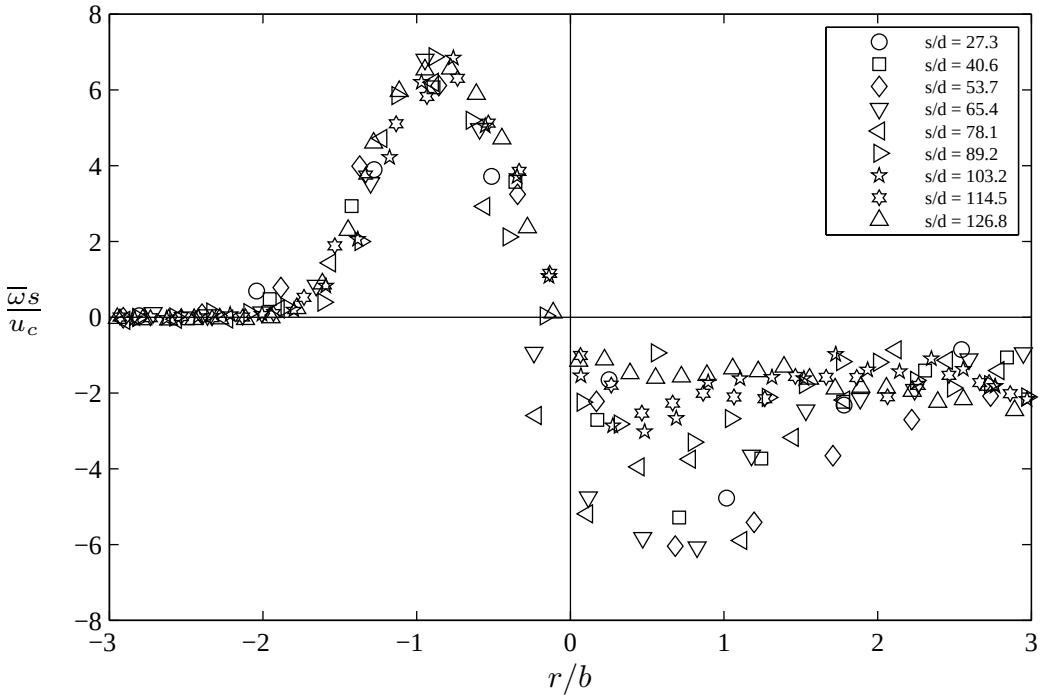

Figure 5.45 – Mean vorticity profiles against path length for one 60° experiment, $F_o = 27.5$. Maximum height at $s/d = 65.4$, return point at $s/d = 126.8$.

INBJs were defined as a two fluid scenario where one fluid is discharged at an angle through a source into stationary fluid of lower density (Section 2.4). The high velocity discharged fluid entrains stationary ambient fluid through eddies that result from shear between the two fluids. The flow fluctuates between turbulent (mixed) and non-turbulent (ambient) behaviour at a fixed location near the boundary between the two fluids as eddies move past. The flow at this fixed point is considered to be intermittent (Pope, 2000). The intermittency factor (γ) is the probability that the flow will be turbulent at any fixed location in the flow (Townsend, 1980). Intermittency was determined using the Heaviside function (H) where a value of 1 or 0 was given if a scalar quantity (ϕ) of the flow related to turbulent behaviour was above or below a threshold at any point in time, as shown in equation 5.10 (Pope, 2000). Velocity fields created using triangulation with no limit on triangle size were used to determine intermittency (more details available in Section 4.4.3).

$$\gamma = H\left(|\phi(x,t)| - \phi_{thresh}\right) \tag{5.10}$$

Instantaneous vorticity (ω) is traditionally the scalar quantity used to determine turbulent and non-turbulent behaviour as non-turbulent fluid is essentially irrotational (Pope, 2000). However, INBJs have counter rotating eddies that fluctuate across the centreline. This results in average ω values at or very close to zero along the centreline (Figures 5.43 - 5.44). Setting a minimum threshold ω was important to remove erroneous ω values as a result of noise associated with the experimental measurements. Intermittency profiles at maximum height found using instantaneous vorticity show a dip in intermittency near the centreline (Figure 5.46). The local minimum of the dip is located slightly on the outer side of the flow and the intermittency factor decreases rapidly between -2 $< r/b <$ -1. However, the intermittency factor remains high on the inner side due to detrainment of rotating fluid parcels. Intermittency profiles at the return point, found using vorticity, have a peak on the outer side of the centreline (Figure 5.47). The intermittency factor decreases rapidly on the outer side as distance from the centreline increases, while values decrease slowly on the inner side. The intermittency factor found using vorticity shows a dependence on Froude number at maximum height and the return point and generally decreases with increasing Froude number. Non-dimensionalised vorticity profiles collapse for all Froude numbers at these locations (Figures 5.43 - 5.44). However, absolute vorticity values are dependent on Froude number. A universal vorticity threshold was applied to all Froude numbers, resulting in a dependence on Froude number for intermittency factor.

The low ω values near the centreline result in low intermittency factors at maximum height (Figure 5.46) and are not representative of the highly turbulent behaviour along the centreline. Therefore, turbulent kinetic energy (k) is also used as an alternative

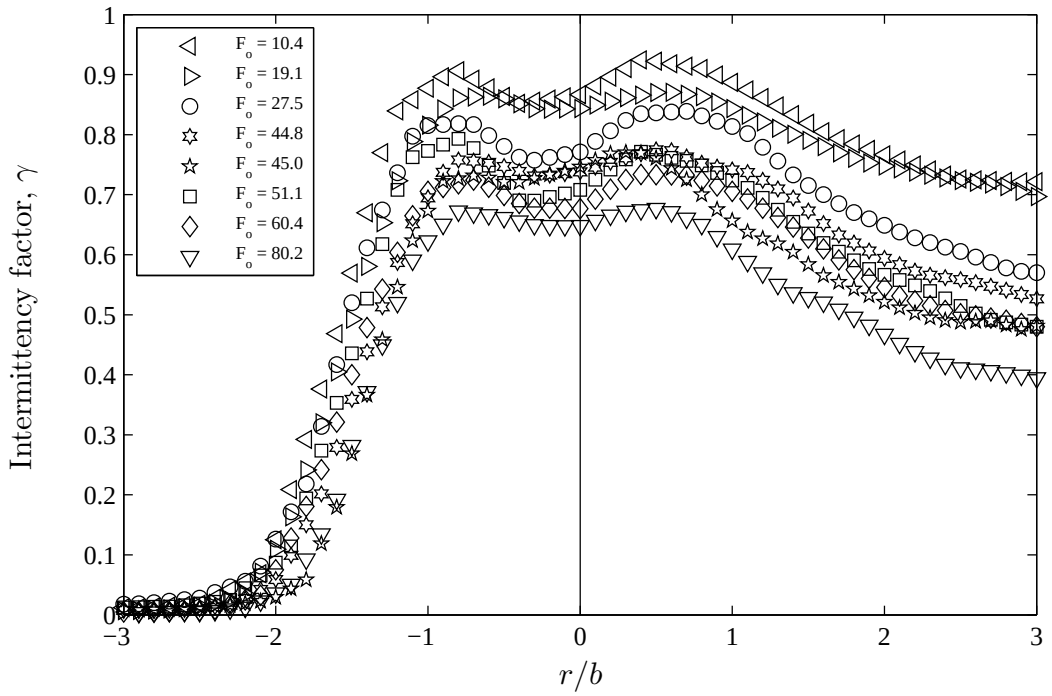

Figure 5.46 – Intermittency profiles for 60° experiments at maximum height determined using vorticity (ω), $\omega_{thresh} = 0.40$.

scalar quantity for determining turbulent fluid behaviour in the present study.

Figures 5.48 - 5.49 show profiles of the intermittency factor found using k at maximum height and the return point for all 60° experiments. Intermittency profiles are similar for all Froude numbers. γ values decrease rapidly on the outer side beyond r/b = -1 and values decrease slightly on inner side at maximum height and the return point (Figures 5.48 - 5.49). γ values remain relatively high on the outer side where axial mean velocities are close to zero ($r/b = 2$, Figure 5.35). The high intermittency factor values on the outer side is associated with sporadic incorrect tracer particle matches on the edges of images due to optical effects (Section 4.2.2.2).

Intermittency profiles for INBJs have previously been determined from concentration measurements by Lai & Lee (2012) and Oliver (2012). The intermittency factor was found to be one at maximum height close to the centreline, where the flow was always rotational. The intermittency factor profiles of Lai & Lee (2012) were roughly top-hat in shape for short path lengths near the source. The top of profiles became rounded with increasing path length. The profiles of Oliver (2012) had a dependence on Froude number for 30° discharges. The intermittency factor profiles determined from ω measurements show the flow fluctuating more between turbulent and non-turbulent behaviour at the return point than at maximum height (Figures 5.46 - 5.47). This plume like behaviour at the return point is consistent with previous findings that plumes fluctuate between turbulent and non-turbulent flow more than jets Wang & Law (2002). The intermittency factor profiles determined from measured velocity in the present study do not have a

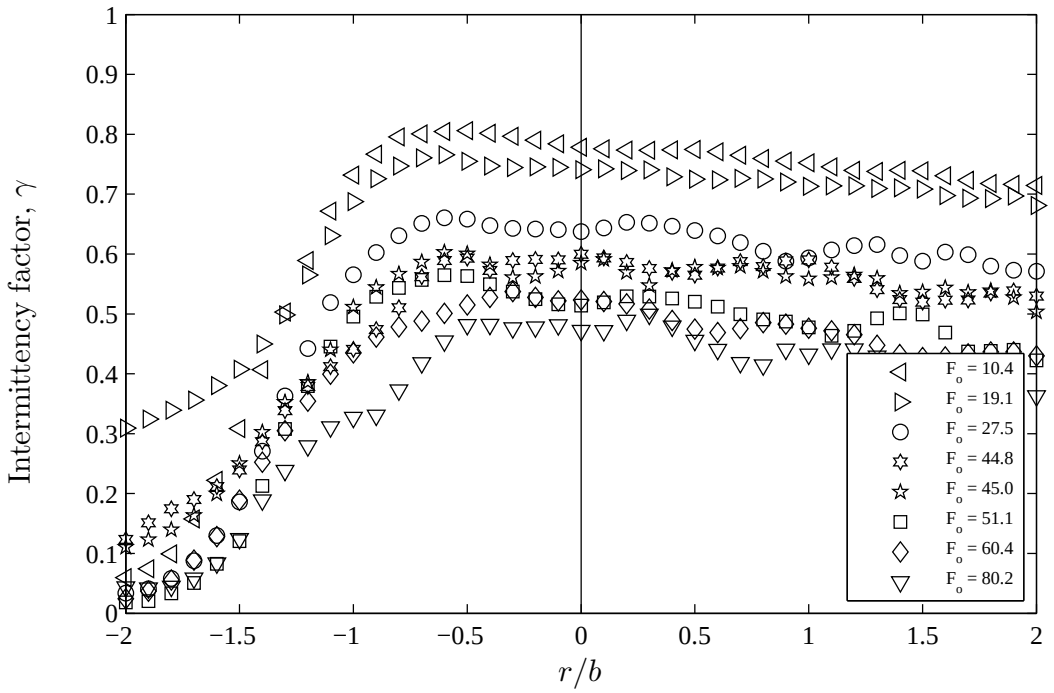

Figure 5.47 – Intermittency profiles for 60° experiments at return determined using vorticity (ω), $\omega_{thresh} = 0.40$.

value of one near the centreline for ω or k. The magnitude of the intermittency factor is always less than one as ω fluctuates above and below zero along the centreline of discharges, resulting in ω values below the threshold. The PTV experimental system was only able to capture larger eddies with a size above a threshold defined by the spatial resolution of the system. This results in lower k and ω measurements than would be present if smaller scale eddies were captured. Therefore, $\gamma > 0.9$ should probably be considered as continuous turbulence for values determined using turbulent kinetic energy.

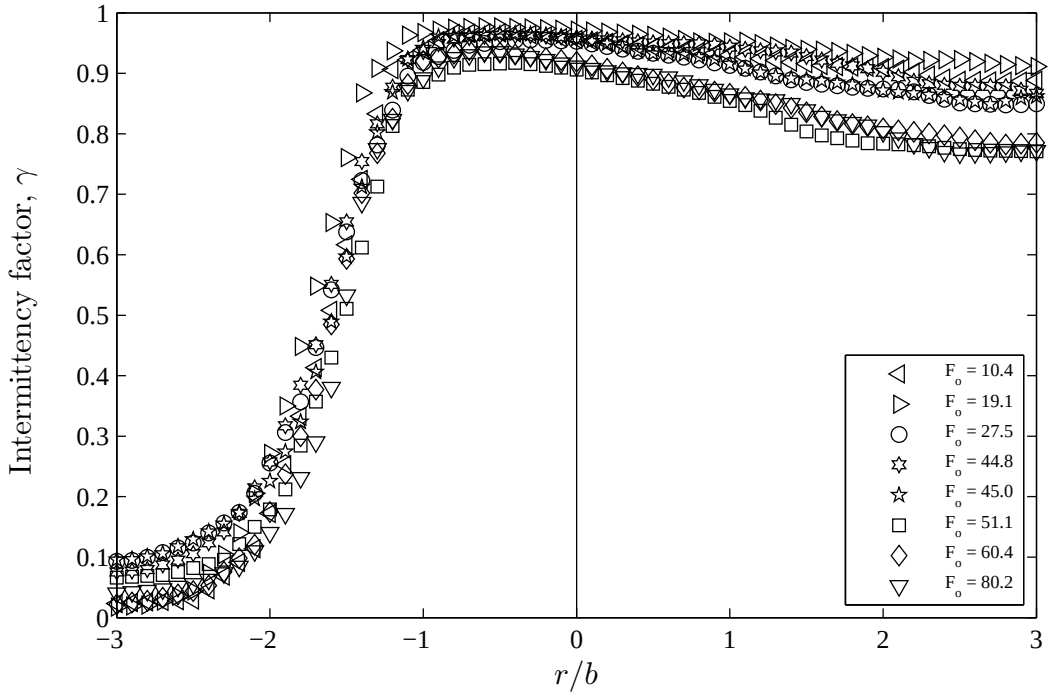

Figure 5.48 – Intermittency profiles at maximum height determined using turbulent kinetic energy (k). All 60° experiments, $k_{thresh} = 10$ mm^2/s^2.

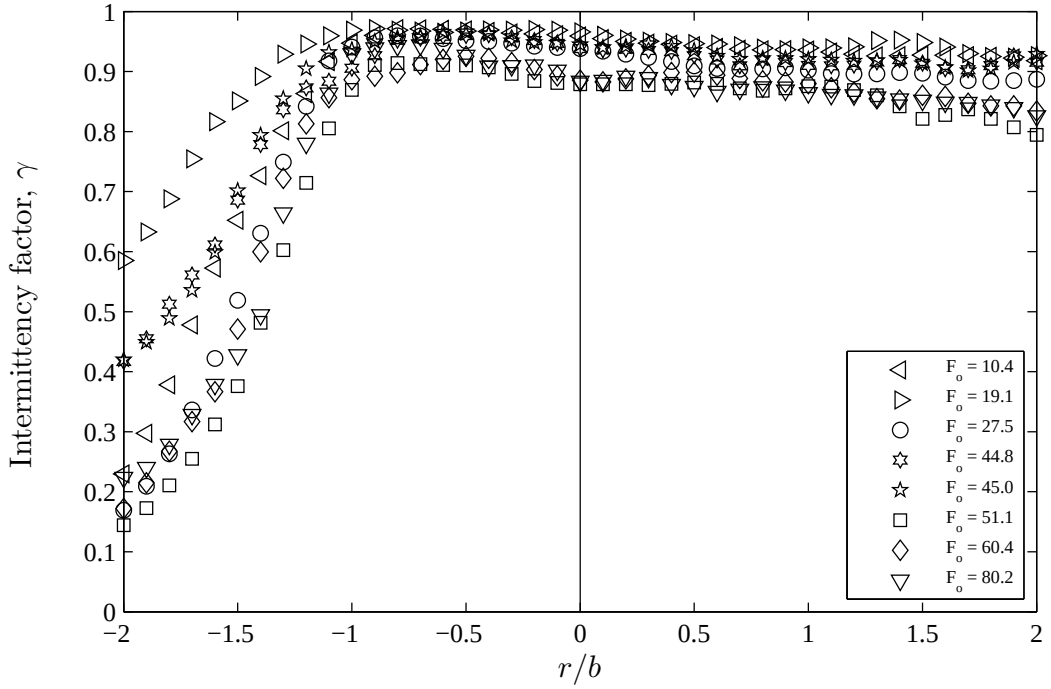

Figure 5.49 – Intermittency profiles at the return point determined using turbulent kinetic energy (k). All 60° experiments, $k_{thresh} = 10$ mm^2/s^2.

5.3.2.2 All Source Angles

The fluctuating characteristics of INBJs, across the range of source angles investigated, are compared in this section. Mean velocity parameters were found to be dependent on source angle (Table 5.5) and it follows that fluctuating characteristics would also be dependent on source angle. Section 5.3.2.1 found that the fluctuating characteristics of 60° discharges were substantially different to the fluctuating characteristics of pure jets. The fluctuating characteristics of INBJs for all source angles will be compared at maximum height and the return point. The profiles in this section were obtain by extracting profiles from each experiment at identical r/b radial increments and averaging the values across all Froude numbers.

Maximum Height

Non-dimensionalised turbulent kinetic energy profiles at maximum height are dependent on source angle, with the magnitude of k values increasing with increasing source angle (Figure 5.50). k values decrease rapidly on the outer side of discharges, while decreasing slowly with radial distance on the inner side for all source angles. The radial location of peak k values is approximately the same for all source angles (Table 5.6). The peaks of turbulent shear intensity profiles also increase for increasing source angle at maximum height (Figure 5.51). The form of turbulent shear profiles are similar for all source angles with the location of peaks at a similar radial distance on the outer side (Table 5.6). The positive peak value for 15° discharges of 0.22 is very close to the peak value of 0.20 for pure jets (Figure 4.22, Section 4.5.2; Wang & Law, 2002). Peak values for higher source angles are much higher than the peak value for pure jets. Turbulent shear intensity profiles on the outer side of 15°, 30°, and 45° discharges show the presence of a negative peak (Figure 5.51). However, the magnitudes are much lower than negative peak values for pure jets, which are identical to positive peak values. Peak values are affected by magnitude of centreline velocity between different source angles. The form of mean vorticity profiles at maximum height are also dependent on source angle (Figure 5.52). The magnitude and location of positive and negative peaks varies substantially for different source angles (Table 5.6). The magnitude of the negative peak $\overline{\omega}$ value is over double the magnitude of the positive peak $\overline{\omega}$ value for 75° discharges. This is likely due to the rapid redirection of the flow on the inner side at maximum height, increasing the measured fluid rotation.

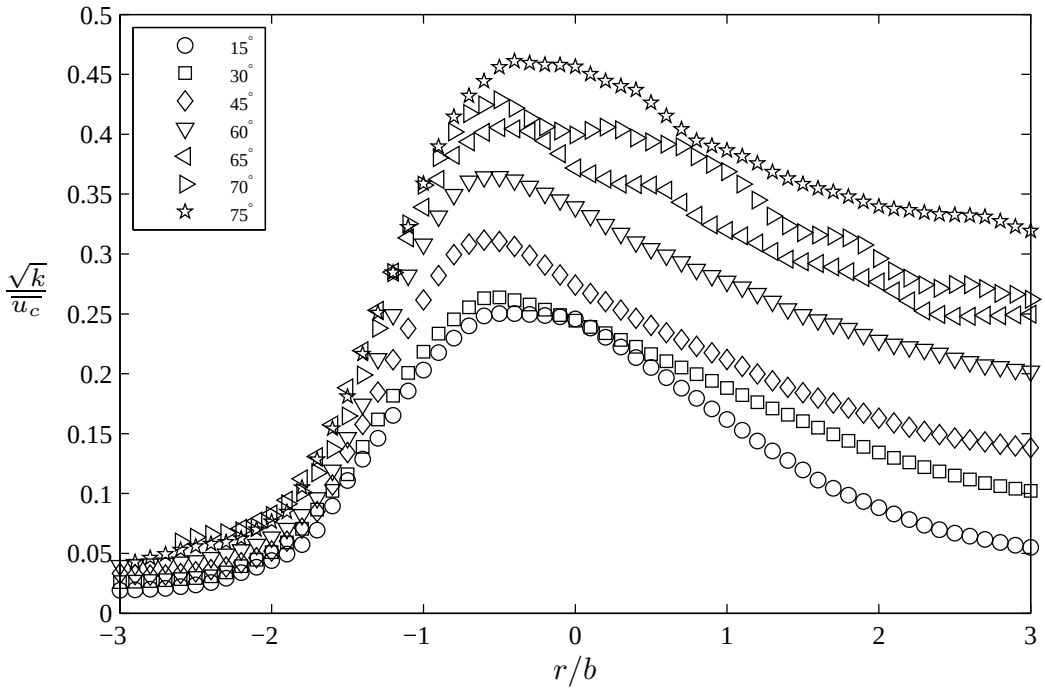

Figure 5.50 – Average turbulent kinetic energy (k) profiles at maximum height for all source angles.

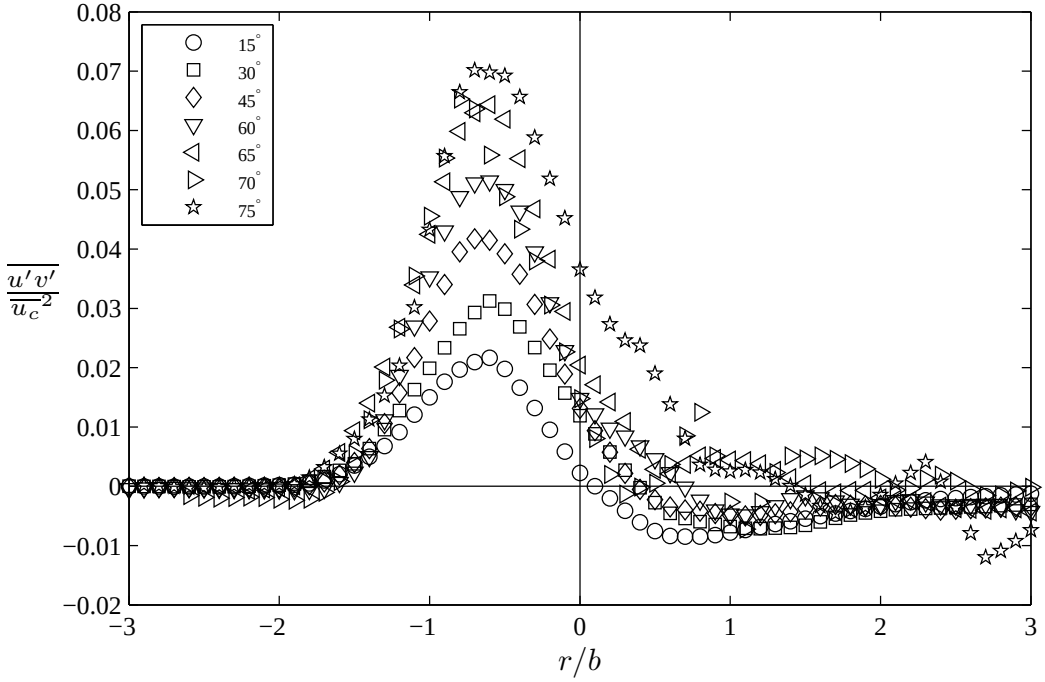

Figure 5.51 – Average turbulent shear intensity profiles at maximum height for all source angles.

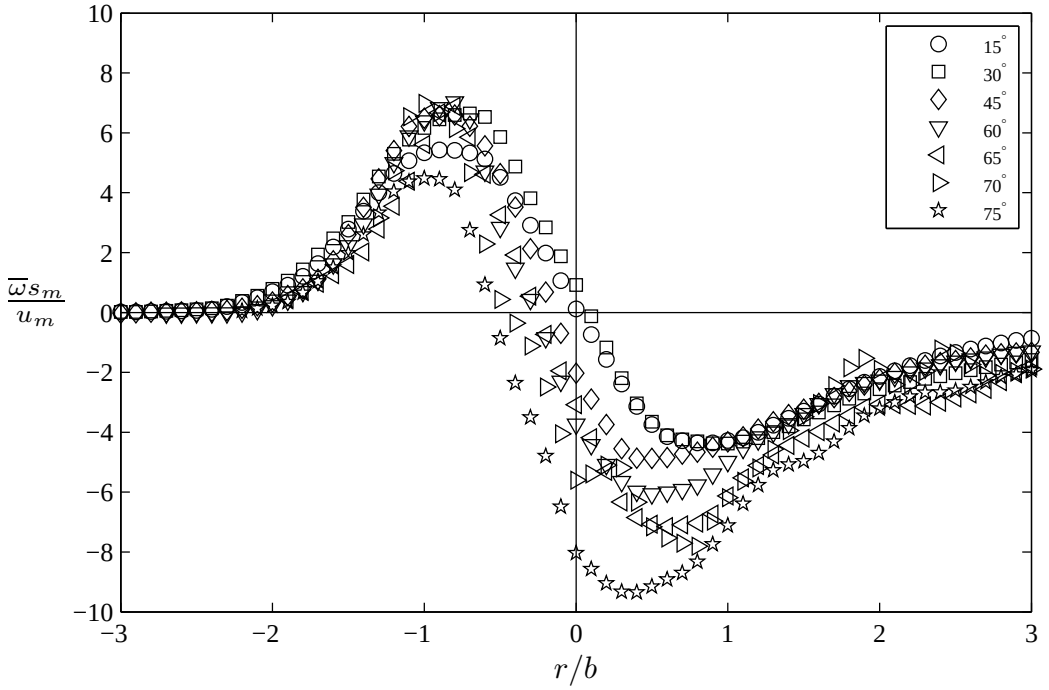

Figure 5.52 – Averaged mean vorticity profiles at maximum height for all source angles.

Table 5.6 – Peaks of fluctuating velocity parameters for different variables at maximum height. Radial locations (loc.) are specified.

θ_o	$\frac{\sqrt{k}}{u_c}$	r/b loc.	$\frac{\overline{u'v'}}{\overline{u_c}^2}$	r/b loc.	$+\frac{\omega s}{u_c}$	r/b loc.	$-\frac{\overline{\omega} s}{u_c}$	r/b loc.
15°	0.250	-0.43	0.022	-0.60	5.44	-0.84	-4.41	0.83
30°	0.264	-0.52	0.031	-0.59	6.66	-0.72	-4.40	0.96
45°	0.312	-0.57	0.042	-0.66	6.62	-0.83	-4.88	0.42
60°	0.365	-0.55	0.051	-0.57	7.11	-0.83	-6.07	0.54
65°	0.406	-0.47	0.065	-0.57	7.01	-0.84	-7.16	0.58
70°	0.429	-0.51	0.066	-0.77	7.19	-1.06	-7.80	0.80
75°	0.461	-0.39	0.070	-0.71	4.51	-0.96	-9.36	0.39

Return Point

Non-dimensionalised turbulent kinetic energy profiles at the return point (Figure 5.53) are less dependent on source angle compared to profiles at maximum height. The radial location of peak k values is again approximately the same for all source angles (Table 5.7), however there are no identifiable trends between the magnitude of peak k values and source angle. The form of turbulent shear intensity profiles is dependent on source angle with the peak values varying substantially (Figure 5.54). This is due to the different orientations of the flow relative to the fixed co-ordinate system at the return point. The correlation of horizontal and vertical velocity fluctuations are dependent on the co-ordinate system if the angle of the flow changes. The magnitude and location of positive peak $\overline{\omega}$ values is similar for all source angles (Table 5.7). A negative peak ω value is only present for the lower source angles of 15° and 30° (Figure 5.55). $\overline{\omega}$ values are relatively constant with radial distance at the return point on the outer side, with some variation on the inner side.

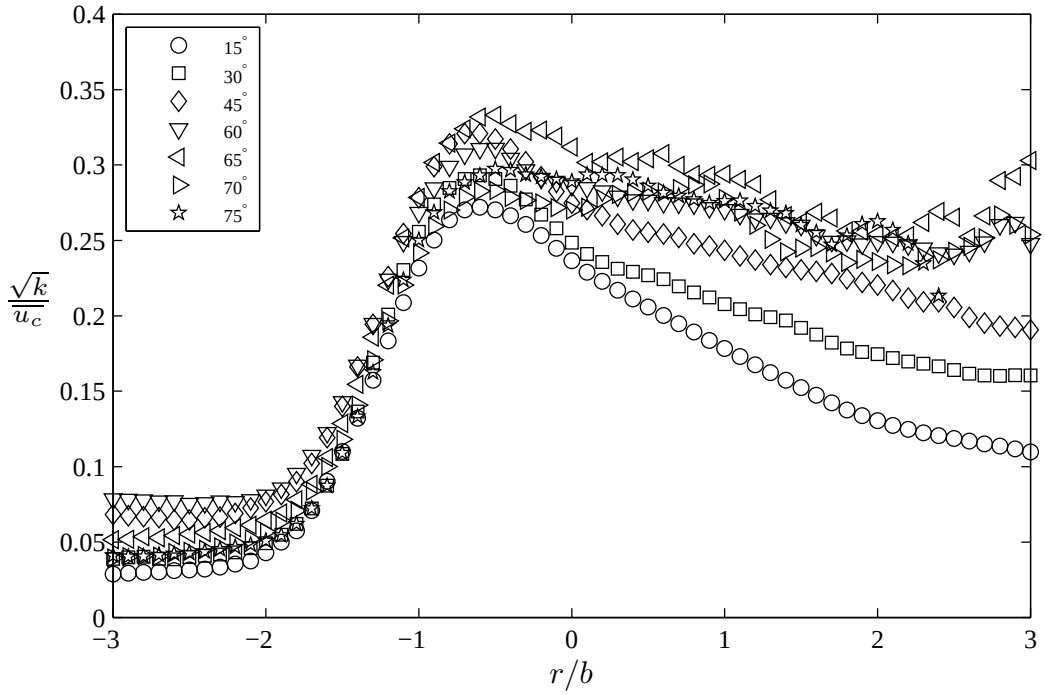

Figure 5.53 – Averaged turbulent kinetic energy (k) profiles at the return point for all source angles.

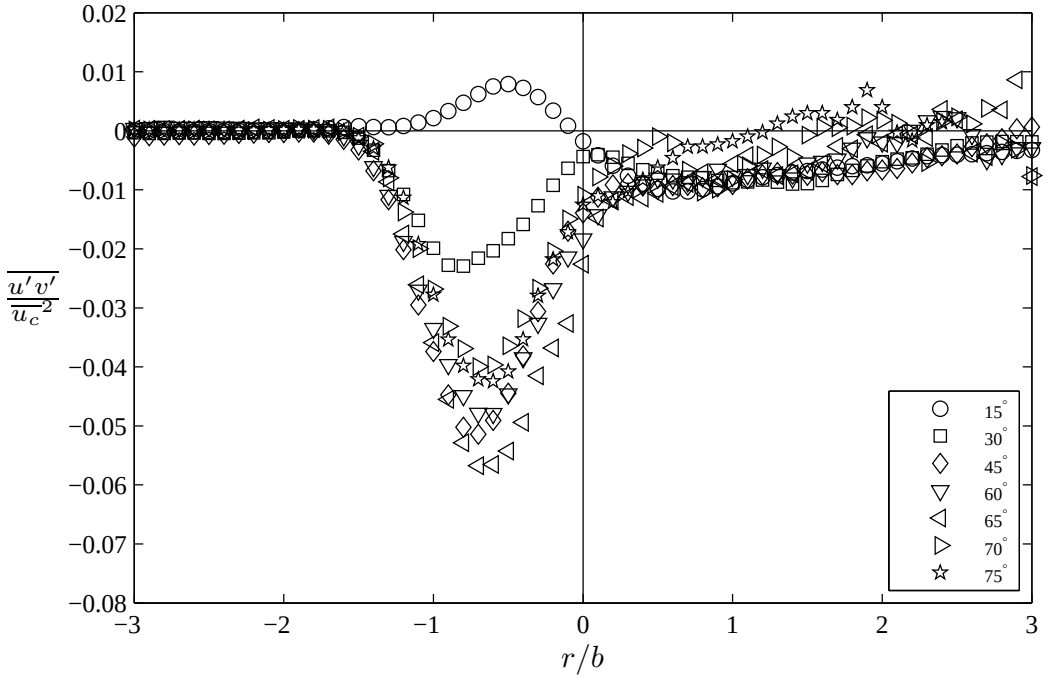

Figure 5.54 – Averaged turbulent intensity profiles at the return point for all source angles.

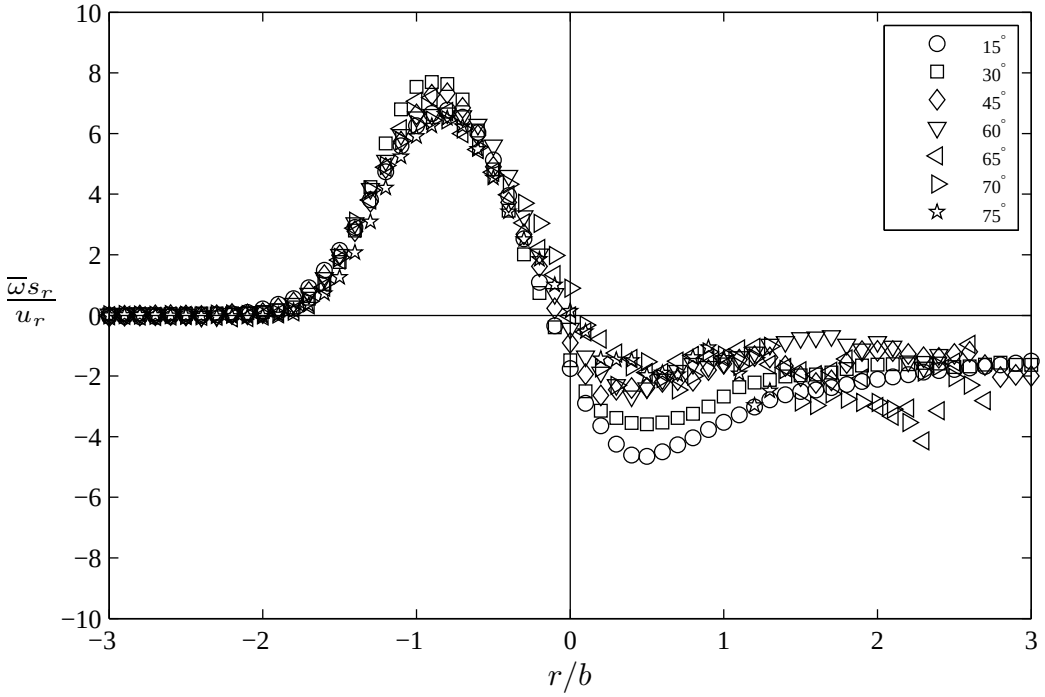

Figure 5.55 – Averaged mean vorticity profiles at the return point for all source angles.

Table 5.7 – Peaks of fluctuating velocity parameters for different variables at return point. Radial locations (loc.) are specified.

θ_o	$\frac{\sqrt{k}}{u_c}$	r/b loc.	$\frac{\overline{u'v'}}{\overline{u_c}^2}$	r/b loc.	$+\frac{\overline{\omega}s}{u_c}$	r/b loc.
15°	0.272	-0.61	0.080	-0.51	6.77	-0.81
30°	0.293	-0.61	-0.023	-0.84	7.70	-0.89
45°	0.322	-0.65	-0.052	-0.72	7.42	-0.84
60°	0.312	-0.54	-0.048	-0.64	6.68	-0.79
65°	0.334	-0.54	-0.057	-0.68	7.27	-0.93
70°	0.284	-0.52	-0.041	-0.65	6.45	-0.82
75°	0.297	-0.46	-0.043	-0.63	6.50	-0.80

5.3.2.3 Spectra

The previous fluctuating characteristics of INBJs had been extracted from velocity measurements in the time domain. Analysis of the frequency domain provides further insight into the behaviour of discharges. A Fourier transform allows for measurements in the time domain to be represented in the frequency domain (Brigham, 1988). A fast Fourier transform (FFT) was applied to absolute velocity measurements with no triangle limit (see Section 4.4.3) at locations near maximum height and near the return point of a 60° discharge. The FFT was implemented using MATLAB code with the mean removed to improve the initial bins. A Hanning window function was applied to reduce leakage or energy smearing as measurements were non-periodic. Finally, the velocity signal was zero-padded to the next power of 2 before the FFT was computed. The velocity signal was 4 minutes 21 seconds long at 32.3 Hz for the experiment analysed. The spectra of the four nearest points on the interpolated velocity field to the location of interest were averaged to produce the final frequency spectrum.

Figure 5.56 shows absolute velocity frequency spectra for three points on a vertical slice through maximum height. Spectra at all three locations are similar. The slope of the spectra is higher on the outer side of the discharge below 1 Hz, with the centreline and inner side slopes approximately equal. The peaks of spectral power are not well defined at all three locations, therefore the following analysis of spectral peaks should be viewed with some caution. Spectral power peaks between 0.1 - 0.2 Hz (5 - 10 seconds), which is similar to the peak power range of 0.1 - 0.5 Hz found by Oliver (2012) for concentration spectra at maximum height. This frequency range was related to shear induced large eddy formation (Oliver, 2012). Spectral power remains high at lower frequencies with a second peak present at all three locations between 0.03 - 0.05 Hz (20 - 33 seconds). These larger time scale events correspond to large scale eddies observed forming intermittently near maximum height for 60° discharges (Section 5.1.1).

Papanicolaou & List (1988) found that spectral power of axial and radial velocity of jets and plumes followed a -5/3 power decay. Oliver (2012) also found the concentration power spectrum closely followed the -5/3 power decay at maximum height of INBJs. The absolute velocity spectrum decays at a slower rate than the -5/3 power decay at all locations near maximum height (Figure 5.56).

Absolute velocity frequency spectra are similar for three locations on a horizontal slice through the return point (Figure 5.57). Spectral power peaks between 0.047 - 0.053 Hz (19 - 21 seconds) at all three locations. However, the slope of the spectra is again higher on the outside of discharges above 1 Hz, compared to the other locations. Spectral power again remains high for lower frequencies. The decay in spectral power is similar to the -5/3 power decay reported by previous studies (Papanicolaou & List, 1988; Oliver, 2012) for frequencies between the peak power and 2 Hz (0.5 seconds). Spectral power levels off for higher frequencies to a slower rate of decay. A similar slowing of the power decay was shown by Oliver (2012) for frequencies above 5 Hz near the return point. There is relatively high noise in all absolute velocity spectra above 1 Hz near maximum height (Figure 5.56) and the return point (Figure 5.57). Noise was substantially reduced by averaging spectra from 4 points surrounding the locations of interest, with Oliver (2012) averaging spectra from 29 concentration points resulting in reduced noise. The PTV experimental system utilised in the present study was not reliable at higher frequencies as shown by the noise in the spectra. This could be due to the intermittent nature of particle matching and limited range of scales that were captured by the system.

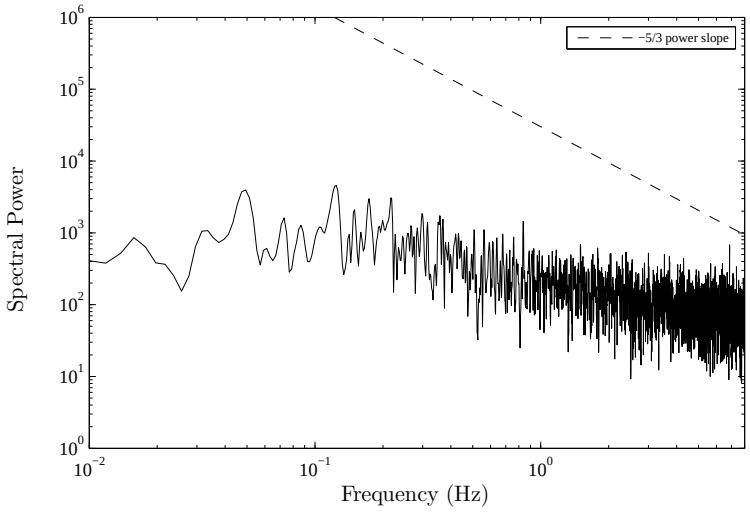

(a) Centreline; x_m, z_m

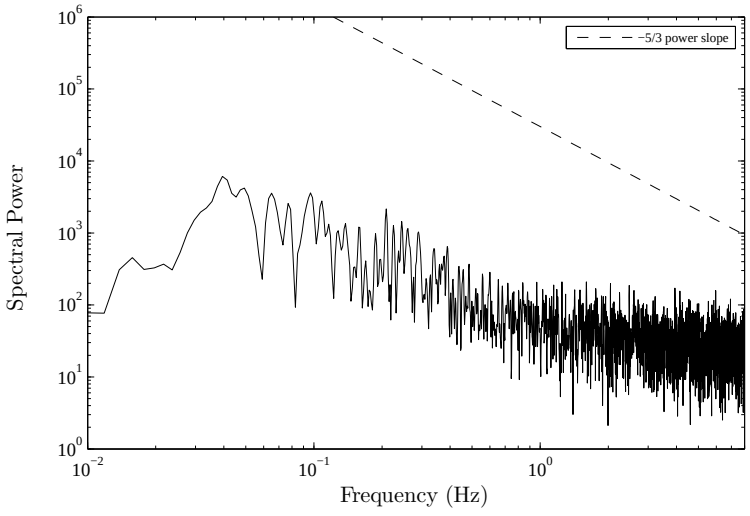

(b) Outer side; x_m, $z_m + b$ (at x_m)

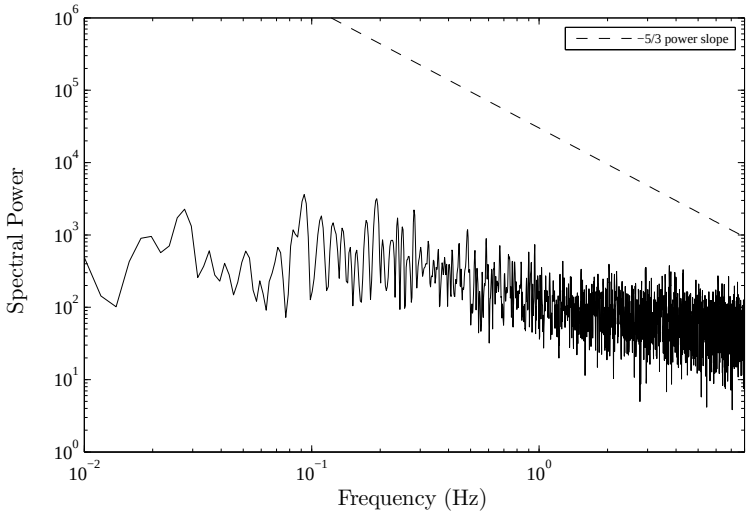

(c) Inner side; x_m,z_m - b (at x_m)

Figure 5.56 – Average of four spectra at three locations on a vertical slice through maximum height of one 60° experiment, $F_o = 27.5$.

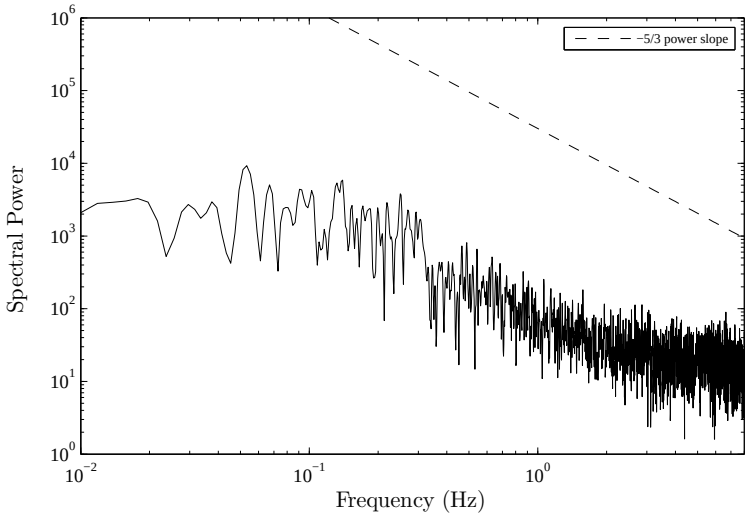

(a) Centreline; x_r, $z = 0$

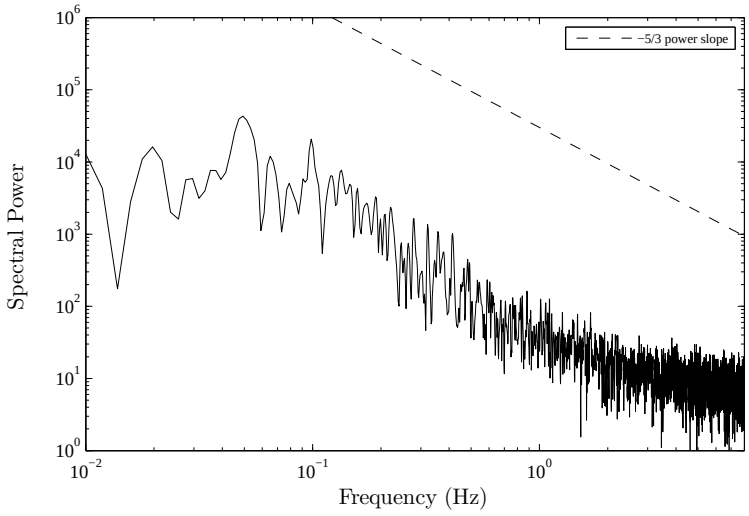

(b) Outer side; $x_r + b$ (at x_r), $z = 0$

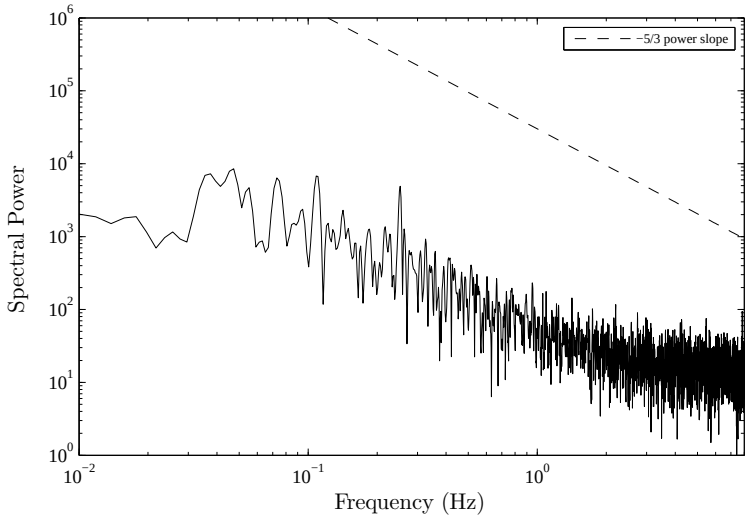

(c) Inner side; x_r - b (at x_r), $z = 0$

Figure 5.57 – Average of four spectra at three locations on a horizontal slice through the return point of one 60° experiment, $F_o = 27.5$.

5.3.2.4 Summary

Turbulent kinetic energy, turbulent shear intensity, and mean vorticity were used to investigate the mixing characteristics of INBJs. Measured quantities were found to be similar for all Froude numbers at the source angle of 60° at maximum height (Figures 5.38, 5.40, 5.43) and the return point (Figures 5.39, 5.41, 5.44). Turbulent kinetic energy profiles had a similar form and magnitude for the full path length (Figure 5.42), but mean vorticity varied substantially with path length (Figure 5.45). The structure of mixing disintegrated on the inner side due to detrainment caused by the unstable density stratification. $\overline{\omega}$ profiles at maximum height showed counter rotating flow on either side of the centreline (Figure 5.43), with rotational fluid moving further away from the centreline on the inner side due to detrainment. The rotation of fluid on the inner side became relatively constant with radial distance at the return point (Figure 5.43).

Instantaneous vorticity and turbulent kinetic energy were used to determine intermittency factor profiles at maximum height (Figures 5.46 and 5.48) and the return point (Figures 5.47 and 5.49). Vorticity intermittency factor profiles dipped near the centreline due to fluctuations around zero. Intermittency factors using both parameters decreased rapidly on the outer side of discharges, similar to the behaviour of pure jets (Pope, 2000). Intermittency factors decreased slightly with radial distance from the centreline on the inner side due to detrained fluid still being turbulent as it moved downwards, out of the flow for 60° discharges.

Fluctuating characteristics were more dependent on source angle at maximum height compared to the return point. Turbulent kinetic energy and mean vorticity profiles showed a strong dependence on source angle at maximum height (Figures 5.50 - 5.52), whereas the form and magnitude of turbulent kinetic energy and mean vorticity profiles were similar at the return point for the range of source angles (Figures 5.53 - 5.55). These fluctuating characteristics were similar at the return point for all source angles as the flow was fully developed and moving in a similar direction. Flow behaviour at maximum height was more variable between different source angles due to the redirection of the flow and detrainment. Detrainment was dependent on the relative sizes of inertia and buoyancy and therefore varied substantially between different source angles at maximum height.

Turbulent shear intensity profiles had a strong dependence on source angle at both maximum height and the return point (Figures 5.51 - 5.54). $\overline{\omega}$ profiles at maximum height illustrate the complex behaviour of INBJs for different source angles (Figure 5.52). Rotation on the inner side increased due to the redirection of the flow at higher source angles ($\theta_o \geq 70°$, Table 5.6). At lower source angles ($\theta_o \leq 45°$), rotation was suppressed by the unstable density stratification as fluid was detrained from the main

flow. The magnitude of positive and negative peaks of $\overline{\omega}$ profiles were similar for 60° and 65° discharges, indicating a balance between these opposing mechanisms at these source angles.

Spectral power was found to peak between 0.1 - 0.2 Hz (5 - 10 seconds) at locations on a vertical slice through maximum height (Figure 5.56), where as spectral power peaked between 0.047 - 0.053 Hz (19 - 21 seconds) at three locations on a horizontal slice through the return point (Figure 5.57). The increased time of peak power indicates the development of large scale eddy structures between maximum height and the return point, which were visually observed during experiments (Section 5.1.1). The outer side had a higher rate of power decay than the inner side for frequencies ≤ 1 Hz at maximum height and the return point (Figure 5.56 - 5.57). This resulted in the peak spectral power being higher on the outer side.

The fluctuating characteristics have shown that the structure of mixing between the inner and outer sides was substantially different. The stabilising density gradient on the outer side results in mixing behaviour that is similar to jets at maximum height and to plumes at the return point. The destabilising density gradient on the inner side results in the collapsing of the mixing structure with distance from the source, with turbulent intensity profiles becoming more distorted.

[Intentionally left blank]

Chapter 6

Boundary Interaction

6.1 Introduction

The interaction of inclined negatively buoyant jets (INBJ) with a lower boundary is investigated in this chapter. Particle tracking velocimetry (PTV) experiments were conducted at source angles of 30°, 45°, and 60° for a range of source heights above the boundary. The majority of previous experimental studies for INBJs have been conducted with a lower boundary influencing observed flow behaviour in the vicinity of the return point (Zeitoun, 1970; Roberts *et al.*, 1997; Nemlioglu & Roberts, 2006; Papakonstantis *et al.*, 2011b; Lai & Lee, 2012). However, the focus has been on the behaviour of the discharges themselves without specifically considering the effect of the boundary on the flow (Papakonstantis & Christodoulou, 2010). Experimentally measured dilution at the return point or at the impingement point are often compared to integral model predictions that do not consider the influence of the boundary (Palomar *et al.*, 2012b). The considerable scatter amongst experimentally measured dilution (Figures 3.3 - 3.4, Section 3.4) makes comparison with integral model predictions difficult. Some of the scatter between different experimentally measured dilution values at the return point could be due to differing lower boundary conditions. The lower boundary conditions for each study were outlined in section 2.4, if specified by the authors.

A generalised characterisation of an INBJ with the presence of a lower boundary is provided in figure 6.1. The redirection of the flow by the lower boundary and development of a radially spreading layer is shown by the shape of the inside and outside edge boundaries. Additional mixing and dilution has been measured in the radially spreading layer that occurs after impingement (Roberts *et al.*, 1997; Shao & Law, 2010). The effect of discharges impinging the lower boundary at arbitrary angles is not fully understood (Papakonstantis & Christodoulou, 2010). Additionally, outfall diffuser design could be made more economical if the mixing mechanisms in the radially spreading layer could be incorporated into the design (Ulasir, 2001).

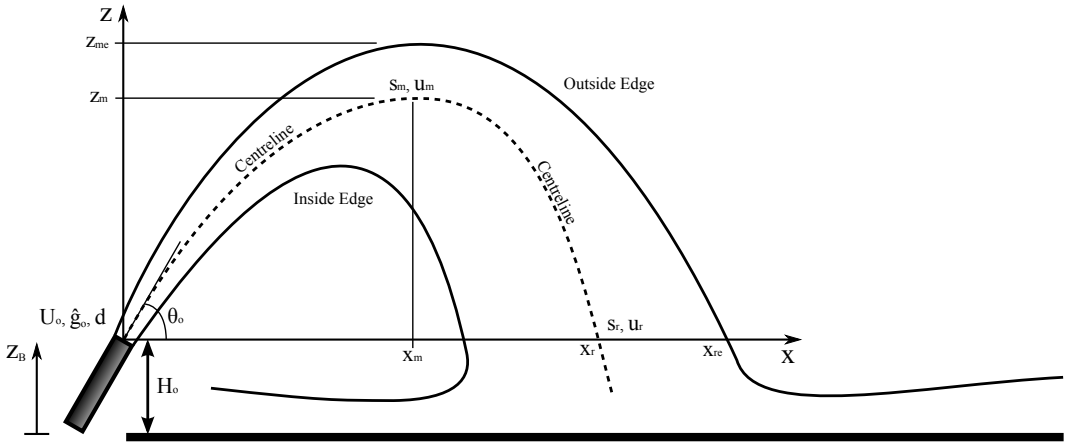

Figure 6.1 – Important parameters of INBJ trajectories with a horizontal boundary depicted as a heavy black line in this diagram: Vertical distance above lower boundary (z_B), vertical distance of source above lower boundary (H_o), horizontal and vertical distance to maximum centreline height (x_m, z_m), vertical distance to the outside edge (z_{me}), horizontal distance to return point and to outside edge (x_r, x_{re}), centreline path length to maximum height and return point (s_m, s_r), mean centreline velocity at maximum height and return point (u_m, u_r).

6.2 Previous Research

A limited number of previous experimental studies have specifically considered lower boundary influences on the behaviour of INBJs. However, more extensive research has been done on the impingement of positively buoyant municipal waste discharges on the free surface of the ocean. These axisymmetric discharges impinge the free surfaces at effectively perpendicular angles and this scenario is much simpler than the oblique impingement of asymmetric INBJs with a lower boundary. The free surface interaction of positively buoyant jets is divided into three distinct regions (Figure 6.2). The submerged buoyant jet zone behaves like a free jet discharged into an unbounded environment. The flow is abruptly redirected into a horizontally spreading layer in the impingement zone and additional mixing occurs when the flow becomes a wall jet in the near field mixing zone on the free surface. The impingement of INBJs can be assumed to have similarly defined regions of no boundary influence, flow redirection, and radial spreading.

Beltaos & Rajaratnam (1974) experimentally investigated the perpendicular impingement of pure jets with a solid boundary. Velocity measurements were taken of air jets with a hot-wire anemometer. The presence of a boundary influenced the centerline velocity decay and spread rate at a distance of 0.14H above the boundary, where H was the distance between the source and boundary. Non-dimensionalised mean velocity profiles were found to be self-similar until 0.07H in a subsequent study by Rajaratnam *et al.* (2010). Turbulent shear stresses were found to decrease rapidly close to the boundary, within 0.04H, when normalised by the values for shear stress at 0.14H (Rajaratnam *et al.*, 2010). These studies indicate that the presence of a boundary

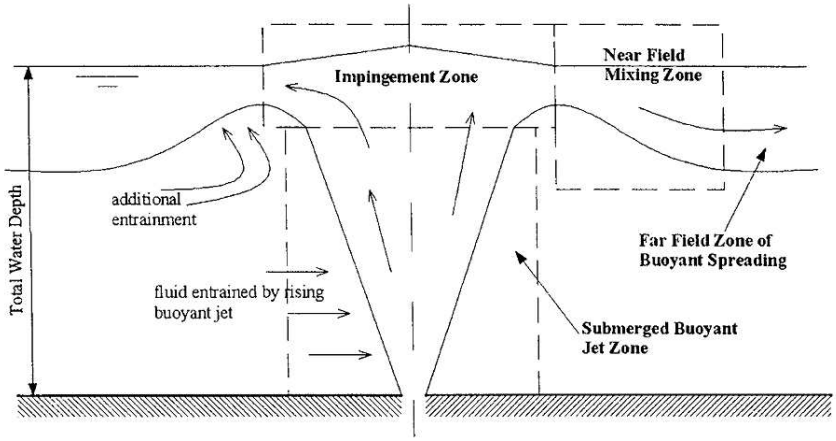

Figure 6.2 – "Definition sketch of submerged round buoyant jet impinging on a free surface." (Ulasir & Wright, 2003, Figure 1).

substantially influences flow behaviour for pure jets.

The radially spreading layer along the boundary experiences additional mixing and dilution (Wright *et al.*, 1991; Roberts & Sternau, 1997; MacLatchy, 1999) before buoyancy effects eventually stabilise vertical mixing and the spreading layer is confined to the boundary (Ulasir, 2001). There have been different formulations used to describe the additional mixing, which are related to the different modelling approaches and downstream controls applied. Wilkinson & Wood (1971) proposed a density jump, analogous to a hydraulic jump, between the two layer system of the radially spreading layer and the bounding ambient fluid. Alternatively, Wilkinson & Wood also found the presence of a weir downstream control created a roller region at the interface between the two layers, in which no entrainment was observed. Removing the weir, and therefore any downstream control, resulted in the maximum amount of entrainment and mixing. Without the presence of a downstream control, radially spreading flows have entrainment mechanisms similar to wall jets (Wilkinson & Wood, 1971).

Ulasir & Wright (2003) investigated the impingement of positively buoyant jets with the free surface by conducting physical experiments with negatively buoyant jets impinging a raised circular solid lower boundary. Point concentration measurements were taken with a conductivity probe and velocity measurements were taken with a MicroADV. Two downstream flow conditions were compared. The first allowed the radially spreading flow to fall over the edge of the boundary, creating a critical flow condition at the edge. The second was to place a weir on the edge of the boundary. The presence of the weir reduced the dilution achieved in the radially spreading layer by restricting the length over which entrainment occurred, similar to the roller region of Wilkinson & Wood (1971). The study of Ulasir & Wright (2003) also compared two different diameters of the circular lower boundary, 150 cm and 300 cm. The average flow properties did not show a dependence on the diameter of circular lower boundary

used.

The impingement of INBJs with a lower boundary was described by Jirka (2008) as *"a complex three-dimensional process, with forward, lateral, and partially reverse spreading, until a density current is formed that propagates downslope"*. Roberts *et al.* (1997) was the first study to quantify the additional mixing that occurred in the radial spreading layer that moved away from the source for 60° INBJ discharges. Roberts *et al.* (1997) described the radially spreading layer as a density current. Concentration measurements were taken along the boundary with a microconductivity probe. Dilution was lowest at the impingement point, with higher dilutions measured along the boundary for the inner and outer sides of the impinging discharge. Concentration fluctuations were higher on inner and outer sides of the discharge in the impingement region, where the flow was redirected, compared to the centre of the discharge. Concentration fluctuations in the density current decreased with distance away from the impingement point as dilution increased. Dilution increased by about 60 % at the location where concentration fluctuations in the density current collapsed ($x/(F_o d) = 9.0$), compared to dilution at the impingement point location ($x/(F_o d) = 2.4$). The density current in the experiments of Roberts *et al.* (1997) was essentially a two-dimensional flow due to the restricted width of the experimental flume (Papakonstantis & Christodoulou, 2010).

The experimental study of Shao & Law (2010) investigated the influence of the lower boundary on the INBJs at source angles of 30° and 45° using a combined PIV and LIF experimental system. The focus of the study was on the Coanda effect of the lower boundary causing reduced entrainment on the inner side of discharges near the source. Non-dimensional source height ($H_o/l_M \propto H_o/(F_o d)$) was found to be the parameter that significantly changed the measured geometric parameters and dilution for 30° discharges. Non-dimensional source height was found to have no significant influence on measurement parameters for the higher source angle of 45°. Source height is relatively small compared to the full geometric size of discharges and Shao & Law (2010) proposed that the differences between measurements at the return point and the impingement point may not be significant. Spread determined from concentration and velocity measurements reduced on the inner side of discharges due to the presence of the boundary for both angles. Mean concentration and velocity profiles transitioned to a wall jet pattern after the impingement region. Dilution was also found to increase with distance from the source in the radially spreading layer, consistent with the findings of Roberts *et al.* (1997).

Papakonstantis & Christodoulou (2010) investigated the time-dependent spreading of the propagating radially spreading layer developed after the impingement zone. Coloured dye flow visualisation experiments were conducted at the source angles of 45°, 60°, 75°, and 85°. A reference grid was used to determine the geometric location of the outer boundary for the radially spreading layer. The flow across the lower boundary

was recorded from above with the camera pointing directly downwards. The ambient fluid was stationary and the lower boundary was horizontal. The source height was approximately 10 cm above the lower boundary, however this height was not varied or considered to be a variable that could influence flow behaviour. The shape of the outer boundary of the radially spreading layer was roughly circular for all source angles studied. This was likely due to the detrainment of dense fluid on the inner side of discharges contributing to boundary flow back towards the source. The radial distance of the propagating radially spreading layer from the impingement point (R) was found to correlate with time (t) by the relationship, $R \sim t^{1/2}$. This relationship shows a balance between buoyancy and viscous drag forces for the radially spreading layer. Therefore, viscous drag forces are much larger than inertia due to the dominance of lower boundary shearing. The radial spreading of the boundary flow was found to be independent of source angle when the radial location was non-dimensionalised by initial or local discharge parameters. However, the radial distance, non-dimensionalised by the initial distance conditions, was found to have a dependence on Froude number at low values ($F_o \leq 20$). A finding in a subsequent study, by the same research group, for the impingement of INBJs with a sloping lower boundary was presented in Christodoulou *et al.* (2011). The identical experimental system was used and the boundary sloped downwards away from the source with an angle of 10°. The propagating outer boundary of the radially spreading layer was no longer found to be roughly circular, rather it conformed to the shape of two semi-ellipses.

An experimental study was conducted by Shao & Law (2011) on the impingement of negatively buoyant jets discharged horizontally above a lower boundary. The findings from their study are relevant to the present study as these horizontally discharged flows impinge the boundary at oblique angles. A combined PIV and LIF experimental system was used to measure concentration and velocity. The concentration and velocity centrelines coincided before impingement, however the concentration centreline descended sooner, with a higher gradient, in the impingement region. Shao & Law (2011) reasoned that the difference in centreline behaviour was due to different boundary conditions for concentration and velocity. Concentration has a no-flux boundary condition, while velocity has a no-slip boundary condition. Downstream of the impingement region, concentration and velocity profiles were self-similar and had a form similar to wall jets. Concentration profiles along the boundary compared well with a half-Gaussian profile, with the maximum local concentration being located close to the boundary. The location of local maximum velocity was elevated above the boundary due to the no-slip boundary condition. The gradients of velocity profiles were much higher between the maximum local velocity and the boundary, when compared to the gradients above the maximum velocity.

The previous research into the effects of a lower boundary on the behaviour of

INBJs is limited. Experimental and analytical research into the simpler impingement of positively buoyant jets with a free surface is more extensive. The studies of Beltaos & Rajaratnam (1974) and Rajaratnam *et al.* (2010) found the presence of a boundary to effect the mean and fluctuating behaviour of impinging jets beyond the region where flow redirection occurs. The downstream boundary conditions influenced the entrainment achieved by the radially spreading layer along the boundary. Boundary impingement studies for INBJs have found additional dilution occurs after impingement (Roberts *et al.*, 1997; Shao & Law, 2010). However, no previous concentration studies have directly compared flow behaviour with and without the presence of the boundary. Therefore, the extent of boundary influence is unknown. This makes the interpretation of highly scattered dilution measurements of previous INBJ studies difficult as there was a wide variation in lower boundary conditions.

6.3 Experimental Method

The purpose of this set of experiments is to provide detailed velocity field information from INBJs with a lower boundary influencing observed flow behaviour. The effect of the lower boundary is quantified by directly comparing results of INBJ experiments without a lower boundary influence (Chapter 5). Six physical experiments were conducted for each source angle at three groups of different non-dimensionalised source heights. Two experiments were conducted with similar non-dimensional source heights at different initial Froude numbers. Table C.1 (Appendix C) contains the important initial conditions for each experiment in this chapter.

A raised platform was present in the experimental configuration (Figure 4.2, Section 4.2). The circular raised platform had a diameter of 1040 mm and was elevated approximately 600 mm above the bottom of the experimental tank, but remained in the view of the camera. The diameter of the platform was limited by the size of the experimental tank. The distance between the edge of the platform and the side of the tank was a minimum of 100 mm. The height of the camera capturing the movement of illuminated tracer particles was above the height of the platform. This ensured that the radially spreading layer could be observed by the camera. The raised platform allowed for longer recording times as the radial spreading layer produced after impingement did not interact with the side boundaries of the experimental tank in the observation region. The negatively buoyant fluid in the spreading layer fell over the edge of the lower boundary to the bottom of the experimental tank. The raised platform was circular in shape to allow the radially spreading layer to developed equally in all directions (Papakonstantis & Christodoulou, 2010). The diameter of the platform was too small to allow for the collapse of turbulent fluctuations (Roberts *et al.*, 1997). A critical downstream flow condition was created near the edge of the raised platform. The

implications of the raised platform design on experimental results will be discussed further in section 6.4.

The experimental system and processes described in chapter 4 were also used for the experiments in this chapter. The recording of each experiment began once the flow had reached a visually determined steady state. This is after the initial propagating radially spreading layer studied by Papakonstantis & Christodoulou (2010) had fallen over the edge of the platform. The time to reach steady state flow conditions was longer for experiments with a lower boundary influencing flow behaviour. This is due to the increased geometric scale of experiments with a boundary. The view of the lower boundary in images was excluded from the PTV analysis in Streams (Nokes, 2012) as laser light reflected off the Perspex material.

6.4 Experimental Results

Experimental results from the INBJ PTV experiments conducted with a lower boundary present will be investigated in the following section with the source angle of 45° used to illustrate the influence of the boundary. Results for the source angles of 30° and 60° will be included where required, with section C.2 (Appendix C) containing the additional figures of 30° and 60° discharges. The mean absolute velocity field determined by the PTV experimental system shows the redirection of the flow by the presence of the lower boundary (Figure 6.3). Absolute velocity tends toward zero near the boundary, with the majority of flow redirected away from the source. Geometric and velocity parameters were extracted from the mean velocity field for each experiment. The source height (H_o) is non-dimensionalised by the source diameter (d) and the initial Froude number (F_o), which is consistent with the non-dimensionalisation of source height by Wang & Law (2002).

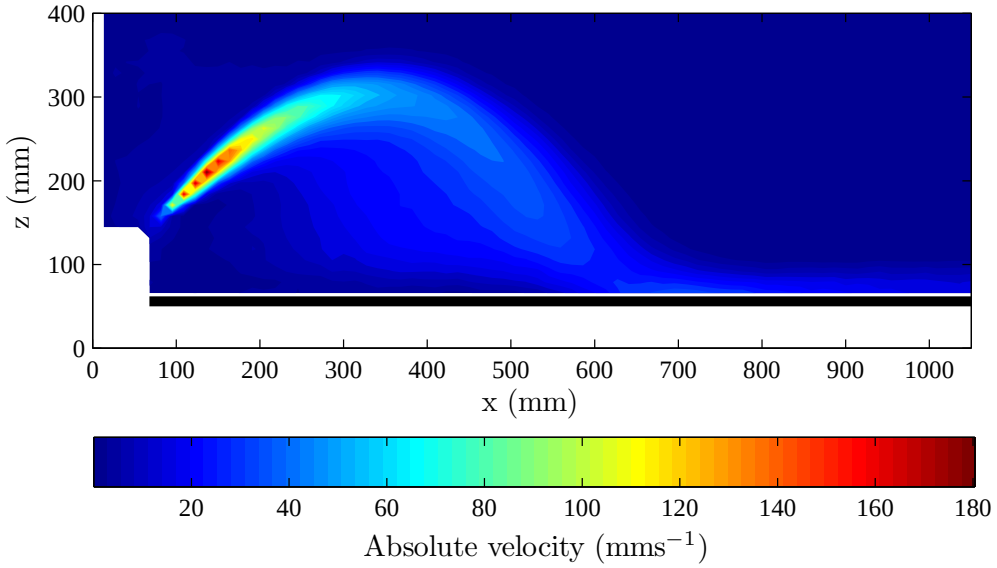

Figure 6.3 – Contours of mean absolute velocity for 45° experiment with a lower boundary present (solid black line), $F_o = 58.1$, $H_o/(F_o d) = 0.57$. The source outlet is located in the white rectangle, this area is excluded from the PTV analysis due to reflections off the source.

6.4.1 General Observations

Observing the flow visually during the physical experiments provides an understanding of bulk behaviour and also provides an important insight into subtle flow behaviour that was not captured by the PTV experimental system. Observations were of the centreline plane of discharges where tracer particles were illuminated by the laser. The main focus of the following observations was on the impingement region and spreading layer. The behaviour of INBJs far above a boundary, without boundary influence, has been previously described in section 5.1.1.

The behaviour of the flow up to maximum height appeared not to be affected by the presence of the lower boundary. Detrainment of negatively buoyant parcels with low velocity on the inner side of the discharge were observed to fall to the lower boundary. The flow trajectory on the falling side of discharges was redirected by the lower boundary. The majority of discharged fluid was redirected radially away from the source after impingement in the two-dimensional view produced by the laser sheet. Entraining eddies formed as the radially spreading layer moved across the lower boundary, indicating additional mixing. The radially spreading layer then fell over the edge of the boundary out of view. Discharged brine could be seen falling over the edge of the boundary perpendicular to the laser sheet, indicating the redirection of flow on the lower boundary occurred in all directions.

The depth of the spreading layer back towards the source was minimal for 30°

discharges, due to the relatively large initial horizontal momentum flux compared to higher source angles. The amount of flow moving back towards the source increased for increasing non-dimensional source height. This is likely due to the larger trajectory angle, below horizontal, before impingement. There was no obvious spreading layer moving back towards the source for the lowest non-dimensional source height, however, it was evident that ambient fluid from just above the boundary was entrained into the discharge near the source. The thin spreading layer moving back towards the source for intermediate non-dimensionalised source heights appeared to be dominated by strong entrainment near the source.

A spreading layer moving back towards the source was present for all source heights at the source angles of 45° and 60°. However, the majority of redirected flow on the lower boundary still moved away from the source. Entrainment by the source of the spreading layer moving back towards the source was visible for 45° and 60° discharges at the lowest non-dimensional source heights. Entrainment of the radial spreading layer moving back towards the source decreased for higher non-dimensionalised source heights at these two source angles.

6.4.2 Experimental Coefficients

This section will focus on the geometric and mean velocity experimental coefficients of discharges with source angles of 30°, 45°, and 60° at maximum height and the return point. The k-notation introduced in section 5.2.1 will again be utilised for the important parameters of INBJs with a lower boundary present (Figure 6.1). Experimental coefficients were found using a linear regression between the geometric parameters non-dimensionalised by the source diameter and the initial Froude number. Experimental coefficients were calculated without specifically considering the influence of the lower boundary through the different non-dimensional source heights. The experimental coefficients for maximum height (Table 6.1) and the return point (Table 6.2) with and without the presence of the lower boundary are compared to determine the influence of the boundary on bulk flow behaviour. The geometric and velocity data from individual experiments are shown in table C.1 (Appendix C).

The majority of geometric and velocity experimental coefficients with and without boundary are within the standard deviations of data at maximum height (Table 6.1). The vertical distance to maximum height (k_{zm}) is the only parameter outside the bounds of standard deviations, however values are still similar. Therefore, the presence of the lower boundary has little or no influence on the behaviour of INBJs at maximum height, which is consistent with visual observations (Section 6.4.1).

Geometric parameters at the return point are not greatly affected by the presence of the lower boundary (Table 6.2). However, visual observations of experiments (Section

Table 6.1 – Comparison of experimental coefficients at maximum height between experiments with (current chapter) and without (Chapter 5) the presence of a lower boundary for source angles of 30°, 45°, 60°. Standard deviations are also shown. B: Boundary.

θ_o	B	k_{xm}	k_{zm}	k_{zme}	k_{sm}	k_{um}	θ_m (rad)
30°	N	1.87 ± 0.03	0.69 ± 0.01	1.09 ± 0.06	2.02 ± 0.03	0.356 ± 0.010	0.042 ± 0.013
30°	Y	1.87 ± 0.02	0.67 ± 0.02	1.09 ± 0.05	2.01 ± 0.03	0.368 ± 0.002	0.040 ± 0.012
45°	N	1.96 ± 0.07	1.22 ± 0.04	1.73 ± 0.05	2.37 ± 0.08	0.481 ± 0.014	0.076 ± 0.028
45°	Y	1.94 ± 0.03	1.18 ± 0.01	1.67 ± 0.02	2.33 ± 0.03	0.483 ± 0.006	0.069 ± 0.026
60°	N	1.69 ± 0.04	1.71 ± 0.03	2.23 ± 0.04	2.50 ± 0.04	0.645 ± 0.010	0.097 ± 0.043
60°	Y	1.71 ± 0.02	1.64 ± 0.03	2.19 ± 0.02	2.48 ± 0.02	0.637 ± 0.015	0.075 ± 0.015

6.4.1) noted that the flow is redirected away from the source above the lower boundary. The horizontal location of the return point should therefore increase where the non-dimensional source height is smaller, because the flow would have been redirected further at the return point. However, the horizontal distance to the return point (k_{xr}) at 30° is smaller and the distance to the outside edge (k_{xre}) is larger when the boundary is present. This indicates the lower boundary distorts the velocity profiles at the return point. Geometric parameters at the return point (k_{xr}, k_{xre}) for source angles of 45° and 60° show that the presence of the lower boundary moves the flow away from the source (Table 6.2). The standard deviations of geometric parameters (k_{xr}, k_{xre}) show there is higher variability in behaviour with the boundary present. The path length to the return point (k_{sr}) is not affected by the presence of the boundary. The magnitude (k_{ur}) and direction (θ_r) of centreline velocity at the return point show the highest change in value and variability due to the presence of the lower boundary (Table 6.2). k_{ur} values are higher for all source angles, indicating that the magnitude of centreline velocity (u_r) at the return point is lower. θ_r values are lower and closer to horizontal for all source angles when the lower boundary is present. Velocities decrease as they approach the lower boundary and are redirected to a horizontal radially spreading layer, resulting in the higher k_{ur} values and lower θ_r values for all source angles. The standard deviations of k_{ur} and θ_r values are much higher when the lower boundary is present (Table 6.2). The non-dimensional source height differs between experiments at each source angle, so the vertical distance of the return point above the boundary is different between experiments. Thus the lower boundary had differing effects on the behaviour of the flow at the return point, resulting in the high variation in k_{ur} and θ_r values between experiments.

The large variation in k_{ur} and θ_r values at the return point requires further investigation to determine the effect of non-dimensional source height on these parameters. k_{ur} values do not change substantially for 30° discharges at different non-dimensional source heights (Figure 6.4), which is shown by the relatively small standard deviation

Table 6.2 – Comparison of experimental coefficients at the return point between experiments with (current chapter) and without (Chapter 5) the presence of a lower boundary for source angles of 30°, 45°, 60°. Standard deviations are also shown.

θ_o	Boundary	k_{xr}	k_{xre}	k_{sr}	k_{ur}	θ_r (rad)
30°	N	3.56 ± 0.05	4.43 ± 0.10	3.62 ± 0.06	0.581 ± 0.020	-0.745 ± 0.027
30°	Y	3.37 ± 0.09	4.61 ± 0.12	3.69 ± 0.08	0.626 ± 0.036	-0.632 ± 0.110
45°	N	3.43 ± 0.09	4.56 ± 0.10	4.39 ± 0.12	0.693 ± 0.031	-1.018 ± 0.028
45°	Y	3.53 ± 0.14	4.74 ± 0.12	4.38 ± 0.10	0.794 ± 0.102	-0.847 ± 0.172
60°	N	2.93 ± 0.06	4.11 ± 0.09	4.74 ± 0.07	0.732 ± 0.012	-1.238 ± 0.022
60°	Y	3.08 ± 0.12	4.33 ± 0.14	4.72 ± 0.09	0.874 ± 0.147	-0.977 ± 0.148

(Table 6.2). k_{ur} values decrease with increasing non-dimensional source height for 45° and 60° discharges. This is due to the increasing influence of the lower boundary on the flow at the return point for lower non-dimensional source heights. θ_r values are similar for the intermediate and highest non-dimensional source heights for 30° and 45° discharges (Figure 6.4). However, θ_r values are lower and closer to horizontal for the lowest non-dimensional source heights at all source angles. Therefore, non-dimensional source height has a large non-linear influence on the behaviour of discharges above the boundary at the return point.

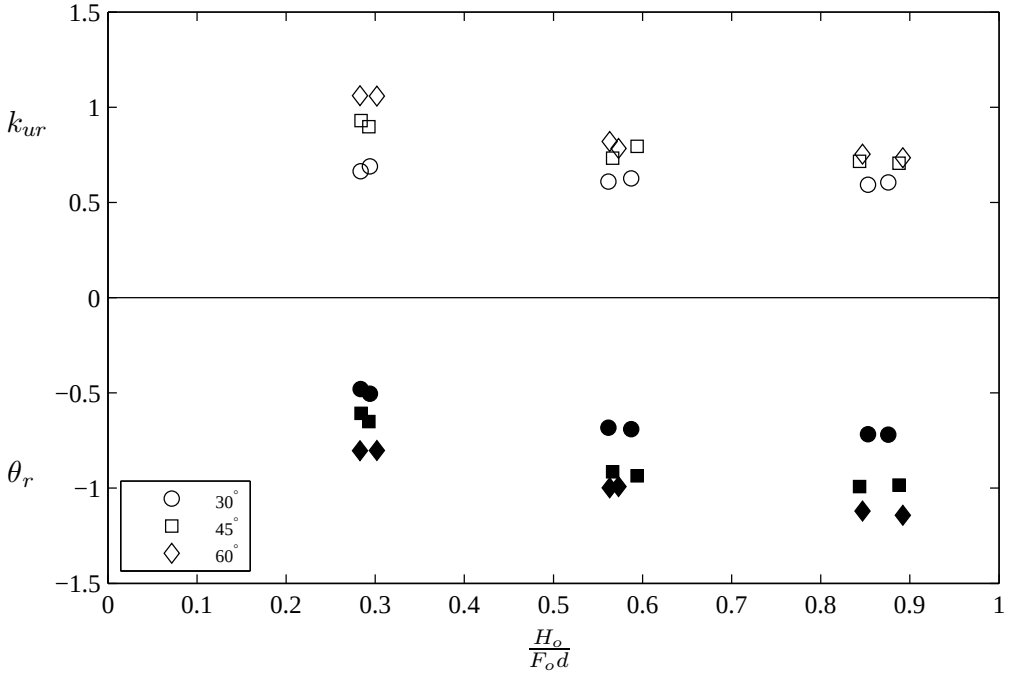

Figure 6.4 – Return point velocity and theta for 30°, 45°, 60° experiments for different non-dimensional source heights.

6.4.3 Spread and Trajectory

The spread and trajectory of 45° INBJs with a lower boundary present will be the focus of the following section. The spread and trajectory of INBJs without a lower boundary present were previously investigated in section 5.2. The outer spread rate of 45° discharges, with a lower boundary present, has a linear relationship with path length before the return point (Figure 6.5). The outer spread rate is found to be 0.107 $\pm$ 0.010 up to a location halfway between maximum height and the return point for 45° discharges with a boundary present. This is similar to the outer spread rate of 0.117 $\pm$ 0.013 found for 45° discharges without a boundary present (Section 5.2.2). The outer spread rate decreases non-linearly in the impingement region near the return point with a boundary present (Figure 6.5). The outer spread rate then increases linearly with path length beyond $s/(F_o d) > 6.25$ with a spread rate of 0.044 $\pm$ 0.026, as the radially spreading layer moves along the lower boundary. The inner spread rate of 45° discharges with a boundary present show similar trends to experiments without a boundary present (Figure 5.13) until just after maximum height. However, the inner spread rates become negative between maximum height and the return point when the boundary is present (Figure 6.5). This differs to the inner spread rates that are always positive when the boundary is not present (Figure 5.13). The proximity of the lower boundary restricts spreading on the inner side of discharges, which is consistent with the study of Shao & Law (2010). The location of maximum non-dimensional inner discharge width is dependent on the non-dimensional source height. The maximum non-dimensional inner discharge width and associated path length location both increase with increasing non-dimensional source height (Figure 6.5). Identical overall behaviour is found for inner and outer spread rates for 30° and 60° discharges (Figures C.1 and C.2, Appendix C).

The trajectories of centreline velocity, non-dimensionalised by the source diameter and initial Froude number, collapse for all experiments at the source angle of 45° up to $x/(F_o d) \approx 3$ (Figure 6.6). Similar behaviour is found for 30° and 60° discharges (Figures C.3 and C.4, Appendix C). The source is located at the origin of figure 6.6, which results in a separation of non-dimensionalised centreline trajectory for different non-dimensionalised source heights at $x/(F_o d) \approx 4$ when the flow is redirected by the lower boundary. Trajectories are subsequently flat as the flow moves along the boundary. Non-dimensionalised centreline trajectory remains similar for each of the three different groups of non-dimensionalised source height. Trajectories tend towards a vertical path past the return point when no boundary is present (Figure 5.3, Section 5.2.1). The trajectories here show that the location of centreline velocity is displaced horizontally by the presence of the lower boundary (Figure 6.6). This deflection by the presence of the lower boundary results in a change of trajectory curvature.

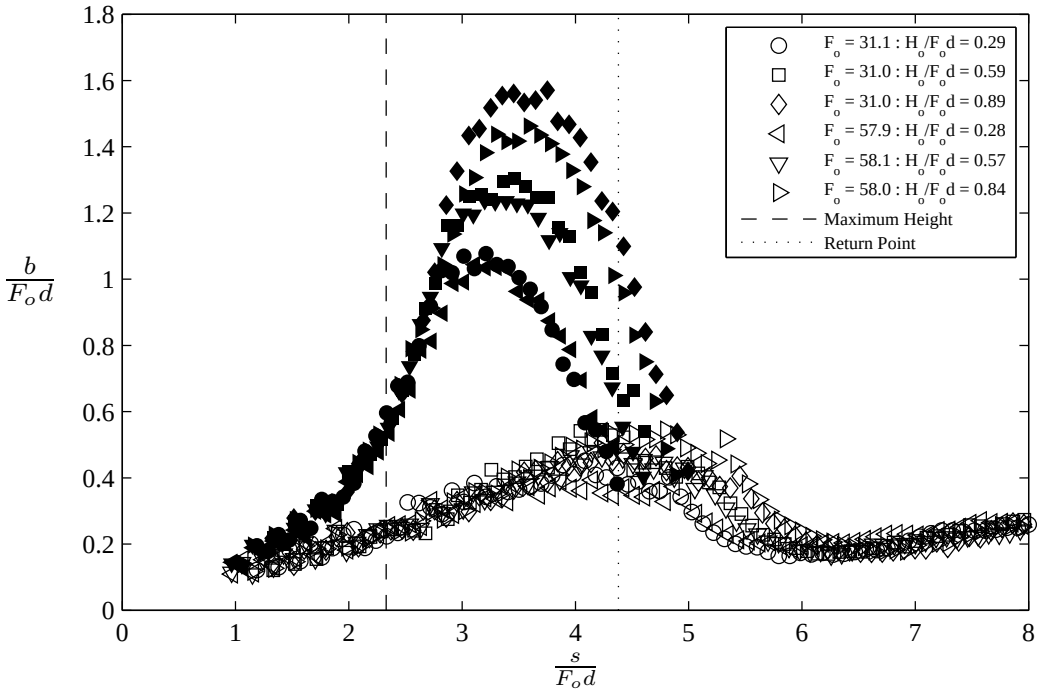

Figure 6.5 – Discharge width against path length for 45° experiments with boundary. Unfilled symbols: outer side, filled symbols: inner side.

An 8$^{\text{th}}$ order Fourier series curve was fitted, using non-linear least squares, through centreline trajectory data points of each experiment. The Fourier series curve provided the best fit to the trajectory of the impinging flow and determined the path of the flow. An inflection point is defined as the location where the gradient of the curve fit is a minimum. The vertical distance of the inflection point above the source (z_i) is the location where the presence of the lower boundary changes flow behaviour. Alternative techniques to determine the location of boundary influence, such as changes in velocity and spread, were difficult to implement for each experiment due to the scatter of experimental data. All combinations of geometric parameters were compared to determine the dependence of z_i on other geometric parameters. The vertical distance of the inflection point above the boundary ($z_i + H_o$) is found to have a linear relationship with the vertical distance of maximum height above the boundary ($z_m + H_o$) for all source angles (Figure 6.7). The gradient of the linear regression for 30° discharges is found to be 0.490 ± 0.010 and the gradient is 0.489 ± 0.014 for 45° discharges. The gradient for 60° discharges is slightly higher at 0.509 ± 0.012. Gradients are similar for all source angles and the gradient of linear regression of data for all source angles is 0.50 ± 0.02. Therefore, the presence of the lower boundary affects the trajectory of INBJs well above the boundary. However, the magnitude of lower boundary influence is also important to determine when flow behaviour is substantially affected. The small deflection of the flow after the inflection point is unlikely to be important for outfall diffuser design. Therefore, the magnitude of lower boundary influence needs to be

determined at different heights above the boundary.

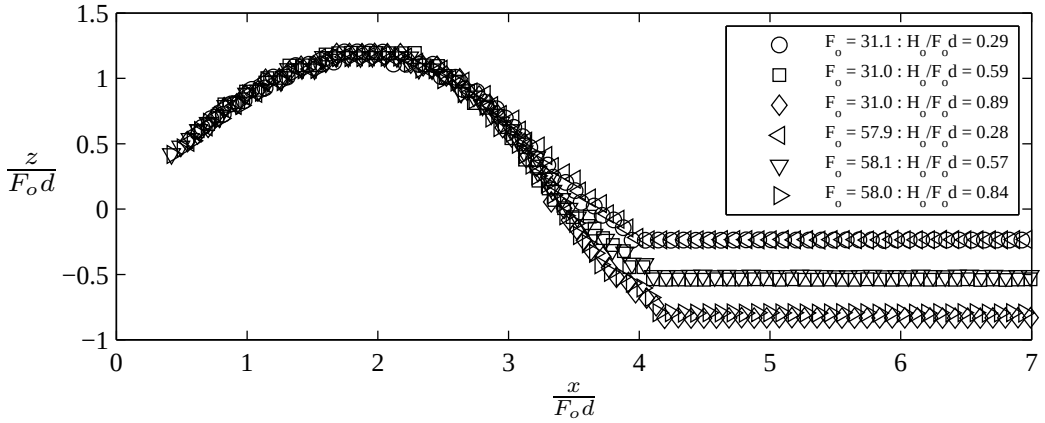

Figure 6.6 – Non-dimensionalised centreline trajectory of 45° INBJ experiments for varying Froude numbers and non-dimensional source heights. The source is located at the origin.

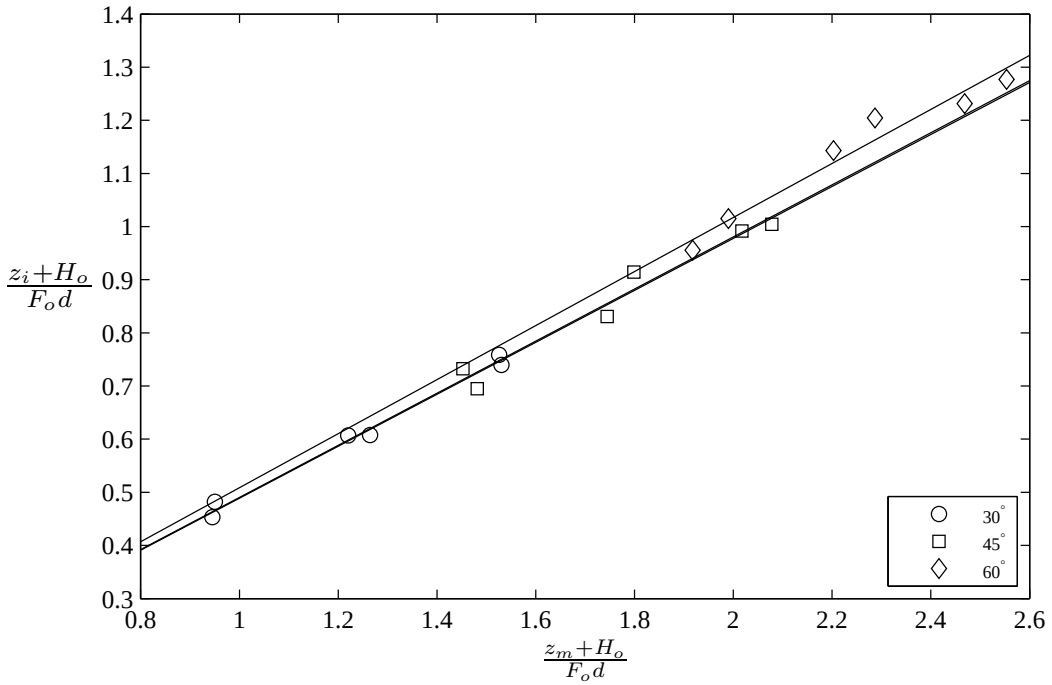

Figure 6.7 – Vertical location of inflection point above source above lower boundary ($z_i + H_o$) compared to vertical distance of maximum height above lower boundary ($z_m + H_o$). All distances have been non-dimensionalised by the source diameter and initial Froude number.

6.4.4 Velocity

Mean or time averaged velocity field experimental data provides important information about bulk flow behaviour. Mean velocity field information was extracted from the experimental data using identical methods to those described in section 4.3.2 for results from chapter 5. Components of centreline velocity in the horizontal (u) and vertical

(v) directions represent the predominant magnitude and direction of INBJs before, during, and after the impingement with the lower boundary. Components of centreline velocity generally scale upon source diameter and Froude number for all experiments at source angle 45° when compared to the horizontal distance from the source (Figure 6.8). Components of centreline velocity for 30° and 60° discharges show similar behaviour (Figures C.5 and C.6, Appendix C). The magnitudes of u and v when the boundary is present (Figure 6.8) are very similar to those without a boundary present (Figure 5.30, Section 5.3.1.1) up until a point between maximum height and the return point. u values increase and v values decrease in the impingement region ($3 \lesssim x/(F_o d) \lesssim 4$) when the boundary is present (Figure 6.8), which is opposite to the behaviour of INBJs without a boundary present (Figure 5.30). u values increase during impingement as the cross-section width of the flow decreases. u values then decrease as the flow moves along the lower boundary (Figure 6.8). v values decrease towards zero during impingement, and have relatively small negative values as the flow moves along the boundary. This is likely due to the radially spreading layer being similar to a wall jet and entraining fluid from above. Figure 6.8 is annotated with letters to indicate the location of important locations in defining the influence of the boundary in the impingement region (Section 6.4.5).

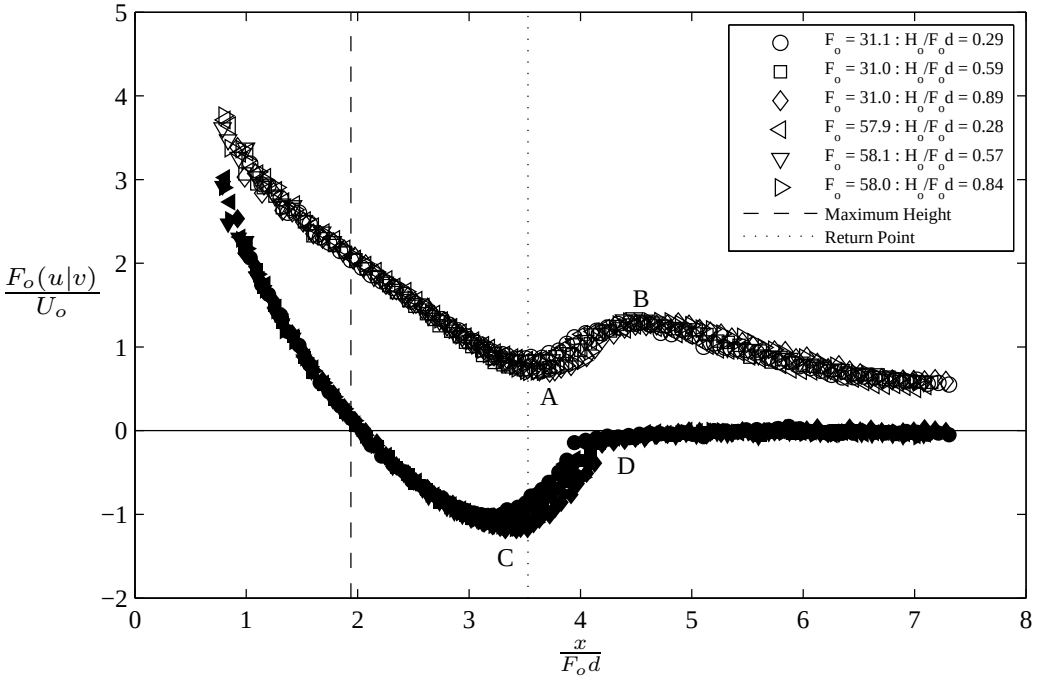

Figure 6.8 – Components of mean centreline velocity for all 45° experiments against horizontal distance from the source. Unfilled symbols: horizontal velocity (u), filled symbols: vertical velocity (v). Locations of local minimum and maximum velocity components annotated with A, B, C, and D.

Components of centreline velocity separate into the three different groups, determined

by their respective non-dimensional source heights, when compared to the vertical distance above the boundary (Figure 6.9). Identical behaviour is seen 30° and 60° discharges (Figures C.9 and C.11, Appendix C). v values decrease rapidly as the flow approaches the boundary and they collapse on to each other near the boundary, independent of the different non-dimensional source heights. u values are shown to increase as the flow approaches the boundary due to the redirection of the flow. The vertical distance of the maximum height above the lower boundary ($z_m + H_o$) was found to be a critical parameter for the behaviour of INBJs (Figure 6.7). Scaling the components of centreline velocity with this critical parameter collapses the experimental data for different non-dimensional source heights for 45° discharges (Figure 6.10). Identical behaviour is seen for 30° and 60° discharges (Figures C.10 and C.12, Appendix C). However, the distribution of v values widens as the flow approaches the boundary when values are scaled with this critical parameter, for all source angles. This suggests the proximity of the flow to the lower boundary becomes more important to the decay of the vertical component of centreline velocity than the vertical distance of maximum height above the boundary, as the flow approaches the boundary.

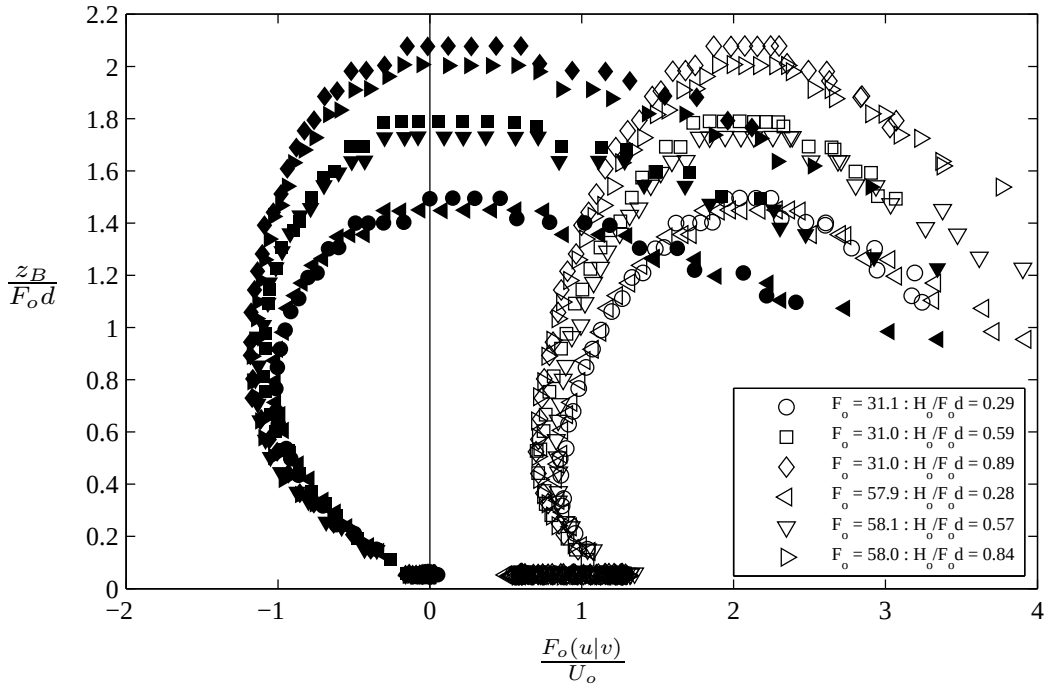

Figure 6.9 – Components of mean centreline velocity for all 45° experiments against vertical distance above the lower boundary. Unfilled symbols: horizontal velocity (u), filled symbols: vertical velocity (v).

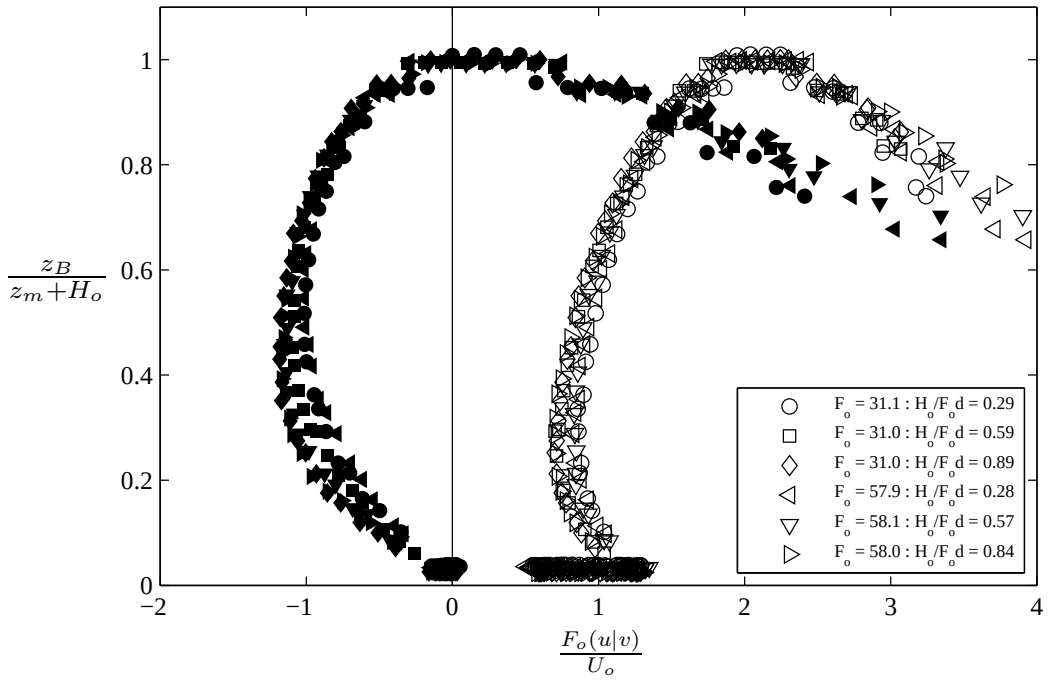

Figure 6.10 – Components of mean centreline velocity for 45° experiments against non-dimensionalised distance above boundary, unfilled symbols: horizontal (u), filled symbols: vertical (v).

Fluctuating characteristics are important for understanding the complex mixing and redirection behaviour of INBJs impinging a lower boundary. Centreline turbulent kinetic energy (k), non-dimensionalised by mean centreline velocity (u_c), increases rapidly as the flow approaches the boundary (Figure 6.11). This occurs at a similar location to the decrease in vertical component of centreline velocity (Figure 6.9). The horizontal component of centreline velocity increases near this location as the flow approaches the boundary. Therefore, the overall change in centreline velocity is minimal and does not account for the large change in non-dimensionalised centreline k values. Identical behaviour is seen in centreline turbulent kinetic energy for 30° and 60° discharges (Figures C.16 and C.18, Appendix C). Non-dimensionalised centreline k values are relatively constant, at approximately 0.3, before impingement on the lower boundary influences flow behaviour (Figure 6.11). The magnitude of values is similar to those found on the centreline at maximum height and the return point for 45° discharges without boundary influence (Figures 5.50 and 5.53, Section 5.3.2). Non-dimensionalised centreline k values increase at height of $z_B/(F_o d) \approx 0.5$ above the boundary for 45° discharges. The location of the increase is similar for 30° and 60° discharges (Figures C.16 and C.18, Appendix C). Non-dimensionalised centreline k values reach approximately 0.6 for 45° discharges just before the flow reaches the lower boundary. Values subsequently increase and decrease when the flow moves along the boundary in the radially spreading layer, which will be further investigated in section 6.4.6.

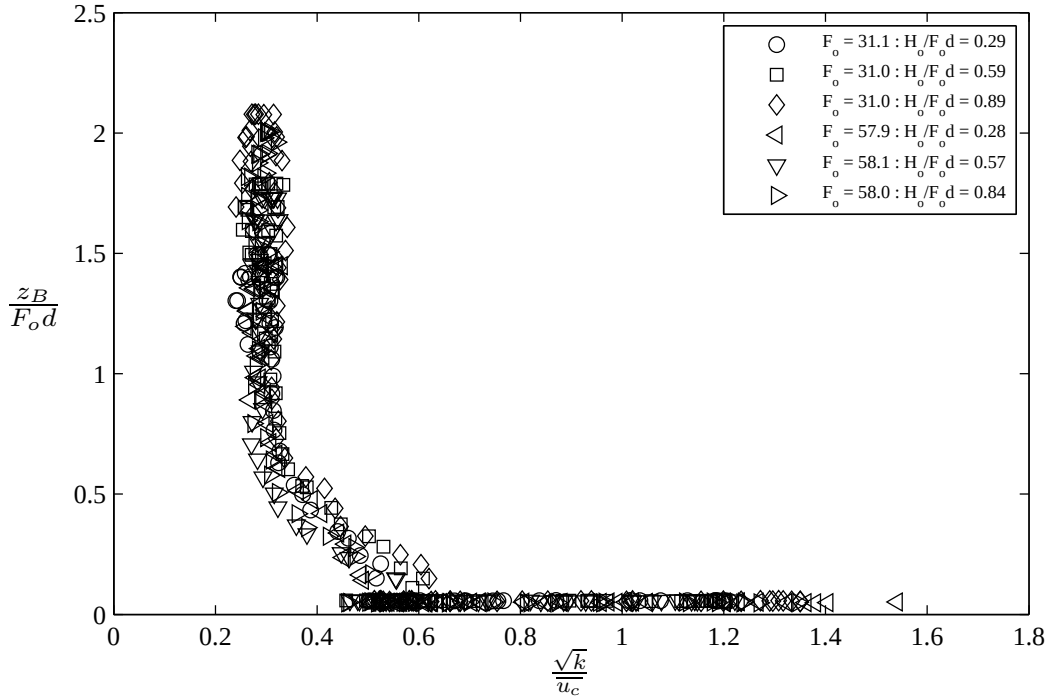

Figure 6.11 – Non-dimensionalised centreline turbulent kinetic energy (k) against distance above boundary for 45° experiments.

6.4.5 Impingement Region

The impingement region contains a complex three-dimensional process where the main flow is redirected horizontally by the presence of a lower boundary. The impingement region occurs between the regions of no boundary influence and radial spreading along the boundary, as defined in section 6.1. This general definition indicates that the start of the impingement region is located at the inflection point (Figure 6.7), where the influence of the lower boundary is first observed on the trajectory. However, the influence on the flow at the inflection location is inconsequential. Therefore, the magnitude of lower boundary influence will be quantified in this section to determine when and how the flow behaviour changes substantially. The end of the impingement region is defined by the start of wall jet type flow behaviour as flow spreads radially along the boundary.

Despite the complexity of the impingement region, the components of centreline velocity show that there are some general trends (Figure 6.8). The first indication that the flow is substantially affected by the presence of the boundary is the occurrence of a local minimum of vertical velocity (C, Figure 6.8), which indicates a slowing of the flow as it approaches the boundary. The redirection of the flow is shown by the local minimum horizontal velocity (A), which precedes an increase in horizontal velocity. Vertical velocity then approaches zero (D) when the flow has been redirected to form a radially spreading layer. The horizontal velocity increases due to the cross-sectional area of the flow decreasing during the redirection. Horizontal velocity reaches a local

maximum (B) then decreases with distance from the source along the boundary as it behaves similar to a wall jet in the radially spreading layer.

There exist locations of local minimum and maximum u and v values near the impingement region, between $3 \lesssim x/(F_o d) \lesssim 5$, in figure 6.8. Local extrema indicate substantial changes in flow behaviour as these were not found to occur for discharges without boundary influence (Figure 5.30, Section 5.3.1.1). No definitive dependence on the non-dimensional source height could be determined for the local extrema in figure 6.8. This is likely due to the low velocity gradients of the flow near extrema and experimental scatter as shown in figures 6.8 and 6.9. The locations of local minimum and maximum u and v values, averaged over all experiments, are dependent on the source angle (Figures 6.12 and 6.14).

The location of local minimum of vertical velocity occurs further above the boundary and horizontally closer to the source than the local minimum of horizontal velocity for all source angles (Figure 6.12). The vertical distances of local minimum vertical and horizontal velocity above the boundary increase for increasing source angle. The location of maximum height above the boundary also increases for increasing source angle, which is consistent with the dependence found for the inflection point (Figure 6.7). The locations of local minimum u and v values and the vertical distance of maximum height above the boundary for each experiment are compared in figure 6.13. u and v points are separated into two groupings for all discharge angles. A linear regression analysis of the data reveals horizontal velocity (u) has a gradient of 0.276 and a vertical axis intercept of -0.057. The linear regression for vertical velocity (v) has a gradient of 0.265 and a vertical axis intercept of 0.269. The coefficients of determination (R^2) for these linear regressions are relatively low, at 0.73 and 0.82 respectively. The gradients for u and v values are similar. This indicates that changes in the vertical distance above the boundary to maximum height produce a related change in the locations of local minimum u and v values. The intercept for u values is approximately zero, while the positive intercept for v values shows there is a dependence on the vertical distance above the boundary. This is supported by the collapsing v values, which have not been non-dimensionalised by the vertical distance above the boundary of maximum height (Figure 6.9).

The locations of local maximum horizontal and vertical velocity occur over a narrow range of vertical distances above the boundary (Figure 6.14). The local maximum vertical velocity is defined to be where the vertical velocity is above a threshold close to zero in the impingement region (D, Figure 6.8). The flow is predominately in the horizontal direction at this location. The location of local maximum vertical velocity again occurs closer to the source than the local maximum horizontal velocity for all source angles. Therefore, vertical velocity should be used to determine the location of substantial changes in flow behaviour. The horizontal distances of local maximum u

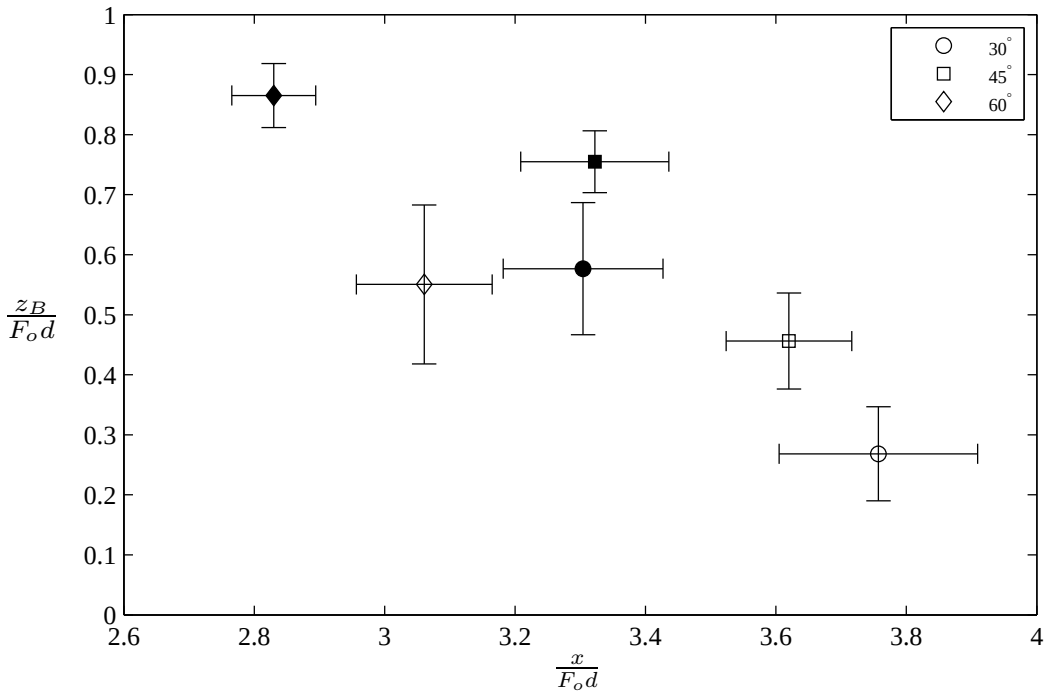

Figure 6.12 – Locations of local minimum near impingement region for vertical and horizontal components of centreline velocity for 30°, 45°, and 60° experiments. Unfilled symbols: horizontal velocity (u), filled symbols: vertical velocity (v). Standard deviations shown by error bars.

and v values generally decrease with an increase in source angle. This is likely related to the smaller horizontal distance to the return point (k_{xr}) at higher source angles (Table 6.2). Smaller k_{xr} values suggest that the impingement region occurs closer to the source and therefore the resulting redirection of the flow also occurs closer to the source.

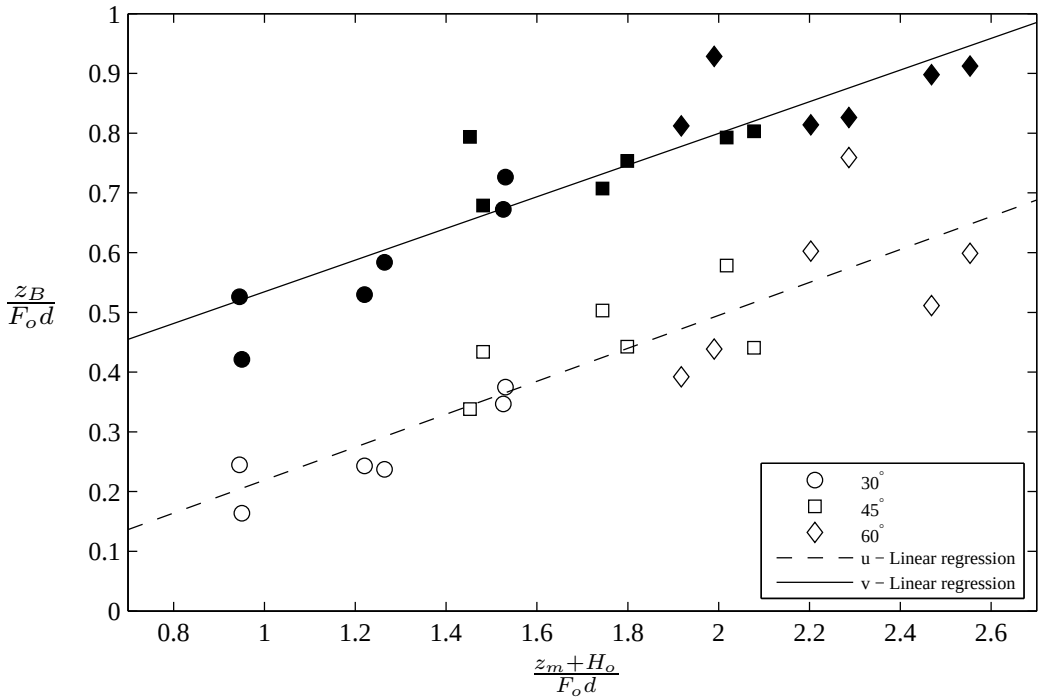

Figure 6.13 – Vertical distance above the boundary of local horizontal and vertical minimum velocity near the impingement region. This is compared to the vertical distance above the boundary of maximum height for each experiment at 30°, 45°, and 60°. Unfilled symbols: horizontal velocity (u), filled symbols: vertical velocity (v).

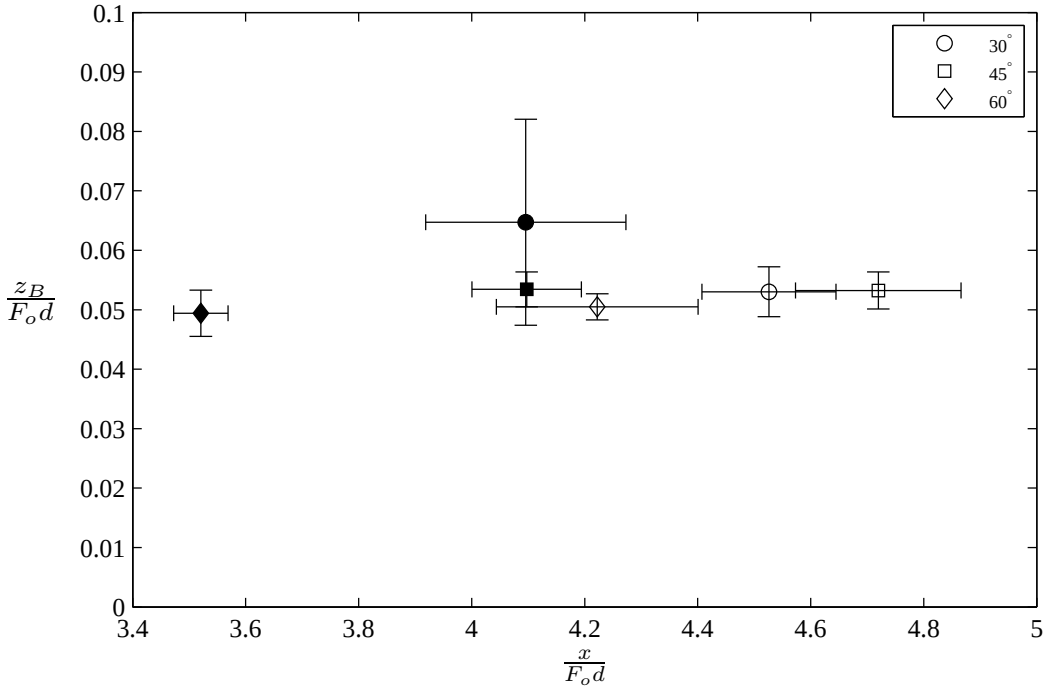

Figure 6.14 – Locations of local maximum near impingement region for vertical and horizontal components of centreline velocity for 30°, 45°, and 60° experiments. Unfilled symbols: horizontal velocity (u), filled symbols: vertical velocity (v). Standard deviations shown by error bars.

The velocity profiles for one experiment at 45° impinging the lower boundary are shown in figure 6.15. Velocity is separated into horizontal and vertical components to clearly illustrate the transformation of velocity profiles. Profiles are located at different path lengths and vertical distances above the boundary, as shown in the figure legend. For the profile furthest from the boundary ($z_B/(F_o d) = 1.02$), horizontal and vertical profiles are approximately Gaussian on the outer side (negative r/b) and are distorted on the inner side (positive r/b). This behaviour is consistent with velocity profiles near the return point without lower boundary influence (Section 5.3.1.2). Profiles remain self-similar on the outer side, up to $z_B/(F_o d) = 0.40$. The gradient of vertical velocity becomes progressively steeper on the inner side as the flow approaches the boundary. This results in a reduction in discharge width, as previously shown in figure 6.5. The local centreline angle (θ) increases as flow is redirected horizontally closer to the boundary. At $z_B/(F_o d) = 0.24$ the magnitude of vertical velocity near the centreline decreases, while the magnitude of horizontal velocity increases. When the flow approaches the boundary ($z_B/(F_o d) = 0.04$), vertical velocities approach zero and the maximum non-dimensional horizontal velocities approach one. The movement of the flow along the boundary is indicated by increasing path length (see legend of figure 6.15). The horizontal profiles along the boundary indicate the development of a wall jet type flow. Shao & Law (2010) experimentally measured a peak in velocity in the wall jet region, however a peak is not found in figure 6.15. This is due to the limited spatial resolution of the experimental system, resulting in a gap between the lower boundary and the first velocity measurements. Similar behaviour is seen for mean velocity profiles of 30° and 60° discharges (Figures C.7 and C.8, Appendix C). Therefore, centreline velocity along the boundary is the maximum measured velocity and the trajectory is determined from the locations of the maximum measured velocities. The error in the centreline velocity measurements is investigated in section 6.4.6.

Turbulent kinetic energy profiles taken at the same locations as mean velocity profiles (Figure 6.15) are shown in figure 6.16(a) for one 45° experiment. Profiles furtherest from the boundary, $z_B/(F_o d) \geq 0.61$, are similar to those found for 45° discharges without boundary influence at the return point (Figure 5.53, Section 5.3.2). The peak k values are approximately 0.3 and are located at $r/b \approx$ -0.5, which is similar to the peak of 0.322 at $r/b =$ -0.65 for 45° discharges at the return point (Table 5.7, Section 5.3.2). The magnitude of k values increase as the flow approaches the boundary and the location of the peak k value changes from the outer side (negative r/b) to the inner side of discharges (positive r/b). Turbulent kinetic energy profiles are self-similar for flow along the boundary ($z_B/(F_o d) = 0.04$) and have a maximum value of approximately 0.6, which is located near the centreline. High turbulent kinetic energy values are consistent with the previously reported additional mixing and dilution in the radially spreading layer (Roberts *et al.*, 1997; Shao & Law, 2010).

Turbulent shear intensity profiles are shown in figure 6.16(b) for the same 45° experiment. Profiles remain self-similar on the outer side for $z_B/(F_o d) \geq 0.08$, which is much closer to the boundary than mean velocity and turbulent kinetic energy profiles. However, profiles vary substantially on the inner side and magnitudes at the return point are generally greater than those found for discharges without a boundary influence (Figure 5.54, Section 5.3.2). The magnitude of turbulent shear intensity for profiles along the boundary ($z_B/(F_o d) = 0.04$) are very small in comparison with values further above the boundary. These low values are possibly due being unable to match particles and measure velocities close to the boundary.

The impingement region is defined to start where the main flow is influenced by the presence of the boundary. An inflection point in the trajectory of INBJs, due to the presence of the boundary, is found to occur at an average height of $0.50(z_m + H_o)$ for all source angles. The vertical component of mean centreline velocity has the first local extrema as the flow approaches the boundary. The local minimum of vertical velocity is found to occur above the boundary and its relationship to maximum height above the boundary is given in equation 6.1 for all source angles. The increase in non-dimensionalised centreline turbulent kinetic energy occurs at a height of $z_B/(F_o d) \approx 0.5$ above the boundary and a dependence on source height can not be determined.

$$\frac{z_B}{F_o d} = 0.265 \left(\frac{z_m + H_o}{F_o d} \right) + 0.269 \tag{6.1}$$

The end of the impingement region is the start of the wall jet region of the radially spreading layer. The location of local maximum horizontal velocity can be assumed to be at or near the start of the wall jet region. The horizontal location of local maximum horizontal velocity is $x/(F_o d) = 4.52 \pm 0.12$ for 30° discharges, $x/(F_o d) = 4.72 \pm 0.15$ for 45° discharges, and $x/(F_o d) = 4.22 \pm 0.18$ for 60° discharges.

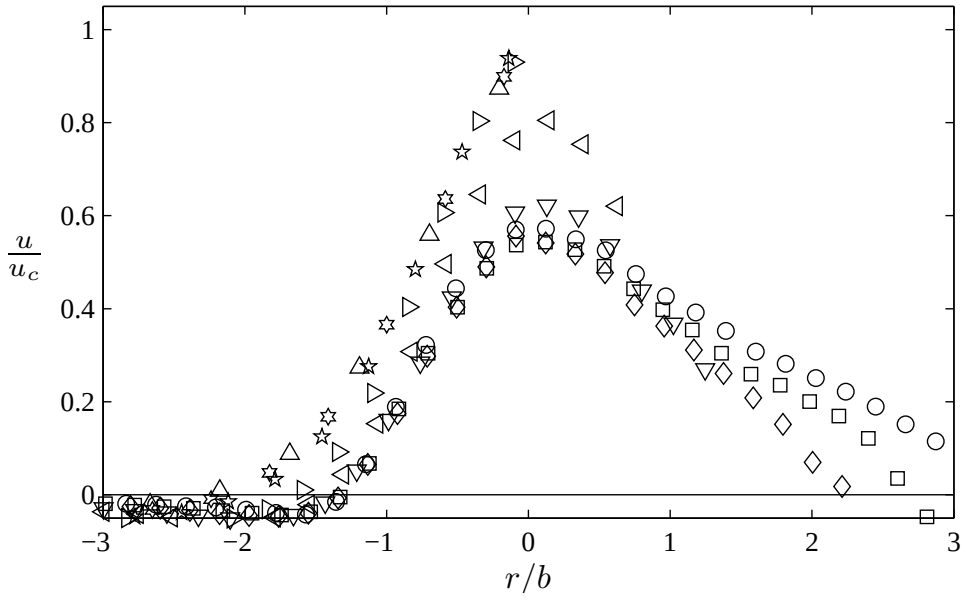

(a) Horizontal velocity

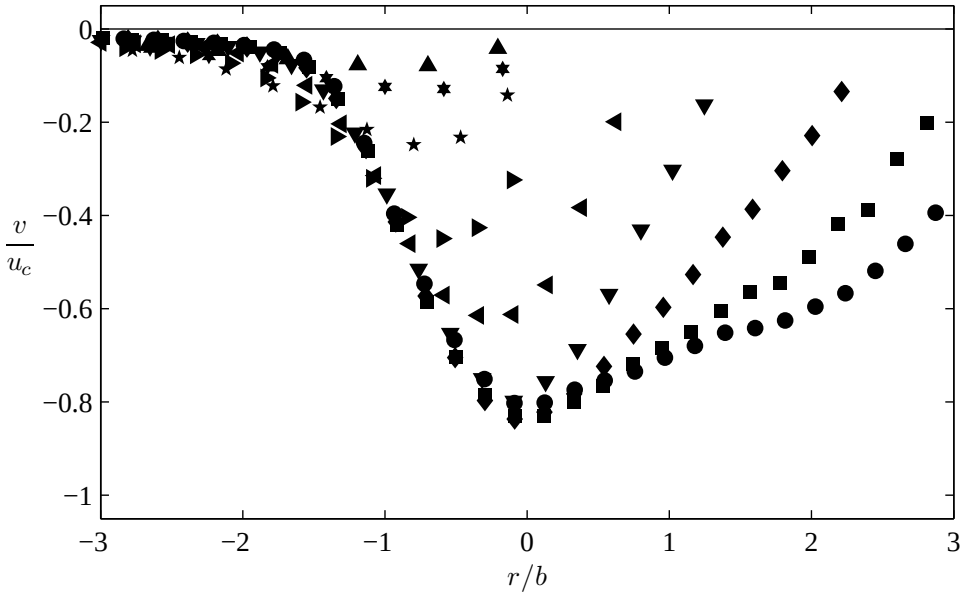

(b) Vertical velocity

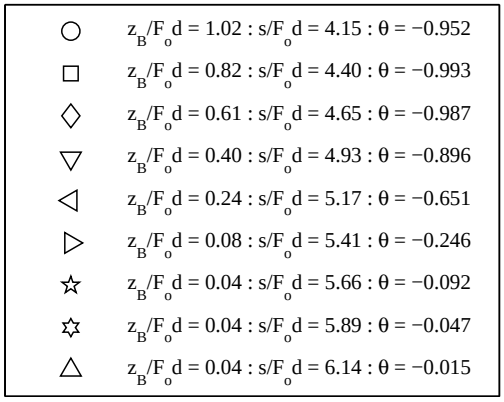

Figure 6.15 – Profiles for horizontal (u) and vertical (v) components of mean velocity in the impingement region for a 45° experiment with a lower boundary present, $F_o = 31.0$ $H_o/(F_o d) = 0.88$.

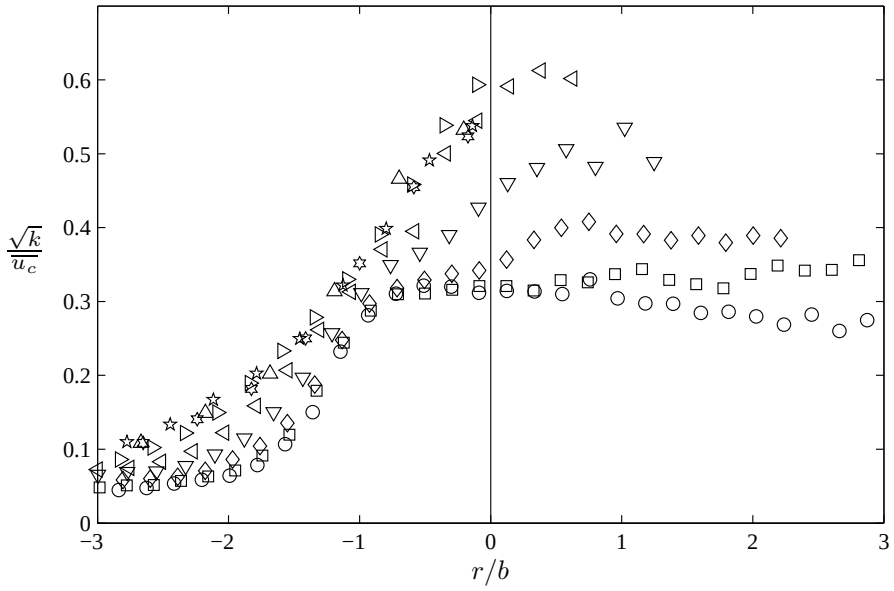

(a) Turbulent kinetic energy

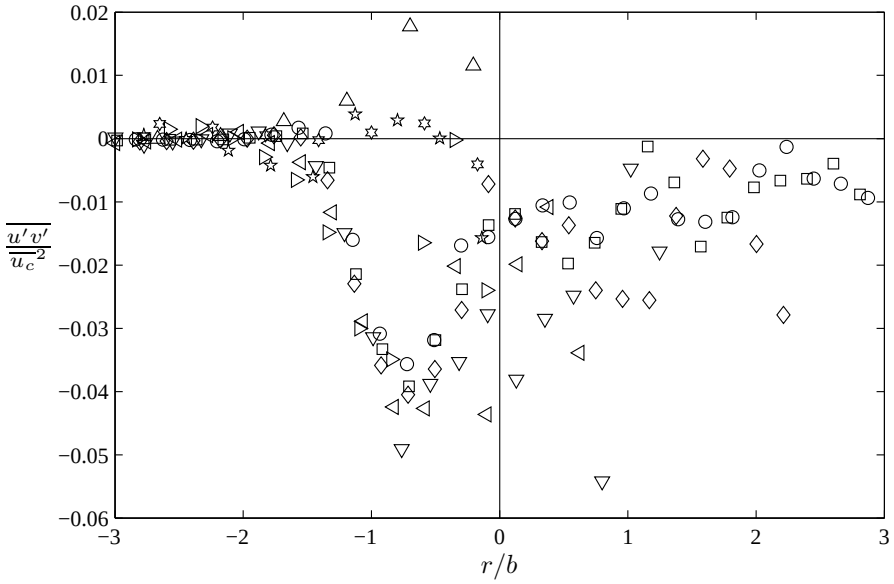

(b) Turbulent shear intensity

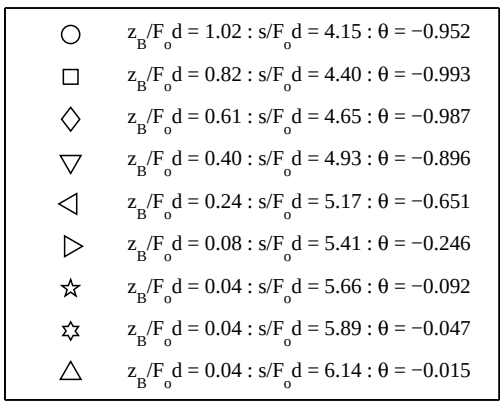

Figure 6.16 – Turbulent kinetic energy (k) and turbulent shear intensity profiles in the impingement region for a 45° experiment with a lower boundary present, F_o = 31.0 $H_o/(F_o d)$ = 0.88.

6.4.6 Radially Spreading Layer

The presence of a lower boundary results in the redirection of INBJs in all directions across the boundary after impingement. The radially spreading layer is important to the engineering design of desalination outfalls due to additional mixing and dilution that occurs after impingement (Roberts *et al.*, 1997; Shao & Law, 2010). Characteristics of the radially spreading layer as it moves away from the source are the focus of the current section, since the majority of observed flow along the boundary is in this direction (Section 6.4.1). The radially spreading layer is defined here to begin where horizontal velocity decreases and spread increases with path length along the boundary.

The spread of discharge width for the flow along the boundary is shown in figure 6.17 for all experiments. The spread rates for all source angles are similar. A linear regression was determined for all experiments at each angle, without considering the effect of different source heights as no dependence could be found. The spread rate for 30° discharges is 0.043 ± 0.022, which is similar to the spread rate of 0.044 ± 0.026 for 45° discharges. The spread rate for 60° discharges of 0.049 ± 0.030 is slightly higher than the lower angles. However, the standard deviations of the linear regressions show large variability in the spread rates, which could result from some undetermined influence of source height. The spread rates are lower than the value of 0.09 measured by Launder & Rodi (1983) for air wall jets. The lower spread rates and high variability in measured values could be due to limited spatial resolution of the system. No measurements were obtained close to the boundary, which is where the maximum velocity is located. Underestimating the magnitude and location of the maximum velocity would decrease calculated spread rates. The vertical intercept of the linear regression increases for increasing source angle. This is due to the longer path lengths to the impingement region, and therefore the start of the radially spreading layer, for higher source angles (Table 6.2).

The components of mean centreline velocity in the radially spreading layer are shown in figure 6.18 for each source angle. Vertical velocities remain close to zero for all experiments at all source angles. Horizontal velocities decrease with increasing path length along the boundary, with the gradient of horizontal velocity also decreasing with path length. The form of the horizontal velocity decay is similar between different source angles. However, there is an offset between source angles due to different path lengths at the start of the radially spreading layer, as previously mentioned. Papakonstantis & Christodoulou (2010) measured the time-dependent velocity of the initial propagating radially spreading layer across a horizontal boundary. However, the steady state velocity fields measured in the present study cannot be directly compared to the findings of Papakonstantis & Christodoulou (2010). The initial behaviour of INBJs, before boundary influence, is different to steady state behaviour. Ferrari & Querzoli (2010)

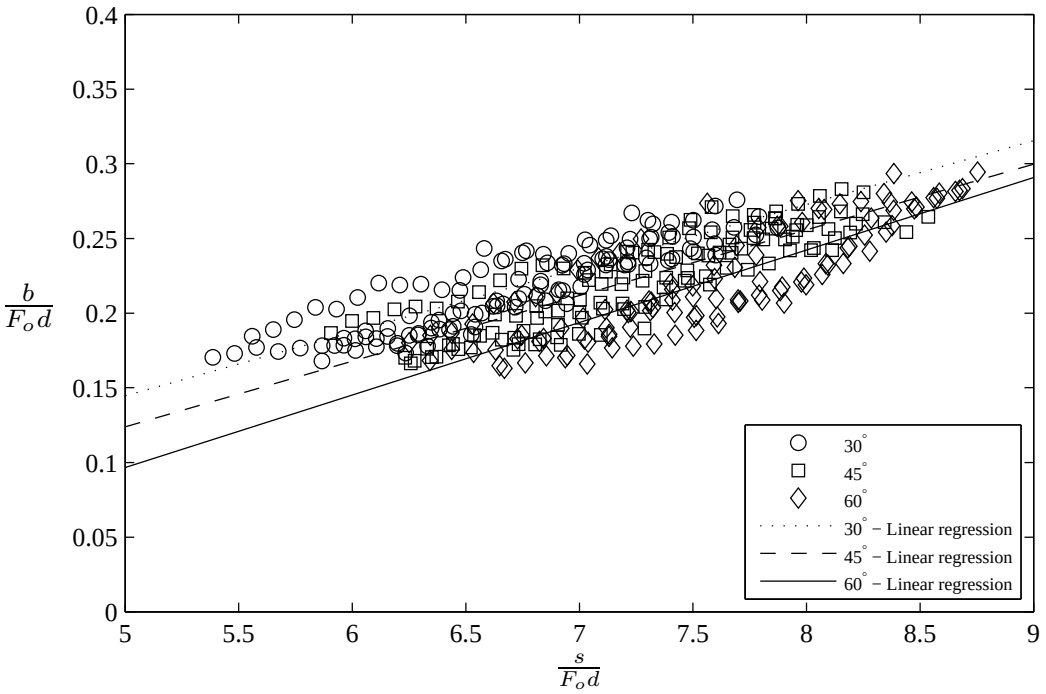

Figure 6.17 – Comparison of spread in the radially spreading layer for all 30°, 45°, and 60° experiments. Linear regression was applied to all experiments at each angle.

found the initial height of the outside edge of INBJs was higher than the steady state value for $\theta_o = 75°$. This was likely due to the initial discharge entraining more ambient fluid through the front of the flow, reducing the relative size of the buoyancy force. Therefore, the behaviour of the flow during and after impingement with the lower boundary is also likely to be different for initial and steady state conditions.

Mean velocity profiles are shown in figure 6.19 for one experiment at 45° to illustrate the behaviour. Profiles do not appear to be self-similar because the vertical distance above the boundary is used on the vertical axis. The spread of the flow along the boundary results in horizontal velocities moving away from the boundary. Figure 6.15 shows that profiles along the boundary ($z_B/(F_o d) = 0.04$) are self-similar when radial distance is non-dimensionalised by discharge width. Horizontal velocity profiles have a form similar to the half-Gaussian curve plotted for $s/(F_o d) = 6.70$. Vertical velocities are negative above the boundary due to the radially spreading layer entraining ambient fluid from above. The decrease in velocity near the boundary measured by Shao & Law (2010) is not observed in the current profiles due to the limited spatial resolution of the system. The real maximum velocity may be below the first data points above the boundary and the value determined here would underestimate the real value. A Gaussian distribution was fitted, for simplicity, to horizontal velocity profiles from figure 6.19. The data was reflected about the location of the lower boundary to fit a full Gaussian distribution. The measured velocity was found to underestimate maximum Gaussian velocity by an average of 11%, while spread was underestimated by an average

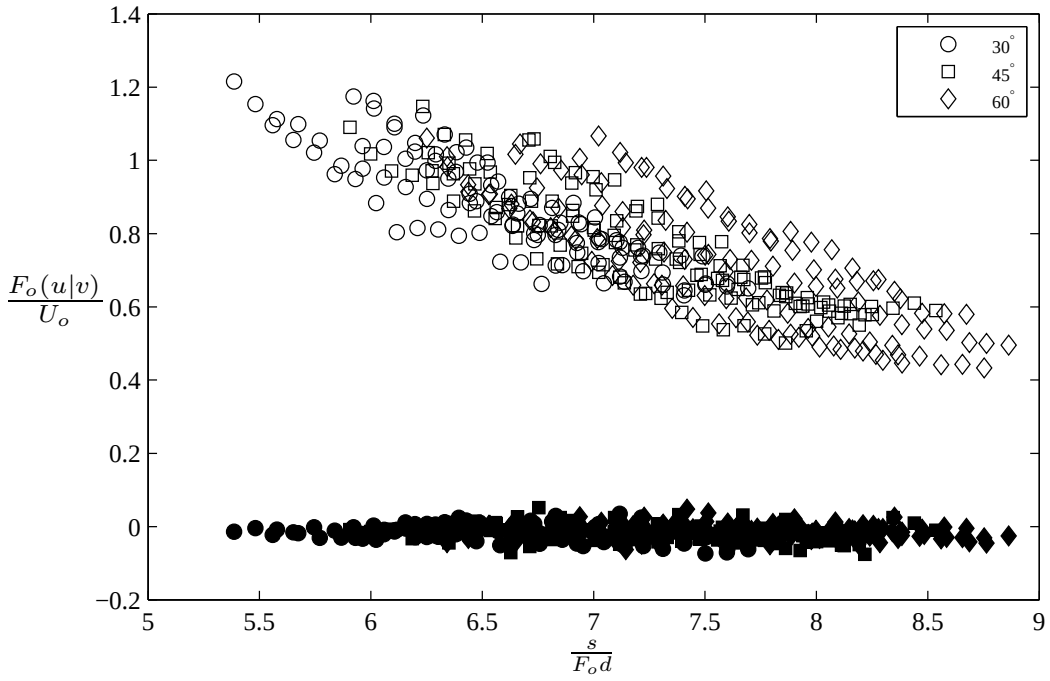

Figure 6.18 – Comparison of mean centreline velocity components in the horizontal (u) and vertical (v) directions for the radially spreading layer of all 30°, 45°, and 60° experiments. Unfilled symbols: horizontal velocity, filled symbols: vertical velocity.

of 12%.

Centreline turbulent kinetic energy (k), non-dimensionalised by mean centreline velocity (u_c), for the full path length of the flow is shown in figure 6.20. Non-dimensionalised centreline k values are relatively constant before the return point, before values increase as the flow approaches the boundary (Figure 6.11). Values then level off in the impingement region ($4 \lesssim s/(F_o d) \lesssim 5$). An increase in values is shown for the radially spreading layer for $s/(F_o d) > 6$. Non-dimensionalised k values are higher than excepted due to inconsistent particle matching near the boundary that artificially increase measured values. The horizontal axis is shortened to remove unrealistic data along the boundary (Figure 6.11). Roberts *et al.* (1997) found turbulence to collapse at ($x/(F_o d) = 9.0$) for concentration experiments. The limited dimensions of the circular raised platform in the present study resulted in measurements being limited to $x/(F_o d) \approx 7$. The increase in centreline k values along the boundary further indicates that additional mixing occurs in this region.

Experiments were typically conducted with a vertical laser sheet through the centre of the flow. However, this limited the observed area to a specific cross-section. To obtain additional information about the radially spreading layer, velocities were measured across the circular raised platform in three experiments. Using a second scanning mirror, a horizontal laser sheet was produced 10 mm above the raised platform. The intensity of the laser sheet was uneven, however it was sufficient to illuminate the tracer

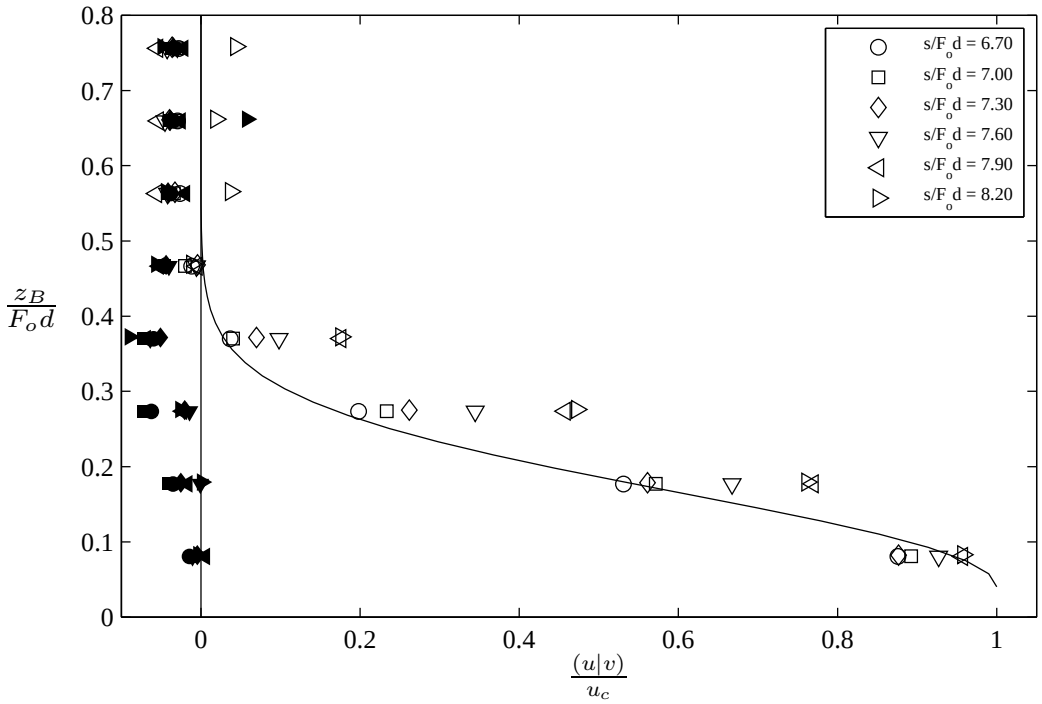

Figure 6.19 – Comparison of mean velocity profiles in the radially spreading layer for one experiment at 45°, $F_o = 31.0$ $H_o/(F_o d) = 0.88$. Half-Gaussian curve plotted was determined using the spread width of the flow for $s/(F_o d) = 6.70$.

particles that were recorded with a camera positioned above the circular platform. One typical experiment was carried out with the horizontal laser sheet for each source angle. The non-dimensional height of the horizontal laser sheet was $z_B/(F_o d) \approx 0.07$, which corresponds to the first data points above the boundary for experiments conducted with the vertical laser sheet (Figure 6.19). The absolute velocities in the whole of the radially spreading layer for one 45° experiment are shown in figure 6.21. The source is located just to the left of the image at roughly the centre of the figure. The figure is roughly centred on the middle of the circular raised platform. A high velocity region is located in the impingement region and velocities decrease radially away from this region. The contour profiles are approximately circular, except in the direction of the source, which is consistent with the shape of the initial propagating radially spreading layer (Papakonstantis & Christodoulou, 2010). There is a narrow low velocity region between the location of the source and the impingement region. This is consistent with the low velocities measured in the radially spreading layer moving towards the source, using the typical experimental configuration with the vertical laser sheet. This low velocity region could be the result of interaction between the detrained fluid from the inner side of the discharge and fluid moving back towards the source from the main impinging flow.

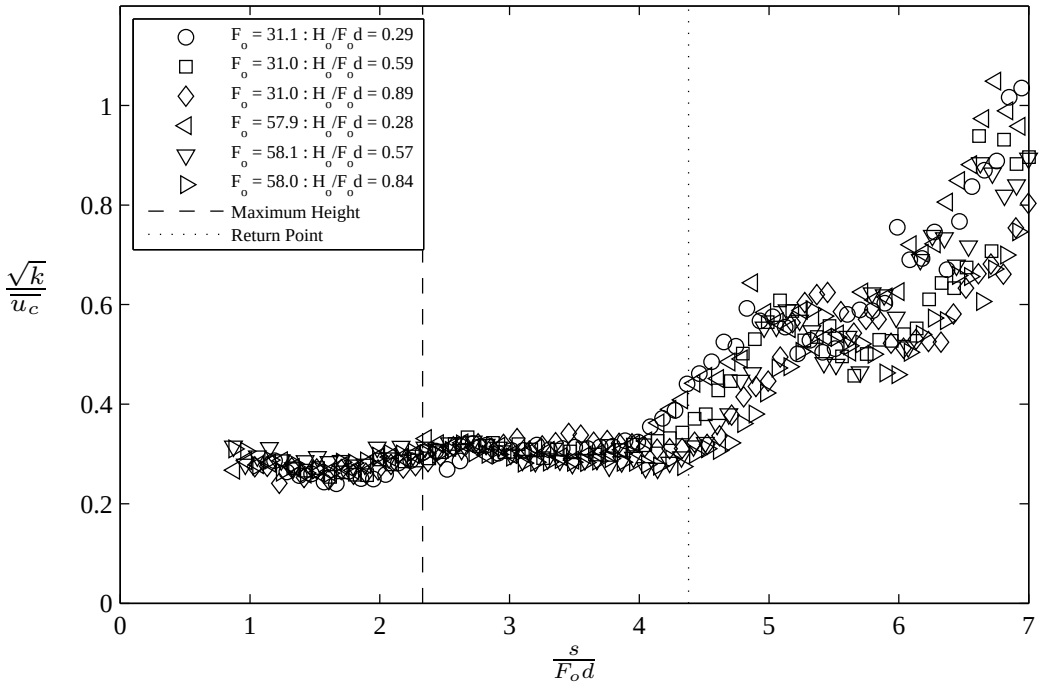

Figure 6.20 – Non-dimensionalised centreline turbulent kinetic energy (k) against path length for all 45° experiments.

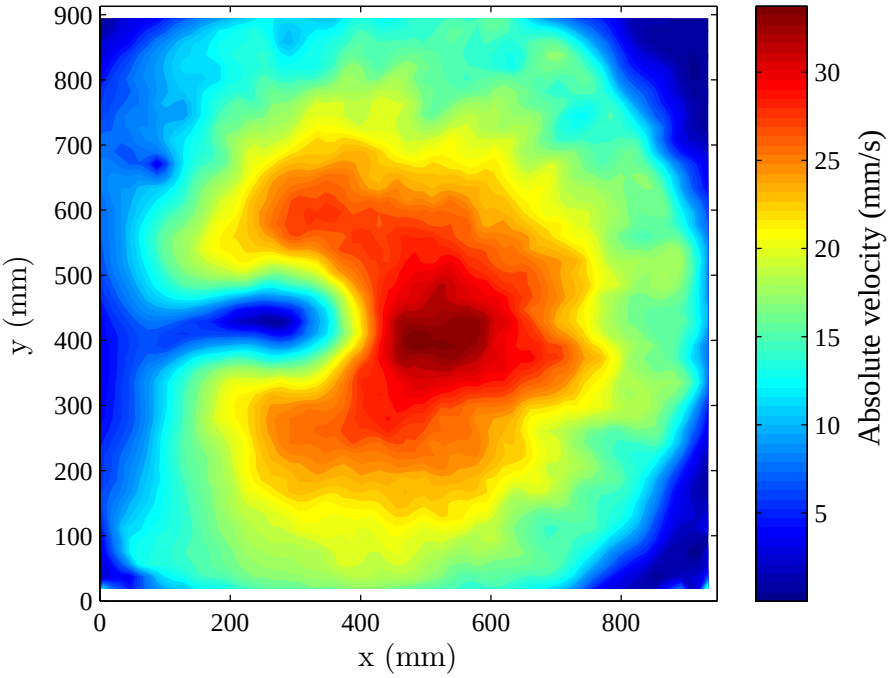

Figure 6.21 – Contours of mean absolute velocity in radially spreading layer across the boundary for one 45° experiment, $F_o = 58.1$, $H_o/(F_o d) = 0.57$. Camera located above raised platform. Source located on the left hand side.

6.5 Summary

The influence of a lower boundary on the behaviour of INBJs has not been generally addressed or quantified in previous studies. This was despite large variations in lower boundary conditions and measured dilutions at the return point between previous studies. Experimental results presented in this chapter aimed to quantity when and how the presence of a lower boundary influences the observed flow behaviour. Results from experiments conducted with boundary influence were compared to results from chapter 5, where there was no boundary influence. Comparison of experimental coefficients at maximum height found the presence of the lower boundary did not affect flow behaviour at this location (Table 6.1). However, experimental coefficients at the return point were substantially affected by the presence of the boundary (Table 6.2). The horizontal distance to the outside edge of the flow at the return point was comparatively further away from the source when a boundary was present. Also, higher variability in coefficients when a boundary was present indicated that behaviour was dependent on source height. The magnitude of centreline velocity at the return point was found to decrease with decreasing non-dimensional source height. The direction of centreline velocity also became closer to horizontal for decreasing non-dimensional source height (Figure 6.4). This was due to the return point being located further into the impingement region for lower source heights. The spread rates on the outer side of discharges were linear before impingement with the boundary, which is consistent with flow behaviour without the boundary (Figure 6.5). The spread rates on the inner side decreased between maximum height and the return point due to the presence of the boundary. The location of maximum discharge width was dependent on the non-dimensional source height of each experiment. Non-dimensionalised trajectories collapsed for all experiments until the presence of the lower boundary redirected the flow horizontally (Figure 6.6). An inflection point was found for each experiment where the flow began to be redirected by the boundary. The height of the inflection point above the boundary for all source angles was found to be linearly dependent on the distance of maximum height above the boundary by the following relationship, $z_i + H_o = 0.50(z_m + H_o)$ (Figure 6.7).

Non-dimensionalised mean centreline velocity components generally collapsed with path length for different Froude numbers (Figure 6.8). However, the distribution of non-dimensional velocity values widened in the impingement region due to differing source heights. Horizontal and vertical components of centreline velocity collapsed when scaled with the height above the boundary for different source heights (Figure 6.10). However, the distribution of vertical velocity values widened near the boundary. The dimensional proximity of the boundary was found to be critical in the decay of vertical velocity near the boundary. Centreline turbulent kinetic energy, non-dimensionalised by mean centreline velocity, collapsed for non-dimensionalised height above the boundary

at different Froude numbers and source heights (Figure 6.11). Values were relatively constant above the boundary, before turbulent kinetic energy increased as the flow approached the boundary.

The start of the impingement region was located where the presence of the lower boundary influenced flow behaviour. The inflection point was the highest location above the boundary where a change in flow behaviour was detected, however the magnitude of the changes here was small. Closer to the boundary, local minimums of horizontal and vertical mean centreline velocity signified locations where the flow was substantially affected by the presence of the boundary. Locations of minimum horizontal and vertical velocity above the boundary were found to be proportional to the distance of maximum height above the boundary by $z_B = 0.276(z_m + H_o)$-0.057 and $z_B = 0.265(z_m + H_o)$+0.269 respectively (Figure 6.13). However, there was some variability in the locations determined for local extrema due to low velocity gradients near these locations and experimental noise. The vertical component was affected by the presence of the boundary before the horizontal component and therefore the relationship for vertical velocity above shows the location of the start of the impingement region above the boundary. Profiles of mean vertical velocity remained self-similar on the outer side of discharges until the centreline value was reduced by the presence of the boundary (Figure 6.15). Profiles of mean horizontal velocity indicated a wall jet type flow along the boundary after the redirection of the flow. Profiles of turbulent intensities showed that behaviour was distorted by the redirection of flow with higher turbulent kinetic energy and turbulent shear intensity values on both sides of the discharge near the boundary (Figure 6.16).

The beginning of the radially spreading layer was defined as the location where horizontal velocity decreases with path length and spread increases with path length along the boundary. The spread rates for the radially spreading layer were linear and of similar magnitudes for all source angles (Figure 6.17), however spreading rates were lower than previously reported for wall jets. This was possibly due to the spatial resolution of the PTV experimental system resulting in a gap between the boundary and the first data points. The maximum velocity could have been located in this gap, resulting in an underestimation of centreline velocity and spreading rates by 11% and 12%, respectively, in comparison to a Gaussian distribution. Non-dimensionalised turbulent kinetic energy increased as the flow moved along the boundary, indicating additional mixing and dilution. The diameter of the raised platform used as the lower boundary in the experimental configuration was limited by the dimensions of the experimental tank. The effect of the diameter of the raised platform on observed behaviour was not directly determined. The range of source heights used in the experiments resulted in different horizontal locations of impingement (Figure 6.6). This resulted in a range of horizontal distances to the edge of the boundary between different experiments. However, the

non-dimensional discharge width (Figure 6.5) and mean centreline velocity (Figure 6.8) collapse along the boundary in the radially spreading layer. This indicates that different horizontal distances to the edge of the boundary do not affect observed behaviour.

[Intentionally left blank]

Chapter 7

Conclusions

Desalination plants have become a preferred method of supplementing the potable water supply in many semi-arid and arid regions around the world. Inclined negatively buoyant jets (INBJs) are produced when the hyper-saline brine produced by desalination plants is discharged at an upward inclined angle via an offshore pipeline and diffuser system. Research into the behaviour of these discharges has expanded due to the increase in the number and scale of desalination plants and their potential to create substantial environmental impacts. There are numerous experimental studies that empirically relate geometric parameters and dilution to source conditions. Substantial scatter exists between the measured dilutions of previous studies. The wide variation of lower boundary conditions adopted between studies is a possible cause of this scatter. Many studies did not specifically consider the effects of the lower boundary on flow behaviour. However, empirical relationships are important for practical design as commercial integral models significantly under predict the experimentally measured dilutions. Integral models used to predict the behaviour of INBJs have been developed from models for positively buoyant jets, but these have had limited success due to the additional detrainment and re-entrainment flow features of INBJs. In addition, integral models do not consider the influence of a lower boundary. This makes direct comparison between model predictions and previous studies difficult, because the majority had a lower boundary influencing observed flow behaviour and the effect of the boundary was not quantified. There is also limited velocity field experimental data available, which is critical for the development of improved predictive models. In the present study, velocity field information was experimentally measured using particle tracking velocimetry. Experiments were conducted with and without the influence of a lower boundary on the observed flow behaviour, so that the influence of the lower boundary could be assessed.

Integral models are a mathematical representation of mean flow behaviour that predict geometric parameters, momentum, and dilution of discharges. Commercial integral models (CorJet, VISJET, and Visual Plumes) predict the behaviour of discharges for

many different flow scenarios, including moving and stratified ambient conditions. It is evident that dilution predictions of all commercial integral models are very conservative, because they substantially underestimate experimentally measured dilutions at maximum height and the return point. Integral models developed specifically for desalination discharges, such as Papanicolaou *et al.* (2008), Yannopoulos & Bloutsos (2012), and the reduced buoyancy flux (RBF) model (Oliver *et al.*, 2013), are limited to stationary ambient conditions. A stationary ambient being the worst case scenario when diluting contaminated fluid in the ambient environment. Geometric predictions of Papanicolaou *et al.* (2008) were generally better than those of commercial models. The model of Yannopoulos & Bloutsos (2012) assumes a loss of buoyancy to simulate detrainment of negatively buoyant fluid from the inner side of discharges due to unstable stratification. However, predictions overestimated measured dilutions indicating buoyancy flux loss is incorrectly modelled. The RBF model assumes that INBJs have the same dilution rates as pure jets up to maximum height. This assumption results in the loss of buoyancy flux, which improves model predictions of dilution at maximum height and the return point compared to commercial models. However, the RBF model does not physically model the mechanism of buoyancy flux loss, rather an assumption is applied that gives the required amount of buoyancy loss to improve predictions.

The purpose of the new detrainment model developed in the present study was to improve predictions of INBJs using a physically based mechanism to represent detrainment on the inner side of discharges. Detrainment from the main flow occurs when negatively buoyant fluid parcels move sufficiently far away from the flow, which the shear generated turbulent eddies are unable to re-entrain these fluid parcels. Therefore, buoyancy loss for the detrainment model along the trajectory of discharges is dependent on the local parameters that affect the inertial and gravitational forces of the flow. Geometric predictions by the detrainment model underestimated the mean experimental values for the source angles assessed. However, geometric predictions were better than those of commercial models (CorJet, VISJET, Visual Plumes) and similar to those of the RBF model. Dilution predictions by the detrainment model underestimated experimental values at maximum height and were within the scatter of experimentally measured values at the return point. Dilution predictions at maximum height and the return point were again better than those of commercial models (Figures 3.3 and 3.4). The small difference between dilution predictions and experimental values indicated that the overall loss of buoyancy flux is being represented well by the detrainment mechanism incorporated into the new detrainment model.

The experimental system was able to obtain detailed two-dimensional velocity field information from INBJs using particle tracking velocimetry. This non-intrusive flow visualisation technique involved seeding the discharged fluid and the ambient fluid with small tracer particles. Tracer particles were illuminated with a thin sheet of laser

light, which allowed the motion of particles to be recorded by a video camera located perpendicular to the discharge. The physical location of tracer particles was recorded by a video camera at a constant frame rate, allowing the velocity to be determined by the change in location of the particles between frames. The velocity of the fluid could be directly inferred from the velocity of the tracer particles, because they were fully mixed and essentially alike. The particle tracking velocimetry system was verified with horizontal pure jet experiments. The performance of the experimental system was satisfactory for determining the mean and turbulent statistics of jet discharges. Mean centreline velocity and spread were within the values of previous studies. Turbulent intensity profiles were very similar in shape to previous studies and were self-similar for different path lengths. However, the centreline magnitudes of axial and normal turbulent intensities were lower than previous studies. This is possibly due to the limited scale of eddy sizes captured by the experimental system. The spatial resolution of the system prevented the movement of small scale eddies from being captured. However, the system captured the movements of larger scale eddies, which contain the majority of momentum and energy in the flow.

INBJ experiments were conducted without the influence of a lower boundary for source angles of 15°, 30°, 45°, 60°, 65°, 70°, and 75°. In total, 49 experiments were conducted, with initial Froude numbers between 10.1 and 81.0. The source was a minimum of 655 mm above the bottom of the experimental tank to ensure there was no lower boundary influence on the observed flow behaviour. Geometric parameters were extracted from mean velocity fields measured using particle tracking velocimetry. All geometric parameters specified, non-dimensionalised by the source diameter, were directly proportional to initial Froude number. This was consistent with dimensional analysis relationships and allowed experimental coefficients to be calculated for each geometric parameter. Experimental geometric coefficients from the present study were generally within the scatter of data of coefficients from previous studies. Geometric coefficients from all previous studies were determined using concentration measurements. Coefficients from the present study were generally greater than the average of previous experimental values across the range of source angles. This could be due differences in the location of local maximum concentration and local maximum velocity. The influence of a lower boundary on geometric parameters determined by previous studies would alter geometric coefficients at the return point.

Mean velocity experimental data illustrated the complex flow behaviour of INBJs. Non-dimensionalised centreline velocity at maximum height and the return point were found to be directly proportional to initial Froude number, which was consistent with dimensional analysis relationships. Centreline velocity at maximum height was found to decrease for increasing source angle. Horizontal momentum fluxes are lower at maximum height for higher source angles due to vertical momentum fluxes being zero,

resulting in lower centreline velocities. Centreline velocity at the return point was found to decrease for increasing source angle up to 65°, before centreline velocity increased for higher angles. Limited velocity data from previous studies was available for comparison. An experimental coefficient at maximum height for 60° discharges was extracted from Lai & Lee (2012) and was found to be lower than the value from the present study. Predictions by commercial models and the detrainment model all underestimated the measured velocity coefficients for all source angles at maximum height and the return point. However, predictions by the detrainment model were found to be more accurate than those of commercial models. Detrainment model predictions underestimated experimental coefficients at the return point more substantially than at maximum height. This was possibly due to less overall detrainment occurring at maximum height, when compared to the return point.

Velocity profiles illustrated the unique asymmetric behaviour of INBJs that is not seen in pure jets and plumes or positively buoyant jets discharged upwards. Non-dimensionalised axial and radial velocity profiles collapsed at maximum height and the return point for different initial Froude numbers at each source angle. Axial velocity profiles collapsed and remained Gaussian on the outer side of discharges for the full trajectory of discharges. Radial velocity profiles on the outer side also collapsed and showed entrainment occurring. Axial velocity profiles were non-Gaussian on the inner side of discharges and detrainment was evident in the radial velocity profiles on the inner side. Velocity profiles on the inner side were dependent on path length, with the maximum radial detrainment velocities occurring near maximum height. Predictions of the radial velocities by the detrainment model were found to have similar form to measured radial velocities on the inner side of discharges. Velocities measured by the experimental system were of the mixed fluid and ambient fluid. Parcels of negatively buoyant detrained fluid drag the surrounding ambient fluid downwards, increasing the measured velocities of the mixed fluid. Therefore, measured radial velocities provide an upper limit to radial velocities.

Fluctuating characteristics of INBJs showed the structure of mixing was substantially different between the inner and outer sides of discharges. A stabilising density gradient on the outer side of discharges resulted in mixing behaviour that was similar to jets at maximum height and similar to plumes at the return point. The destabilising density gradient on the inner side resulted in the collapsing of the mixing structure with distance from the source, shown by turbulent intensity profiles becoming more distorted.

Fluctuating characteristics were found to be similar for all Froude numbers at the source angle of 60° at maximum height and the return point. Turbulent kinetic energy profiles had a similar form and magnitude for the full path length, but turbulent intensity and mean vorticity varied substantially with path length. The large-scale mixing structures disintegrated on the inner side of discharges due to detrainment

caused by the unstable density stratification. Mean vorticity profiles showed rotational fluid moving further away from the centreline on the inner side of discharges due to the unstable stratification.

Turbulent kinetic energy and mean vorticity profiles were strongly dependent on source angle at maximum height, whereas the form of these profiles was similar at the return point for the range of source angles. Flow behaviour at maximum height was more variable between different source angles due to the redirection of the flow and detrainment. Whereas, the flow was fully plume-like and moving in a similar direction at the return point.Turbulent shear intensity profiles had a strong dependence on source angle at both maximum height and the return point.

The influence of a lower boundary was determined by placing a raised platform inside the experimental tank. Experiments were conducted with this configuration for the source angles of 30°, 45°, and 60° for the non-dimensional source heights between $0.28 \leq H_o/(dF_o) \leq 0.89$. Discharges were visually observed to impinge upon the lower boundary and to form a radially spreading layer along the boundary. The presence of a lower boundary did not affect experimental coefficients at maximum height. The spread rates on the outer side of discharges were linear before impingement, while spread rates on the inner side increased but then decreased between maximum height and the return point due to the presence of the boundary. The location of the decrease in spreading rates was dependent on the non-dimensional source heights.

An inflection point in flow trajectory was the highest location above the boundary where an influence was determined, however the magnitude of the influence at this location was minimal. The started of the impingement region was where the presence of the lower boundary noticeably influenced flow behaviour. Experimental coefficients at the return point were substantially altered by the presence of the boundary. Lower source heights resulted in the return point being closer to the boundary, where the flow is redirected. Thus, for lower source heights, velocities at the return point had a lower magnitude and a direction closer to horizontal. Locations of minimum horizontal and vertical velocity signified substantial changes in flow behaviour due to the presence of the boundary. These were found to be proportional to the distance of maximum height above the boundary for all source angles. The local minimum of vertical velocity occurred before the local minimum of horizontal velocity. Profiles of mean velocity and turbulent intensities were distorted in the impingement region due to the redirection of the flow. Centreline turbulent kinetic energy collapsed for non-dimensionalised heights well above the boundary and values increased as the flow approached the boundary.

A radially spreading layer formed along the boundary after the impingement. Profiles of mean horizontal velocity indicated a wall jet type flow and profiles were self-similar. The spread rates were linear and of similar magnitudes for all source angles. It is possible that the maximum velocity could have been located in a gap between the boundary and

the first data points, resulting in an underestimation of centreline velocity and discharge width. Non-dimensionalised turbulent kinetic energy increased as the flow moved along the boundary, indicating additional mixing and dilution. Non-dimensional discharge width and components of centreline velocity decay collapsed for all experiments with different distances between the impingement region and the edge of the boundary. This indicates that the diameter of the raised platform, which was limited by the dimensions of the experimental tank, did not affect observed flow behaviour.

7.1 Future Work

There is substantial scope for further work on inclined negatively buoyant jets. The majority of experiments have been conducted along the centreline of discharges, however little is known about the distribution of concentration and velocity in two-dimensional cross-sections perpendicular to the centreline. In addition, further experimental studies are required to understand the behaviour of discharges in stratified or flowing ambient conditions. Further experimental velocity and concentration data without the presence of the boundary is needed to verify the results found in the present study and that of Oliver (2012). This would assist in the direct comparison of predictive models where the influence of a lower boundary is removed from experimental data.

Integral models have been relatively unsuccessful in predicting the behaviour of inclined negatively buoyant jets in comparison to the predictions of positively buoyant discharges. The additional flow features of detrainment and re-entrainment of inclined negatively buoyant jets are difficult to implement appropriately using integral models. Therefore, computational fluid dynamics (CFD) models, such as large eddy simulation (LES), should be the focus of future predictive modelling for these discharges. There is a need for multiple investigations into these types of models to provide a clear framework for accurate and efficient models.

Finally, there needs to be further studies into the boundary interaction of inclined negatively buoyant jets. Concentration experiments with a lower boundary present, at a range of different source heights, is needed to determine the influence of the boundary on dilution. The potential influence of the free surface on discharge behaviour is also unknown and is of importance for discharges into shallow ambient waters.

Appendix A

Experimental Conditions and Coefficients

Table A.1 – Experimental conditions and coefficients from chapter 5 of the present study.

θ_o	F_o	d (mm)	Q_o (L/min)	Duration (s)	x_m/d	z_m/d	s_m/d	U_o/u_m	b/d (at x_m)	z_{me}/d	x_r/d	s_r/d	U_o/u_r	b/d (at x_r)	x_{me}/d
15°	10.1	7.19	1.12	297	12.5	2.2	12.8	3.3	1.6	5.3	23.0	23.5	4.2	3.0	37.5
15°	18.2	7.19	2.01	278	24.0	3.6	24.3	5.4	3.1	9.7	41.8	42.7	7.0	4.6	64.2
15°	22.9	4.40	0.74	280	31.5	5.0	32.0	6.5	4.9	14.8	56.4	57.6	9.8	7.4	90.6
15°	30.5	4.40	0.98	287	44.7	7.8	45.5	7.9	5.1	17.9	76.5	78.6	12.8	9.0	114.2
15°	39.3	4.40	1.27	297	55.1	10.5	56.2	9.7	5.2	21.0	96.4	99.3	15.9	10.8	144.4
15°	46.7	4.40	1.51	297	69.4	11.2	70.6	12.1	8.7	28.6	118.1	121.1	20.0	12.2	169.7
15°	62.2	2.43	0.46	297	90.7	15.9	92.3	15.9	10.2	36.2	160.7	164.8	25.5	17.2	237.9
15°	80.4	2.43	0.59	297	117.5	21.1	119.7	19.2	11.6	44.2	200.0	205.7	31.4	22.8	297.0
30°	10.3	7.19	1.14	281	18.6	6.4	19.8	4.1	2.1	10.6	31.4	34.6	6.0	4.2	42.4
30°	18.1	7.19	1.99	297	32.8	11.5	35.1	6.3	3.4	18.2	56.2	62.1	10.3	6.5	73.6
30°	23.1	4.40	0.75	297	42.6	16.1	46.0	8.7	4.2	24.5	75.3	83.6	13.5	10.2	102.7
30°	30.8	4.40	0.99	297	58.1	21.2	62.6	11.5	5.2	31.7	100.3	111.3	18.5	14.0	137.7
30°	40.1	4.40	1.29	249	72.8	27.3	78.5	14.1	6.3	40.0	127.0	141.1	23.7	15.8	170.0
30°	46.2	4.40	1.49	199	86.7	32.2	93.6	16.2	10.2	52.6	153.5	169.8	26.3	19.8	208.7
30°	60.8	2.43	0.45	261	114.5	41.9	123.3	22.1	11.0	63.9	198.6	220.9	37.0	27.0	267.4
30°	81.0	2.43	0.59	297	152.3	56.0	164.1	28.3	18.1	92.1	265.8	294.6	45.8	35.6	362.5
45°	10.2	7.19	1.12	263	19.1	10.9	22.6	5.3	3.1	17.1	33.2	41.3	7.0	5.2	44.7
45°	18.5	7.19	2.03	297	35.0	20.8	41.8	8.6	3.9	28.7	59.3	75.6	13.0	9.7	80.8
45°	21.6	4.40	0.70	278	42.5	25.9	51.1	11.0	5.2	36.4	72.8	93.2	15.2	10.7	96.8
45°	31.1	4.40	1.00	222	61.2	38.3	73.9	15.1	7.5	53.3	105.6	135.6	21.4	16.7	143.1
45°	40.8	4.40	1.32	297	76.5	47.6	92.5	19.5	10.9	69.3	135.0	171.8	30.4	19.2	178.7
45°	45.4	4.40	1.47	297	85.2	53.6	103.0	20.9	11.2	76.0	151.9	192.6	33.6	22.1	202.9
45°	60.5	2.43	0.45	291	117.5	75.5	143.2	28.4	15.9	107.4	212.1	271.3	41.3	31.8	281.1
45°	78.8	2.43	0.59	270	160.1	97.8	192.7	38.7	19.9	137.7	273.9	351.2	52.7	40.2	363.5

Table A.1 – Experimental conditions and coefficients from chapter 5 of the present study (continued).

θ_o	F_o	d (mm)	Q_o (L/min)	Duration (s)	x_m/d	z_m/d	s_m/d	U_o/u_m	b/d (at x_m)	z_{me}/d	x_r/d	s_r/d	U_o/u_r	b/d (at x_r)	x_{me}/d
60°	10.4	7.19	1.14	230	16.8	15.8	24.1	7.3	3.1	22.0	28.9	45.5	7.8	5.5	40.4
60°	19.1	7.19	2.11	204	31.1	31.2	45.6	11.7	4.6	40.5	54.9	87.0	13.2	9.7	74.9
60°	27.5	4.40	0.92	261	43.3	45.6	65.4	17.8	7.6	60.8	78.3	126.8	19.9	16.2	112.0
60°	37.7	4.40	1.26	297	60.6	63.5	91.4	30.3	9.7	82.9	103.6	172.6	27.9	20.7	146.7
60°	44.8	4.40	1.45	194	75.2	78.1	112.5	28.7	11.0	100.1	132.3	214.6	33.5	24.0	182.8
60°	45.0	4.40	1.46	281	75.4	77.4	112.1	28.8	13.2	103.9	133.7	214.5	33.3	22.9	182.0
60°	51.1	2.43	0.37	297	87.0	87.4	128.6	32.4	14.2	115.8	150.0	244.0	37.5	32.4	217.0
60°	60.4	2.43	0.44	287	103.3	103.4	152.5	39.6	15.6	134.6	180.0	288.9	44.6	31.9	247.6
60°	80.2	2.43	0.59	297	138.1	136.5	202.4	51.8	19.9	176.3	234.3	379.8	57.9	47.1	332.4
65°	30.0	4.40	0.97	264	43.9	54.4	73.0	22.7	7.7	69.9	70.9	138.0	25.3	22.1	115.6
65°	40.0	4.40	1.29	297	59.8	73.7	99.1	27.7	11.1	96.0	101.8	188.9	27.9	24.3	151.6
65°	60.3	2.43	0.44	297	92.8	109.1	150.4	42.1	11.9	132.9	155.7	286.2	44.1	43.9	245.0
65°	80.4	2.43	0.59	250	118.7	145.8	197.0	56.5	18.8	183.4	202.8	375.4	59.9	47.1	301.7
70°	30.8	4.40	0.99	297	40.5	60.2	76.2	24.1	8.6	77.3	72.1	148.0	21.1	19.6	112.3
70°	40.0	4.40	1.29	297	52.4	77.7	99.0	31.4	12.0	101.7	91.5	191.1	27.9	25.2	143.3
70°	61.0	2.43	0.45	297	67.4	111.7	136.1	72.1	12.0	135.8	66.9	-	66.4	-	-
70°	78.4	2.43	0.58	297	106.2	154.1	195.8	59.7	20.2	194.4	177.6	374.5	55.4	45.4	269.9
75°	10.1	7.19	1.12	297	10.6	19.1	23.0	9.4	2.9	24.9	18.2	44.5	7.1	6.7	31.7
75°	17.9	7.19	1.98	297	19.6	35.6	42.7	16.6	5.3	46.2	32.2	82.4	12.7	10.8	54.0
75°	22.4	4.40	0.72	180	24.0	43.9	52.6	21.0	7.7	59.3	42.7	103.3	16.1	15.2	73.5
75°	30.8	4.40	0.99	127	26.1	57.1	64.8	35.8	10.8	78.6	32.1	-	31.0	32.9	-
75°	39.4	4.40	1.27	287	42.0	80.7	96.0	34.3	10.7	102.1	71.7	188.3	26.9	27.8	127.6
75°	50.7	2.43	0.38	297	57.6	102.6	124.1	43.2	14.1	130.8	97.2	240.5	36.0	33.5	164.8
75°	60.1	2.43	0.44	297	63.7	118.4	140.9	90.2	16.0	150.5	65.6	-	60.4	71.0	-
75°	78.7	2.43	0.58	297	78.5	150.6	177.2	82.9	18.9	188.4	93.7	-	72.5	85.0	-

Appendix B

Additional Figures

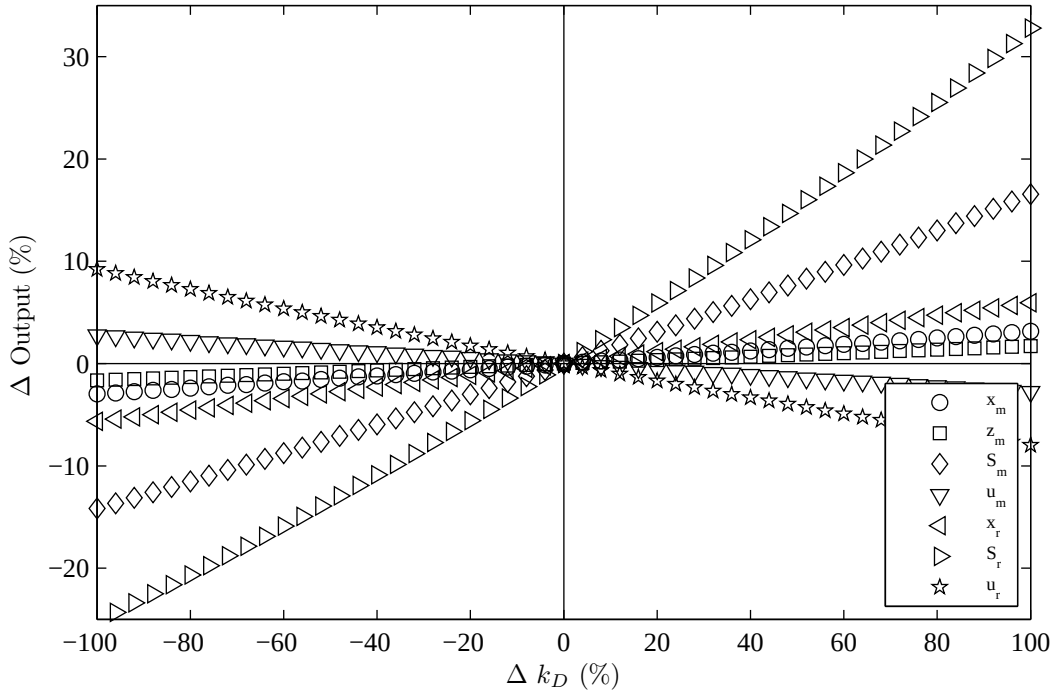

Figure B.1 – Sensitivity analysis of detrainment model output parameters to k_D at the source angle of 45°, base k_D value of 0.25.

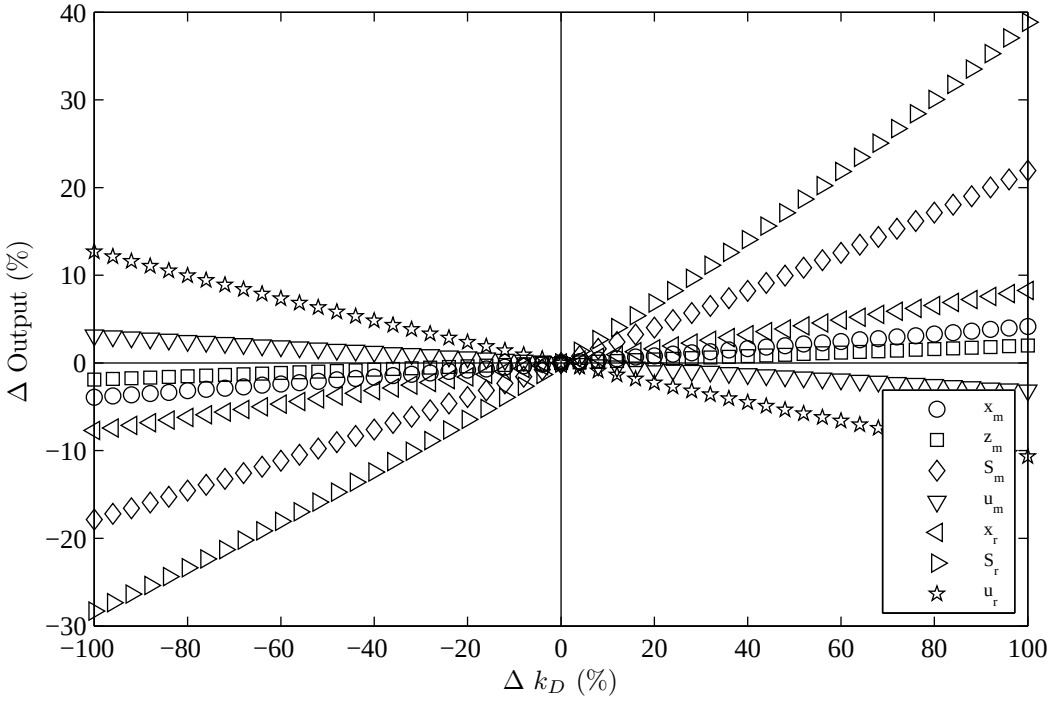

Figure B.2 – Sensitivity analysis of detrainment model output parameters to k_D at the source angle of 60°, base k_D value of 0.25.

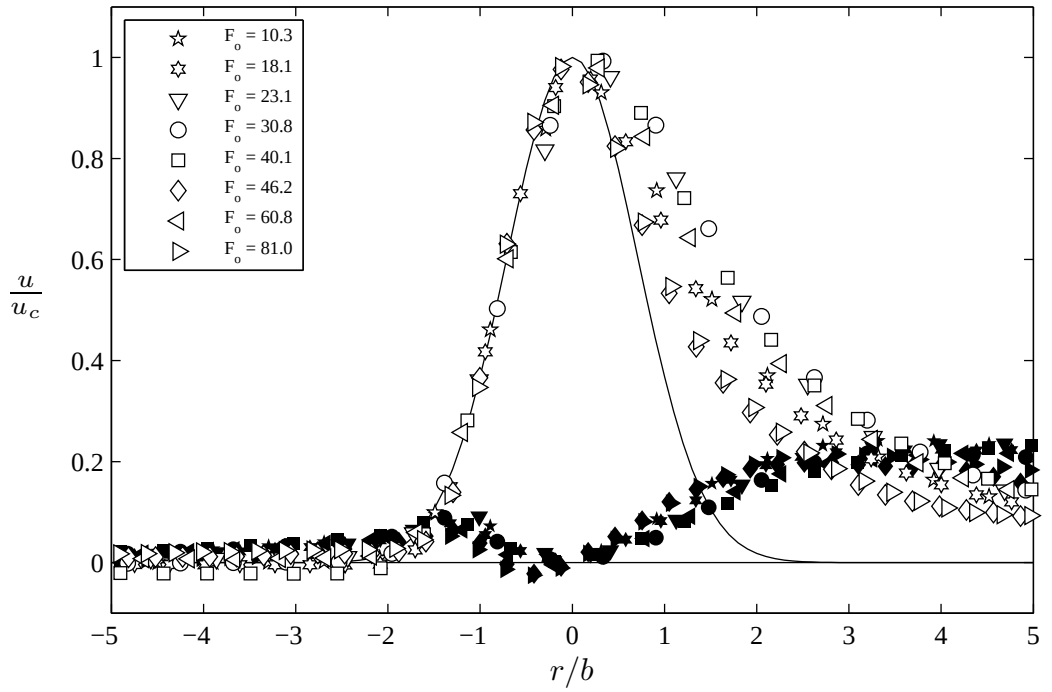

Figure B.3 – Velocity profile components at maximum height for 30° experiments, unfilled symbols: axial (u_s), filled symbols: radial (u_n).

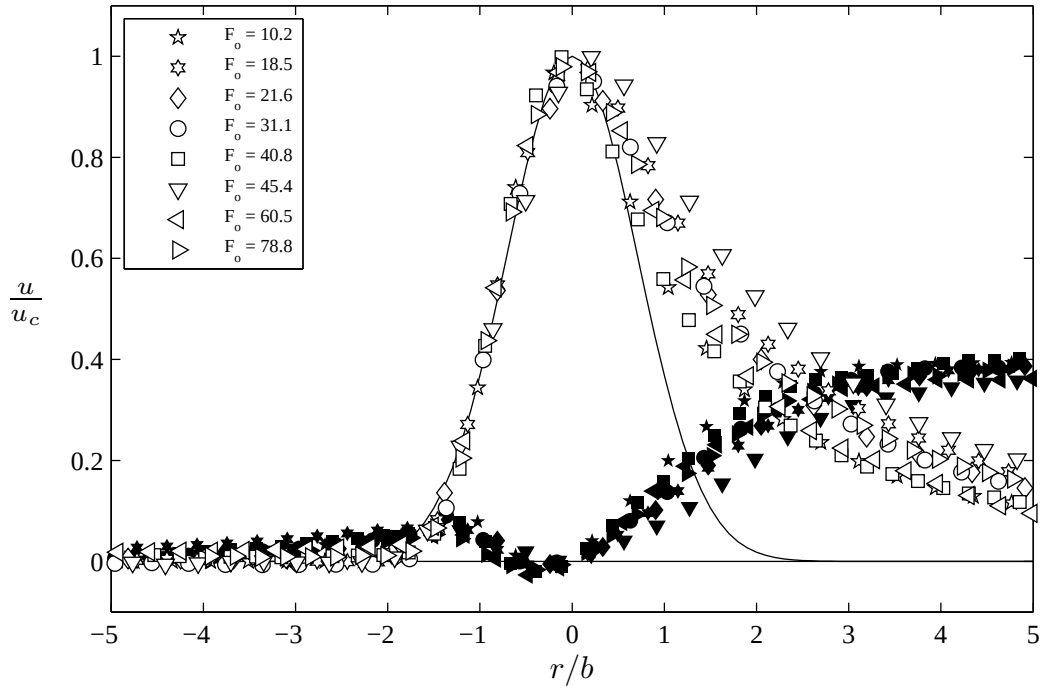

Figure B.4 – Velocity profile components at maximum height for 45° experiments, unfilled symbols: axial (u_s), filled symbols: radial (u_n).

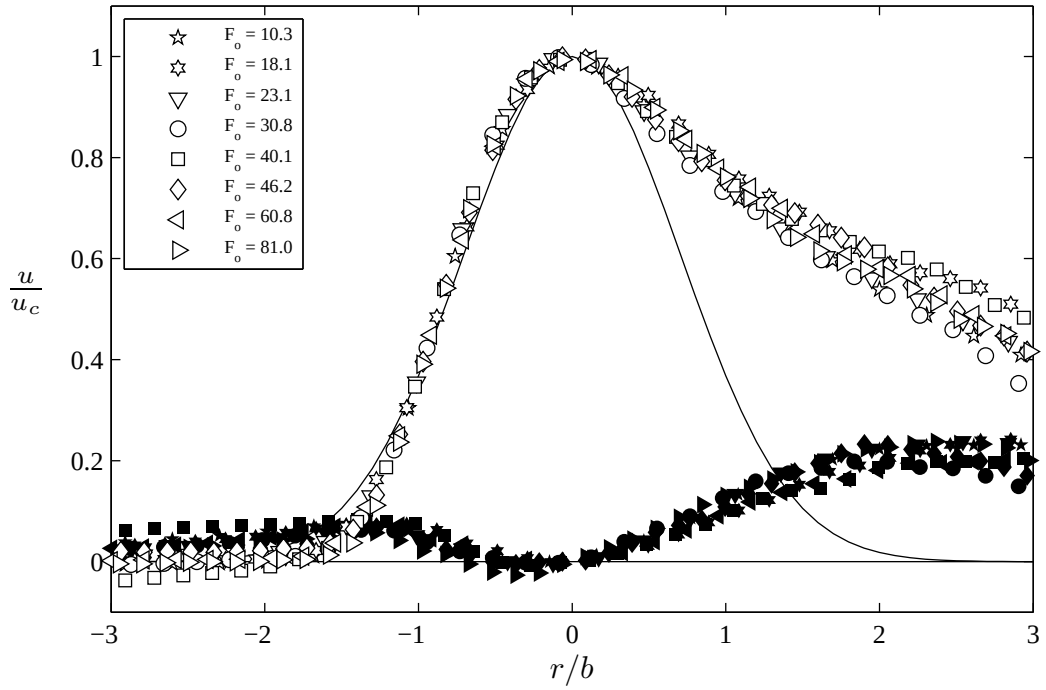

Figure B.5 – Velocity profile components at return point for 30° experiments, unfilled symbols: axial (u_s), filled symbols: radial (u_n).

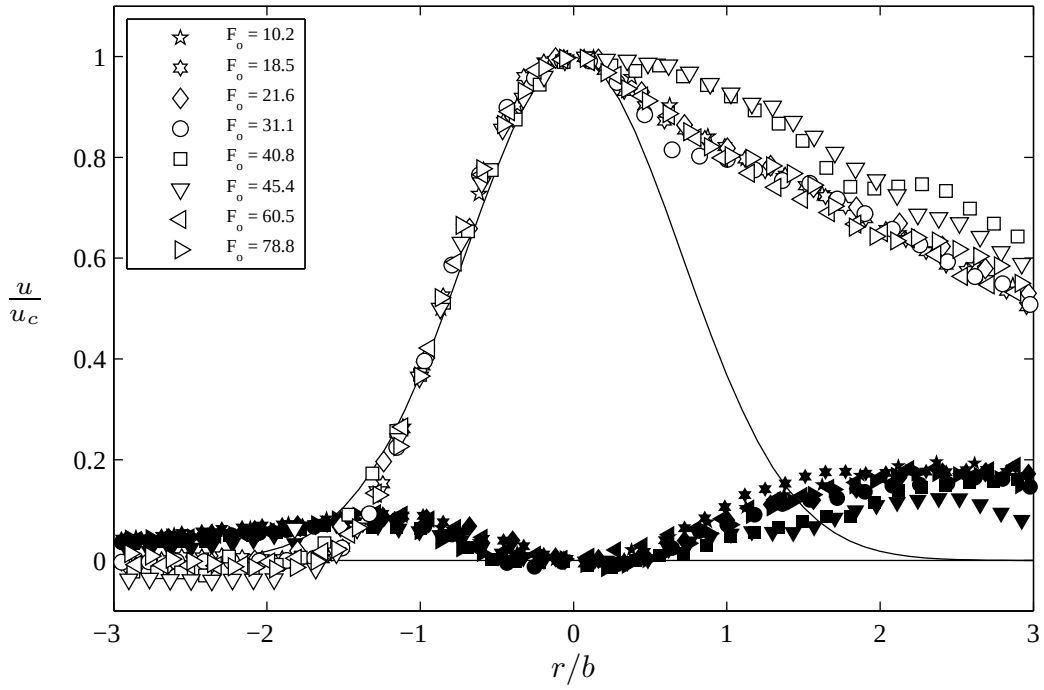

Figure B.6 – Velocity profile components at return point for 45° experiments,unfilled symbols: axial (u_s), filled symbols: radial (u_n).

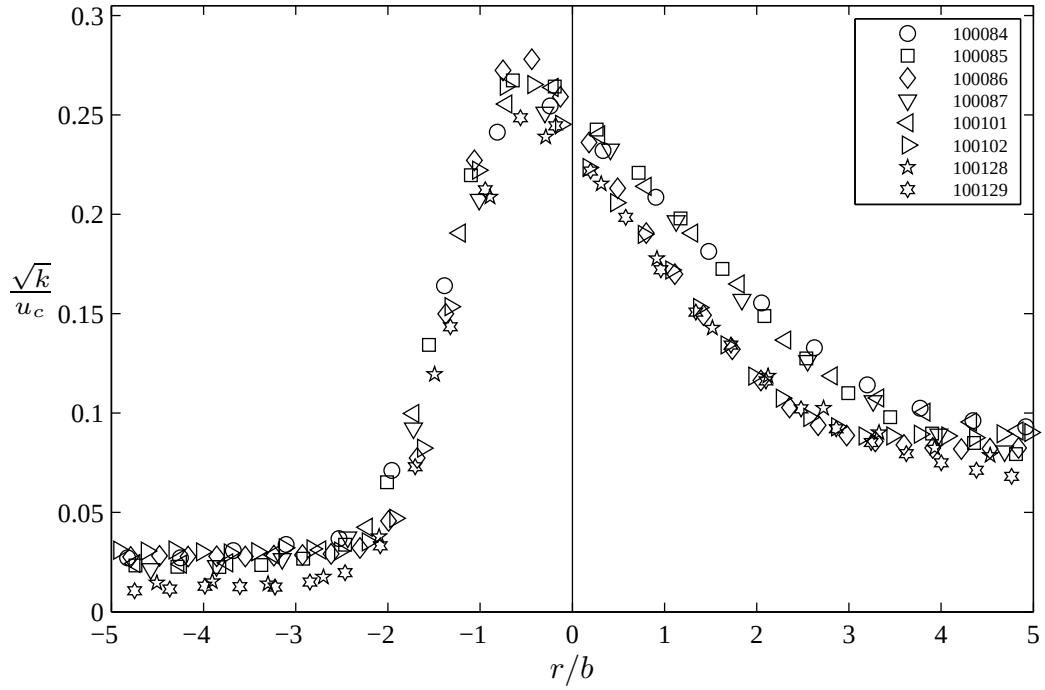

Figure B.7 – Turbulent kinetic energy (k) profiles at maximum height for all 30° experiments.

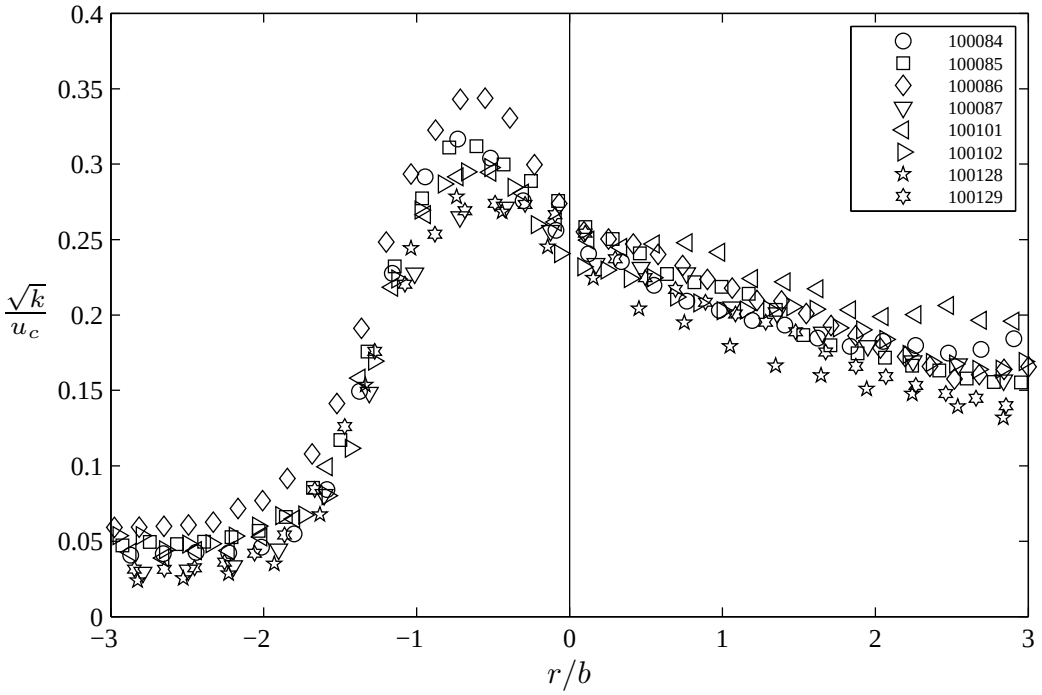

Figure B.8 – Turbulent kinetic energy (k) profiles at return point for all 30° experiments.

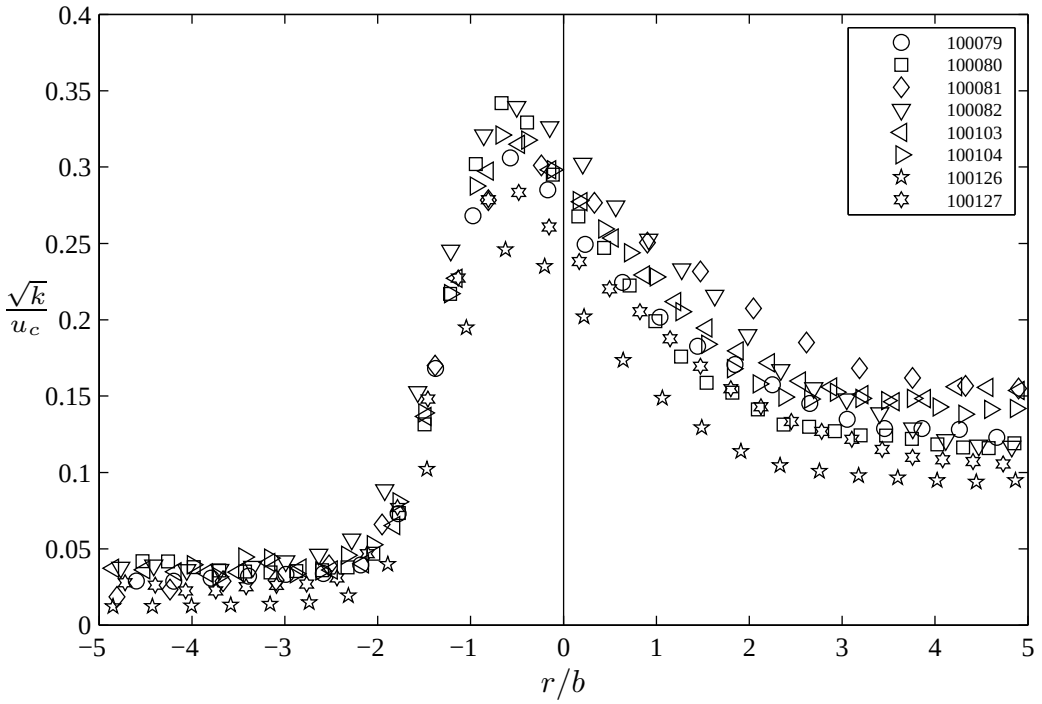

Figure B.9 – Turbulent kinetic energy (k) profiles at maximum height for all 45° experiments.

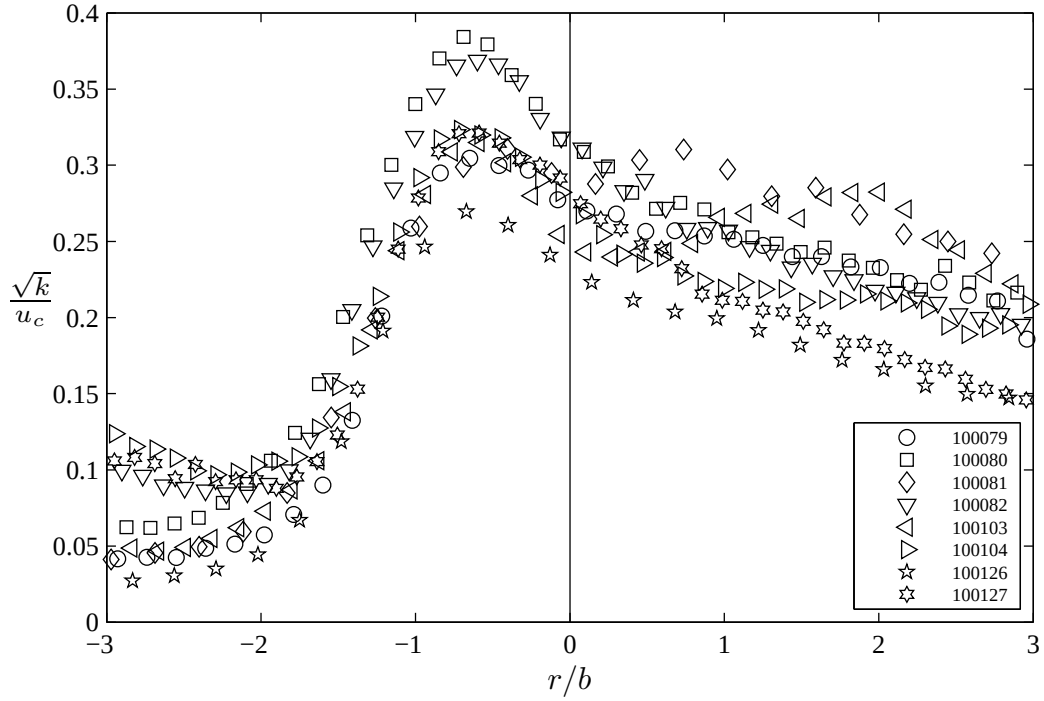

Figure B.10 – Turbulent kinetic energy (k) profiles at return point for all 45° experiments.

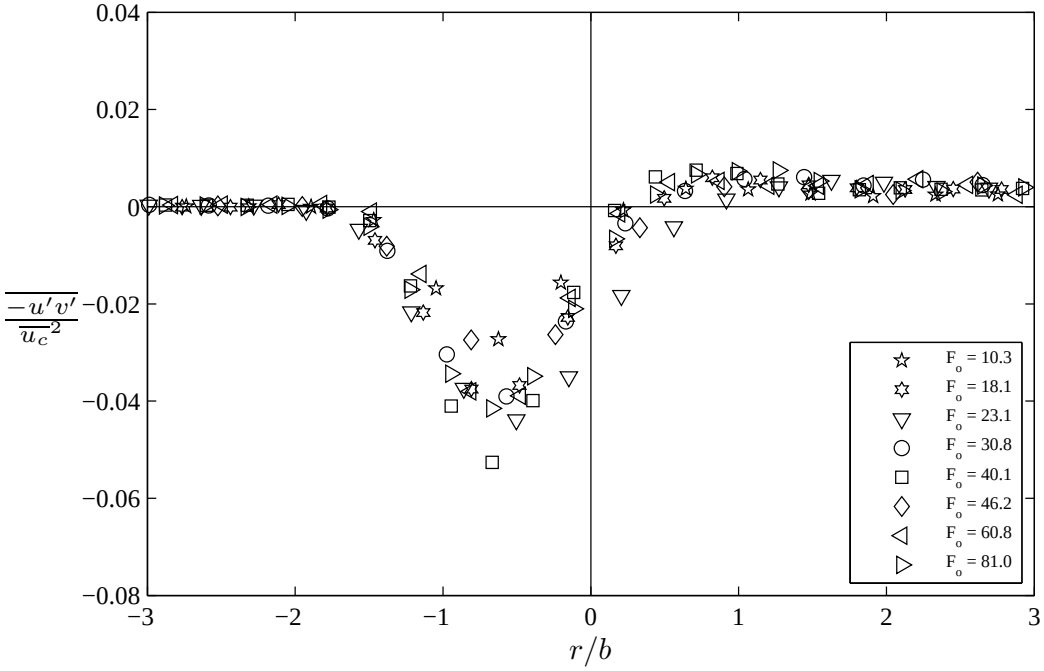

Figure B.11 – Turbulent shear intensity profiles at maximum height for all 30° experiments.

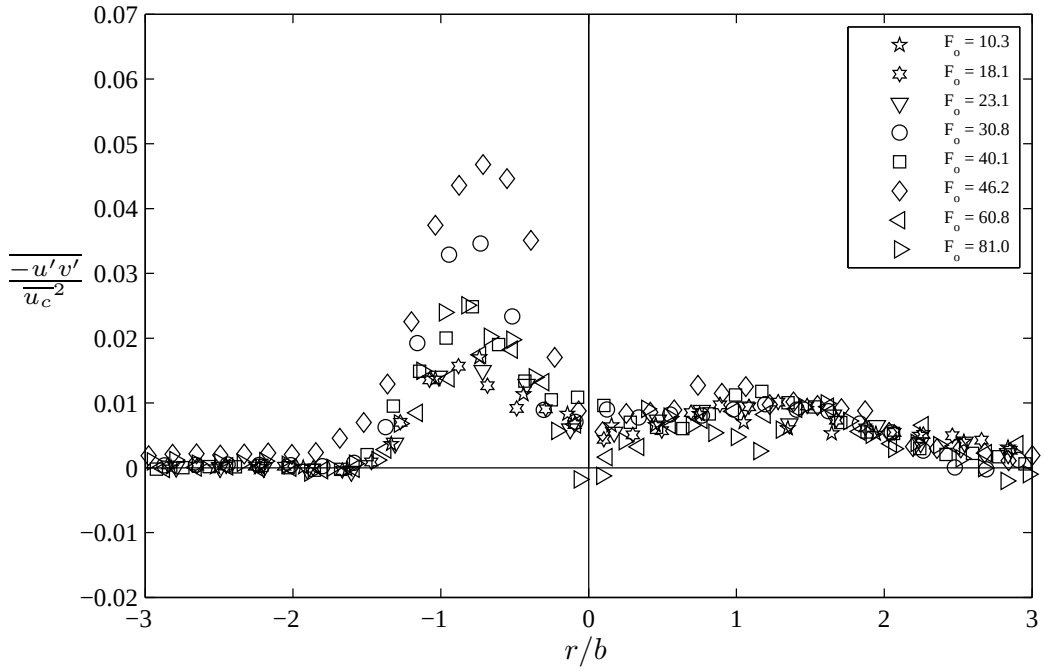

Figure B.12 – Turbulent shear intensity profiles at the return point for all 30° experiments.

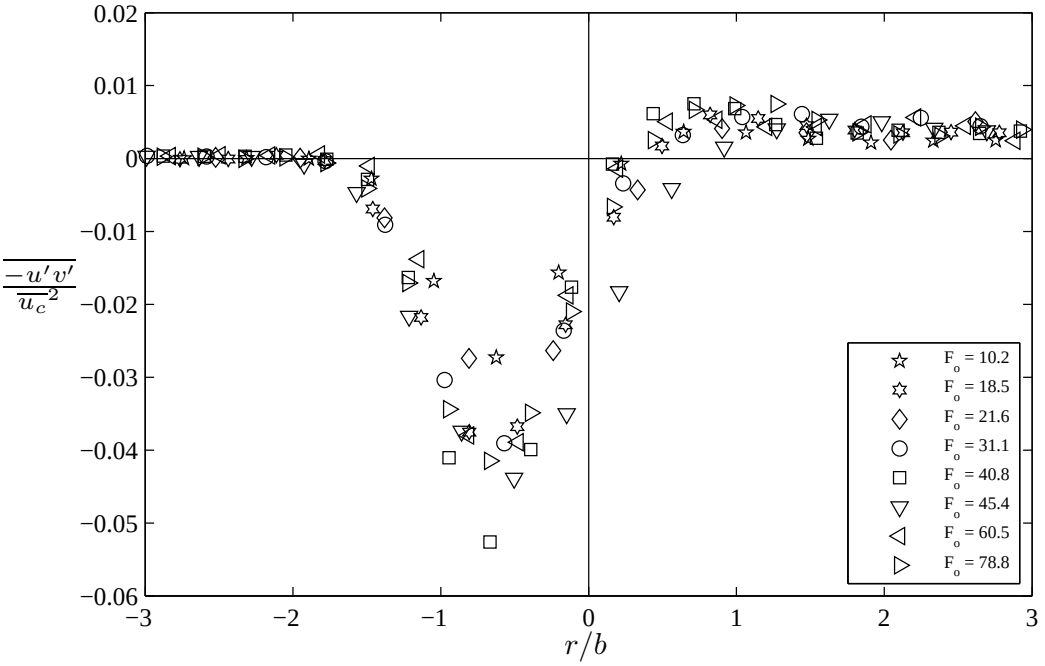

Figure B.13 – Turbulent shear intensity profiles at maximum height for all 45° experiments.

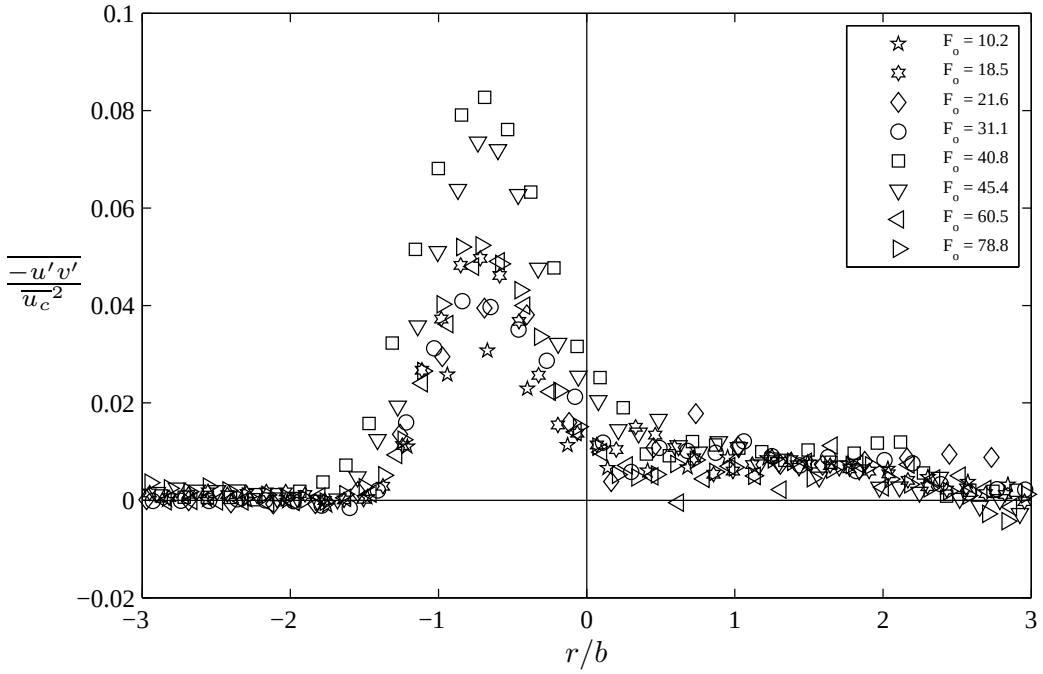

Figure B.14 – Turbulent shear intensity profiles at the return point for all 45° experiments.

Appendix C

Additional Boundary Interaction Material

C.1 Experimental Conditions

Table C.1 – Experimental conditions and coefficients from chapter 7 of the present study.

θ_o	F_o	d (mm)	H_o (mm)	Q_o (L/min)	Duration (s)	x_m/d	z_m/d	s_m/d	U_o/u_m	b/d (at x_m)	z_{me}/d	x_r/d	s_r/d	U_o/u_r	b/d (at x_r)	x_{me}/d
30°	30.9	4.40	40	1.00	297	56.8	20.1	61.0	11.3	8.1	36.2	107.5	116.5	21.3	9.7	145.7
30°	31.0	4.40	80	1.00	229	57.8	19.6	62.0	11.6	7.8	35.1	101.3	111.3	19.4	12.5	138.6
30°	30.9	4.40	119	1.00	297	56.4	20.1	60.8	11.2	7.7	35.5	100.4	110.6	18.7	14.1	141.7
30°	58.0	2.43	40	0.43	297	107.8	38.7	115.9	21.3	10.8	60.3	200.6	217.9	38.5	17.6	273.9
30°	58.6	2.43	80	0.43	226	111.2	41.2	119.8	21.6	12.5	66.1	199.3	218.7	35.7	21.1	273.3
30°	57.9	2.43	120	0.42	297	108.6	39.2	116.8	21.4	10.7	60.7	189.4	209.2	34.3	23.6	258.5
45°	31.1	4.40	40	1.00	297	59.1	36.9	71.3	15.0	6.9	50.7	113.2	138.8	27.9	11.9	151.2
45°	31.0	4.40	81	1.00	297	61.0	37.3	73.4	15.3	7.6	52.5	106.3	134.6	24.6	16.7	149.4
45°	31.0	4.40	121	1.00	297	60.2	36.9	72.5	14.7	7.6	52.0	106.2	134.3	21.9	14.1	140.2
45°	57.9	2.43	40	0.42	297	115.1	67.7	137.1	28.4	14.7	97.1	215.6	261.7	53.8	20.0	282.7
45°	58.1	2.43	80	0.43	195	111.4	68.5	134.1	28.1	14.7	97.9	202.4	252.3	42.6	27.0	273.2
45°	58.0	2.43	119	0.43	297	111.9	68.1	134.0	27.7	13.6	95.3	197.9	248.5	41.5	29.7	270.0
60°	30.9	4.40	41	1.00	297	52.8	52.1	77.3	20.0	8.1	68.4	98.9	149.4	32.7	11.2	130.1
60°	30.9	4.40	78	1.00	144	53.8	53.0	78.3	20.3	7.7	68.3	94.7	147.8	24.2	14.3	128.9
60°	30.8	4.40	121	1.00	259	52.5	51.2	77.1	20.3	7.7	66.6	90.7	144.6	22.6	17.2	128.6
60°	58.2	2.43	40	0.43	297	97.5	95.2	142.7	36.2	16.8	128.7	188.7	280.6	61.7	25.5	259.5
60°	58.5	2.43	80	0.43	215	101.2	95.9	144.9	36.6	15.2	126.2	177.3	272.3	47.9	34.5	259.5
60°	58.3	2.43	120	0.43	174	99.9	94.6	143.9	37.7	16.3	127.2	173.5	270.5	44.0	32.2	245.0

C.2 Additional Figures

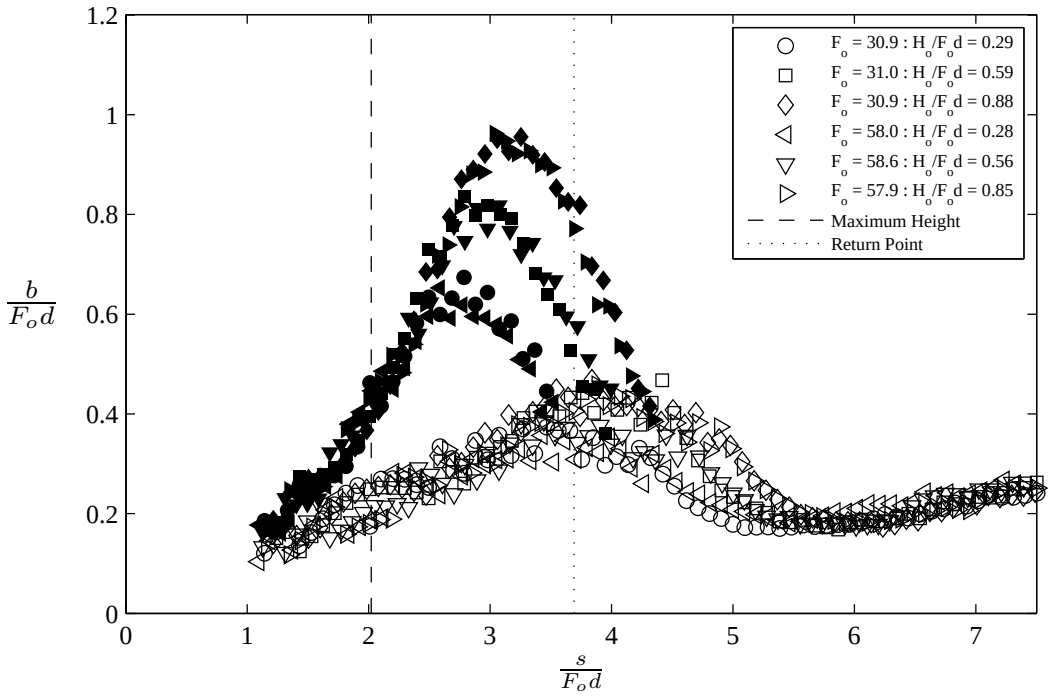

Figure C.1 – Discharge width against path length for 30° experiments with boundary. Unfilled symbols: outer side, filled symbols: inner side.

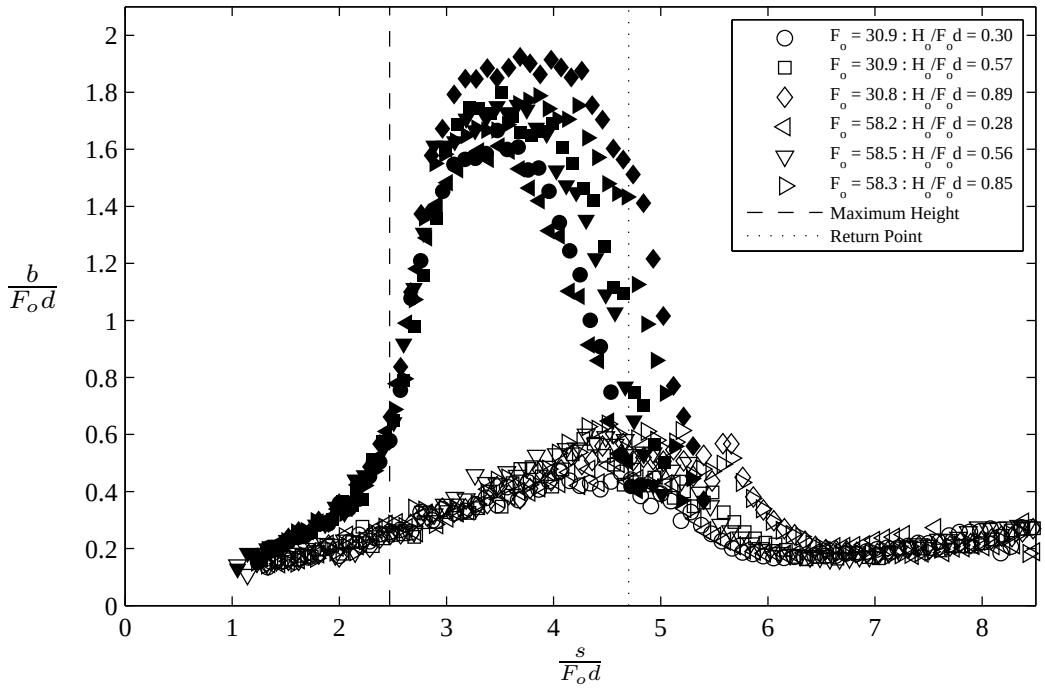

Figure C.2 – Discharge width against path length for 60° experiments with boundary. Unfilled symbols: outer side, filled symbols: inner side.

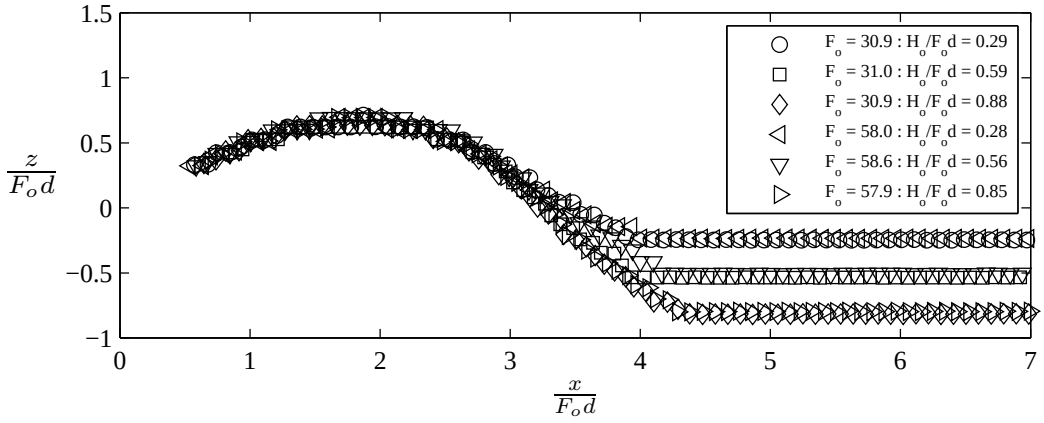

Figure C.3 – Non-dimensionalised centreline trajectory of 30° INBJ experiments for varying Froude numbers and non-dimensional source heights. The source is located at the origin.

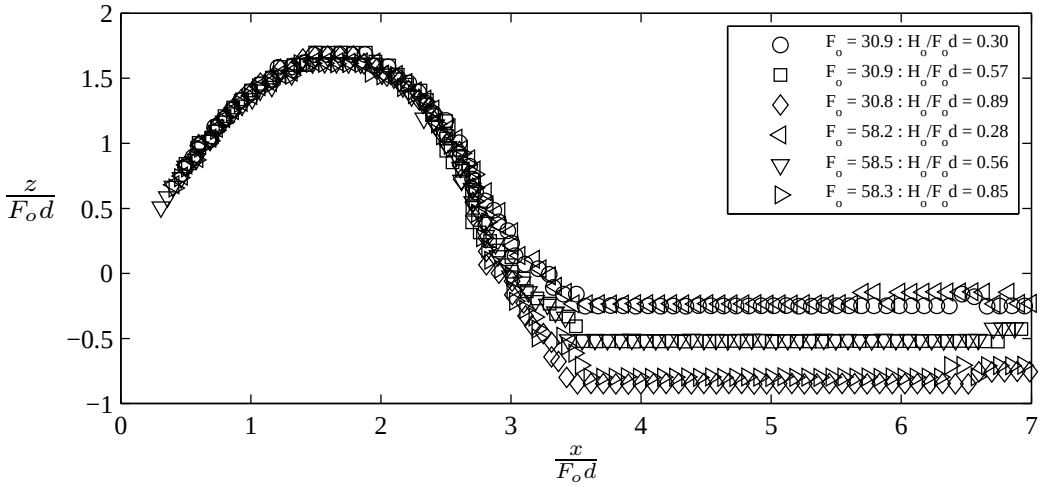

Figure C.4 – Non-dimensionalised centreline trajectory of 60° INBJ experiments for varying Froude numbers and non-dimensional source heights. The source is located at the origin.

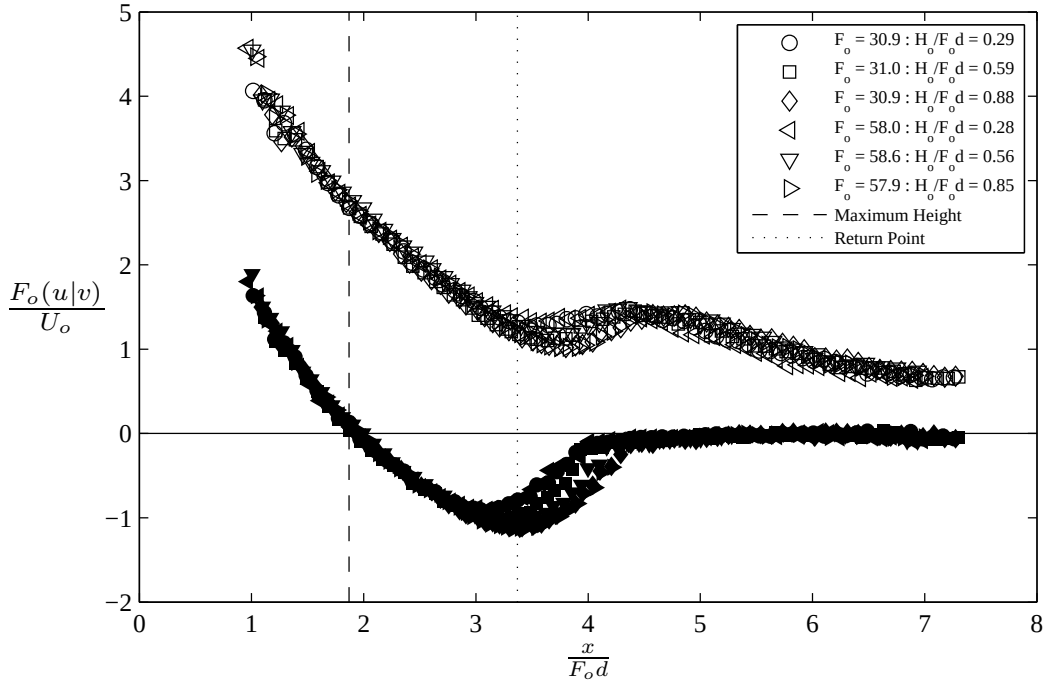

Figure C.5 – Components of centreline velocity for all 30° experiments. Unfilled symbols: horizontal velocity (u), filled symbols: vertical velocity (v).

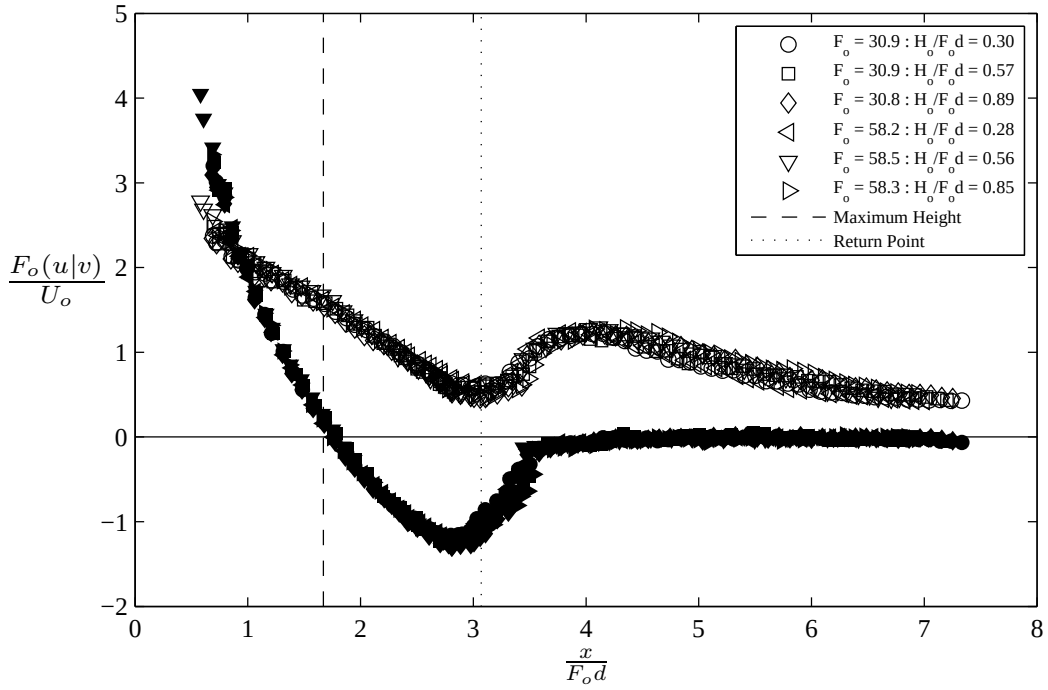

Figure C.6 – Components of centreline velocity for all 60° experiments. Unfilled symbols: horizontal velocity (u), filled symbols: vertical velocity (v).

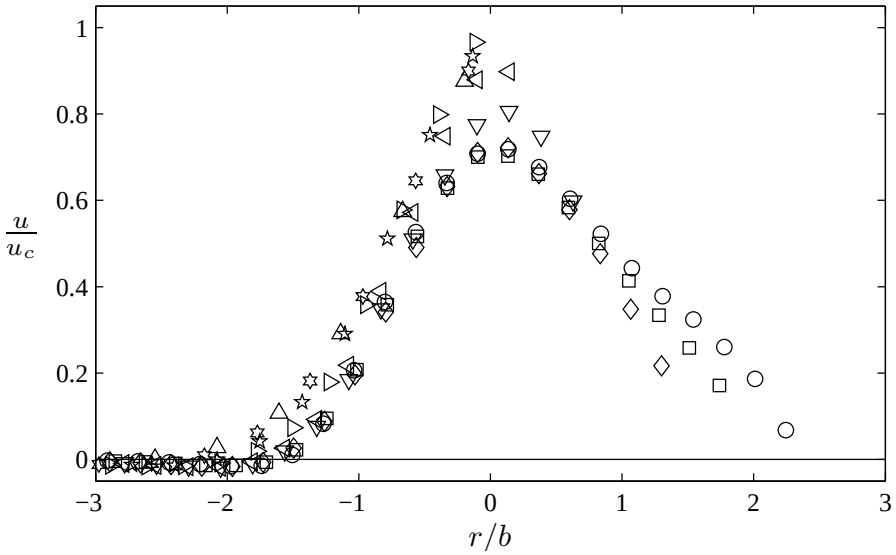

(a) Horizontal velocity

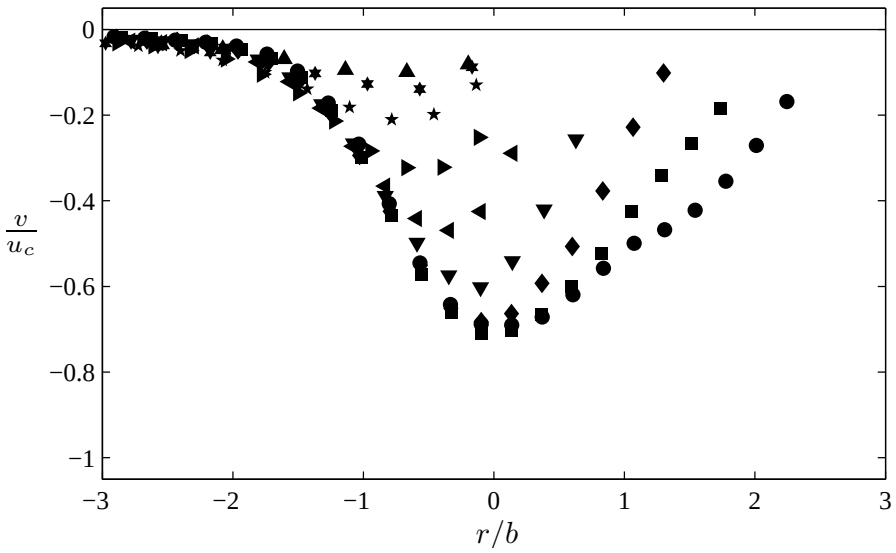

(b) Vertical velocity

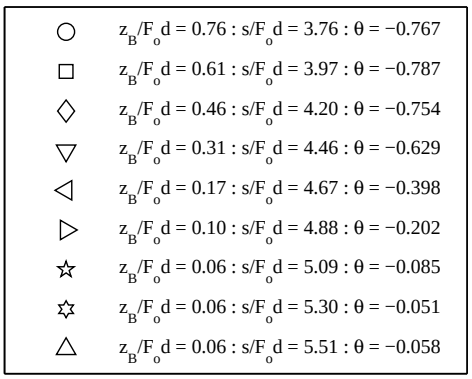

Figure C.7 – Profiles for horizontal (u) and vertical (v) components of mean velocity in the impingement region for 30° experiment with lower boundary present, $F_o = 30.9$ $H_o/(F_o d) = 0.88$.

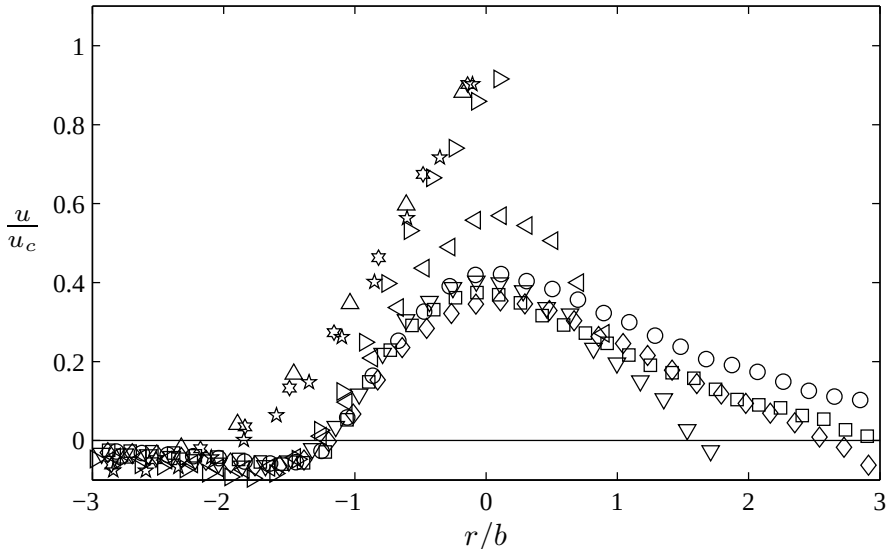

(a) Horizontal velocity

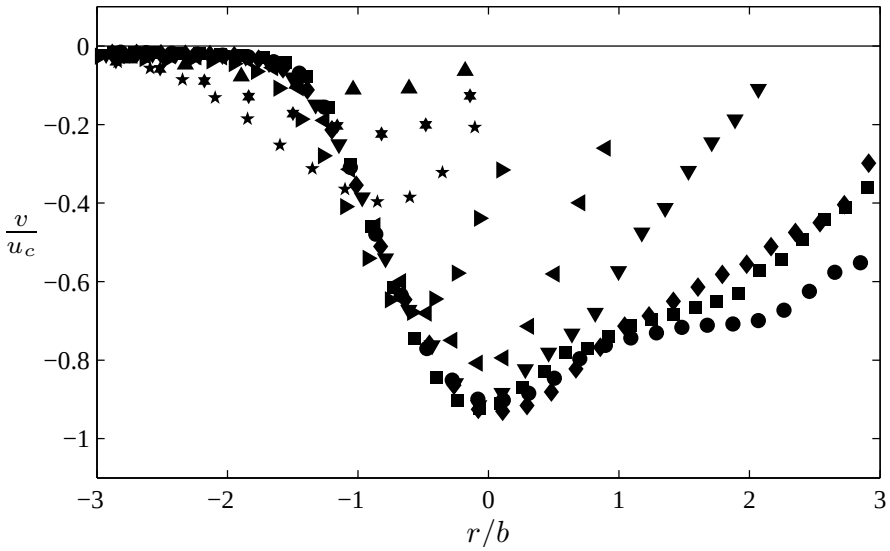

(b) Vertical velocity

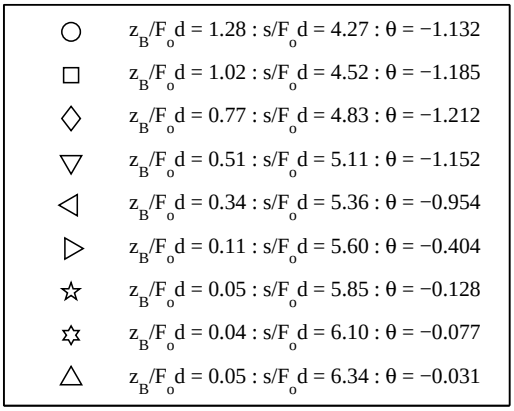

Figure C.8 – Profiles for horizontal (u) and vertical (v) components of mean velocity in the impingement region for 60° experiment with lower boundary present, $F_o = 30.8$ $H_o/(F_o d) = 0.89$.

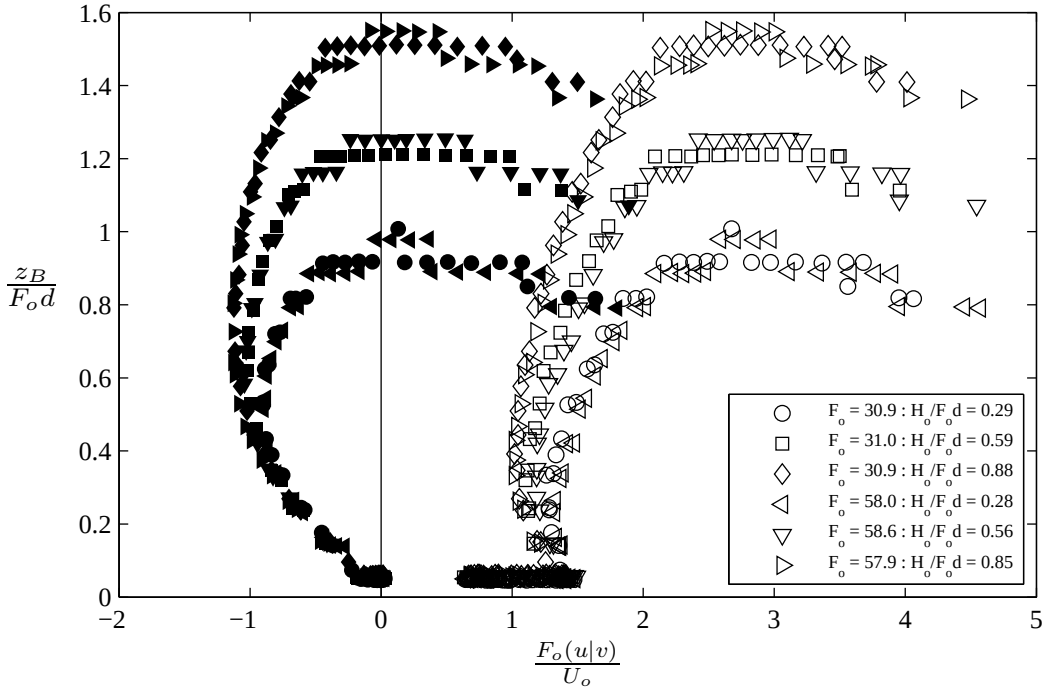

Figure C.9 – Components of mean centreline velocity for 30° experiments against distance above boundary, unfilled symbols: horizontal (u), filled symbols: vertical (v).

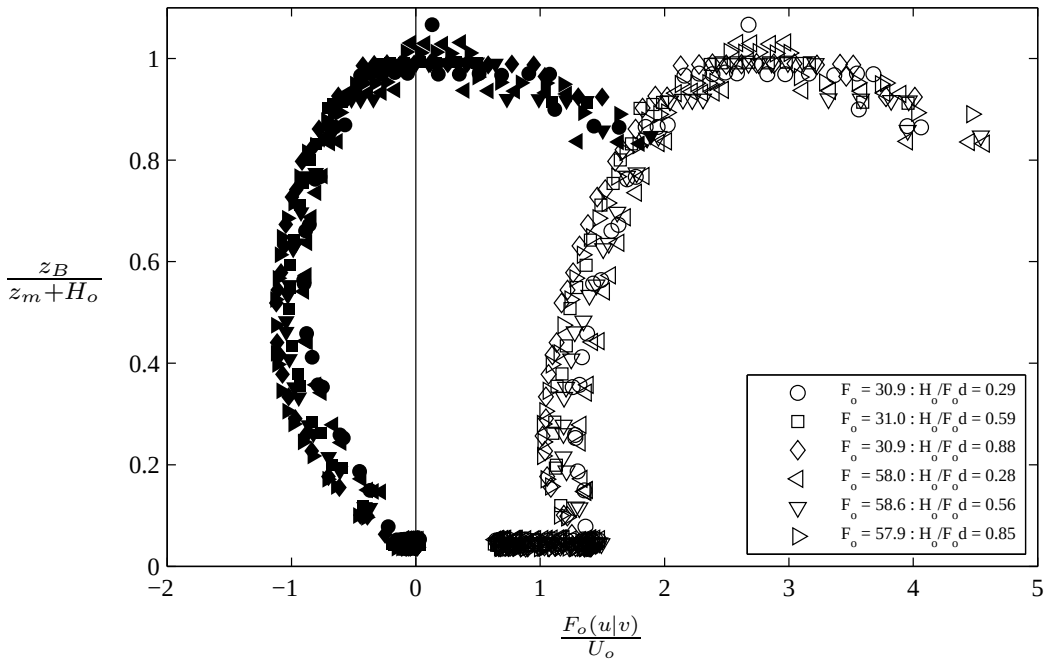

Figure C.10 – Components of mean centreline velocity for 30° experiments against non-dimensionalised distance above boundary, unfilled symbols: horizontal (u), filled symbols: vertical (v).

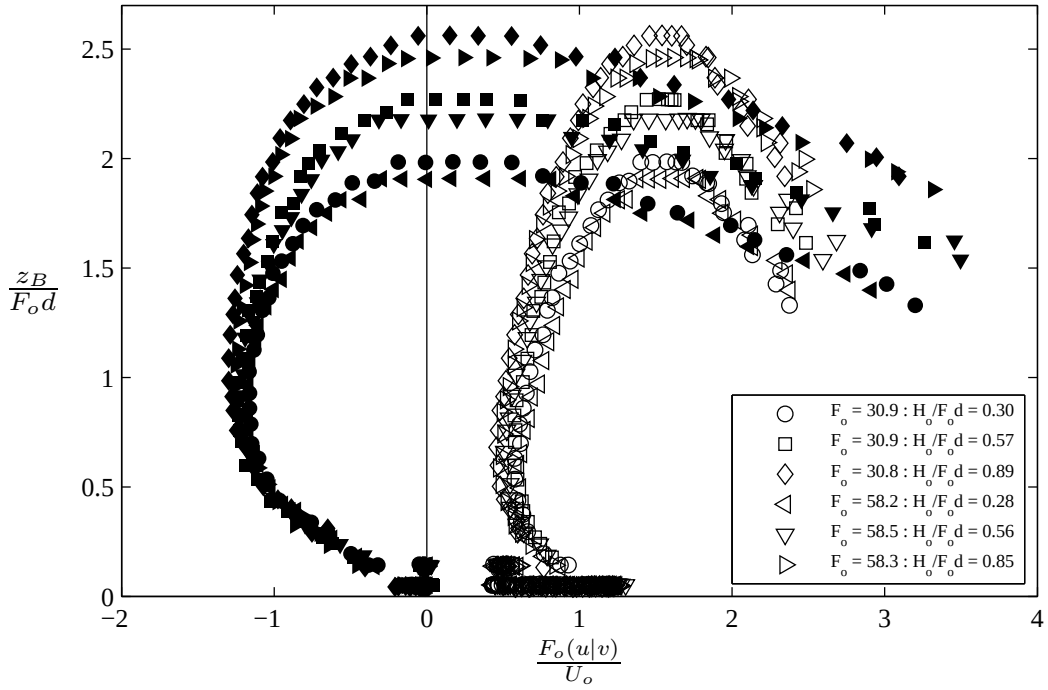

Figure C.11 – Components of mean centreline velocity for 60° experiments against distance above boundary, unfilled symbols: horizontal (u), filled symbols: vertical (v).

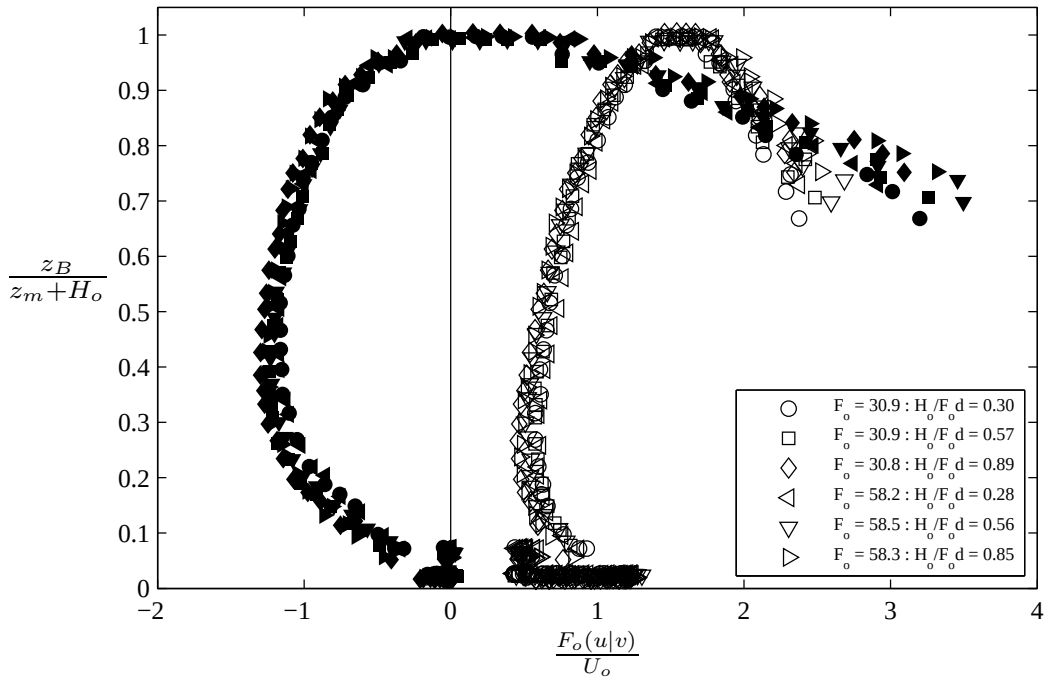

Figure C.12 – Components of mean centreline velocity for 60° experiments against non-dimensionalised distance above boundary, unfilled symbols: horizontal (u), filled symbols: vertical (v).

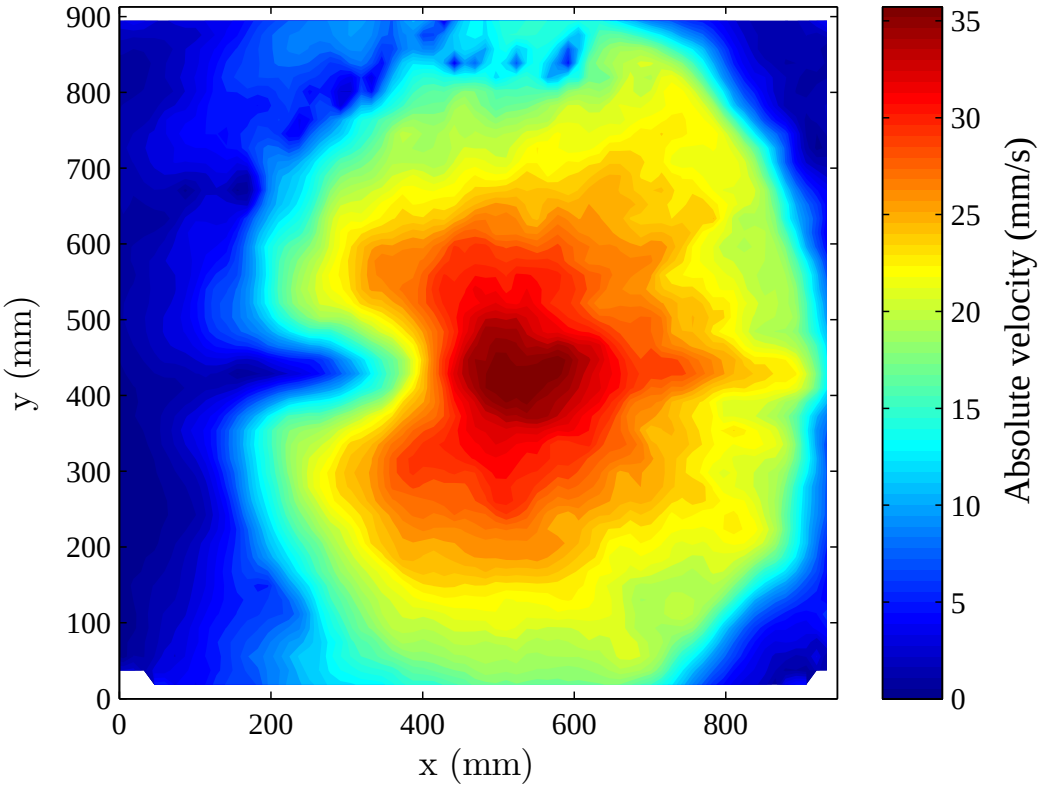

Figure C.13 – Contours of mean absolute velocity in radially spreading layer across the boundary for one 30° experiment, $F_o = 58.6$, $H_o/(F_o d) = 0.56$. Camera located above raised platform. Source located on the left hand side.

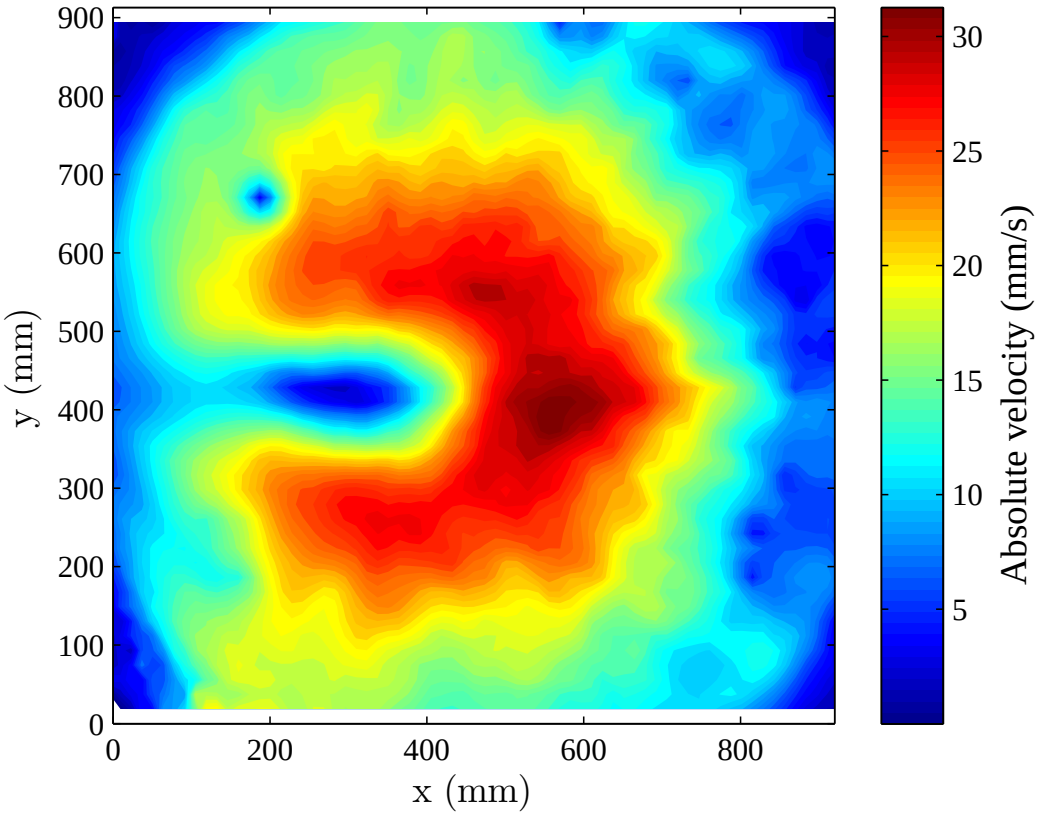

Figure C.14 – Contours of mean absolute velocity in radially spreading layer across the boundary for one 60° experiment, $F_o = 58.5$, $H_o/(F_o d) = 0.56$. Camera located above raised platform. Source located on the left hand side.

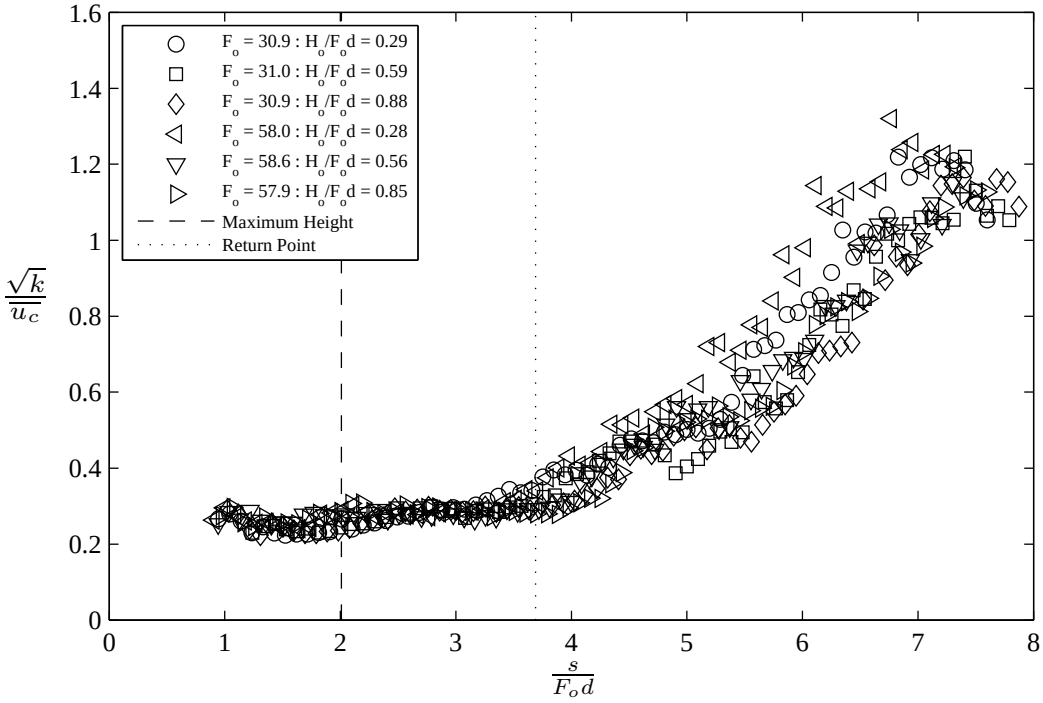

Figure C.15 – Centreline turbulent kinetic energy (k) against path length for all 30° experiments.

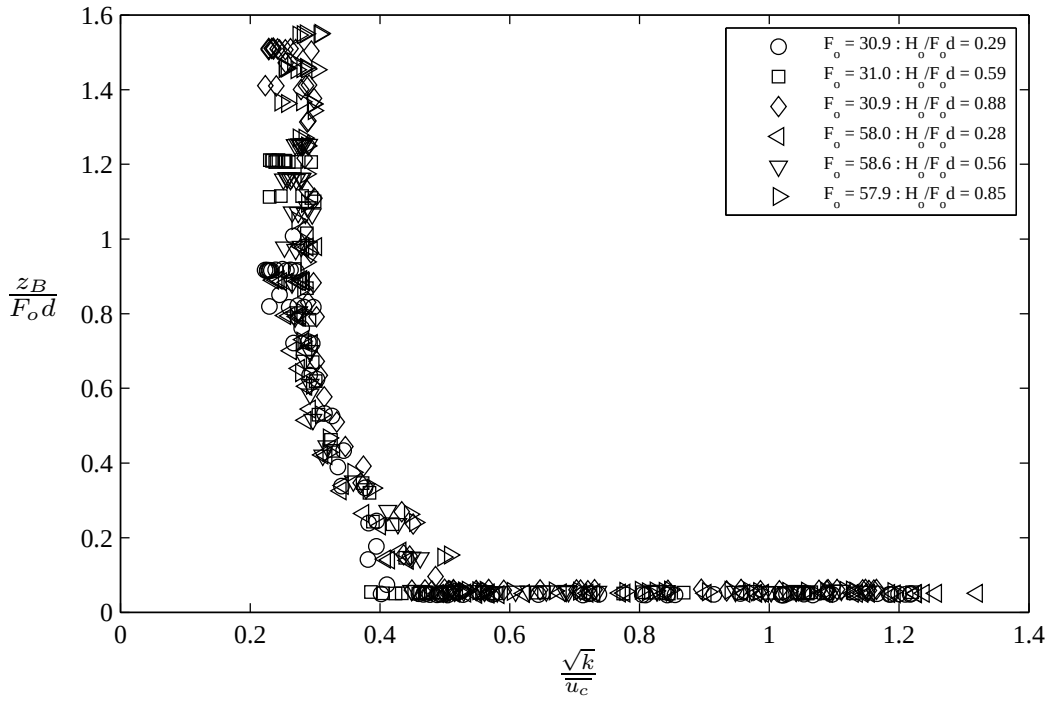

Figure C.16 – Centreline turbulent kinetic energy (k) against distance above boundary for all 30° experiments.

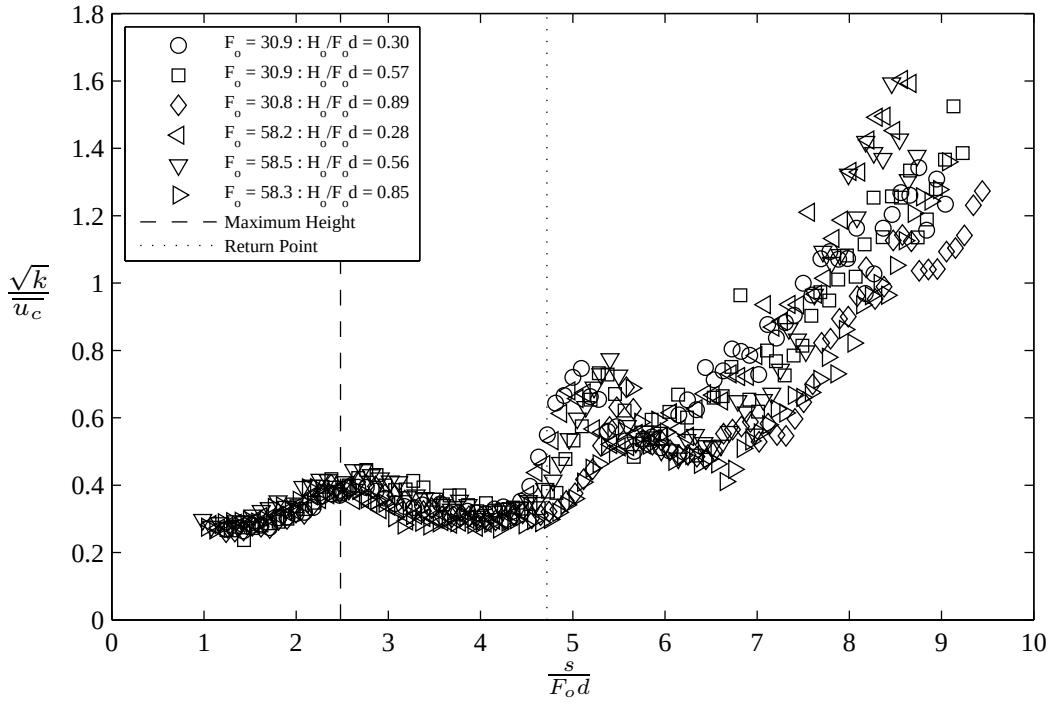

Figure C.17 – Centreline turbulent kinetic energy (k) against path length for all 60° experiments.

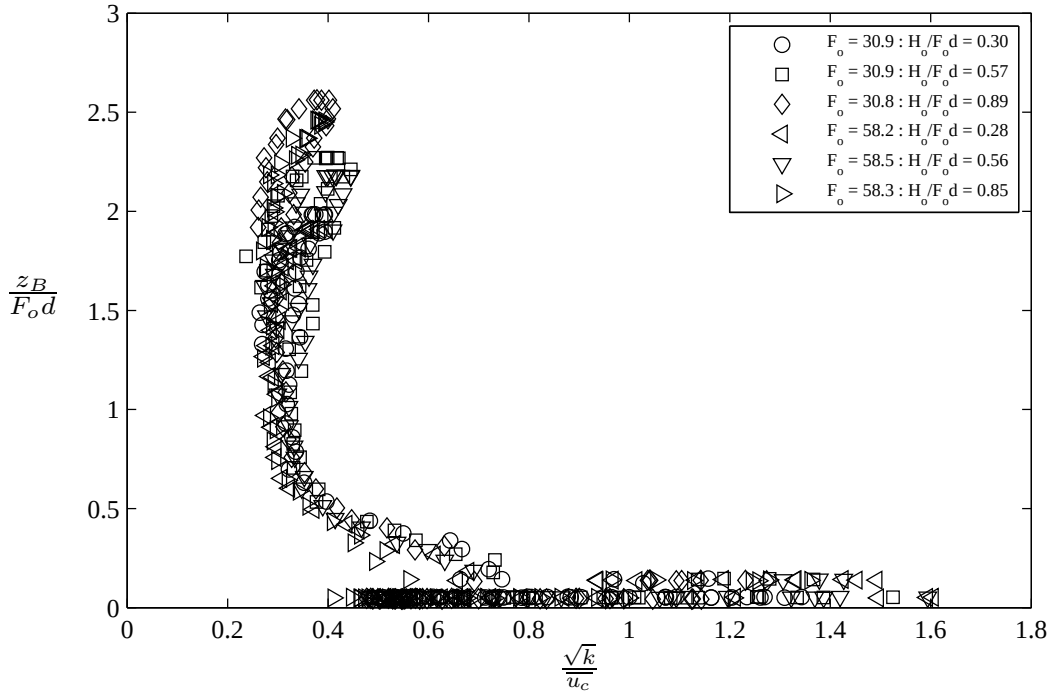

Figure C.18 – Centreline turbulent kinetic energy (k) against distance above boundary for all 60° experiments.

References

Baumgartner, D., Frick, W., & Roberts, P. 1994. Dilution Models for Effluent Discharges. *EPA/600/R-94/086, U.S. Environmental Protection Agency*, **Third Edition**.

Beltaos, S., & Rajaratnam, N. 1974. Impinging Circular Turbulent Jets. *Journal of the Hydraulics Division*, **100**(10), 1313–1328.

Blackett, S.A. 1994. *Particle Tracking Velocimetry.* M.Phil. thesis, University of Auckland.

Bleninger, T., & Jirka, G.H. 2009. *Environmental planning, prediction and management of brine discharges from desalination plants.* Tech. rept. Middle East Desalination Research Center.

Bloomfield, L.J., & Kerr, R.C. 2002. Inclined turbulent fountains. *Journal of Fluid Mechanics*, **451**, 283–294.

Brigham, E.O. 1988. *The Fast Fourier Transform and its applications.* Prentice Hall.

Cheung, S.K.B., Leung, D.Y.L., Wang, W., Lee, J.H.W., & Cheung, V. 2000. VISJET - a computer ocean outfall modelling system.

Christodoulou, G.C., Nikiforakis, I.K., & Papakonstantis, I.G. 2011. Spreading of a Negatively Buoyant Jet on a Sloping Bottom. *In: 7th International Symposium on Stratified Flows.*

Cipollina, A., Brucato, A., Grisafi, F., & Nicosia, S. 2005. Bench-scale investigation of inclined dense jets. *Journal of Hydraulic Engineering*, **131**(11), 1017–1022.

Cooley, H, Gleick, P.H., & Wolff, G. 2006. Desalination, with a grain of salt: a California perspective. *Oakland, CA: Pacific Institute for Studies in Development, Environment, and Security.*

Corrsin, S., & Uberoi, M.S. 1951. *Spectra and diffusion in a round turbulent jet.* Tech. rept. National Advisory Committee for Aeronautics.

Crowe, A.T., Davidson, M.J., & Nokes, R.I. 2010. Inclined negatively buoyant jets and seabed impingement. *In: International Conference on Marine Waster Water Discharges & Coastal Environment*.

Davidson, M.J., & Pun, K.L. 2000. Locating discharge trajectories in still and moving ambient fluids. *Journal of Hydraulic Engineering*, **126**, 513–524.

Dolnicar, S., & Schäfer, A.I. 2009. Desalinated versus recycled water: Public perceptions and profiles of the accepters. *Journal of Environmental Management*, **90**(2), 888–900.

Doneker, R.L., & Jirka, G.H. 2001. CORMIX-GI systems for mixing zone analysis of brine wastewater disposal. *Desalination*, **139**(1-3), 263–274.

Einav, R., & Lokiec, F. 2003. Environmental aspects of a desalination plant in Ashkelon. *Desalination*, **156**(1-3), 79–85.

Einav, R., Harussi, K., & Perry, D. 2003. The footprint of the desalination processes on the environment. *Desalination*, **152**(1-3), 141–154.

El Saliby, I., Okour, Y., Shon, H.K., Kandasamy, J., & Kim, I.S. 2009. Desalination plants in Australia, review and facts. *Desalination*, **247**(1-3), 1–14.

Ferrari, S., & Querzoli, G. 2010. Mixing and re-entrainment in a negatively buoyant jet. *Journal of Hydraulic Research*, **48**(5), 632–640.

Fischer, H.B., List, J.E., Koh, R.C., Imberger, J., & Brooks, N.H. 1979. *Mixing in Inland and Coastal Waters*. Academic Press, Inc.

Frick, W.E. 2004. Visual Plumes mixing zone modeling software. *Environmental Modelling and Software*, **19**(7-8), 645–654.

Frick, W.E., Roberts, P.J.W., Davis, L.R., Keyes, J., Baumgartner, D.J., & George, K.P. 2003. Dilution models for effluent discharges. *Visual Plumes, EPA/600/R-03/025*, **Fourth Edition**.

Hodgkiess, T. 2009. *Assessment Of The Composition Of Desalination Plant Disposal Brines*. Tech. rept. Middle East Desalination Research Center.

Hussein, H.J., Capp, S.P., & George, W.K. 1994. Velocity measurements in a high-Reynolds-number, momentum-conserving, axisymmetric, turbulent jet. *Journal of Fluid Mechanics*, **258**, 31–75.

Jirka, G.H. 2004. Integral Model for Turbulent Buoyant Jets in Unbounded Stratified Flows. Part I: Single Round Jet. *Environmental Fluid Mechanics*, **4**(1), 1–56.

Jirka, G.H. 2008. Improved discharge configurations for brine effluents from desalination plants. *Journal of Hydraulic Engineering*, **134**(1), 116–120.

Kikkert, G.A. 2006. *Buoyant jets with two and three-dimensional trajectories*. Ph.D. thesis, University of Canterbury.

Kikkert, G.A., Davidson, M.J., & Nokes, R.I. 2007. Inclined negatively buoyant discharges. *Journal of Hydraulic Engineering*, **133**(5), 545–554.

Lai, C.C.K., & Lee, J.H.W. 2012. Mixing of inclined dense jets in stationary ambient. *Journal of Hydro-environment Research*, **6**(1), 9–28.

Lane-Serff, G.F., Linden, P.F., & Hillel, M. 1993. Forced, angled plumes. *Journal of Hazardous Materials*, **33**(1), 75–99.

Lattemann, S., & Höpner, T. 2008. Environmental impact and impact assessment of seawater desalination. *Desalination*, **220**(1-3), 1–15.

Lattemann, S., Kennedy, M.D., Schippers, J.C., & Amy, G. 2010. *Chapter 2 Global Desalination Situation*.

Launder, B.E., & Rodi, W. 1983. The turbulent wall jet measurements and modeling. *Annual Review of Fluid Mechanics*, **15**(1), 429–459.

Law, A.W.K., & Wang, H. 2000. Measurement of mixing processes with combined digital particle image velocimetry and planar laser induced fluorescence. *Experimental Thermal and Fluid Science*, **22**(3-4), 213–229.

Lee, J.H.W., & Chu, V.H. 2003. *Turbulent jets and plumes: a Lagrangian approach*. Springer Netherlands.

Lee, Joseph H.W., & Cheung, V. 1990. Generalized Lagrangian model for buoyant jets in current. *Journal of Environmental Engineering*, **116**(6), 1085–1106.

Lindberg, W.R. 1994. Experiments on negatively buoyant jets, with and without cross-flow. *NATO ASI Series E Applied Sciences-Advanced Study Institute*, **255**, 131–146.

Loya-Fernández, Á., Ferrero-Vicente, L.M., Marco-Méndez, C., Martínez-García, E., Zubcoff, J., & Sánchez-Lizaso, J.L. 2012. Comparing four mixing zone models with brine discharge measurements from a reverse osmosis desalination plant in Spain. *Desalination*, **286**, 217–224.

MacLatchy, Michael Ray. 1999. *Radially spreading surface flows*. Ph.D. thesis, The University of British Columbia, Canada.

Marti, C.L., Antenucci, J.P., Luketina, D., Okely, P., & Imberger, J. 2010. Near-field dilution characteristics of a negatively buoyant hypersaline jet generated by a desalination plant. *Journal of Hydraulic Engineering*, **137**(1), 57–65.

Morton, B.R., Taylor, G., & Turner, J.S. 1956. Turbulent gravitational convection from maintained and instantaneous sources. *Proceedings of the Royal Society of London. Series A. Mathematical and Physical Sciences*, **234**(1196), 1–23.

Nemlioglu, S., & Roberts, P. J. 2006. Experiments on Dense Jets Using Three-Dimensional Laser-Induced Fluorescence (3DLIF). *In: International Conference on Marine Waster Water Discharges & Coastal Environment (MWWD).*

NIST-SEMATECH. 2012. *e-Handbook of Statistical Methods.* Retrieved from http://www.itl.nist.gov/div898/handbook/.

Nokes, R. 2012. *Streams Version 2.00 - System Theory and Design.*

Oliver, C.J. 2012. *Near Field Mixing of Negatively Buoyant Jets.* Ph.D. thesis, University of Canterbury.

Oliver, C.J., Davidson, M.J., & Nokes, R.I. 2008. k-ϵ Predictions of the initial mixing of desalination discharges. *Environmental Fluid Mechanics*, **8**(5-6), 617–625.

Oliver, C.J., Davidson, M.J., & Nokes, R.I. 2013. Predicting the near-field mixing of desalination discharges in a stationary environment. *Desalination*, **309**, 148–155.

Otranto, F. 2004. *Laboratory modeling of sea-brine discharges.* Undergraduate Report. The University of Western Australia.

Palomar, P., & Losada, I.J. 2011. *Desalination, trends and technologies.* InTech.

Palomar, P., Lara, J.L., & Losada, I.J. 2012a. Near field brine discharge modeling part 2: Validation of commercial tools. *Desalination*, **290**, 28–42.

Palomar, P., Lara, J.L., Losada, I.J., Rodrigo, M., & Alvárez, A. 2012b. Near field brine discharge modelling part 1: Analysis of commercial tools. *Desalination*, **290**, 14–27.

Panchapakesan, N.R., & Lumley, J.L. 1993. Turbulence measurements in axisymmetric jets of air and helium. Part 1. Air jet. *Journal of Fluid Mechanics*, **246**, 197–223.

Papakonstantis, I.G., & Christodoulou, G.C. 2010. Spreading of round dense jets impinging on a horizontal bottom. *Journal of Hydro-Environment Research*, **4**(4), 289–300.

Papakonstantis, I.G., Christodoulou, G.C., & Papanicolaou, P.N. 2011a. Inclined negatively buoyant jets 1: Geometrical characteristics. *Journal of Hydraulic Research*, **49**(1), 3–12.

Papakonstantis, I.G., Christodoulou, G.C., & Papanicolaou, P.N. 2011b. Inclined negatively buoyant jets 2: Concentration measurements. *Journal of Hydraulic Research*, **49**(1), 13–22.

Papanicolaou, P.N. 1984. *Mass and Momentum Transport in a Turbulent Buoyant Vertical Axisymmetric Jet*.

Papanicolaou, P.N., & List, E.J. 1988. Investigations of round vertical turbulent buoyant jets. *Journal of Fluid Mechanics*, **195**, 341–391.

Papanicolaou, P.N., Papakonstantis, I.G., & Christodoulou, G.C. 2008. On the entrainment coefficient in negatively buoyant jets. *Journal of Fluid Mechanics*, **614**, 447–470.

Pope, S.B. 2000. *Turbulent flows*. Cambridge University Press.

Raffel, M., Willert, C.E., Wereley, S.T., & Kompenhans, J. 2007. *Particle Image Velocimetry: A Practical Guide*. Springer.

Rajaratnam, N., Zhu, D.Z., & Rai, S.P. 2010. Turbulence measurements in the impinging region of a circular jet. *Canadian Journal of Civil Engineering*, **37**(5), 782–785.

Roberts, P.J.W., & Sternau, R. 1997. Mixing zone analysis for coastal wastewater discharge. *Journal of Environmental Engineering*, **123**(12), 1244–1250.

Roberts, P.J.W., & Toms, G. 1987. Inclined Dense Jets In Flowing Current. *Journal of Hydraulic Engineering*, **113**(3), 323–341.

Roberts, P.J.W., Ferrier, A., & Daviero, G. 1997. Mixing in inclined dense jets. *Journal of Hydraulic Engineering*, **123**(8), 693–699.

Shao, D., & Law, A.W. 2010. Mixing and boundary interactions of 30° and 45° inclined dense jets. *Environmental Fluid Mechanics*, **10**(5), 521–553.

Shao, D., & Law, A.W.K. 2011. Boundary impingement and attachment of horizontal offset dense jets. *Journal of Hydro-Environment Research*, **5**(1), 15–24.

Townsend, A.A.R. 1980. *The structure of turbulent shear flow*. Cambridge University Press.

Ulasir, M. 2001. *Experimental and numerical study of submerged, round buoyant jets impinging on a horizontal surface*. Ph.D. thesis, University of Michigan.

Ulasir, M., & Wright, S.J. 2003. Influence of downstream control and limited depth on flow hydrodynamics of impinging buoyant jets. *Environmental Fluid Mechanics*, **3**(2), 85–107.

Voutchkov, N. 2011. Overview of seawater concentrate disposal alternatives. *Desalination*, **273**(1), 205–219.

Wang, H., & Law, A. 2002. Second-order integral model for a round turbulent buoyant jet. *Journal of Fluid Mechanics*, **459**, 397–428.

WHO. 2007. *Desalination for safe water supply: Guidance for the health and environmental aspects applicable to desalination.* Tech. rept. World Health Organization.

Wilkinson, D. L., & Wood, I. R. 1971. A rapidly varied flow phenomenon in a two-layer flow. *J. Fluid Mech.*, **47**(2), 241–256.

Wright, S.J., Roberts, P.J., Yan, Z., & Bradley, E.N. 1991. Surface dilution of round submerged buoyant jets. *Journal of Hydraulic Research*, **29**(1), 67–89.

Wyganski, I., & Fielder, H. 1969. Some measurements in the self-preserving jet. *Journal of Fluid Mechanics*, **38**(3), 577–612.

Yannopoulos, P.C., & Bloutsos, A.A. 2012. Escaping mass approach for inclined plane and round buoyant jets. *Journal of Fluid Mechanics*, **695**, 81–111.

Ying, C., Davidson, M.J., Wang, H.W., & Law, A.W.K. 2004. Radial velocities in axisymmetric jets and plumes. *Journal of Hydraulic Research*, **42**(1), 29–33.

Zeitoun, M.A. 1970. *Conceptual Designs of Outfall Systems for Desalting Plants.* Tech. rept.